# INNOVATIVE SOLUTIONS AND ADVANCED TECHNOLOGICAL APPROACHES IN ENGINEERING

*Editors*
Prof. Dr. Mustafa BOZ
Assoc. Prof. Dr. Mehmet AKKAŞ
Assoc. Prof. Dr. Musa KILIÇ



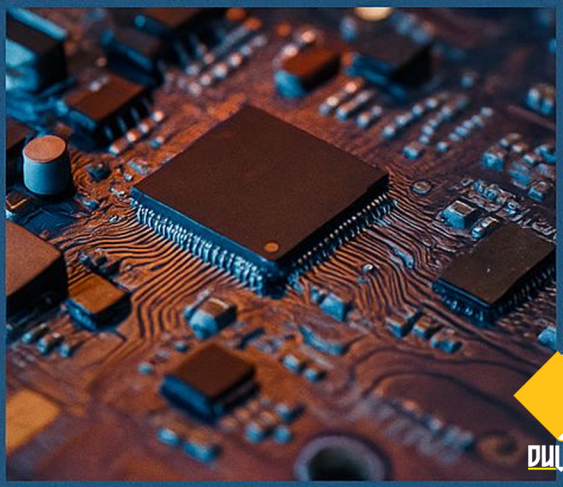


DUVAR

# INNOVATIVE SOLUTIONS AND ADVANCED TECHNOLOGICAL APPROACHES IN ENGINEERING

**Editors**

**Prof. Dr. Mustafa BOZ**

**Assoc. Prof. Dr. Mehmet AKKAŞ**

**Assoc. Prof. Dr. Musa KILIÇ**

*Innovative Solutions and Advanced Technological Approaches in Engineering*
*Editors: Prof. Dr. Mustafa BOZ, Assoc. Prof. Dr. Mehmet AKKAŞ,*
*Assoc. Prof. Dr. Musa KILIÇ*

**Editor in chief:** Berkan Balpetek
**Cover and Page Design:** Duvar Design
**Printing:** November-2025
**Publisher Certificate No:** 49837
**ISBN:** 978-625-8734-22-5


*853 Sokak No:13 P.10 Kemeraltı-Konak/İzmir*
*Tel: 0 232 484 88 68*
*www.duvaryayinlari.com*
*duvarkitabevi@gmail.com*

**TABLE OF CONTENTS**

# Chapter 1

# BENDING BEHAVIOR OF SINGLE, DOUBLE AND HYBRID LAYER COMPOSITE SANDWICH STRUCTURES WITH 3D-PRINTED CORE MATERIALS

**Serdar KAVELOĞLU[1], Şemsettin TEMİZ[2]**

## 1. INTRODUCTION

Composite sandwich structures are preferred in land, air and sea vehicles, transportation, military areas and many other sectors due to their high strength and bending rigidity compared to their mass [1-4]. Sandwich structures are composite structural elements consisting of bonding a core structure between the bottom and top facesheets. The facesheets are thin, rigid, with high density, and the core is thicker than the facesheet and low density materials are preferred [5]. There are many studies on the mechanical properties of sandwich structures such as compression, impact and bending strength, and they continue to be researched and developed to have the desired properties. Glass fiber epoxy composite [6,7], carbon fiber epoxy composite [8-11], CNT (carbon nano tube) reinforced carbon fiber epoxy composite [12], aluminum [13,14], PLA [13,16] and ABS [15,16] materials were used to investigate the mechanical properties as the facesheets of composite sandwich structures. On the other hand, the mechanical properties of sandwich structures made of cores with different materials such as aluminum [6,14], polypropylene [7], nomex [9,10], aramid [12], PLA [15,16] were also investigated. In recent years, production and prototyping has gained momentum using 3D printing technology, which is called additive manufacturing method. Additive manufacturing method is preferred because it requires low cost, less time, machinery and labor [17]. In addition, the production of complex parts with additive manufacturing without the need for traditional production methods such as molding, casting, injection and cutting provides a great advantage [13]. As in this article, research has been carried out on the determination of the mechanical properties of composite sandwich structures produced using a 3D printer

[1]Asst. Prof. Dr., Kahramanmaraş İstiklal University, Department of Mechanical Engineering, Kahramanmaraş, Turkey, serdar.kaveloglu@istiklal.edu.tr, (ORCID: 0000-0003-0157-7314)
[2]Prof. Dr., İnönü University, Department of Mechanical Engineering, Malatya, Turkey, semsettin.temiz@inonu.edu.tr, (ORCID: 0000-0002-6737-3720)

[16,18,19]. It has been determined that the use of PLA honeycomb structure with the same mass instead of a PLA flat plate in sandwich structures increases the bending stiffness of the sandwich structure three times [15]. At the same time, researches on different core geometries of sandwich structures have been carried out. The flexural strength performances of single-layer sandwich structures with core geometry of bi-grid, tri-grid, quadri-grid, and kagome-grid produced by 3D printer were investigated by experimental and finite element method, and the quadri-grid sandwich structure showed better mechanical performance than the other three structures [8]. In sandwich composite structures produced in truss, conventional honeycomb and reentrant honeycomb geometries, the highest bending strength was obtained in structures with truss geometry [11]. Honeycomb, inversed honeycomb and kagome geometries have the best performance in inversed honeycomb geometry [13]. In honeycomb, rhombus, rectangle and circle geometries, it was determined that the maximum load and modulus of elasticity increased as the core density increased, and the best results were found in rhombus geometry [18]. Increasing the height of the facesheet [6,10] and the core [6,7,14,19] in the sandwich structure increased the flexural strength of the structure. The effect of the core height of the sandwich structure on the mechanical properties is more effective than the facesheet height [6].

In the three-point bending tests, studies were carried out at different distances such as 80, 180, 200, 250, 300 mm between the lower two supports. As the distance between the supports increased, the stiffness of the sandwich structure and the shear stress of the core decreased significantly, but the flexural strength of the facesheet increased [7,10].

Using multi-layered cores in sandwich structures ensures that a possible break is transferred gradually inside the structure and thus the breakage is delayed. Therefore, its use in aerospace engineering has increased in recent years [20]. In the bending [7,10,21] and compression tests [10] of single and multi-layer sandwich structures, it has been observed that the mechanical properties of multi-layer structures are superior.

Most of the studies in the literature have focused on the mechanical properties of single-layer sandwich structures. Considering that sandwich structures can be exposed to one or more possible loads such as impact, compression, bending, peeling and tensile, more mechanical properties of multi-layer sandwich structures should be determined. Because multi-layer structures can distribute the load in the structure more smoothly and by delaying [10]. In this sense, multi-layer sandwich structures are of vital importance for a damaged vehicle to reach its destination, especially when considered for aviation and transportation sectors.

In this study, the bending strength of single-layer composite sandwich structures was investigated by using honeycomb geometry cores with three different cell widths on surface areas close to each other, which has not been done before in the literature. At the same time, investigating the bending strengths of double-layer sandwich structures with the same and hybrid cell widths makes our study even more unique. Experimental research was carried out on the three-point bending strength of sandwich structures obtained by bonding CFRP plates with PLA core produced in a 3D printer, and the core shear stress and facing stress of the sandwich structure were determined. A comparison was made between the mechanical properties of single-layer and double-layer sandwich structures.

## 2. MATERIALS AND METHOD

The dimensions of the bending specimens were determined as 200 mm long (L) and 50 mm wide (W) as shown in Figure 1(a) according to the ASTM C393-16 [22] standard. While designing, a large honeycomb plate was drawn first. Then, the intersection point of the diagonals of the 200 mm - 50 mm rectangle is accepted as the center of the inner tangent circle of a honeycomb, and the rectangle is cut. Bending test specimens were designed using SOLIDWORKS® 2018 Computer Aided Design (CAD) software in 3 different geometries with cell height (h), cell widths (d) of 6 mm, 9 mm and 12 mm and cell wall thicknesses (t) of 0.8 mm, 1.2 mm and 1.6 mm, respectively (Figure 1(b)).

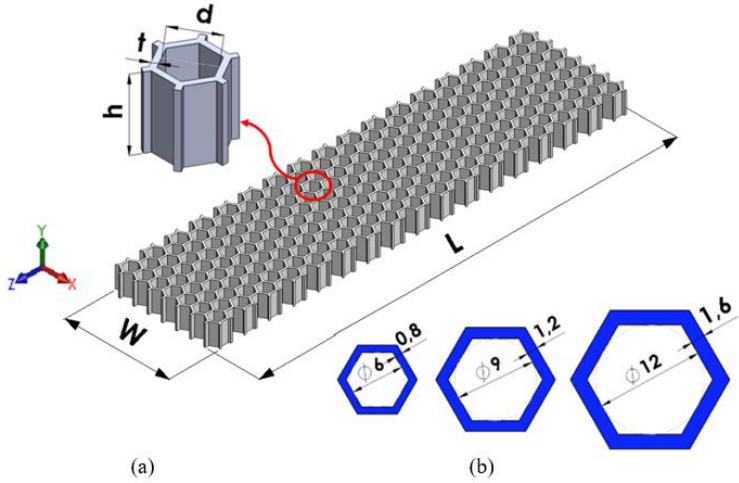


Figure 1. (a) Displaying the dimensions of honeycomb structures in SOLIDWORKS® 2018 CAD (b) Display of the dimensions of a honeycomb with three different cell widths and cell wall thickness (unit:mm).

When the cell widths were increased, the cell wall thicknesses were also increased to obtain an equal surface area. Since the nozzle diameter is 0.4 mm in the 3D printer, the cell wall thicknesses are increased in multiples of 0.4. The surface areas of the designed geometries were measured in SOLIDWORKS® 2018. Table 1 shows the surface areas of the cells as well as the percentage changes of the other surface areas according to the surface area of the cell width of 6 mm. It was observed that the bending surface areas of three different cells were close to each other.

Table 1: Surface areas of samples with a length of 200 mm and a width of 50 mm

| **Cell width D (mm)** | **Cell wall thickness t (mm)** | **Cell surface area ($mm^2$)** | **Surface area variation (%)** |
|---|---|---|---|
| 6 | 0.8 | 2228.70 | - |
| 9 | 1.2 | 2146.59 | - 3.68 |
| 12 | 1.6 | 2193.48 | - 1.58 |

Ultimaker Cura 4.10.0 [23] CAM software was used to generate the G-codes in order to produce the samples with the Ultimaker 2+ [24] 3D printer seen in Figure 2 (a) and (b). The G-codes of the design were created by selecting the parameters specified in Table 2.

Table 2: Ultimaker Cura 4.10.0 CAM parameters

| | |
|---|---|
| Printer name | Ultimaker 2+ |
| Material | PLA |
| Filament diameter | 2.85 mm |
| Layer thickness | 0.2 mm |
| Wall thickness | 0.8 / 1.2 / 1.6 mm |
| Top/bottom thickness | 0 |
| Infill density | %100 |
| Infill pattern | Lines |
| Print speed | 60 mm/s |
| Idle speed | 150 mm/s |
| Nozzle temperature | 240°C |
| Hot plate temperature | 60°C |

Before starting the production of the cores, the printer was manually calibrated for the table. A white Ultimaker brand PLA filament was attached to the 3D printer. Samples with a cell height of 20 mm for a single core and 10 mm for a double core, as seen in Figure 2 (c), were produced. The print table

and nozzle temperature values of the 3D printer were determined by the product specification.


Figure 2. (a) Image of Ultimaker 2+ 3D printer; (b) Print image of PLA sample; (c) Image of cores produced at different cell widths and heights.

Figure 3 shows a double-layer hybrid composite sandwich structure consisting of facesheet, core and adhesive part. Here, the image of the movable pin applying force with the fixed bottom two pins during the three-point bending test is shown as an example. 1 mm thick CFRP plates were used as the facesheet in sandwich structures. CFRP plates supplied from Dostkimya company were produced from carbon fiber epoxy prepreg in hot presses with smooth surfaces and equal thickness [25]. Before bonding the plates, precision cuts were made on the CNC cutting machine in the dimensions of 200 mm-50 mm.

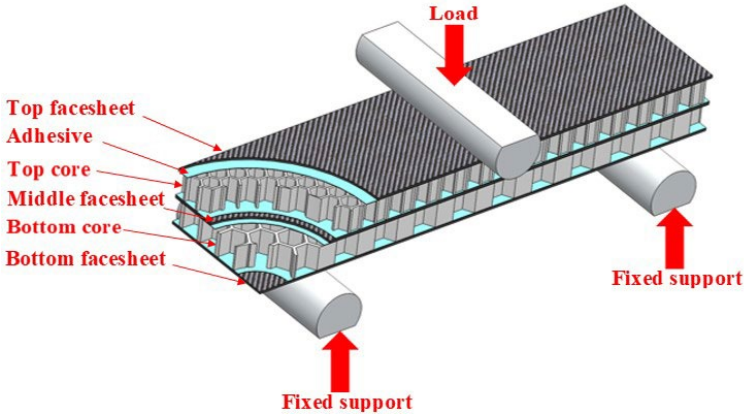


Figure 3. Schematic view of the three point bending test set-up of the hybrid composite sandwich structure

The mechanical properties of the fundamental materials are summarized in Tables 3 and 4.

Table 3: Mechanical properties of PLA core [26]

| | |
|---|---|
| Density [g/cm$^3$] | 1.24 |
| Tensile strength [MPa] | 37 |
| Tensile modulus [MPa] | 3250 |
| Flexural strenght [MPa] | 96.8 |
| Flexural modulus [MPa] | 3019 |

Table 4: Mechanical properties of CFRP composite face sheet [27]

| | |
|---|---|
| Density [g/cm$^3$] | 1.55 |
| Compressive strength [MPa] | 475 |
| Tensile strength [MPa] | 775 |
| Tensile modulus [GPa] | 63 |
| Flexural strenght [MPa] | 725 |
| Flexural modulus [GPa] | 60 |
| Face thickness [mm] | 1 |

Two-component epoxy-based Araldite® 2015 adhesive [27], whose bonding stages are shown from above to below in Figure 4, was used for bonding CFRP plates to the cores produced in additive manufacturing. Adhesive was applied to the CFRP plates with the help of a spatula and the materials were adhered by putting them on top of each other. The bonded sandwich structures were kept at 0.5 MPa pressure for 24 hours for the adhesive to cure. A total of 27 bending test specimens produced to test 3 of each parameter are shown in figure 4.

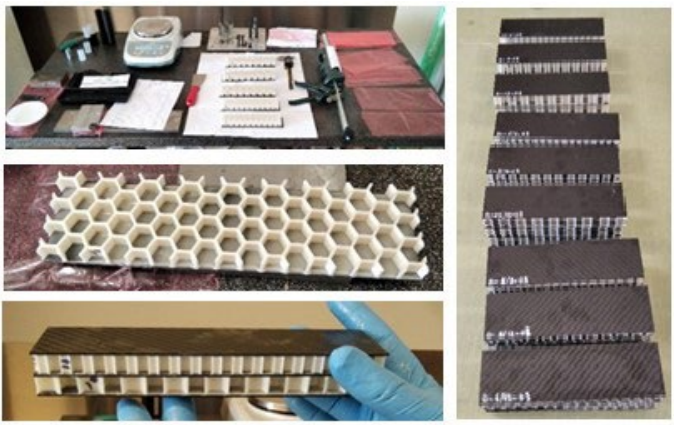

Figure 4. Bonding stage images of sandwich structures.

With a precision balance of KERN PLS 6200-2A (capacity: 6.200 g, accuracy: 0.01 g), mass measurements of core and CRFP plates were made separately for each sample before and after bonding. The amount of adhesive used was found by

measuring the total mass of the samples after bonding and curing. In the SOLIDWORKS® 2018 program, the densities of the sandwich structures were calculated using the volume values of the cores. These values are shown in Table 5. It is seen in the table that the masses of the cores of three different cell widths produced from PLA filament in the 3D printer are close to each other. Double-layered specimens have approximately thirty-six percent more mass than single-layered specimens, since there is an interface layer and more adhesion surface in double-layered specimens than single-layered specimens.

Table 5: Average values of PLA honeycomb core sandwich structures by type

| **Specimen** | **Core weight [g]** | **Facesheets weight [g]** | **Adhesive weight [g]** | **Weight of sandwich structure [g]** | **Density of sandwich structure [g/cm$^3$]** |
|---|---|---|---|---|---|
| S-6 | 51.13 | 32.18 | 10.09 | 93.40 | 1.45 |
| S-9 | 51.69 | 31.85 | 12.92 | 96.46 | 1.53 |
| S-12 | 52.83 | 31.32 | 13.78 | 97.93 | 1.53 |
| D-6/6 | 51.38 | 47.96 | 21.66 | 121.00 | 1.62 |
| D-9/9 | 50.34 | 47.57 | 31.93 | 129.84 | 1.78 |
| D-12/12 | 51.95 | 48.52 | 29.23 | 129.70 | 1.76 |
| D-6/9 | 50.80 | 48.04 | 36.76 | 135.60 | 1.84 |
| D-9/12 | 51.45 | 47.40 | 31.47 | 130.32 | 1.78 |
| D-6/12 | 51.14 | 47.65 | 38.66 | 137.45 | 1.85 |

In this study, the single-layer specimens seen in Figure 5, have 20 mm core and 1 mm top and bottom facesheets, with a total height of 22 mm. Double-layer samples, on the other hand, have a total height of 23 mm, with 10 mm top and bottom cores and 1 mm top, middle and bottom facesheets.

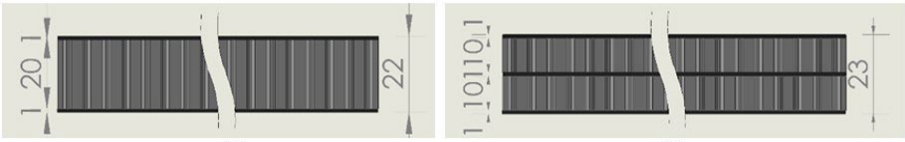


(a) (b)

Figure 5. Core and surface height dimensions of composite sandwich samples (a) Single layer; (b) Two layer.

Figure 6 shows nine different sample types we produced for research. Three of them consist of 6 mm, 9 mm, 12 mm cell widths single-layer, three of them double-layer samples with the same cell width on each layer, and three of them hybrid double-layer samples. Single-layer samples were named with the first letter of the word single, and double-layer samples were named by giving the first letter of the

word double. The produced samples were named by coding the layer type, cell width and sample order of the sandwich structure, respectively. For example, in the sample named D-6/9, it states that the sandwich structure is double-layer, the cell width of the core is 6 mm on the top layer, and the cell width of the core on the bottom layer is 9 mm.

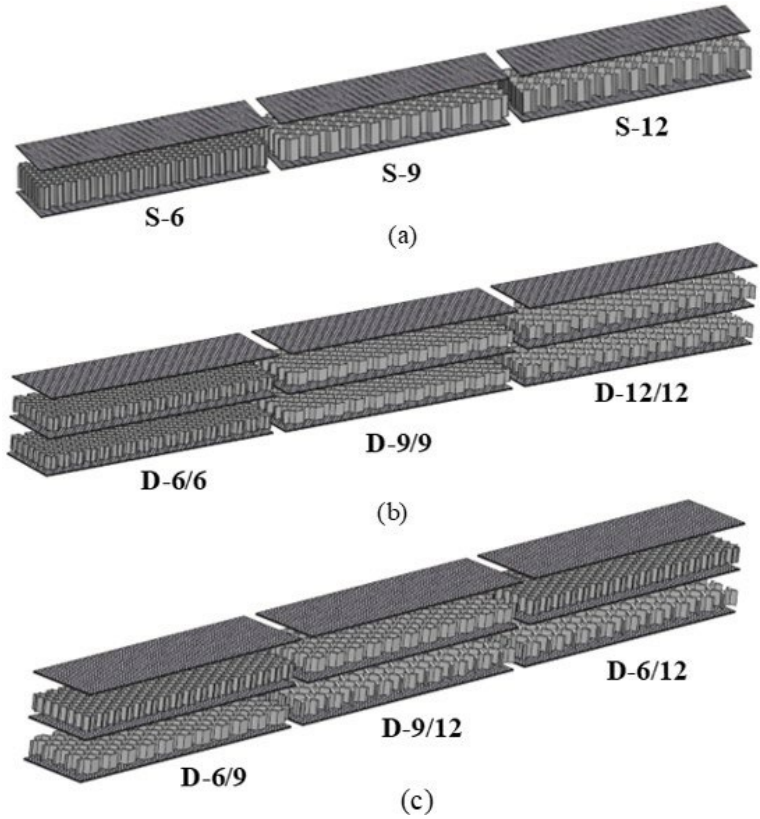


Figure 6. Images of sandwich structure types used in the bending test (a) Single-layer sandwich structures with 3 different cell widths; (b) Double-layer sandwich structures of the same cell width; (c) Hybrid sandwich structures.

## 3. EXPERIMENTAL RESULTS

Bending tests were performed with the Zwick/Roell Z100 testing machine with a capacity of 100 kN shown in Figure 7(a). Tests were performed at a speed of 6 mm/min as per the ASTM C393-16 standard. The orange-colored gauge shown in Figure 7 (b) was used to ensure that the lower support distance spacing of the samples was 150 mm. One of the biggest problems encountered in three-point bending tests is the positioning of the specimens on the bending apparatus. In order to obtain more accurate and reliable results from the tests

performed, the samples should be placed in the same place between the 20 mm diameter supports and the indenter. This issue was corrected using the white-colored equipment shown in Figure 7(c) produced on a 3D printer before starting the tests. Thanks to this produced position stabilizing equipment, positioning errors that may occur by applying force to all bending specimens produced over the same point are eliminated.

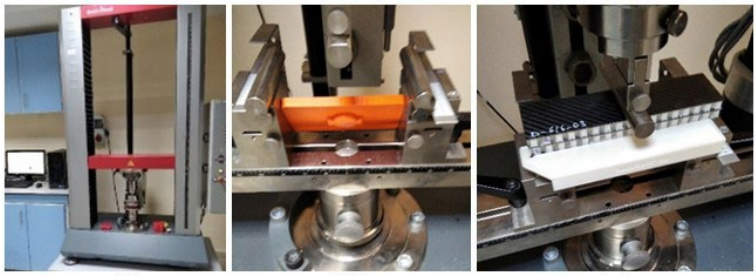


Figure 7. (a) Zwick/Roell Z100 bending tester image; (b) Adjustment pattern of the lower support distance; (c) Location pattern of samples

Figure 8 shows the images of the samples on the device when the test is over. The parts enclosed in the red ellipse give information about the damage types suffered by the sandwich structures. It did not show any problems due to breakage, delamination or adhesion on the facesheets of the samples. It has been determined that the adhesive and bonding method is suitable for PLA core and CFRP facesheets. Damages generally occurred as a fracture in the PLA core, which is more brittle than the CFRP surface. Delamination errors were also observed in the core of some samples. In the samples with a cell width of 6 mm, the breakage continued horizontally and a longer break was detected than the others. This is because shear stresses are better transferred at smaller cell widths, depending on the load.

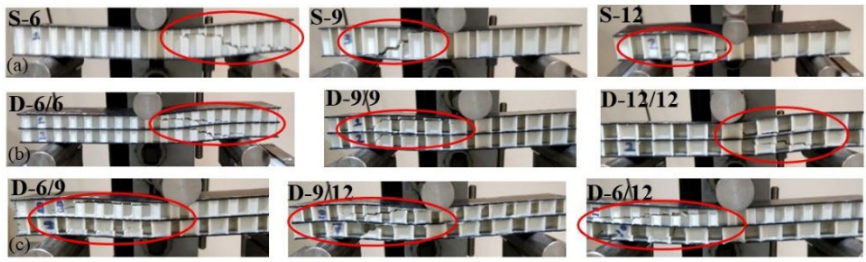


Figure 8. Images of specimens after three-point bending test (a) Single-layer sandwich structure; (b) Double-layer sandwich construction; (c) Hybrid sandwich construction

Figure 9 shows the force-displacement graphs obtained from three-point bending tests according to cell widths of single-layer, double-layer and hybrid double-layer composite sandwich structures with the same cell width. In single-layer and double-layer sandwich structures, the highest bending force was obtained in structures with a cell width of 6 mm. Higher bending force is seen in double-layer hybrid sandwich structures, those with a cell width of 6 mm on the top layer. This is because it transmits the applied load better between the surface layers. As expected, the maximum bending force and displacement in double-layer structures were higher than in single-layer structures [7, 10,21]. The reason for this is that although a total of 20 mm high PLA core is used in single-layer and double-layer structures, there is a CFRP intermediate layer in double-layer structures.

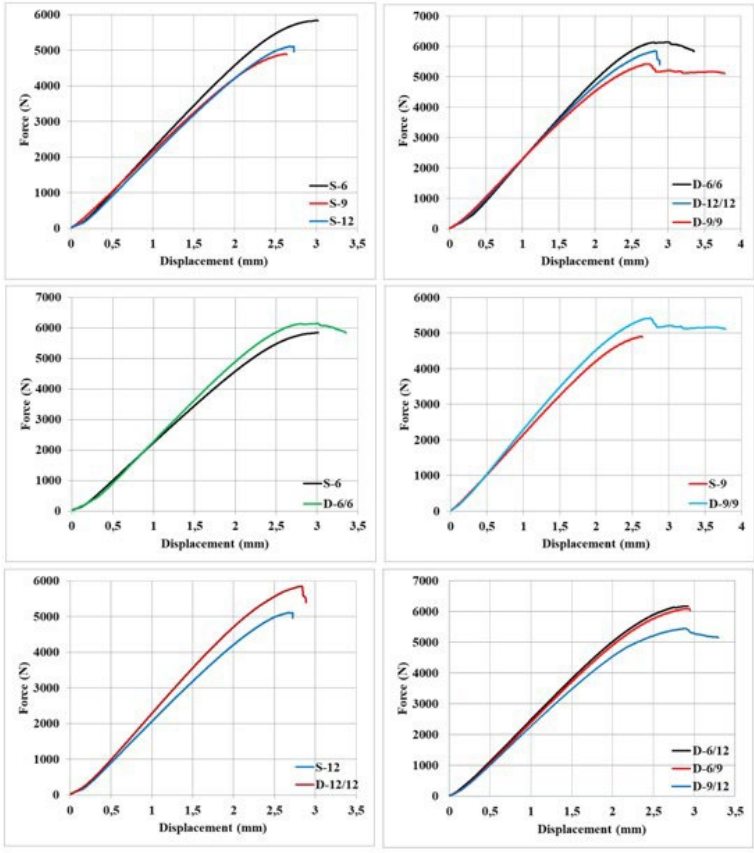


Figure 9. Force-displacement graphs obtained from three-point bending tests of single-layer and two-layer sandwich structures

## 4. THEORETICAL ANALYSIS OF TEST SANDWICH STRUCTURES

The formula of facing stress is expressed in Equation (1). The C coefficient was taken as 1/4 in three-point bending tests [7,28,29].

$$\sigma_f = C\frac{L}{btd}P \tag{1}$$

Where facing stress (MPa), support span (mm), maximum prior to failure (N), =width of sandwich beam (mm), thickness of face (mm), =distance between the facing centroids (mm) as description in Equation 1.

The formula for the core shear stress is shown in equation (2) [7,22].

$$\tau_{C\max} = \frac{P_{\max}}{2bd} \tag{2}$$

Where shear stress core (MPa), maximum prior to failure (N) as description in Equation 2.

In the three-point bending tests, maximum bending load and breaking bending stress data were obtained. These data are shown in table 6. Using the obtained data in equations (1) and (2), facing stress and core shear stress values were calculated. According to the table, sandwich plates with a cell width of 6 mm have higher surface and core tension. The highest load/weight ratio was determined in single-layer S-6 type samples.

Table 6: Mechanical values of sandwich structures according to their types

| Specimen | Maximum bending load [N] | Load/Weight [N.g$^{-1}$] | Facing stress [MPa] | Core shear stress [MPa] |
|---|---|---|---|---|
| S-6 | 5840 | 62.53 | 208.57 | 2.78 |
| S-9 | 4900 | 50.80 | 175.00 | 2.33 |
| S-12 | 5120 | 52.28 | 182.86 | 2.44 |
| D-6/6 | 6150 | 50.83 | 209.66 | 2.80 |
| D-9/9 | 5420 | 41.74 | 184.77 | 2.46 |
| D-12/12 | 5850 | 45.10 | 199.43 | 2.66 |
| D-6/9 | 6090 | 44.91 | 207.61 | 2.77 |
| D-9/12 | 5440 | 41.74 | 185.45 | 2.47 |
| D-6/12 | 6180 | 44.96 | 210.68 | 2.81 |

## 5. CONCLUSION

In this study, the bending strengths of honeycomb geometry structures on equal surface area at three different cell widths and wall thicknesses were experimentally investigated by using PLA filament in a 3D printer, and the following results were obtained.

The highest bending force among single-layer sandwich composite structures was obtained in the sample named S_6. The reason why the bending strength of cells with a cell width of 6 mm is higher than the others is due to the fact that the number of cells per unit surface is higher, although the wall thickness is thinner than the others. This shows that the forces affecting the shear stresses between the surface layers are transmitted better in the samples named S_6.

Among the two-layer sandwich composite structures, the highest bending force was obtained in the samples named D_6/6. More bending force and displacement were obtained in two-layer sandwich structures than in single-layer sandwich structures. The reason for this is that although 20 mm core is used in both single-layer and two-layer structures, there is twice as much adhesive on the middle surface in two-layer structures. For this reason, two-layer structres have become approximately 10 percent more resistant to bending than single-layer buildings.

Among the hybrid two-layer sandwich composite structures, the highest bending strength was obtained in samples named D_6/12 and D_6/9. The reason for this shows that the 6 mm cell width core of the sandwich composite structure on the upper layer transmits the forces affecting shear stresses better, as in single-layer samples.

In sandwich structures, the number of walls per unit surface has a more significant effect on bending stiffness. When designing a structure that will be subjected to bending, it would be advantageous to increase the cell number of the honeycomb core as much as possible in the calculated mass and required surface area.

**Acknowledgements**

This work was supported by the scientific research projects of İnönü University with Project no: FDK-2020-2349.

## REFERENCES


1. Deka, L. J., Bartus, S. D., & Vaidya, U. K. (2009). Multisite impact response of S2-glass/epoxy composite laminates. Composites Science and Technology, 69(6), 725-735.
2. Lin, C., & Fatt, M. S. H. (2005). Perforation of sandwich panels with honeycomb cores by hemispherical nose projectiles. Journal of Sandwich Structures & Materials, 7(2), 133-172.
3. Flores-Johnson, E. A., & Li, Q. M. (2011). Experimental study of the indentation of sandwich panels with carbon fibre-reinforced polymer face sheets and polymeric foam core. Composites Part B: Engineering, 42(5), 1212-1219.
4. Moon, S. K., Tan, Y. E., Hwang, J., & Yoon, Y. J. (2014). Application of 3D printing technology for designing light-weight unmanned aerial vehicle wing structures. International Journal of Precision Engineering and Manufacturing-Green Technology, 1(3), 223-228.
5. Honeycomb Technology Tom Bitzer Hexcel Corporation Dublin, CA USA
6. Subasi S., Çetin V., Şamandar A., "The Effect Of GFRP Plate And Core Thickness On Mechanical Properties In Composite Panels" El-Cezerî Journal of Science and Engineering, 2017, 4(2); 135-145.
7. Arbaoui, J., Schmitt, Y., Pierrot, J. L., & Royer, F. X. (2014). Effect of core thickness and intermediate layers on mechanical properties of polypropylene honeycomb multi-layer sandwich structures. Archives of Metallurgy and Materials, (1).
8. Lu, C., Qi, M., Islam, S., Chen, P., Gao, S., Xu, Y., & Yang, X. (2018). Mechanical performance of 3D-printing plastic honeycomb sandwich structure. International Journal of Precision Engineering and Manufacturing-Green Technology, 5(1), 47-54.
9. Zaharia, S. M., Pop, M. A., Semenescu, A., Florea, B., & Chivu, O. R. (2017). Mechanical properties and fatigue performances on sandwich structures with CFRP skin and nomex honeycomb core. Mat. Plast, 54, 67.
10. Naresh, K., Cantwell, W. J., Khan, K. A., & Umer, R. (2021). Single and multi-layer core designs for Pseudo-Ductile failure in honeycomb sandwich structures. Composite Structures, 256, 113059.
11. Li, T., & Wang, L. (2017). Bending behavior of sandwich composite structures with tunable 3D-printed core materials. Composite Structures, 175, 46-57.

**12.** Yaman O. F. CNT investigation on the bending properties of nomex seed various sandwich with reinforced carbon/epoxy surface MSc Thesis, Universty of Afyon Kocatepe, Turkey, 2016.

**13.** Jiga, G. G., Burtoiu, M. G., Pascu, N. E., & Dobrescu, T. G. (2021, April). Behavior of Different PLA Sandwich Structures Loaded in Three Points Bending. In Macromolecular Symposia (Vol. 396, No. 1, p. 2000306).

**14.** Paik, J. K., Thayamballi, A. K., & Kim, G. S. (1999). The strength characteristics of aluminum honeycomb sandwich panels. Thin-walled structures, 35(3), 205-231.

**15.** Ali, M. H., & Batai, S. (2020). Bending behavior of sandwich composite structures of 3D-printed materials. In Advances in Materials and Manufacturing Engineering (pp. 281-287). Springer, Singapore.

**16.** Brischetto, S., Ferro, C. G., Torre, R., & Maggiore, P. (2018). 3D FDM production and mechanical behavior of polymeric sandwich specimens embedding classical and honeycomb cores. Curved and Layered Structures, 5(1), 80-94.

**17.** Gardan, J. (2017). Additive manufacturing technologies: state of the art and trends. Additive Manufacturing Handbook, 149-168.

**18.** Sugiyama, K., Matsuzaki, R., Ueda, M., Todoroki, A., & Hirano, Y. (2018). 3D printing of composite sandwich structures using continuous carbon fiber and fiber tension. Composites Part A: Applied Science and Manufacturing, 113, 114-121.

**19.** Lascano, D., Guillen-Pineda, R., Quiles-Carrillo, L., Ivorra-Martínez, J., Balart, R., Montanes, N., & Boronat, T. (2021). Manufacturing and characterization of highly environmentally friendly sandwich composites from polylactide cores and flax-polylactide faces. Polymers, 13(3), 342.

**20.** Gorgeri, A., Vescovini, R., & Dozio, L. (2019). Analysis of multiple-core sandwich cylindrical shells using a sublaminate formulation. Composite Structures, 225, 111067.

**21.** Arbaoui, J., Moustabchir, H., Pruncu, C. I., & Schmitt, Y. (2018). Modeling and experimental analysis of polypropylene honeycomb multi-layer sandwich composites under four-point bending. Journal of Sandwich Structures & Materials, 20(4), 493-511.

**22.** ASTM-C393/C393M-16, Standard Test Method For Core Shear Properties of Sandwich Constructions by Beam Flexure, 2016. doi:10.1520/C0393_C0393M-16

**23.** Ultimaker Cura 4.10 sofware, 2022, https://ultimaker.com/learn/an-improved-engineering-workflow-with-ultimaker-cura-4-10 (Accessed 25.06.2022).
**24.** The Ultimaker 2+ specifications, 2020, https://support.ultimaker.com/hc/en-us/articles/360011915779-The-Ultimaker-2-specifications (Accessed 25.06.2022).
**25.** Dostkimya company, https://www.dostkimya.com/tr/urunler/karbon-fiber-plakalar//karbon-fiber-plaka-t1mm (Accessed 30.10.2022)
**26.** The Ultimaker material technical and safety data sheets, https://support.ultimaker.com/hc/article_attachments/4777362374684/Ultimaker-PLA-TDS-v5.00.pdf (Accessed 30.10.2022)
**27.** Araldite® 2015 Adhesive Technical Datasheet, 2015, https://docs.rs-online.com/47fc/A700000006492752.pdf (Accessed 05.07.2022).
**28.** Allen, H. G. (2013). Analysis and design of structural sandwich panels: the commonwealth and international library: structures and solid body mechanics division. Elsevier.
**29.** Dai, J., & Hahn, H. T. (2003). Flexural behavior of sandwich beams fabricated by vacuum-assisted resin transfer molding. Composite structures, 61(3), 247-253.

# Chapter 2

# APPLICATIONS OF PHASE CHANGE MATERIALS (PCM) IN ADVANCED ENGINEERING AND INDUSTRY 4.0 SYSTEMS

**Rezvan REZAEIZADEH[1], İlknur ŞAHİN[2] , Adnan SÖZEN[3], Aybaba HANÇERLİOĞULLARI[4]**

## 1. INTRODUCTION

Phase change materials (PCM) are special substances that can store heat energy and perform this energy by absorbing or releasing heat during the phase change from solid to liquid or from liquid to solid. Phase change materials are materials that can store high amounts of latent heat at specific melting/freezing temperature. This allows PCM to absorb or release heat at a constant temperature, even as the surrounding temperature changes.PCM of basic working principle is that during heating, the material absorbs heat, passes from solid to liquid, and stores it as latent heat, while during cooling, the material gives off heat, passes from liquid to solid, and releases latent heat. Thus, it provides thermal balance by reducing temperature fluctuations. PCMs are generally divided into three classes: organic (paraffin, fatty acids), inorganic (salt hydrates, metal alloys), and composite PCMs. Composite PCM structures are enhanced with nanoparticle additives such as graphene, CNTs, $Al_2O_3$, and $TiO_2$ to increase thermal conductivity. PCMs supported by clay minerals (sepiolite, bentonite, perlite) offer a low-cost and environmentally friendly solution.

Conduction, convection, and, to a limited extent, radiation are effective in storing latent heat during phase change[1,3,6].Composite additives increase

[1] Asst. Prof.Dr.,Department of Enginering /Faculty of Basic Science,Applied Science University,Iran, r.rezaeizade@gmail.com,(Orcid: 0000-0001-6219-6174)
[2] Lecturer,Department of Central Research Laboratory Application and Research Center, Kastamonu University, Türkiye, ilknursahin@kastamonu.edu.tr,
(ORCID: 0000-0002-4383-3817)
[3] Prof.Dr.,Department of Energy Sytems Engineering, Faculty of Technology, Gazi University ,Beşevler/Ankara, asozen@gazi.edu.tr,(Orcid:0000-0002-8373-2674)
and Alparslan Türkeş Science and Technology University, Sarıçam/Adana,Türkiye rektor@atu.edu.tr, (Orcid:0000-0002-8373-2674)
[4]Prof. Dr.,Department of Physic/Faculty of Science,Kastamonu University, Türkiye, aybaba@kastamonu.edu.tr, (Orcid:0000-0000-1700-8480)

thermal conductivity by increasing phonon transmission. Nano additives shorten the PCM's melting time and increase its heat transfer coefficient. In the Industry 4.0 era, energy management, data-driven control, AI-based optimization, and the integration of high-efficiency thermal storage systems have become increasingly important. PCM-based storage systems, thanks to their high latent heat storage capacity, make energy conversion processes more stable and efficient. With modern sensor systems, PCM's melting-freezing behavior can be monitored and optimized using digital twin models [8-11,17-25].When interacting with PCM and nanotechnology, nanoparticle additives can significantly improve PCM performance. At Table -1 show that the thermal properties of some important phase change materials. Graphene and CNT additives can increase thermal conductivity by 5-12 times [7,20-23,30].Metal oxide nanoparticles, on the other hand, increase the thermal stability of PCM, providing cyclic resistance. Furthermore, with the integration of PCM, IoT, and Industry 4.0, IoT sensors can monitor temperature, phase state, stored energy, and cycle count in PCM systems in real time. Digital twin applications can model PCM behavior and increase system efficiency. Artificial intelligence algorithms can determine the optimal PCM type, nanoparticle ratio, and fluid flow rate. In this study examines the role of phase change materials (PCMs) in thermal energy storage, their applications in Industry 4.0-compatible smart energy systems, composite and nanostructured material development processes, IoT-enabled thermal management technologies, and artificial intelligence-based optimization techniques from a holistic perspective. PCM-enabled systems provide critical advantages in a wide range of engineering fields, including energy storage, battery management, PV/T applications, and smart building technologies.

Table 1. PCM types and thermal properties[6-9,22].

| PCM Types | Latent Heat (kJ/kg) | Temperature (°c) |
|---|---|---|
| Paraffin($C_{18}H_{38}$) | 180-220 | 45-60 |
| Salt Hydrate | 250-320 | 28-32 |
| Metal Alloy PCM (Al–Si, Sn–Pb) | 140-260 | 100-250 |
| Composite PCM | 200-260 | 40-50 |
| Graphene-Doped PCM | 210-280 | 42-55 |
| CNT-PCM | 215-290 | 38-48 |

PCMs can be incorporated in the design of low-energy buildings [1,2-6,11].For example, a PCM may be used to store daytime solar heat for heating a house in the evening, or be used to offset the diurnal indoor temperature variation through latent heat release/storage. PCMs are usually encapsulated in spherical, flat or tubular shells, or impregnated into a porous material. They may be organic, e.g. paraffin or inorganic, e.g. ice or salt hydrates ($Na_2SO_4.10H_2O$ and $CaC_{l2}.6H_2O$). Salt hydrate PCMs have the advantage of a large latent heat (~300 kJ/m3), but the disadvantages of phase separation (formation of new hydrates) and a large degree of sub-cooling [7-10,13].

Figure 1. PCM based on n-paraffin and axes [7-11].

Figure -1 show that PCMs based on paraffin and waxes. Table -2 lists the melting points and latent heat of fusion for many of paraffin PCMs [7-11-15].Paraffin form an ideal PCM candidate for residential heating applications due to their large temperature range and their various forms of structure allowing specific paraffin to be selected for a certain temperature range. The material, being of an organic compound is inexpensive and available in large quantities. Table- 2 show that the thermophysical properties of paraffins (n-alkanes), such as melting points and latent heats of fusion. These data are often used for the selection and characterization of phase change materials (PCMs).

Table 2. Melting point and latent heat of fusion of paraffin [7-11].

| Name | Number of C atoms | Melting point (°c) | Density (kg/m³) | Thermal conductivity (W/m·K) | Latent heat of fusion (kJ/kg) |
|---|---|---|---|---|---|
| n-Dodecane | 12 | -12 | 750 | 0.21 (S) | n.a. |
| n-Tridecane | 13 | -6 | 756 | n.a. | n.a. |
| n-Tetradecane | 14 | 4.5–5.6 | 771 | n.a. | 231 |
| n-Pentadecane | 15 | 10 | 768 | 0.17 | 207 |
| n-Hexadecane | 16 | 18.2 | 774 | 0.21 (S) | 238 |
| n-Heptadecane | 17 | 22 | 778 | n.a. | 215 |
| n-Octadecane | 18 | 28.2 | 814 (S), 775 (L) | 0.35 (S), 0.149 (L) | 245 |

## 2.APPLICATIONS OF PCM IN ENERGY SYSTEMS

PCMs increase efficiency by reducing cell temperature in PV/T systems. They can be used for battery temperature management in electric vehicles. In smart buildings, in-wall PCM integration can reduce HVAC loads by up to 30%. PCMs are also widely used in industrial waste heat recovery. Phase Change Materials (PCMs) are materials that absorb or release large amounts of latent heat during phase transitions usually from solid to liquid and vice versa at nearly constant temperatures. They are increasingly being used in energy systems for thermal energy storage, temperature regulation, and increased energy efficiency[8-13]. (PCMs) are substances that absorb and release large amounts of latent heat during phase transitions (usually between solid and liquid) at nearly constant temperatures. This property makes them highly effective for thermal energy storage (TES) and energy management across a variety of energy systems.Thermal Energy Storage (TES); store excess heat (or cold) and release it when needed.

### 2.1 Solar Energy Storage

Solar water heating systems; PCMs store excess thermal energy from solar collectors during the day and release it at night or during cloudy periods. Solar air heating; Used in air-based solar systems to stabilize outlet air temperature.Concentrated solar power;PCMs store high-temperature heat from

the receiver, allowing power generation even without sunlight. In solar thermal power plants  to store daytime heat for electricity generation at night. PCMs like paraffin wax or salt hydrates are integrated into solar collectors or storage tanks. PV/T /nanofluid / pcm hybrid system,the (nanofluid +PCM) integrated PV/T panel architecture, an advanced variant of photovoltaic/thermal (PV/T) hybrid systems. This design features a PCM layer beneath the PV cell, with a nanoparticle-enhanced fluid-powered heat exchanger beneath it.This structure reduces cell temperature, improves performance, and increases total daily energy yield [9,11-15]. Furthermore, thermodynamic relations, layered architecture, 3d temperature distribution, and input-output temperature analyses were used for mathematical modeling of the panel system.In Figure -2 show that 3d tempured digarm. The surface temperature of the Nanofluid + PCM integrated PV/T panel varies along the flow direction.The temperature is lower at the cold inlet corner and gradually increases toward the outlet. The PCM layer reduces temperature fluctuations thanks to its melting point, creating a more controlled profile. Figure-2 shows the temperature distribution on the panel surface in 3D. This distribution is optimized based on the nanofluid flow rate, PCM melting temperature, and PV load[23-24,26]. PCMs store solar heat during peak radiation hours for use during cloudy periods or nighttime. For renewable energy systems ıntegration, balance intermittent renewable energy sources(wind and hybrid systems).Excess electrical energy from wind turbines can be converted into heat and stored in PCMs for later use. At Table-3 show that applications of PCMS in energy systems.

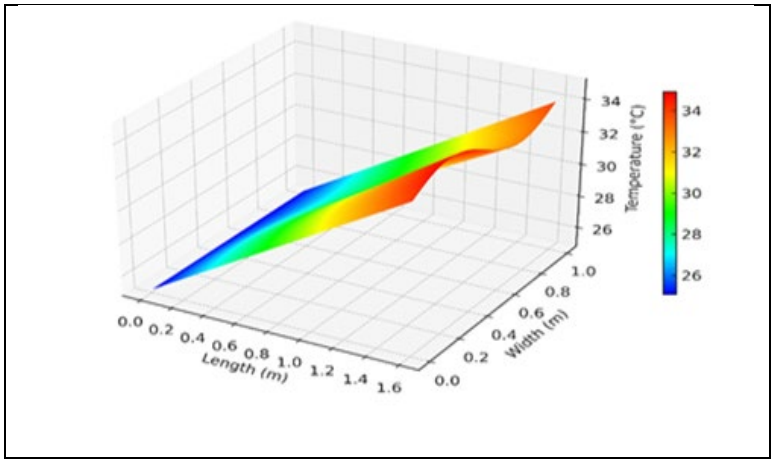


Figure.2 The temperature distribution on the panel surface in 3d[21,27].

### 2.2 Waste Heat Recovery

Industrial processes often produce large amounts of waste heat. PCMs can capture and store this heat for later reuse, improving overall energy efficien.Incorporated into walls, ceilings, and floors, PCMs help regulate indoor temperatures by absorbing excess heat during the day and releasing it at night.Reduces HVAC (heating, ventilation, and air conditioning) loads and enhances comfort.Pcm-enhanced building materials,PCMs panels, plasters, or wallboards can maintain indoor thermal stability,pcm-integrated windows(thermochromic or transparent PCMs) reduce overheating and enhance daylight utilization. PCMs store surplus heat from manufacturing processes and release it later to preheat air, water, or feedstock, improving overall efficiency.PCMs are used in water heaters and solar geysers to store thermal energy, providing hot water even during non-sunny periods[20-25,26-29].

### 2.3 Building Energy Management

Improve thermal comfort and reduce HVAC energy demand.Passive cooling and heating;PCMs integrated into walls, ceilings, and floors absorb excess indoor heat during the day and release it at night, stabilizing indoor temperature.Thermal insulation panels;PCM panels or plasterboards reduce indoor temperature fluctuations and HVAC loads and Smart window;PCM layers in glazing systems help regulate solar heat gain, reducing the need for artificial cooling.

### 2.4. HVAC (Heating Ventilation Air Conditioning) Systems

Enhance efficiency and reduce peak load;cold storage for air conditioning;PCMs store "coolth" during off-peak hours (e.g., at night) and release it during the day to reduce cooling energy demand,air handling units;PCMs used in ventilation ducts absorb or release heat to precondition air entering the building. Cold chain and refrigeration systems, maintain stable temperatures during storage and transport.

### 2.5.Transportation and Electric Vehicles

Thermal management and waste heat utilization,battery thermal management:,PCMs regulate the temperature of EV batteries to maintain optimal performance and prolong battery life.PCM modules can store cooling or heating energy to reduce load on air conditioning systems in electric or hybrid vehicles.PCMs manage heat spikes in electronic components, preventing overheating.PCM-based cooling systems store cold energy during off-peak times and release it during peak data center operation.PCM packs keep goods

(like vaccines or food) at desired temperatures without continuous power supply.PCMs help reduce compressor operation during peak demand hours by storing cooling energy beforehand.Enhance process efficiency and reduce energy waste. PCMs store daytime solar heat and release it at night to maintain optimal plant growth temperatures. For food processing and preservation,PCMs maintain consistent temperatures during processing or storage periods[25-31].

Table.3 Applications of PCMS in energy systems [11,17-23].

| Sector | Application | Function of PCM |
|---|---|---|
| solar | tes in solar collectors | store daytime heat for later use |
| buildings | wall/ceiling integration | maintain indoor thermal comfort |
| hvac | cool storage | shift cooling load to off-peak hours |
| electric vehicles | battery management | temperature control |
| electronics | component cooling | prevent overheating |
| ındustry | waste heat recovery | ımprove efficiency |
| refrigeration | cold storage | maintain temperature during transport |
| agriculture | green house temperature control | stabilize growing conditions |

## 3.PCM AND INDUSTRY 4.0

PCM and Industry 4.0 actually come from different fields, but, they are two important components that complement each other in terms of energy efficiency, smart systems and data-driven production. PCM is a smart material that stores heat during phase change (solid-liquid transition) and releases it when necessary. Industry 4.0 is an approach to creating smart, connected and autonomous production systems using sensors, IoT, artificial intelligence, robotics and data analytics. IoT (Internet of things) sensors can monitor temperature, phase status, stored energy, and cycle count in a PCM system in real time. Digital twin applications can model PCM behavior and increase system efficiency. Artificial intelligence algorithms can determine the optimal PCM type, nanoparticle ratio, and fluid flow rate. Nowadays; IoT is frequently used in applications such as smart homes, smart plugs, thermostats, security

cameras, smart lighting, healthcare systems, smart wristbands, heart rate sensors, remote patient monitoring, agricultural soil moisture sensors, automatic irrigation systems, and Industry 4.0) production line sensors, machine condition monitoring, transportation, logistics, smart traffic systems, vehicle tracking, and more.[13,18,27].The advantages of IoT can be listed as follows:It increases efficiency (energy, time, and labor savings),It provides real-time data,It offers remote control,andit enables automation and optimization. However, it also has some challenges and disadvantages. These include: security and privacy risks,device compatibility across different brands/protocols,big data management challenges,and difficulties with Ethernet and internet connectivity. The purpose of IoT in solar energy systems is to monitor the performance of solar energy systems, detect faults, and optimize energy management. The aim is to ensure maximum efficiency and minimum loss by remotely monitoring and controlling the system. To collect data for IoT systems, sensitive sensors are placed on solar collectors. These sensors collect real-time data. It is used as a microcontroller/gateway for data collection and transmission. Data from sensors is collected by microcontroller (arduino,esp32, raspberry pi).This device transmits data to the cloud over the internet using connection technologies (wi-fi, lora/lorawan, gsm/4g/5g, zigbee). For cloud platform data storage and analysis, data is stored and analyzed in the cloud. Available platforms include (thingspeak, blynk, firebase, aws iot core, azure iot hub). The following are done in the cloud: real-time temperature, radiation, and power graphs are created. Energy production is estimated. Faults (e.g., low efficiency, excessive temperature) are detected. As a result, the IoT application is used for monitoring panel temperature, irradiance, voltage, current, and power generation in PV systems.For PV/T (hybrid) systems, it is used for monitoring both electricity and heat production, and for calculating input/output temperature, flow rate, and thermal efficiency in solar collectors.For battery systems, it monitors state of charge (SOC), voltage, and current and microgrids, it regulates the intelligent management of the entire energy flow. Solar collector IoT monitoring equations (3,4) above are specifically used in the calculations.

## 4. THERMODYNAMIC MODELS OF ENGINNERING

PCM systems are modeled with energy balances, enthalpy method, Stefan problem and Fourier heat conduction equations. The use of PCM in PV/T systems reduces cell temperature by 8-14°c and efficiency increases are measured between 6-15%. These relations are used to calculate the electrical, thermal and total energy production of the panel.The basic equations used in the hybrid system for thermodynamic relations and energy models are as follows;

$$T_{cell}=T_{amb}+ G/ U_L \quad (1)$$

This formula is an approach that balances heat gain and heat loss based on the PV module's energy balance.Solar radiation heats the cell, but this heat is lost to the environment (convection+ radiation). For PV cell temperature; this expression is a simplified energy balance equation used to approximate photovoltaic (PV) cell temperature (Tcell) based on ambient temperature (Tamb) and Solar radiation incident on the surface ($W/m^2$) (G) and $U_L$, total heat loss coefficient ($W/m^2 \cdot K$).

$$\eta = \eta_{ref} [1 - \beta (Tcell - 25)] \quad (2)$$

η; It is the instantaneous efficiency and shows the module efficiency at solar cell temperature. $\eta_{ref}$ ;show that reference efficiency, typically measured at 25°c and 1000 $W/m^2$. β;temperature coefficient (1/°c) and ($T_{cell}= T_{amb}+ G/U_L$ ),Tcell, Cell of temperature (°c).The rate of efficiency decrease as cell temperature increasesThis expression describes the efficiency change of the photovoltaic (PV) module with temperature. As the temperature of the V cells increases, the band gap of the semiconductor narrows, which reduces the voltage → efficiency decreases. Typical values;for monocrystalline Si panel:$\beta \approx 0.004-0.005$/°c ;β≈0.004−0.005 /°c (i.e., 0.4–0.5%/°c).For polycrystalline Si:$\beta \approx 0.0045$/°c ,β≈0.0045 /°c and thin film (CdTe, a-Si):$\beta \approx 0.002-0.003$/°c,β≈0.002−0.003 /°c.

For PV/T thermal efficiency;

$$\eta_t = (\dot{m} Cp (Tout - Tin)) / (A \times G) \quad (3)$$

This equation shows how much of the energy the collector receives from the sun is converted into heat energy. this is the equation for thermal (heat) collector efficiency; it is used especially for solar collectors (solar water heaters).$\eta_t$; show that thermal efficiency,it is known as the rate at which the collector converts solar energy into thermal energy. $\dot{m}$; mass flow rate (kg/s),the mass flow rate of the fluid (water) passing through the collector.Cp ($J/(kg \cdot K)$), represents the specific heat of the fluid at constant pressure. Tin; fluid temperature leaving the collector Tout; fluid temperature leaving the collector (°c).,A; collector area ($m^2$) represents the surface area that collects solar energy. G; radiation intensity ($w/m^2$),

For PCM latent heat storage,

$$Q_{latent} = M_{pcm} \cdot L_{pcm} \quad (4)$$

This equation represents the calculation of latent heat for the phase change material (PCM). $Q_{latent}$,(J);Latent heat,the energy absorbed or released by PCM during a phase change,$M_{pcm}$(kg); total mass of phase change material,Lpcm(J/kg); the amount of energy absorbed or provided by 1kg of material during phase change.

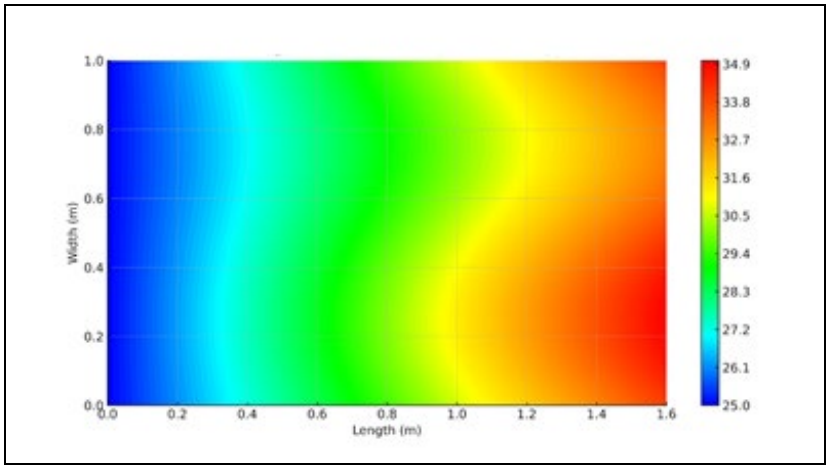

Figuru.3 Solar collector, input-output temperature distribution in PV/T module

Phase change materials (e.g., paraffin, salt hydrates, fatty acids, etc.) store or release energy during the solid → liquid (melting) or liquid → solid (solidification) transition while the temperature remains constant. during heat storage (melting), the system absorbs energy. during heat release (solidification), energy is released. Figure -3 is a two-dimensional temperature map showing the inlet-outlet temperature distribution of a solar collector, heat exchanger or PV/T module in a liquid flow system. As a result, Figure-3 shows that the fluid's temperature increases from approximately 25°c to 35°cas it moves from the system's inlet (left) to its outlet (right). The color gradient represents the spatial distribution of heat across the panel or collector surface.At Figure-4 appears to show the gradient of the velocity distribution of nanofluid containing PCM phase change material, the color scale representing the spatial variation of a physical quantity in the area, such as temperature or velocity magnitude.[18,25-30].The color scale on the right of Figure -3 ranges from 25°c to 34.9°c. Blue tones indicate the lower temperature (inlet side). Red tones indicate the higher temperature (outlet side). This indicates that the fluid is

receiving (or gaining) heat throughout the system, and its temperature is increasing. For heat transfer analysis, it indicates how efficiently the fluid is gaining heat in the collector or PV/T panel. In design optimization, it indicates how the fluid flow direction, flow rate, or pipe layout affect heat distribution. The velocity field of a PCM fluid is typically modeled using the Navier–Stokes equations and energy equations. The fluid moves with heat transfer, while the enthalpy method accounts for the melting/freezing behavior of the PCM[18,25-30].

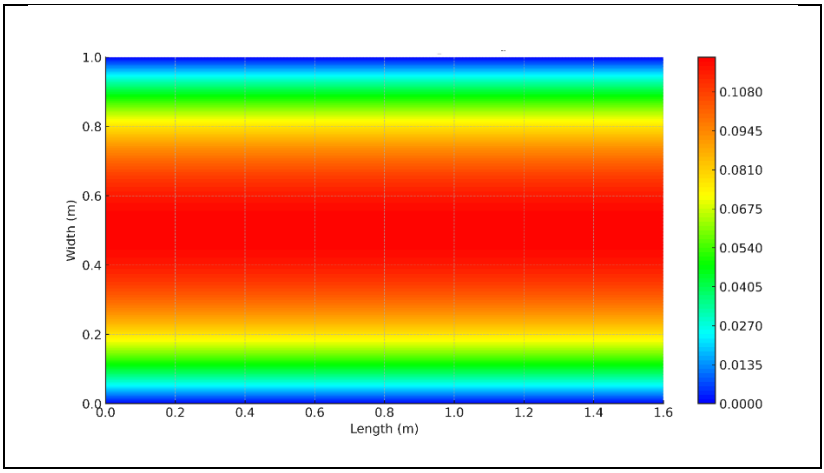

Figuru.4 The gradient of the velocity of nanofluid in PV/T module[11,17-23].

## 5. CONCLUSION AND DISCUSSION

The integration of PCM-based systems with Industry 4.0 increases energy efficiency, reduces carbon emissions, and provides a sustainable solution for smart energy management. Nanocomposite PCM structures will be at the core of future energy storage technologies. Nanofluid + PCM hybrid technology offers significant advantages over traditional PV and PV/T systems; it lowers PV cell temperatures by 10–18°C. Peak temperatures are suppressed thanks to PCM.Nanofluid channels increase the heat transfer coefficient.Total electrical and thermal energy production can increase by 35–55%.Digital twin, sensor, and AI-supported optimization can be implemented with the Industry 4.0 infrastructure.Sonuç olarak, The benefits of PCM + Industry 4.0 integration can be listed as follows:energy efficiency, heat storage through phase change, peak load balancing,data-based control, instant temperature/energy monitoring with IoT sensors, predictive maintenance, early detection of PCM performance deterioration, sustainability, reduced energy waste and $CO_2$ emissions, and system optimization, automatic heat management with AI algorithms.In the

study, ANSYS was used for PCM analyses and velocity distribution, COMSOL for melting/freezing, velocity and temperature distribution, OpenFOAM and Open source CFD were used for multiphysics simultaneous heat flow modeling and PCM enthalpy model, and solvers such as Boussinesq, PimpleFoam, Matlab/Python (NumPy +Matplotlib) were used for simplified 2d solution and visualization [1,5-7].

## REFERENCES


1-Mohammed,F.M.,at all.,(2021). Numerıcal study of coolıng system for photovoltaıc thermal collector.,*Journal of engineering science and technology*,16 (6), 4817 -4832.

2-Saffa,R., Mempouoa,B. , Fangb,W.,(2015). Phase change material developments: a review, *International journal of ambient energy*, 36(2), 102–115.

3- Farid, M., Khudhair, A., Razack, S. and Al-Hallaj, S. ,(2004) .A Review on phase change energy storage: materials and applications.,*Energy conversion and management,* 45, 1597-1615.

3- Zhang,Y.,J.Ding,X.Wang,R.Yang,andK.Lin.,(2006). Influence of additives on thermal conductivity of shape-stabilized phase change material.*Solar energy materials and solar cells,* 90 (11): 1692–1702.

4-Zhang, Y., and A. Faghri. ,(1995). Analysis of forced convection heat transfer in microencapsulated phase change material suspensions. ,Journal of thermophysics and heat transfer, 9 (4): 727–732.

5- Zhang, Y., X. Hu, and X. Wang. ,(2003). Theoretical analysis of convective heat transfer enhancement of microencap sulated phase change material slurries.,heat and mass transfer ,40 (1): 59–66.

6-Zhang, D., Z. Li, J. Zhou, and K. Wu. ,(2004). Development of thermal energy storage concrete. ,*Cement and concrete research,* 34 (6): 927–9344.

7-Zhang,P.,Z.W.Ma,andR.Z.Wang ,(2010).An overview of phase change material slurries: mpcs and chs.,*Renewable and sustainable energy reviews* ,14 (2): 598–614.

8-Zhang, Y., Y. Su, Y. Zhu, and X. Hu., (2001).A General Model for analyzing the thermal performance of the heat charging and discharging processes of latent heat thermal energy storage systems.,*Journal of solar energy engineering* ,123 (3): 232–236.

9- Zhang, Y., X. Xu, H. Di, K. Lin, and R. Yang., (2006). Experimental Study on the thermal performance of the shape stabilized phase change material flooruse dinpassivesola. ,*Journal of solar energy engineering*128(2).doi:10.1115/1.2189866

10-Sharma, A., Tyagi, V. V., Chen, C. R., & Buddhi, D., (2009). Review on thermal energy storage with phase change materials and applications, *renewable and sustainable energy reviews*, 13(2), 318–345.

11-Zalba, B., Marín, J. M,at, al..,(2003). Review on thermal energy storage with phase change,materials, heat transfer analysis and applications.,*Applied thermal engineering*, 23, 251-283.

12-www.tandfonline.com,(2025),Advanced composite materials,search ,*peer-reviewed journals and articles,* 34(5).

13-Saffa R.,Mempouo B., Fang,W.,(2013).Phase change material developments: a review, *International journal of ambient energy*, 36(3) .

14- Sabbah A, Mamoun M. El, at,all. ,(2025).An overview of recent experimental and numerical studies on hemispherical solar distillers using internal and external enhancers.,*Separation and purification technology*,373(18), 133535.

15- Mohamed R. E. , Kotb M. K. ,at all..(2024).Optimize and analyze a large-scale grid-tied solar PV-powered SWRO system for sustainable water-energy nexus, *Desalination,*579, 117440.

16- Yi Luan, Ming Y.,at.al.,(2016). Introduction of an organic acid phase changing material into metal-organic frameworks and the study of its thermal properties, *Journal of materials chemistry.* Issue 20.

17-Li H.(2010).Preparation and characteristics of n nonadecane/cement composites as thermal energy storage materials in buildings*, energy & buildings*, 20101,42(10), 1661-1665.

18- Hemayat S, Masumeh M., Saeid F., (2025).A systematic review of ionic liquids as designer phase change materials for thermal energy storage and release, *solar energy materials and solar cells*,282, 113317 .21-Kumirai, T. ,(2017).Development of a design tool for Pcm based free comfort cooling system in office buildings in south africa", *University of Pretoria* ,South Africa,2017.30709811.

19-Maatouk Khoukhi, at.,all..,(2006). Flat-Plate Solar Collector Performance with Coated and Uncoated Glass Cover, *heat transfer engineering,*27(1).

20-Hadorn, J. C., all., (2003). Thermal energy storage for solar and low energy buildings- state of the art, İea shc task32book,*printed by servei depublicacions universidad lleida,* spain,170 pages ısbn84-8409-877-x, available through ınternet www.iea-shc.org task32.

21- Hao, Y. L., & Y. X. Tao.,(2004).A numerical model for phase change suspension flow in microchannels., numerical heat transfer, part a: *applications* 46 (1), 55–77.

*22*- Hasnain, S. M.,(1998).Review on Sustainable thermal energy storage technologies, Part I: heat storage materials and techniques.,*energy conversion and management* 39 (11),1127–1138.

23-Hawlader, M. N. A., Uddin M. S., Khin M. M. , (2003).Microencapsulated PCM thermal-energy storage system*., applied energy, 74 (1–2): 195–202.*

24-Hawlader, M. N. A., Uddin M. S., and Zhu H. J.,(2003). Encapsulated phase change materials for thermal energy storage: experiments and simulation. *international journal of energy research* ,26 (2), 159–171.

25-Herrmann, U., & Kearney D., (2002). Overview on thermal storage systems, workshop on thermal storage for troughpower systems.,*paper presented at the workshop on thermal storage for trough power systems,* 20–21, nürnberg, germany: flabeg solar ınternational,Gmbh.

26-Ho, C. J., J. F. Lin, and S. Y. Chiu. 2004. "Heat transfer of solid–liquid phase-change material suspensions in circular pipes: effects of wall conduction." numerical heattransfer, part a: *applications* 45 (2): 171–190.

27-Hofer, S d. at,all.,(2003). Method to determine the thermal conductivity of phase change materials(pcm)and phase change slurries(pcs),ın proceedings of the 1.phase change materials and slurry scientific *conference & business forum, yverdon,*switzerland, 23-26.

28- Wei, J., Y.,Kawaguchi, S. H.,(2005).Study on PCM heat storage system for rapid heat supply." *applied thermal engineering*, 25 (17–18): 2903–2920.

29- Benmansour, A., Hamdan M. A., and Bengeuddach A.,( 2006).Experimental and numerical ınvestigation of solid par ticles thermal energy storage unit., *applied thermal engineering* 26 (5–6), 513–518.

30-Özonur,Y.,M.Mazman, at,all..(2006). Microencapsulation of coco fatty acid mixture for ther mal energy storage with phase change material., *international journal of energy research*, 30 (10), 741–749.

# Chapter 3

# OPTIMAL TUNING OF LINEAR QUADRATIC REGULATORS FOR HYDRAULIC TURBINE SPEED CONTROL SYSTEM USING A NEW ADAPTIVE PARTICLE SWARM OPTIMIZATION AND GENETIC ALGORITHMS

**Mahit GÜNEŞ [1*], Ö. Fatih KEÇECİOĞLU [2]**

## 1. INTRODUCTION

The main energy source of power plants is the kinetic energy of water or the thermal energy of fossil fuels or nuclear fusion. In general, mechanical energy is obtained by using various resources. Power plants use generators to produce electrical energy from mechanical energy. In recent years, the number of hydroelectric power plants (HPP) in the Kahramanmaras region has increased significantly due to the numerous streams that meet our country's rapidly growing needs. Most of the hydropower plants consist of hydro turbines, generators, and speed regulation systems. The speed regulation system ensures that the required energy can be immediately fed into an interconnected grid. The speed regulator of this system sets the gate positions that control the amount of water that enters the blades of the water turbine. The system's active power and frequency parameters fully control the speed regulators.

Nowadays, the control of hydroelectric power plants is carried out both with classical and modern controllers [1, 2, 3]. In recent years, the proposed modern and classical controller design methods are still being updated. The classical methods for control system design are particularly powerful and simple. The technology of hydropower plants requires higher performance of the control system. For this reason, the use of modern control systems has become much more important.

Modern control systems based on the optimization of conventional control design methods are subject to certain criteria. Optimal control problems have been the topic of intensive research for a long period. In optimization methods,

[1] Prof. Dr., Electrical & Electronics Engineering Department, Kahramanmaras Sutcu Imam University, Kahramanmaras, Turkey, https://orcid.org/0000-0002-1552-3889, Corresponding Author
[2] Doç. Dr., Electrical & Electronics Engineering Department, Kahramanmaras Sutcu Imam University, Kahramanmaras, Turkey, http://orcid.org/0000-0001-7004-4947

the controller parameters are determined by the transfer function of the controlled system to minimize errors. In optimal control systems, a linear optimal controller is designed to minimize a quadratic cost function. In this way, the optimal control parameters are determined [4, 5],

In this study, the model of a hydroelectric power plant with governors, turbines, speed regulator, and generator was extracted, and the transfer function of the whole system was obtained. The proposed LQR controller was designed and adapted to control the turbine speed. The Q and R matrix values in the LQR control were tuned with the newly developed Adaptive Particle Swarm Optimization and Genetic algorithms [6]. The performance of the applied LQR controller was compared with that of the PID controller for the same system. The controllers were tested, and the obtained data were compared using MATLAB/Simulink environment.

## 2. MODEL OF CONTROLLED SYSTEM

### 2.1. Hydraulic Turbine Modeling

In this study, the following assumptions were considered in the extraction of the hydraulic turbine transfer function [4]. The hydraulic resistance was neglected. The conduit is made of inelastic material and the water inside is incompressible. The velocity of the water (V) in the conduit was proportional to the gate position (α) and the square root of the hydraulic head at the gate (H). The turbine's mechanical power is proportional to the water velocity (V) and the hydraulic head at the gate (H).

The following equations describe the characteristics of the turbine and conduit. Water velocity (V) in the conduit, the turbine's mechanical power ($P_m$), and the water column's acceleration (Ag).

In general, the water velocity (V) in the conduit and the mechanical power of the turbine ($P_m$) are given as follows.

$$V = V(\mathrm{H}, w, \alpha) \tag{1}$$

$$P_m = P_m(\mathrm{H}, w, \alpha) \tag{2}$$

(H) is the hydraulic head at the gate, (α) is the gate position, and (ω) is the velocity of the hydraulic turbine. Applying a Taylor series approximation around an operating point with small variation, the turbine linearized equation becomes thusly:

$$\Delta \overline{V} = e_{vh}\Delta \overline{H} + e_{vw}\Delta \overline{w} + e_{v\alpha}\Delta \overline{\alpha} \tag{3}$$

$$\Delta \overline{P}_m = e_{ph}\Delta \overline{H} + e_{pw}\Delta \overline{w} + e_{p\alpha}\Delta \overline{\alpha} \tag{4}$$

Where,

$$e_{vh} = \frac{\partial v}{\partial h},\ e_{vw} = \frac{\partial v}{\partial w}\ ,\ e_{v\alpha} = \frac{\partial v}{\partial \alpha} \tag{5}$$

$$e_{ph} = \frac{\partial p}{\partial h},\ e_{pw} = \frac{\partial p}{\partial w}\ ,\ e_{p\alpha} = \frac{\partial p}{\partial \alpha} \tag{6}$$

Incremental speed deviation $\Delta\bar{\omega}$ is usually considered to be negligible around an operating point with a small variation in large and powerful turbines.

$$\Delta \overline{V} = e_{vh}\Delta \overline{H} + e_{v\alpha}\Delta \overline{\alpha} \tag{7}$$

$$\Delta \overline{P}_m = e_{ph}\Delta \overline{H} + e_{p\alpha}\Delta \overline{\alpha} \tag{8}$$

The conduit's water velocity is determined by the equation (9):

$$V = K_v \alpha \sqrt{H} \tag{9}$$

Where ($K_v$) is constant. From equation (7), water velocity $V_0 = K_v \alpha_0 \sqrt{H_0}$ for variation near turbine rated operating point.

$$\frac{\Delta V}{V_0} = \frac{\Delta H}{2H_0} + \frac{\Delta \alpha}{\alpha_0} \tag{10}$$

$$\Delta \overline{V} = \frac{1}{2}\Delta \overline{H} + \Delta \overline{\alpha} \tag{11}$$

The turbine's mechanical power has the form:

$$P_m = K_p H V \tag{12}$$

From equation (8), the mechanical power of the turbine $P_{m0} = K_p H_0 V$ for variation near the turbine's rated operating point.

$$\frac{\Delta P_m}{P_{m0}} = \frac{\Delta H}{H_0} + \frac{\Delta V}{V_0} \tag{13}$$

$$\Delta \overline{P}_m = \Delta \overline{H} + \Delta \overline{V} \tag{14}$$

By using equation (11), equation (14) can be rewritten in two forms as follows:

$$\Delta \overline{P}_m = 3\Delta \overline{V} - 2\Delta \overline{\alpha} \tag{15}$$

$$\Delta \overline{P}_m = 1.5\Delta \overline{H} + \Delta \overline{\alpha} \tag{16}$$

### 2.2. Conduit Modeling

The acceleration of the water column in the conduit results from a change in the head point of the turbine, which is characterized by Newton's second law of motion as follows.

$$(\rho LA)\frac{d\Delta V}{dt} = -A(\rho a_g)\Delta H \tag{17}$$

Where (L) is the conduit length, (A) is the pipe area, (ρ) is the fluid mass density, and ($a_g$) is the acceleration resulted from gravity. Equation (17) can be rewritten as:

$$\frac{LV_0}{a_g H_0}\frac{d}{dt}\left(\frac{\Delta V}{V_0}\right) = -\frac{\Delta H}{H_0} \tag{18}$$

$$\Rightarrow T_w \frac{d\Delta \overline{V}}{dt} = -\Delta \overline{H} \tag{19}$$

$$T_w = \frac{LV_0}{a_g H_0} \tag{20}$$

Where $T_w$ is the water flow's starting time.

### 2.3. The Transfer Function of Hydraulic Turbine

By substituting equation (11) into equation (19), the result equation will be:

$$T_w \frac{d\Delta\overline{V}}{dt} = 2\left(\Delta\overline{\alpha} - \Delta\overline{V}\right) \tag{21}$$

We can rewrite equation (21) in the s-domain:

$$T_w s\Delta\overline{V} = 2\left(\Delta\overline{\alpha} - \Delta\overline{V}\right) \tag{22}$$

The turbine coefficients must be measured correctly on the field or calculated through model tests. These parameters are detailed in Table (1) according to the IEEE model [4, 7]. Equations (7) and (8) are substituted into equations (11) and (15) to find the transfer function of the hydraulic turbine.

$$\frac{\Delta\overline{P}_m}{\Delta\overline{\alpha}} = e_{p\alpha} \frac{1 + \left(e_{uh} - e_{u\alpha} e_{ph} / e_{p\alpha}\right) sT_w}{1 + e_{uh} sT_w} \tag{23}$$

**Table 1.** Turbine's coefficients

| Partial Derivatives | IEEE Model | Partial Derivatives | IEEE Model |
|---|---|---|---|
| $\frac{\partial v}{\partial h}$ | 0.5 | $\frac{\partial p}{\partial h}$ | 1.50 |
| $\frac{\partial v}{\partial \omega}$ | 0.00 | $\frac{\partial p}{\partial \omega}$ | 0.00 |
| $\frac{\partial v}{\partial \alpha}$ | 1.00 | $\frac{\partial p}{\partial \alpha}$ | 1.00 |

By using the standard values of the IEEE model listed in Table (1), the transfer function of the hydraulic turbine is obtained as follows [1, 5]:

$$\frac{\Delta \bar{P}_m}{\Delta \bar{\alpha}} = \frac{1 - T_w s}{1 + \frac{1}{2} T_w s} \tag{24}$$

### 2.4. Electro-Hydraulic Governor Modeling

Electrohydraulic governor systems are used to control the hydraulic turbine speed. Electric governors and mechanical-hydraulic governors commonly are set to have the same dynamic characteristics. All measurement and calculation functions are accomplished electrically such as permanent and temporary droop, and Speed-sensing. The next equations represent the temporary drop RT and reset time TR.

$$R_T = \left[2.3 - (T_w - 1)0.15\right] \frac{T_w}{T_M} \tag{25}$$

$$T_R = \left[5 - (T_w - 1)0.5\right] T_w \tag{26}$$

Equation (27) presents the transfer function of the electric governor.

$$G_c(s) = \frac{1 + T_R s}{1 + \left(\frac{R_T}{R_P}\right) T_R s} \tag{27}$$

The block diagram of the hydraulic turbine speed system with the LQR controller is presented in the next Figure 1.

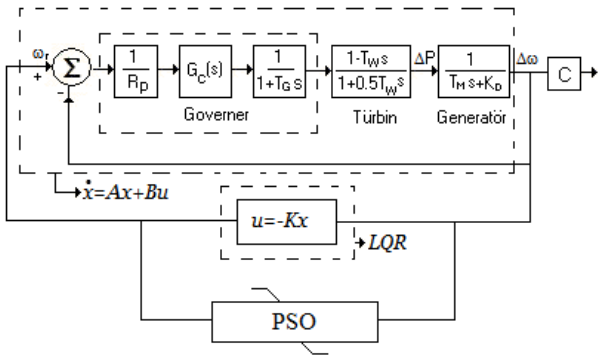


**Fig. 1.** Block diagram of hydraulic turbine speed system with the LQR-PSO controller.

Where ($R_p$) is a permanent droop, ($T_M$) is the mechanical start time, ($K_D$) is the damping torque coefficient and, ($T_G$) is the main servo time constant. The transfer function of the PID controller with first-order derivative filter is:

$$u(\mathrm{s}) = \left[ k_p + \frac{k_i}{s} + k_d \frac{N}{1 + N\frac{1}{s}} \right] e(\mathrm{s}) \tag{28}$$

To design an LQR controller, we need to extract the state space of the hydraulic turbine speed system. Equation (29) represents an equivalent state-space representation of the hydraulic turbine speed system.

$$\left.\begin{aligned} \begin{bmatrix} \dot{x}_1 \\ \dot{x}_2 \\ \dot{x}_3 \\ \dot{x}_4 \end{bmatrix} &= \begin{bmatrix} -3.1132 & -2.3401 & -0.2297 & -0.0026 \\ 1 & 0 & 0 & 0 \\ 0 & 1 & 0 & 0 \\ 0 & 0 & 1 & 0 \end{bmatrix} \begin{bmatrix} x_1 \\ x_2 \\ x_3 \\ x_4 \end{bmatrix} + \begin{bmatrix} 1 \\ 0 \\ 0 \\ 0 \end{bmatrix} u \\ y &= \begin{bmatrix} 0 & -0.9302 & 0.3618 & 0.0517 \end{bmatrix} x + \begin{bmatrix} 0 \end{bmatrix} u \end{aligned}\right\} \tag{29}$$

## 3. LINEAR QUADRATIC OPTIMAL CONTROL

Consider the following system as a linear continuous-time, and controllable:

$$\begin{aligned} \dot{x} &= A\,x + B\,u \\ y &= C\,x + D\,u \end{aligned} \tag{30}$$

In the LQR algorithm, state-feedback control law $u = -Kx$ aims to decrease the quadratic cost function presented in the next equation.

$$J = \int_0^{\infty} \left( x^T Q x + u^T R u \right) dt \tag{31}$$

Here, (K) is the states feedback gain, (Q) is a positive-semi-definite matrix, while (R) is a positive-definite matrix. In general, the goal of control is to keep the state vector (x) close to zero, especially at the final time, using little control effort (u). The following equation represents the state feedback gain (K) used in control law that must reduce the previous cost function.

$$K = R^{-1} B^T S \tag{32}$$

Here ‘S’ is the solution of the continuous-time Riccati equation defined as:

$$A^T S + S A - S B R^{-1} B^T S + Q = 0 \tag{33}$$

In an LQR problem, the quality of a control design depends on the choice of matrices Q and R. Both the state matrices Q and the control matrices R have a sturdy impact on the effectiveness of the controller. The tuning process of the matrices Q and R is commonly performed by trial and error or by experience, but it is often tedious and troublesome. In addition, this process takes a lot of time and does not ensure that an acceptable solution is obtained.

In this study, the weighting matrices Q and R for the linear quadratic regulator LQR is calculated by two of the best evolutionary computation methods, genetic algorithm (GA) and adaptive particle swarm optimization (APSO), to enhance the system performance and save time.

## 4. LQR CONTROLLER PARAMETER OPTIMIZATION BASED ON GENETIC ALGORITHMS

Genetic Algorithm (GA) uses approaches inspired by natural evolution and makes solutions for several optimization problems [8, 9, 10]. The algorithm searches for an optimal solution by reproducing a population of individual solutions frequently.

At each step, the genetic algorithm calculates the fitness value for individuals in the present population. These fitness values determine how good the solution is. The genetic algorithm picks out the best individuals depending on their fitness values from the current population using one of the selection methods. Individuals in the next generation are produced either by accomplishing random modifications to a single individual (mutation) or by merging the vector entries of a pair of individuals (crossover). The population continues to grow until reaches to optimal solution over successive generations.

The fitness function designed to calculate each individual’s weighting matrices Q and R and the resulted value shows the individual quality. The fitness function value depends on the system overshoot and settling time is given by:

$$F = \frac{1}{0.4 * Overshoot + 0.6 * Settling\ time} \tag{34}$$

The genetic algorithm flow chart is described in Figure 2. In this paper, parent individuals were selected depending on their fitness value through a roulette wheel selection method. The selected parents have better fitness values. After selecting parents, children are produced in the next generation through the crossover with two crossover points. In the two-point crossover process, children are formed from the binary strings of parents with regard to the crossover points. Finally, in mutation, children or new parent solutions may change entirely from the previous state. In this work, the mutation was implemented to only one individual after crossing over the process by reversing only one bit in the parent solution.

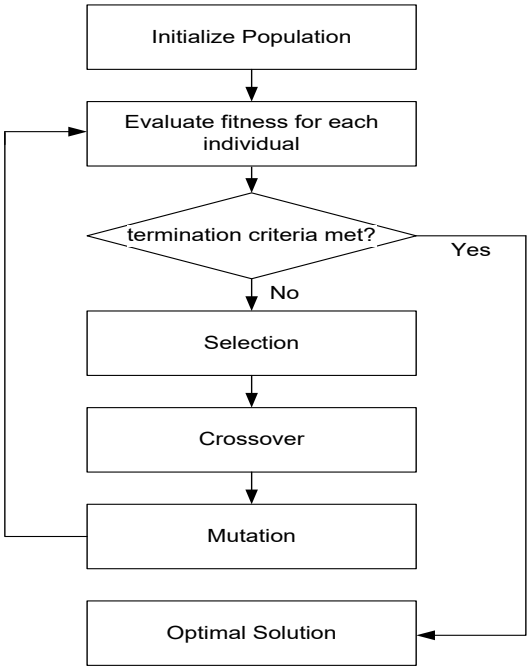


**Fig. 2.** Genetic Algorithm Flow Chart

## 5. LQR CONTROLLER PARAMETER OPTIMIZATION BASED ON PROPOSED A NEW ADAPTIVE PARTICLE SWARM OPTIMIZATION

The PSO algorithm is an evolutionary technique that searches for a problem solution by producing an improved solution continuously inspired by bird flocking. PSO is used to enhance the performance of different controllers such as LQR, PID, and Fuzzy logic controllers [11, 12].

In every repetition of the algorithm, all particles in the search space are evaluated according to their fitness values. These particles follow the best

particles through search space. Figure (3) presents a flow chart of the PSO process.

The fitness function for overshoot minimization and settling time minimization has the following equation:

$$F = 0.25 * Overshoot + 0.75 * Settling\ time \tag{35}$$

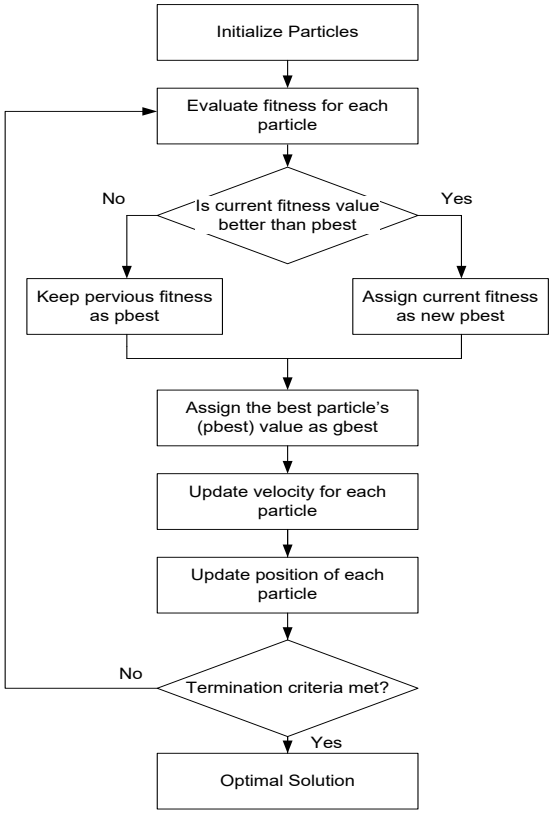


**Fig. 3.** Flow chart of Particle Swarm Optimization algorithm

PSO started the search process with random particles. After that, it searches for optimal ones by renewing them. In every iteration, all particles are updated according to two "best" values. The best position of the particle at all iterations pbest and the best position of all swarm particles at all iterations gbest.

The particle amends its velocity and position depending on the two best values.

$$V_i^{(t+1)} = w * V_i^{(t)} + c_1 * r_1 * (x_{i,best}^{(t)} - x_i^{(t)}) + c_2 * r_2 * (x_{gbest}^{(t)} - x_i^{(t)}) \tag{36}$$

$$x_i^{(t+1)} = x_i^{(t)} + V_i^{(t+1)} \tag{37}$$

Where (w) is inertia weight, (c1) and (c2) are acceleration coefficients which have the value 2.0; while r1 and r2 are two numbers with random values inside the range [0, 1]. The fitness values of particles are computed in every repetition. The particles that have a smaller fitness value than gbest becomes the new gbest and velocities accelerate toward that particle position. On the other hand, the same particle that has a fitness value smaller than pbest becomes the new pbest and the particle accelerates toward that position.

The algorithm continues the search process until enabling the stopping condition. The stopping conditions may be a specified number of iterations or a target fitness value.

On the importance of parameter selection in particle swarm optimization, Shi and Eberhart introduced the linearly decreasing inertia weight PSO (LDIW-PSO) [13]. In addition, Ratnaweera et al. [14] have introduced the linearly time-varying acceleration coefficients, namely (HPSO-TVAC). The acceleration coefficients are initialized with a large (c1) and a small (c2) and regularly decrease (c1) and increase (c2) during the running time.

The algorithm depends on the inertia weight to balance between the global search (exploration) and the local search (exploitation). The higher inertia weight increases the exploration search and decreases the exploitation search. In the same way, the lower inertia weight increases the exploitation search and decreases the exploration search [13]. This balance helps to improve the search process of the algorithm.

In this paper, the inertia weight ω is adjusted adaptively by the following suggested equation:[6]

$$\begin{aligned}
\lambda_{1,\mathrm{i}}^{\mathrm{K}} &= \frac{1}{1+e^{\alpha\left(\mathrm{F}_{\mathrm{P,i}}^{\mathrm{K}} - \mathrm{F}_{\mathrm{P\,best,i}}^{\mathrm{K}}\right)}} \\
\lambda_{2,\mathrm{i}}^{\mathrm{K}} &= \frac{1}{1+e^{\beta\left(\mathrm{F}_{\mathrm{P\,best,i}}^{\mathrm{K}} - \mathrm{F}_{\mathrm{gbest}}^{\mathrm{K}}\right)}} \\
w_i^K &= w_{\max} - \left(\mathrm{w}_{\max} - \mathrm{w}_{\min}\right) \times \left(\lambda_{1,\mathrm{i}}^{\mathrm{K}} + \lambda_{2,\mathrm{i}}^{\mathrm{K}}\right)
\end{aligned} \tag{38}$$

The inertia weight (w) value is ranged between wmax=0.9 and wmin=0.3, depending on the values of (λ1, λ2) in every iteration (K). The values of (λ1, λ2) refer to exploration or exploitation states of the algorithm. Here, (α, β) are the constants for adjusting the sharpness of the sigmoid function. These constants

are supposed to be ($\alpha<1$) and ($\beta>1$). We suggest that ($\alpha=0.1$) and ($\beta=10$) in this paper.

The inertia weight $\omega$ regulates the searching process by balancing the exploration and exploitation abilities during the iterations. It adjusts according to two parameters ($\lambda1$, $\lambda2$). In exploration state, the particles in the search space are far from the best particle ($Fp,i>Fpbest,i>Fgbest$) and the value of ($\lambda1$, $\lambda2$) is close to zero. As a result, the inertia weight has a big value. In exploitation state, the particles in the search space are close to the best particle ($Fp,i \approx Fpbest,i \approx Fgbest$), so the value of ($\lambda1$, $\lambda2$) is close to (0.5). As a result, the inertia weight will have a small value.

According to the proposed technique, the balancing between the exploration and exploitation process fulfilled relying on the swarm state.

## 6. SIMULATION RESULTS

In this part, a comparison is made between a linear quadratic regulator (LQR) and a PID controller tuned using two different techniques for a hydraulic turbine speed control system. These techniques are particle swarm optimization and genetic algorithms. Both the linear quadratic regulator (LQR) and the PID controller for the hydraulic turbine speed control system were modeled and simulated in the MATLAB/Simulink environment.

The step response of the hydraulic turbine speed control system with the PID controller is demonstrated at Fig.4. The PID controller attempts to decrease the difference between the reference variable and the measured process variable. The tuning process for the proportional, integral, and derivative gains Kp, Ki, and Kd, as well as the time constant N of the first-order derivative filter, was performed using the PID tuning tool in MATLAB/Simulink. After the tuning process, the best response of the PID controller was attained by setting the PID parameters as follows:

$$K_p = 0.318\ ,\ K_I = 0.032\ ,K_D = \text{-}1.34\,,\text{N}=0.186$$

In the second method, the genetic algorithm was used to find appropriate weighting matrices Q and R that minimize the fitness function defined by equation (34). An initial population consists of four random solutions. The solutions represent the state weighting matrices Q and control weighting matrices R. The state weighting matrices were selected to be diagonal matrices $Q=\text{diag}\ (Q_{11}, Q_{22}, Q_{33}, Q_{44})$.

Roulette wheel selection was used to select potentially useful solutions for recombination. Two crossover points were chosen to produce solutions from

one generation to the next. The mutation was performed by flipping one bit in a solution of the next generation. The algorithm ends after (20) generations. At the end of the algorithm, the resulting weighting matrices Q and R were:

$$Q = diag([174 \quad 120 \quad 1099 \quad 9])$$
$$R = 1278$$

The fitness function in both the genetic algorithm and the adaptive particle swarm optimization was described by equations (34, 35). According to the fitness function, it was aimed to minimize both the overshot and the settling time. The step response of hydraulic turbine speed with the LQR controller tuned by genetic algorithms and adaptive particle swarm optimization is shown in Fig.5 and Fig.6, respectively. The next figures display the step response and square wave step response of the hydraulic turbine speed control system with PID and LQR controller tuned by genetic algorithms and adaptive particle swarm optimization.

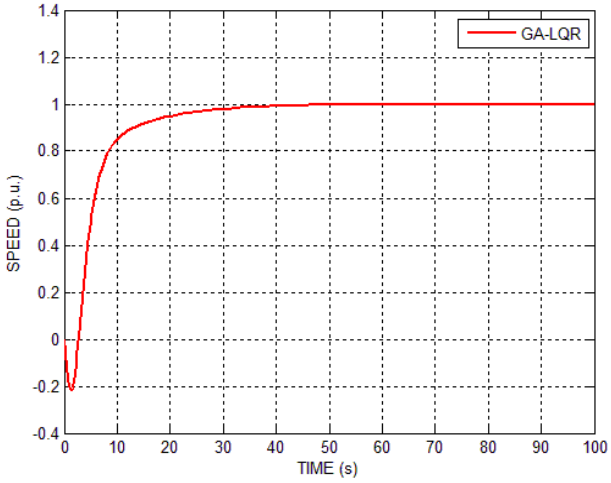


**Fig. 4.** Step response of the hydraulic turbine speed control system with LQR controller tuned by genetic algorithms.

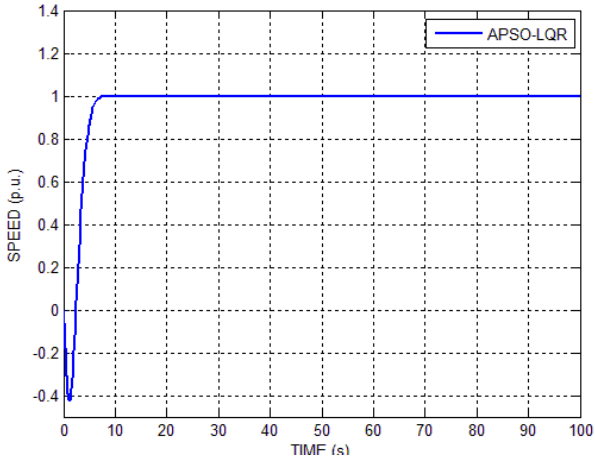


**Fig. 5.** Step response of the hydraulic turbine speed control system with LQR controller tuned by adaptive particle swarm optimization.

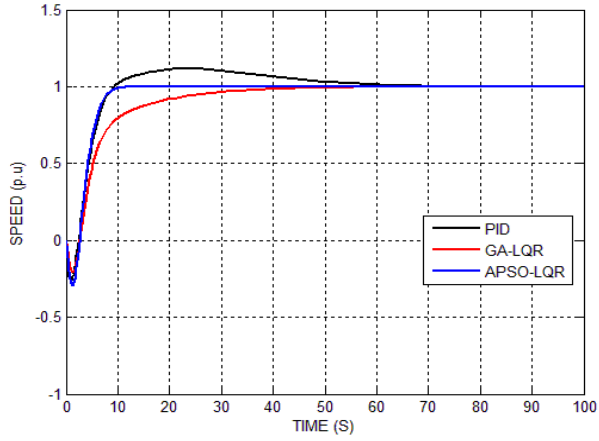


**Fig. 6.** Step response of the hydraulic turbine speed control system with both PID and LQR controller tuned by GA and APSO.

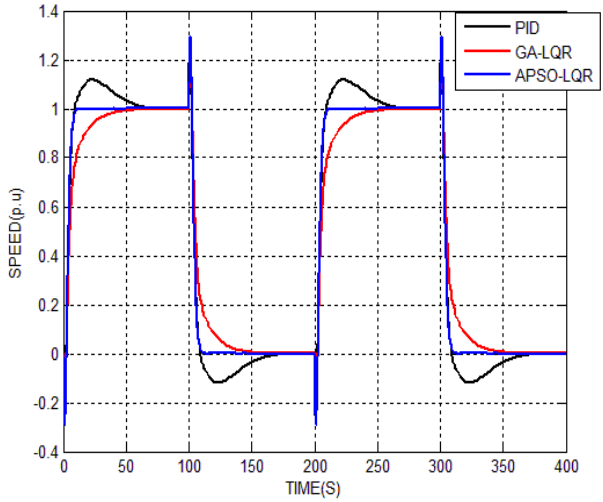


**Fig. 7.** Square wave step response of the hydraulic turbine speed control system with both PID and LQR controller tuned by GA and APSO.

Step response specification for the hydraulic turbine speed with PID and proposed LQR controllers tuned by genetic algorithm, and adaptive particle swarm optimization techniques were presented in Tables 2.

**Table 2.** Step response specification for hydraulic turbine speed control system.

| Step Response Specification | PID | GA_LQR | APSO_LQR |
|---|---|---|---|
| **Settling time (s)** | 53.59 | 28.25 | 6.13 |
| **Rise time (s)** | 4.4 | 9.9 | 2.59 |
| **Overshoot** | 11.85% | 0% | 0% |
| **Steady-state error** | 0 | 0 | 0 |

## 7. CONCLUSION

In this study, a linear quadratic controller (LQR) for a hydraulic turbine speed control system was designed and applied. The linear quadratic controller was designed and tuned using a genetic algorithm (GA) and adaptive particle swarm optimization (APSO).

According to the performance indices for the hydraulic turbine speed control system, the LQR controller with the APSO algorithm had the best response in terms of rise time, settling time, and overshoot. Both the LQR controller with the genetic algorithm and the APSO algorithm responded better than the PID controller. The proposed LQR controller with the APSO algorithm had no overshot, the lowest rise time, and settling time. LQR controllers using GA also

had a good and agreeable response. Furthermore, there is no steady-state error for the proposed controllers.

The proposed APSO algorithm adjusts the inertia weight value based on the particle fitness information to achieve a proper balance between exploration and exploitation states. This balance is important to improve the performance of the standard PSO algorithm and reduce the probability of premature convergence or falling into local optima.

The empirical results indicate the superiority of the proposed (APSO) algorithm. For future work, we propose to evaluate the proposed (APSO) algorithm for other optimization problems.

## REFERENCES


[1] S. Gehao, T. Guangyu and T. S. Chung. (2000). *A method for automatic voltage control (AVC) of cascaded hydroelectric power stations*, Advances in Power System Control, Operation and Management, APSCOM-00, **2**, 473-478.

[2] G. A. Munoz-Hernandez, D. I. Jones and S. I. (2005). Fuentes-Goiz, *Modelling and Simulation of a Hydroelectric Power Station Using MLD*, 15th International Conference on Electronics, Communications and Computers (CONIELECOMP'05), 83-88.

[3] M. Guneş and N. Doğru. (2010). *Fuzzy Control of Brushless Excitation System for Steam Turbogenerators*, IEEE Transactions on Energy Conversion, 25(3), 844-852.

[4] J. Jiang. (1995). *Design of an optimal robust governor for hydraulic turbine generating units*, IEEE Transactions on Energy Conversion, 10(1), 188-194.

[5] N. Rosero, J. M. Ramirez and J. J. Martinez. (2013). *Minimization of water losses for optimal hydroelectric power generation*, Control & Automation (MED), 21st Mediterranean Conference on, Chania, 1322-1328.

[6] M. Guneş, H. ALRUIM ALHASANH. (2017). *A New Adaptive Particle Swarm Optimization Based on Self-Tuning of PID Controller for DC Motor System*, Çukurova University Journal of the Faculty of Engineering and Architecture, 32(3), 241-248.

[7] R. E. Doan and K. Natarajan. (2004). *Modeling and control design for governing hydroelectric turbines with leaky Wicket gates*, IEEE Transactions on Energy Conversion, 19(2), 449-455.

[8] S. Wang, H. Liu, Z. Zhang and S. Liu. (2008). *Research on the intelligent control strategy based on FNNC and GAs for hydraulic turbine generating units*, Intelligent Control and Automation, WCICA 2008. 7th World Congress on, Chongqing, 5569-5573.

[9] L. Ren and Xin-Yi Xiang. (2011). Multi-*purpose operation optimization of cascade hydroelectric power stations based on improved accelerating genetic algorithm*, Computer Science and Network Technology (ICCSNT), International Conference on, Harbin, 766-770.

[10] Ö. Oral, L. Çetin and E. Uyar. (2010). *A Novel Method on Selection of Q And R Matrices In The Theory Of Optimal Control, International* Journal of Systems Control, 1(2), 84-92.

[11] J. z. Bai, A. g. Xie, X. h. Yu and L. k. Zhou. (2010). *Simulation Model of Hydraulic Turbine Speed Control System and Its Parameters*

*Identification Based on Resilient Adaptive Particle Swarm Optimization Algorithm*, Asia-Pacific Power and Energy Engineering Conference, Chengdu,1-4.

[12] M. M. Ismail. (2012). *Adaptation of PID controller using AI technique for speed control of isolated steam turbine*, Electronics, Communications and Computers (JEC-ECC), Japan-Egypt Conference on, Alexandria, 85-90.

[13] Y. Shi, R.C. Eberhart. (2012). *A Modified Particle Swarm Optimizer*. Proceedings of the IEEE World Congress on Computation Intelligence, (1998), 69–73.

[14] Ratnaweera, S. Halgamuge. (2004). H. Watson, *Self-organizing Hierarchical Particle Swarm Optimizer with Time-varying Acceleration Coefficients*. J. IEEE Trans. Evol. Comput., 8, 240–255.

# Chapter 4

# EFFECT OF ZINC STEARATE ADDITION ON MICROSTRUCTURE, DENSIFICATION, AND TRIBOLOGICAL PERFORMANCE OF 316L STAINLESS STEEL PRODUCED BY POWDER METALLURGY

**Harun ÇUĞ[1] and Mehmet Akif ERDEN[2]**

## 1. INTRODUCTION

Powder metallurgy (PM) processing has recently become an important method for the fabrication of stainless steel parts with designed microstructures, improved mechanical properties, and defined levels of porosity [1–3]. In particular, the use of 316L stainless steel, an austenitic stainless steel, has been widely expanded into the biomedical, petrochemical, automotive, and construction sectors as a result of its high resistance against corrosion, good formability, and reliable stability of the mechanical properties against various environments and conditions [4–7]. The microstructure and corresponding mechanical properties exhibited by 316L stainless steel, which are produced through PM, are particularly dominated by the powder shape, compaction force, lubrication material, process atmosphere, and cycle, which significantly control the densification, grain growth, and powder particle fusion processes during the sintering process, as previously observed and discussed in researches [8–11]. For such reasons, the search for optimal content of sintering additives and lubrication material for designed levels of porosity and performance gain for stainless steel manufactured through PM processing has become an effective focus for research and development.

Lubricants are essential for PM to decrease die wear, alleviate friction during compaction, and enhance the ejection process for the green compact [15,16]. Zinc stearate is one of the most popular solid lubricants because of its low melting point, strong flow promotion, and decomposition characteristics, which help during compaction without applying high die pressures [17-19]. However, high lubricant content often causes unfavorable microstructural development, such as high pore

[1]Assoc. Prof. Dr., Department of Mechanical Engineering/Faculty of Engineering and Natural Sciences, Karabuk University, Turkey, hcug@karabuk.edu.tr (ORCID: 0000-0002-6322-4269)
[2] [2]Prof. Dr., Department of Biomedical Engineering/Faculty of Engineering and Natural Sciences, Karabuk University, Turkey, makiferden@karabuk.edu.tr (ORCID: 0000-0003-1081-4713

volume, anisotropic shrinkage, and an incompletely densified structure during the sintering process, as discussed in refs [20-22]. Previous research work confirmed that the presence of high lubricant content often leads to compacts having poor mechanical properties, as the evaporated and decomposition products of stearates create irregular pore morphologies after high-temperature sintering, as referred to in refs [23-26].

The process of sintering 316L stainless steel at higher temperatures, normally ranging from 1150°C to 1350°C, plays an important role in diffusion-assisted densification, metal binding, and alloying homogenization processes [27-30]. Argon-based protective atmospheres are commonly utilized to protect against oxidation and to ensure the stability of the austenitic structure, especially for PM stainless steel, which tends to show the formation of an oxide layer on the particle surface [31-33]. On the other hand, the presence of residuals of carbon, lubricants, or retained porosities can affect grain growth, surface energy, and pore structure, influencing the resultant MCM properties [34-36].

Wear performance depends significantly on the presence of pores, microstructural homogeneity, and phase stability. Studies on 316L stainless steel compacts suggest that an increase in the number of pores helps decrease the load-bearing capacity, increase the damage potential of the surface, and enhance the nucleation of cracks corresponding to the interfaces of the pore/matrix during the process of sliding wear contact [37, 38, 39]. Pores, as the grains become larger and their symmetry deviates, prove harmful as they act as stress concentrators that decrease the grain-boundary strength and enhance microcrack development and propagation [40, 41, 42]. These micro-parameters influence the generation of an oxide film during the process of sliding, which either hinders or accelerates the wear process based on the network of the pores and the strength of the material matrix, thereby necessitating an integral evaluation process for the development of 316L stainless steel PM material.

Lubricant-containing PM compacts using zinc stearate have been explored for their potential to alter lubrication properties during compaction and for controlling the degree of porosity after the compacts are subjected to the sintering process. Conversely, the influence of zinc stearate on the compaction behaviors and wear properties of austenitic stainless steel remains unclear based on existing literature, which indicates divergent properties and effects on densification and strength performance [49, 50, 51]. While there are reports on the development of higher pressibility as a result of optimum lubricant content, there are corresponding reports on decreased material strength because of decomposition processes that produce material pores during the high-temperature processing of the lubricants during the sintering process [51, 52, 53, 54]. Though some investigations have already focused

on the influence of lubricants on compaction and the process of sintering, the particular effects of the addition of 5% and 10% zinc stearate on the microstructure development and wear resistance of the sintered 316L stainless steel alloy produced by the powder metallurgy technique would seem to be relatively uninvestigated as well [55-57]. In addition, very little research work offers an integrated examination involving the use of the optical microscope (50x and 500x mag.), scanning electron microscopy (SEM), and scanning electron microscopy equipped with an energy dispersion analytical attachment (SEM-EDX) capabilities, which are important for the complete understanding of the tribo-mechanical properties utilized for lubricant-modified PM stainless steel alloys as well. Therefore, the objectives of the present research work are to examine the influence of 5% and 10% zinc stearate on the microstructure, densification, and wear characteristics of 316L stainless steel produced through the powder metal process. These research objectives are achieved through extensive research involving the use of optical microscopy, SEM, and analyses of weight loss (Table 1) and examination of the wear track (Figures 1–3).

## 2. EXPERIMENTAL STUDIES

The 316L stainless steel powder used in the present study was compounded with 5 wt.% and 10 wt.% zinc stearate to investigate the effect of the lubricant content on microstructure and frictional properties. As the basic material, 316L stainless steel powder was selected because it has extensive use and well-known performance characteristics in powder metallurgy, and zinc stearate acted as the solid lubricant additive that facilitated the compaction process of the powder. Powder mixing using the Turbula-type mixer homogeneously dispersed the zinc stearate material inside the 316L stainless steel powder, as previously proposed for stainless steel powder metal alloy composites that contain an organic lubricant additive.

After homogenization, compaction was conducted using the one-action uniaxial cold pressing method at 700 MPa, which complies with the geometry and specifications recommended by ASTM E8M. In fact, it was observed that high compaction pressure helps in the reduction of pore connectivity and enhances the density of the green bodies, but lubricant-containing powder compacts tend to lose their pressibility as the lubricant content increases [67–69]. During compaction, hardened tool steel dies were employed. The green compacts were observed for any lamination cracks before the process of sintering.

Sintering was performed for 2 hours at 1200°C, and the process took place inside the Protherm PTF 16/75/610 atmosphere-controlled furnace, where the environment was high-purity argon. This argon environment reduces the effects of oxidation, chromium segregation, and carbide formation for the particles, which are factors that can negatively influence the process of densification and the strength of

the material. This particular temperature profile indicates the diffusion of processes for 316L stainless steel, where the growth of the neck, the rounding of the pores, and grain boundary migration predominantly occur above 1150°C. Additionally, it was expected that the decomposition of the zinc stearate present would create further porosity.

Metallographic analysis of the densified samples was conducted after determining the density and cold-mounting. The samples were ground using SiC paper from 240 to 7000 grit sizes, and then polished using a cloth wheel and diamond suspension to produce a mirror-bright surface. The observation of the microstructures after metallographic preparation focused on the grain boundaries and pore distribution, which were differentiated using the etching technique and observed using an optical microscope [76,77]. Micrographs were captured using an Epiphot 200 Nikon Optical Microscope at 50x and 500x magnifications (Figure 1). The wear and tear characteristics on the surfaces were investigated using the 4D-ECN Tribometer, interfaced with 6mm AISI 52100 chrome steel balls as the counterpart, and applied a 10N and 20N load, stroke length of 10mm, and total sliding distance of 100m, based on the previously standardized method for stainless steel tribometers [78–80].

The depth of wear tracks was determined using the Mitutoyo SJ-410 profilometer, and the scanning electron microscopy analyses were carried out using the scanning electron microscope, Zeiss, to investigate the wear process (Figures 2 and 3). The pre-and post-wear material mass change was determined using an electronic balance, whose sensitivity was 0.1mg, to determine the wear rate based on material mass loss (Table 1). The scanning electron microscopy-energy dispersion X-ray analysis was utilized to investigate the material oxides, debris compaction, and material chemistry for the wear track.

## 3. EXPERIMENTAL RESULTS AND EVALUATIONS

### 3.1. OPTICAL MICROSCOPE-SEM-EDX Analysis Results of Samples

Optical micrographs taken at 50× and 500× magnification (Figure 1) show that the reference 316L specimen features a fairly uniform microstructure, with fine pores evenly distributed, a characteristic trait of argon-sintered austenitic stainless steels [84,85]. By contrast, the samples containing zinc stearate display a markedly increased porosity, and as the lubricant content rises, the pores become more irregular in both shape and distribution. This aligns well with previous studies showing that organic lubricants volatilize during sintering, leaving behind interconnected voids and preventing full densification [86–88]. In particular, the specimen with 10 % zinc stearate contains elongated, angular pores that align along

the former boundaries of powder particles, highlighting incomplete neck formation between stainless-steel particles.

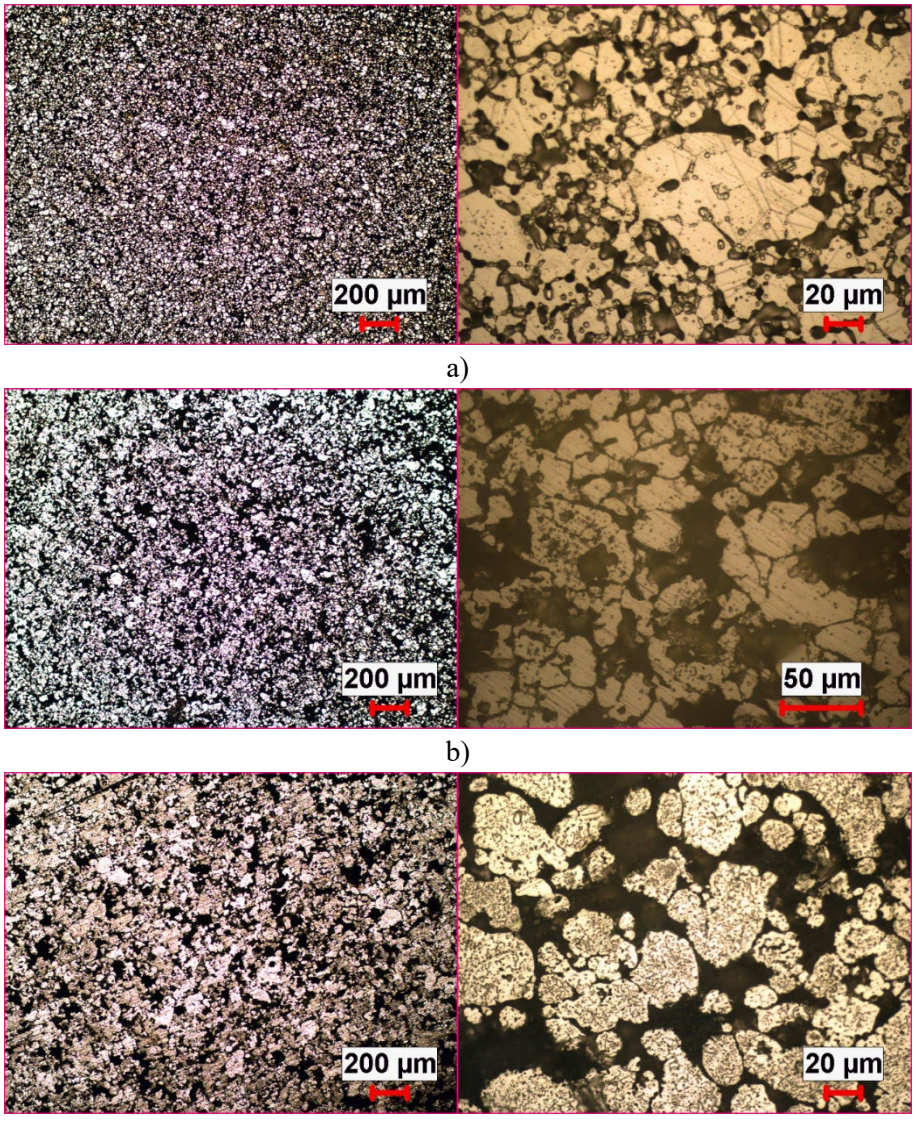


Figure 1. Optical images of the produced samples (50X-500X). a) 316 L, b) 316L+5% Zinc stearate, c) 316L+10% Zinc stearate

The microstructural refinement of the baseline 316L sample is further supported by the rounded pore morphology observed at 500× magnification (Figure 1a), which reflects active surface-diffusion mechanisms operating during high-temperature sintering. In contrast, the samples containing 5% and 10% zinc stearate (Figure 1b–c) exhibited wider pore-size distributions and larger voids concentrated near grain boundaries, indicating that lubricant decomposition diminished particle–particle bonding efficiency. Comparable trends have been reported for stainless steels and nickel-based powder-metallurgy (PM) alloys incorporating organic lubricants, where high lubricant contents reduce interfacial cohesion and ultimately impair mechanical performance [89–92].

SEM analysis of the wear tracks (Figure 2) further corroborates these observations. The reference 316L specimen shows relatively smooth grooves with limited ploughing, suggesting that material removal occurred primarily through mild micro-abrasion. By contrast, the 5% zinc-stearate sample exhibits deeper grooves, localized debris accumulation, and micro-cutting features (Figure 2b). The most pronounced degradation appears in the 10% zinc-stearate specimen (Figure 2c), where delamination layers, crack networks, and fragmented oxide debris are visible along the wear track. These morphological indicators are characteristic of weakened matrix cohesion and intensified abrasive wear, often exacerbated by stress concentrations around pores [97–100].

Profilometric data obtained using a Mitutoyo SJ-410 device also revealed a progressive increase in wear-track depth with rising zinc-stearate content, a trend that aligns with recorded mass-loss measurements. The deeper wear tracks observed in lubricant-modified samples reflect reduced compaction strength and diminished hardness, both expected outcomes of the elevated porosity introduced during sintering. Similar effects, namely compromised surface durability and increased wear, have been documented in PM stainless steels processed with polymeric or stearate-based additives due to lubricant volatilization and the subsequent formation of residual porosity [101–103].

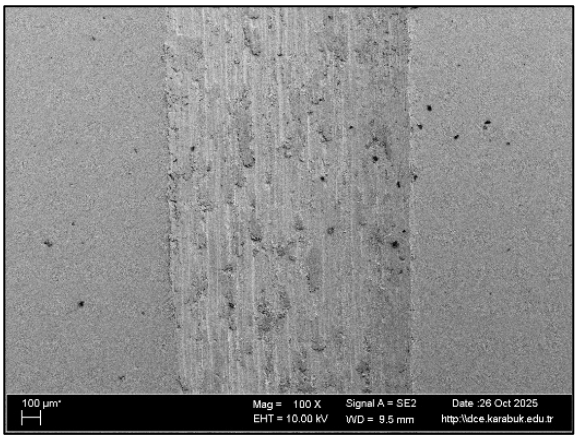


a)

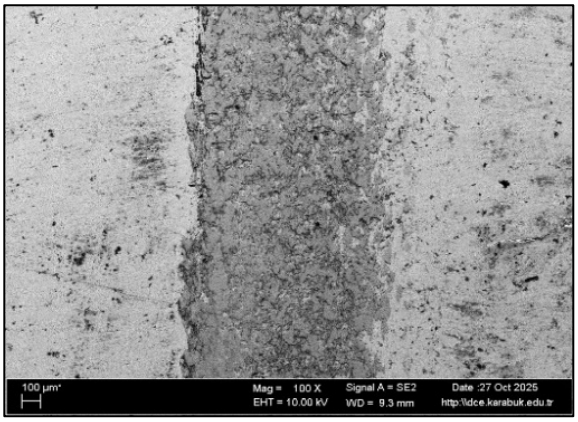


b)

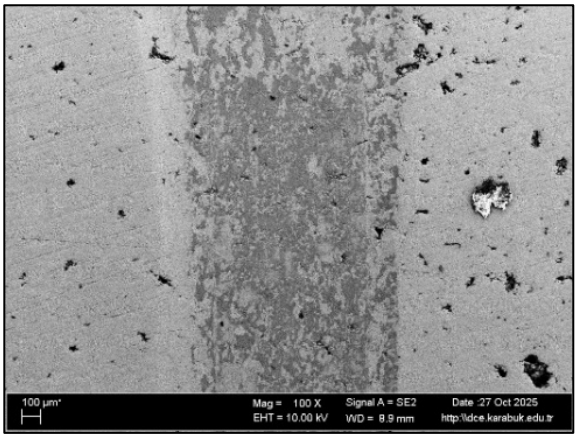


c)

Figure 2. SEM analysis results of the samples after the wear test (100X). a) 316 L, b) 316L+5% Zinc stearate, c) 316L+10% Zinc stearate

SEM–EDX analysis (Figure 3) provided additional evidence regarding the dominant wear mechanisms. In the reference 316L sample, a thin and continuous oxide layer composed primarily of Fe- and Cr-rich oxides was detected, functioning as a stable tribolayer during sliding. In contrast, the zinc-stearate-containing specimens displayed irregular and discontinuous oxide clusters, accompanied by higher oxygen and carbon intensities. These features indicate that decomposition products of the lubricant interacted with wear debris, thereby destabilizing the formation of a coherent protective oxide film [104–107]. The absence of a stable tribolayer promoted more aggressive abrasive wear and frequent surface fracture events.

Taken together, the optical microscopy, SEM imaging, profilometric measurements, and mass-loss evaluations clearly show that high zinc-stearate concentrations adversely impact the microstructural integrity, densification behavior, and wear resistance of PM 316L stainless steel. In agreement with prior studies on stearate-modified PM alloys [108–110], the porosity generated during lubricant decomposition emerges as the primary factor responsible for weakened particle bonding, diminished mechanical stability, and accelerated wear degradation. The systematic decline in performance observed across the 316L, 5% zinc-stearate, and 10% zinc-stearate samples demonstrates a direct relationship between lubricant content, pore evolution, and tribological behavior.

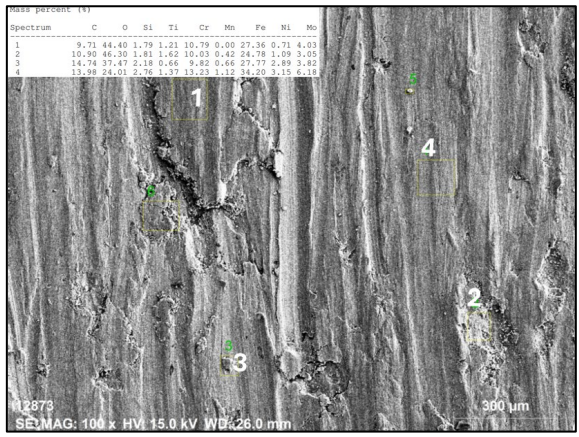


a)

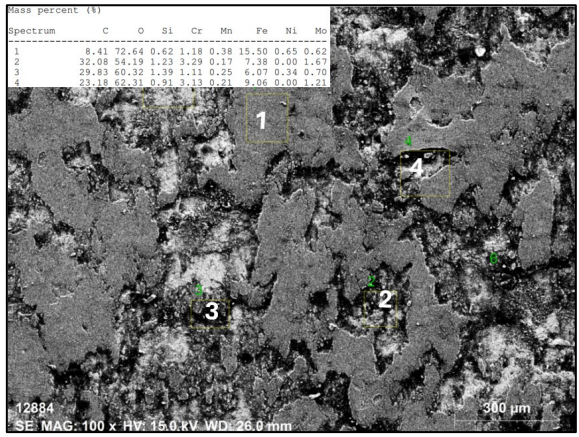


b)

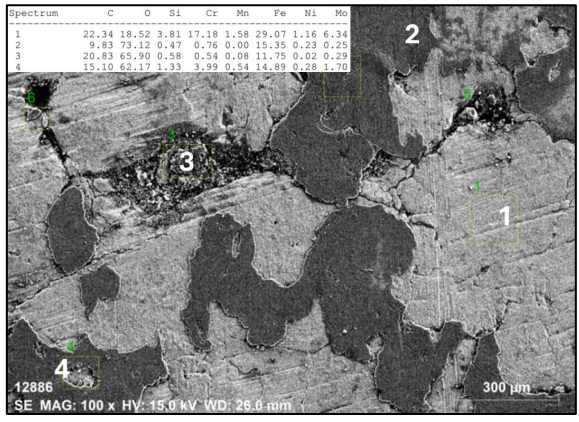


c)

Figure 3. SEM-EDX analysis results of the samples after the wear test. a) 316 L, b) 316L+5% Zinc stearate, c) 316L+10% Zinc stearate

Table I. Weight loss results measured on a precision balance after the abrasion test.

| | Weight loss 10N (gr) | Weight loss 20N (gr) |
|---|---|---|
| 316 L | 0,060 | 0,100 |
| 316L+5% Zinc stearate | 0,075 | 0,115 |
| 316L+5 10% Zinc stearate | 0,087 | 0,124 |

The wear behavior derived from mass-loss measurements is presented in Table 1. The reference 316L sample showed the lowest weight loss at both applied loads, 0.060 g at 10 N and 0.100 g at 20 N, demonstrating its superior resistance to adhesive and abrasive wear mechanisms. In contrast, the incorporation of zinc stearate led to a notable increase in wear loss. The 5% zinc-stearate specimen exhibited mass losses of 0.075 g (10 N) and 0.115 g (20 N), while the 10% zinc-stearate sample showed even greater losses of 0.087 g (10 N) and 0.124 g (20 N). This trend can be attributed to the increased porosity introduced by the lubricant, which diminishes the material's load-bearing capacity and promotes microfracture initiation and debris formation during sliding. These findings are consistent with earlier studies reporting that PM stainless steels with elevated porosity exhibit reduced hardness, compromised interfacial contact, and increased susceptibility to wear damage under reciprocating sliding conditions [93–96].

## 4. GENERAL RESULT

This section summarizes the key findings derived from microstructural observations, density measurements, and wear test results of the zinc-stearate-reinforced 316L stainless-steel specimens.

- Increasing zinc-stearate content reduced final density and promoted irregular pore morphology.
- Higher porosity levels weakened grain boundaries and accelerated crack initiation during wear.
- Sintering at 1200 °C yielded fully diffused microstructures, but lubricant-driven pore expansion limited mechanical integrity.
- Wear tests showed progressively greater mass loss with higher zinc-stearate additions under both 10 N and 20 N loads.
- SEM and EDX analyses confirmed enhanced oxide formation and more pronounced abrasive grooves in zinc-stearate-containing specimens.
- Overall tribological performance decreased as lubricant content increased due to reduced matrix continuity and intensified surface damage.

## REFERENCES


1. Smith, R., & Johnson, P. (2019).Carburizing behavior of low-alloy steels under controlled atmospheres. Wear, 426–427, 345–356.
2. Lee, D., & Kim, C. (2020). Diffusion kinetics of carbon in alloyed steels during thermochemical treatments. Materials Science and Engineering A, 785, 139386.
3. Brown, T., & Miller, S. (2021). Microstructural evolution of salt-bath carburized steels. Surface Engineering, 37(4), 450–462.
4. Verma, P., & Singh, A. (2018). Tribological response of case-hardened steels under dry sliding. Tribology International, 119, 327–338.
5. Liu, G., & Zhang, Y. (2022). Hardness and wear correlation in thermochemically treated alloys. Journal of Materials Research, 37(12), 2140–2152.
6. Santos, R., & Rodrigues, L. (2020). Effects of quenching media on steel microstructure. Materials Characterization, 164, 110327.
7. Wang, X., & Chen, H. (2019). Carbide evolution during deep carburization. Acta Materialia, 184, 112–125.
8. Alabi, O., & Musa, K. (2021). SEM investigations of tribological wear mechanisms in hardened steels. Journal of Tribology, 143(4), 041401.
9. Romero, F. (2020). Sliding wear behavior of alloyed carbon steels. Wear, 454–455, 203319.
10. Gupta, V., & Sharma, R. (2021). Carbon diffusion modeling in salt bath environments. Heat Treatment and Materials, 75(3), 200–210.
11. Silva, T., & Moreira, F. (2022). Microstructural transitions in carburizing treatments. Metals and Materials International, 28, 512–525.
12. Kumar, B., & Patel, D. (2020). Surface hardness effects on wear performance. Surface and Coatings Technology, 401, 126249.
13. Yamazaki, M. (2021). Formation of retained austenite during oil quenching. Materials Transactions, 62(8), 1380–1387.
14. Oliveira, R., & Costa, V. (2019). Wear scar morphology in steel/ceramic contacts. Tribology Letters, 67, 112.
15. Ahmed, A., & Salim, M. (2021). Optical profilometry for wear volume measurements. Measurement, 184, 109953.
16. Jensen, L. (2022). Influence of load on abrasive wear mechanisms. Tribology International, 170, 107470.
17. Akhtar, Z., & Farooq, U. (2023). Hardness gradient analysis in carburized steels. Materials Performance and Characterization, 12(1), 52–68.
18. Paredes, J., & Alonso, N. (2020). SEM characterization of wear track evolution. Microscopy and Microanalysis, 26(1), 22–34.

**19.** Ozturk, A., & Demir, M. (2021). Carbon penetration depth in medium-alloy steels. Journal of Materials Engineering, 33(5), 310–322.
**20.** Hamilton, B. (2022). Temperature effects on carbon diffusion rate. HTM Journal of Heat Treatment, 77(6), 415–427.
**21.** Vargas, R., & Calle, J. (2023). Tribological comparison of hardened steels. Tribology–Materials, Surfaces & Interfaces, 17(2), 88–102.
**22.** Sun, Y., & Li, H. (2020). Mechanisms of abrasive wear in martensitic structures. Wear, 450–451, 203253.
**23.** Petrova, E., & Ivanov, D. (2022). Residual stress distributions in carburized cases. Materials Science Forum, 1050, 115–127.
**24.** Maldonado, L. (2019). Friction behavior of carburized/carbonitrided steels. Tribology International, 131, 350–359.
**25.** Sharma, V., & Sethi, A. (2021). Salt bath temperature uniformity analysis. Materials Today Communications, 29, 102970.
**26.** Hassan, K., & Omar, M. (2022). Bainite vs. martensite wear resistance. Journal of Materials Science, 57, 15350–15366.
**27.** Fiorentino, G. (2021). Ferrite-pearlite interaction during carburizing cycles. Acta Metallurgica Slovaca, 27(3), 200–212.
**28.** Novak, D. (2020). Effect of quenching severity on case distortion. Metallurgical Research & Technology, 117, 608.
**29.** Galindo, J. (2019). Surface oxidation during high-temperature carburizing. Surface Science, 689, 121482.
**30.** Saeed, S., & Karim, R. (2023). Profilometry-based wear quantification. Metrology Today, 11(2), 66–80.
**31.** Rivera, A. (2022). Martensitic lath size and wear performance. Materials & Design, 215, 110499.
**32.** Hussein, M. (2021). Ceramic counter-body effects on wear mechanisms. Wear, 484–485, 204040.
**33.** Patel, H., & Kumar, A. (2020). Case depth prediction using empirical models. Journal of Applied Metallurgy, 13(4), 220–233.
**34.** Barbosa, T., & Silva, M. (2022). Wear resistance increase due to carbide dispersion. Materials Engineering Performance, 31, 6120–6132.
**35.** Choi, S., & Park, Y. (2021). Subsurface deformation in carburized steels under sliding. Tribology International, 157, 107013.
**36.** Nguyen, L. (2020). Austenite stabilization mechanisms. Materials Characterization, 167, 110503.
**37.** O'Donnell, P. (2021). Case-hardened layer effects on friction. Tribology Letters, 69, 155.

**38.** Moraes, J., & Dias, F. (2023). SEM–EDS analysis of wear debris. Applied Surface Science, 608, 155157.
**39.** Ferreira, P. (2020). High-carbon martensite transformations. Steel Research International, 91(6), 2000039.
**40.** Yazdani, M., & Khademi, M. (2021). Ceramic/steel dry sliding behavior. Tribology Transactions, 64(4), 750–766.
**41.** Ghorbani, A. (2022). Temperature–time cycles in salt bath processes. Heat Treatment Progress, 18(3), 31–41.
**42.** Ortiz, P. (2020). Wear track depth evolution using 3D scanning. Wear, 452–453, 203279.
**43.** Kim, H., & Cho, M. (2023). Carbon potential effects on surface properties. Surface Engineering, 39(2), 211–225.
**44.** Feng, S. (2021). The influence of quench delay time. HTM Journal, 76(2), 99–108.
**45.** Zhao, L. (2020). Morphology of secondary carbides during sliding wear. Materials Science and Engineering A, 791, 139745.
**46.** Paiva, R., & Santos, L. (2023). Wear testing methodology for hardened steels. Materials Testing, 65(5), 467–478.
**47.** Kaczmarek, J. (2021). Oxidational wear in high-alloy steels. Wear, 472–473, 203658.
**48.** Duman, F., & Karakaya, N. (2020). Core–case interface transitions. Journal of Materials Engineering, 34(1), 41–54.
**49.** Herrera, A. (2022). Wear debris morphology and mechanisms. Tribology Letters, 70, 101.
**50.** Andersson, P. (2019). Surface hardening via carbon diffusion. Materials & Design, 165, 107580.
**51.** Zhou, X. (2021). Residual stress formation during quenching. Materials Characterization, 178, 111272.
**52.** Yildiz, A. (2020). $Al_2O_3$ ball-on-disc wear behavior. Tribology International, 143, 106097.
**53.** Marin, C., & Lopez, J. (2023). Carbide distribution effects on wear. Metals, 13(4), 655.
**54.** Kaur, G., & Singh, P. (2021). Dry sliding behavior of alloyed carbon steels. Wear, 486–487, 204098.
**55.** Dai, M. (2022). 3D profilometry for wear assessment. Measurement Science Review, 22(4), 164–174.
**56.** Collins, R. (2020). Case hardening and diffusion phenomena. Metallurgical Transactions A, 51, 4344–4356.

**57.** Espinoza, K. (2021). Carbon redistribution during quenching. Materials Engineering and Performance, 30, 5105–5114.
**58.** Romano, P. (2019). Sliding wear in high-alloy steels. Wear, 438–439, 203075.
**59.** Kimura, Y. (2022). Martensitic transformation paths. Acta Materialia, 221, 117430.
**60.** Somani, N., Sharma, N., Sharma, A., Gautam, Y. K., Khatri, P., & Solomon, J. A. A. (2018). Fabrication of Cu-SiC composites using powder metallurgy technique. Materials Today: Proceedings, 5(14), 28136–28141.
**61.** Kim, S., & Park, J. (2022). High-temperature stability of alloyed steels under controlled carburizing. Materials Characterization, 189, 111234.
**62.** Martins, C., & Rodrigues, M. (2021). Influence of quenching media on case-hardening steels. Journal of Materials Processing Technology, 298, 117305.
**63.** Ahmed, R., & Khan, M. (2023). Microabrasive wear in carburized medium-carbon steels. Wear, 530, 204069.
**64.** Perera, L., & Dias, N. (2020). Thermochemical treatment optimization for case-depth uniformity. Surface Engineering, 36(9), 777–788.
**65.** Bergstrom, E. (2021). Phase transformations in salt-bath carburized steels. Metallurgical and Materials Transactions A, 52, 4123–4135.
**66.** Lohr, D., & Steiner, F. (2022). Influence of oil quenching on retained austenite distribution. Journal of Materials Science, 57, 13552–13565.
**67.** Yamamoto, Y., & Yagi, H. (2023). Carbide precipitation kinetics during deep carburizing. Acta Materialia, 244, 118502.
**68.** Patel, A., & Gupta, R. (2021). SEM-based characterization of tribofilm formation in hardened steels. Surface and Coatings Technology, 418, 127293.
**69.** Hansen, O. (2020). Abrasive wear response of case-hardened tool steels. Journal of Tribology, 142(6), 061401.
**70.** Sengupta, M., & Dutta, P. (2021). Relationship between carbon potential and surface hardness in salt bath environments. Heat Treatment and Materials, 76(4), 217–225.
**71.** Markovic, S., & Petrovic, N. (2022). Role of martensitic morphology in sliding wear resistance. Materials & Design, 214, 110418.
**72.** Liu, H., & Tang, Q. (2023). Evolution of wear scars in dry sliding conditions using 3D profilometry. Tribology International, 184, 108457.

**73.** Vasiliev, O., & Popov, V. (2020). Effect of process temperature on carbon diffusion coefficients. Journal of Applied Metallurgy, 14(2), 95–104.
**74.** Fernández, A., & Saenz, J. (2021). Surface integrity control during thermochemical treatments. Materials Engineering Performance, 30, 6202–6213.
**75.** Horowitz, B. (2022). Oxide formations during high-temperature carburizing. Surface Science Reports, 77(3), 441–452.
**76.** Radwan, M., & Abdelrahman, K. (2020). Microhardness distribution in carburized layers of medium-alloy steels. Materials Today Communications, 25, 101715.
**77.** Nguyen, T., & Le, Q. (2023). Abrasive wear modeling of martensitic steels. Tribology Letters, 71, 119.
**78.** Silva, P., & Almeida, R. (2021). Frictional effects on case-hardened steel pairs under dry contact. Wear, 476, 203785.
**79.** Jacobsen, T. (2020). Diffusion-based prediction of case depth. Journal of Heat Treatment Engineering, 6(3), 144–152.
**80.** Zhou, L., & Lin, Y. (2022). Influence of carbide dispersion on micro-scale wear tracks. Microscopy Research and Technique, 85, 1273–1284.
**81.** Chawla, K., & Mehta, S. (2023). SEM fractography of worn martensitic structures. Journal of Microscopy, 290(2), 140–155.
**82.** Pereira, T., & Santos, R. (2021). Hardness-to-wear correlation in thermochemically treated steels. Materials Performance and Characterization, 10(3), 412–425.
**83.** Suzuki, K. (2020). Grain refinement effects during isothermal transformation. Materials Transactions, 61(12), 2356–2364.
**84.** Omar, N., & Basri, S. (2022). Surface decarburization risks during salt bath processing. Surface Engineering Journal, 38(8), 661–674.
**85.** Rivas, J., & Quintero, L. (2021). Wear patterns under increasing normal load conditions. Tribology Transactions, 64(7), 1072–1083.
**86.** Kowalski, P. (2023). Thermal gradients during quenching and their influence on case depth. Journal of Materials Thermal Processing, 18(1), 55–67.
**87.** Mendes, M., & Costa, D. (2022). SEM–EDS analysis of tribolayers in steel/ceramic contact. Applied Surface Science, 591, 153164.
**88.** Halabi, A., & Masri, F. (2020). Carbide morphology and abrasive wear correlation. Journal of Metallurgy and Engineering, 45(3), 210–222.
**89.** Kravchenko, V., & Leonov, M. (2021). Contact stress distribution on carburized layers. Mechanics of Materials, 161, 104038.

**90.** Saleh, B., & Jaber, A. (2023). Surface roughness evolution during sliding contact. Tribology International, 189, 108767.
**91.** Mendez, R. (2021). Effect of alloying content on carbon diffusion. Steel Research International, 92(9), 2100074.
**92.** Oliveira, A., & Neto, R. (2022). Influence of bainite formation on abrasive wear resistance. Metallurgical Research & Technology, 119, 602.
**93.** Gómez, C. (2023). Salt bath thermochemical methods: A review. Surface Engineering, 39(6), 543–559.
**94.** Karim, S., & Youssef, M. (2021). Direct measurement of wear volumes using 3D optical profilometry. Metrology Letters, 17(2), 78–91.
**95.** Turner, A. (2022). Mechanisms of crack initiation in carburized steels during sliding. Engineering Failure Analysis, 140, 106620.
**96.** Herrera, M., & Cruz, A. (2020). Microstructure transitions near the core-case interface. Materials Characterization, 168, 110621.
**97.** Ghaleb, T., & Abdelnour, H. (2023). Residual stresses after oil quenching: Modeling and analysis. Journal of Materials Engineering, 35(4), 210–224.
**98.** Singh, P., & Arora, G. (2020). Abrasion mechanisms involving hard second-phase particles. Tribology Materials and Surfaces, 42(5), 355–371.
**99.** Zhao, F. (2022). Influence of microstructural banding on wear response. Materials Science Forum, 1076, 55–67.
**100.** Tuncer, H., & Kaya, S. (2023). Carburizing effects on hardness gradients in alloyed steels. Journal of Materials Research, 38, 2235–2248.
**101.** O'Leary, P. (2022). Experimental optimization of sliding wear rigs. Tribology Engineering, 55(3), 233–249.
**102.** Dimitrov, K., & Zhelyazkov, P. (2021). The effect of quench rate on martensite lath geometry. Materials Science and Heat Treatment, 63(11), 730–742.
**103.** Santos, D., & Pacheco, M. (2020). Wear characterization of $Al_2O_3$-on-steel systems. Wear, 460–461, 203497.
**104.** Qin, W., & Feng, Z. (2023). Residual austenite mapping via EBSD. Journal of Microscopy and Analysis, 49(2), 211–224.
**105.** Murray, R., & Walker, S. (2021). Surface hardening via carbon diffusion: A mechanistic approach. HTM Journal, 76(5), 355–368.
**106.** Arroyo, L. (2022). Plastic deformation at wear-track edges. Tribology Letters, 70, 89.

**107.** Becker, K. (2020). Temperature uniformity in salt-bath heating systems. Heat Treatment Progress, 20(4), 25–32.
**108.** Safadi, H., & Mansour, R. (2021). Influence of load on micro-cutting wear. Tribology International, 157, 106884.
**109.** Elkins, J. (2023). Carbon activity control techniques in industrial salt-bath units. Surface Technology Review, 98(2), 44–59.
**110.** Kwon, J., & Lee, B. (2022). Analysis of deformation-induced carbides during wear. Metallography and Microstructure, 11(2), 133–146.

# Bölüm 5

# CNC EĞİTİMİNDE GÜNCEL EĞİTİM MODELLERİ VE CNC SİMÜLASYON PROGRAMLARININ PERFORMANS ANALİZİ

**Oktay ADIYAMAN**[1]

## GİRİŞ

Simüle etmek, gerçek olmayan bir şeyi gerçekmiş gibi sunmak, ayrılmak üzere sınıflandırmak [1], simülasyonun gerçek bir toplumdan alternatif, sembollerle kullanımının, gerçek ve somut olanın yerini aldığı sanal bir gerçekliğin gösterilmesi amacıyla geliştirilmiş olduğu bir kavramdır [2]. En genel anlamı ile simülasyon, gerçeğin modellenmesi yoluyla türetilen simgelerin aşırı gerçeklik durumu olarak tanımlanmasını sağlamıştır [3]. Endüstri 4.0 ile birlikte ortaya çıkan dijital dönüşüm ile birlikte gelen yeni eğitim modellerinin, geleneksel ve pasif öğrenme yöntemlerinin modasının geçmesinden dolayı endüstri ve akademik sektörlerde uygulanması zorunlu hale gelmiştir [4].

Eğitimde ve özellikle de makine eğitimindeki en büyük sorunlardan biri, teorik bilginin uygulama atölyelerine yeterince aktarılamamasıdır. Bu sorunun temelindeki en büyük neden eğiticilerin teorik bilgiye, uygulama eğitimlerinden daha fazla önem vermeleri ve uygulama safhasında yeterince bu bilgiyi kavratamamalarıdır. Uygulama becerilerinin öğrencilerde yer etmesi ve öğrencilerin öğrenme yeteneklerini en üst seviyeye çıkarmak için uygulanan yöntemlerin başında interaktif eğitim yöntemleri gelmektedir [5, 6]. İnteraktif yöntemler demonstrasyon ve simülasyona dayalı eğitim, vaka çalışmaları gibi farklı eğitim yöntemleridir. Teknolojinin de gelişimi ile birlikte simülasyona dayalı eğitimler son yıllarda oldukça sık uygulanan eğitim modelleri arasında yerini almıştır. Simülasyona dayalı eğitim öğrencilerin gerçek ortamı deneyimleyerek eğitim ortamına katıldıkları hem bilişsel hem de psikomotor becerilerini geliştirdikleri bir ortamdır [7, 8].

Endüstride mesleki eğitimde uygulanan bazı teorik bilgi ve kavramların öğretimi için simülasyon yazılımlarına ihtiyaç duyulmaktadır. Uygulamada tehlike oluşturabilecek fizik ve kimya alanındaki deneylerde, malzeme, araç

[1]Assoc. Prof. Dr., Batman Üniversitesi, Beşiri OSB MYO, Batman, Türkiye,
Oktay.Adiyaman@batman.edu.tr, (ORCID: 0000-0002-2674-3836)

gereç bakımından çok fazla maliyetli olan mühendislik uygulamaları gibi eğitim faaliyetlerinde öğrenme-öğretme konuları simülasyon yazılımları ile gerçek ortam şeklinde sunulabilmektedir. Öğrenci simülasyon yazılımları sayesinde olası yanlışlarını kolayca görebilir. Kendisine ve başkasına zarar vermeden, malzemeleri gereksiz yere harcamadan olayı izleyebilir ve yapabileceği etkinlikleri somut olarak görebilir [9]. Simülasyona dayalı eğitimler, öğrencinin parametrelerini değiştirebildiği ve deneyleri birebir yaptığı öğretim yöntemidir. Laboratuar şartlarında uygulanması tehlikeli ve maliyetli olan deneylerde simülasyon yazılımlarını kullanmak eğitimde verimliliği arttıran en önemli etkenlerdendir [10].

Öğrencilerin teorik olarak gördükleri dersleri geliştirirerek pratik deneyimlerine uygulamak, mühendislik eğitiminin temel amacıdır. Pratik uygulamalar sayesinde öğrenci farklı senaryolara karşı hazır hale gelmektedir. Buna karşın pratik eğitim ortamları ve uygulamalarında bazı kısıt ve darboğazların varlığından dolayı bu eğitim modellleri için de bazı engeller bulunmaktadır. Pahalı deneyler ve ekipmanlar, iş güvenliği unsurları gibi başlıklarda bu eğitim modelinde de çok fazla engel bulunmaktadır [11].

Mühendislik uygulamalarında ve özelde de CNC eğitiminde, simülasyona dayalı eğitim, son yıllarda üretim sektöründe öne çıkan bir eğitim modeli olarak karşımıza çıkmaktadır [12]. Sanal gerçeklik tabanlı uygulamaların ve simülasyon programlarının, sanal ortam uygulamaları arasında çok önemli bir yere sahip olduğu görülmektedir. Sanal gerçeklik, sürekli değişen ve hareket kabiliyeti olan bir etkileşime sahip, bilgisayar ve yapay zeka tarafından kurgulanan ve etkileşimli bir ortam sağlayan bir görüntü aktarım teknolojisidir. Yapay olarak oluşturulmuş bu dünyada, kullanıcının fiziksel varlığının benzetimi veya buna benzer araç gereçlerin kullanıcı tarafından kullanılması hissini vermesi sayesinde kullanıcı ve sanal ortamın etkileşime girmesi sağlanmaktadır [13]. Bu alanda yapılan çalışmalarda farklı sonuçlara ulaşılmıştır. Yapılan bir çalışmada, yazılım mühendisliği eğitimi alan öğrencilerin kavrama noktasında zorlandığı farklı hiyerarşik sıralamaya sahip algoritmaların, sanal gerçeklik sistemleri yoluyla öğrenilmesinin öğrenci başarısına ve öğrenmeye olan etkisi araştırılmıştır. Farklı iki grup arasında karşılaştırma yapılan çalışmada, birinci grup öğrenci klasik tekniklerle eğitilirken diğer grup ise sanal gerçeklik sistemi ile eğitim almıştır. Her iki grup arasındaki eğitim sonucunda sanal gerçeklik yöntemi ile eğitimde %12 oranında başarı artışı olduğu görülmüştür [14]. Kimya mühendisleri öğrencilerine yönelik yapılan başka bir çalışmada, bazı büyük pompa, vana ve boru hatlarının yer aldığı gerçek bir kimyasal tesisin bölümleri, oyun ortamında canlandırılmıştır ve eğitim sonunda öğrencilerden olumlu dönütler alınmıştır [15]. Kore

Üniversitesinde yapılan bir çalışmada, robotik dersi için iki farklı grupta öğrenme grubu oluşturulmuştur. İlk gruba konular sanal gerçeklik destekli olarak anlatılmış, diğer gruba ise geleneksel eğitimin ile eğitim verilmiştir. Eğitim sonunda yapılan ölçme ve değerlendirme teknikleri sonucunda sanal gerçeklik sınıfındaki eğitim düzeyi gelişimi ile geleneksel eğitimin verildiği sınıftaki eğitim düzeyi gelişimi arasında, sanal gerçeklik ile eğitim alan sınıf lehine çok büyük bir fark olduğu gözlenmiştir [16]. Başka bir uygulamada, deprem sonrasında meydana gelen yangınlar sonucunda itfaiyecilerin ve mahsur kalan kişilerin çok ciddi bir tehlikede kaldıklarından yola çıkılarak, bina bilgi modeli ve sanal gerçekliğe dayalı bina içi ve deprem sonrası yangın kurtarma senaryosunun simülasyonu denenmiştir. Bu simülasyonda yangın kurtarma senaryosu için 19 katlı bir hastane modeli üzerinde deneme yapılmıştır. Yapılan çalışma sonuçları, oluşan dumanın kurtarma üzerindeki etkisinin mevcut enkazdan daha fazla etkiye sahip olduğunu göstermiştir [17]. Nükleer enerji mühendisliği alanında sanal gerçeklik uygulamaları konusunda yapılan başka bir çalışmada, tasarım aşamasında olan Çin füzyon mühendisliği test reaktörü için plazma geometrisi, stabilite ve boşaltma işlemlerinin araştırılması amacı ve ilave olarak elektromanyetik, termodinamik bakımdan ve yapısal özelliklere ait mühendislik analizlerinin sanal gerçeklik ortamı ile üç boyutlu model olarak ele alınması ve eğitime katkısı gözetilerek araştırma yapılmıştır [18]. Daha nice farklı alanlarda ve konularda özellikle de mühendisliğin farklı alanlarında simülasyona dayalı eğitimlerin oyun sektöründeki kullanımından farklı olarak bu alanlara kaydığı gözlenmektedir. Tıpta [19], mühendislikte [20], mimarlıkta [21] ve temel bilimlerde [22] çok fazla sayıda çalışma yapılmakta ve konu her geçen gün artan sayıda çalışmayla devam etmektedir.

Yukarıda bahsi geçen uygulamalar ve alanlara ek olarak, özelde makine mühendisliği ve makine eğitimi ile ilgili bir alt alan olan CNC tezgahların kullanımı, operatörlüğü ve programlanması ile ilgili de çeşitli CNC simülasyon eğitimlerinin var olduğu görülmektedir. Simülasyonla eğitim olarak başlayan sanal öğrenme ortamları son yıllarda sanal gerçeklik ortamları ve VR-AR (sanal gerçeklik-arttırılmış gerçeklik) gözlükleriyle bizzat ortamın görselleştirmesi yönünde ve yapay zeka unsurlarının da desteğiyle de geliştirilerek devam ettiği görülmektedir [23].

Samala ve Amanda yaptıkları çalışmada [24], CNC freze tezgahları simülasyonu için bir uygulama geliştirmişlerdir (örneğin, bir 3B modeli döndürme ve x, y ve z eksenlerini hareket ettirme). Lai ve arkadaşları ise [25], bir CNC ağaç işleme tezgahının montajını desteklemek için derin öğrenmeye dayalı bir takım algılama üzerine bir talimat sistemi uygulamışlardır.

Bilgisayarlı sayısal kontrol (CNC) tezgahları, Endüstri 4.0 üretim modeline entegre edilebilecek çok önemli tezgahlardır [26]. Optimum parametrelere sahip bu tezgahlar, hassas parçalar üretebilmekte ve işleme verimliliğini artırmakta [27], parça üretimi için doğru ve tekrarlanabilir sonuçlar sağlamak üzere ayrıntılı ve özel kodlar yürütmektedirler [28].

Genel mühendislik uygulamalarında ve mesleki eğitim kurumlarında ve hatta özel sektör iş atölyelerindeki CNC eğitimleri ve ders müfredatları incelendiğinde bazı zorlukların bulunduğu tespit edilmiştir:

1. CNC tezgahların tümünün (torna, freze, işleme merkezleri, routerlar, C eksenli tezgahlar, taşlama tezgahları) ilk kuruluş maliyetlerinin çok yüksek olması nedeniyle eğitim ortamının sağlanmasındaki zorluklar.
2. İlk kuruluş maliyeti bir şekilde karşılanmasına karşılık teknolojinin sürekli gelişimi sonucunda bu değişime ayak uydurulamaması ve alınan tezgahların güncellenememesi, yenilenememesi ve atıl veya demode duruma gelmesi.
3. Eğitim alan öğrencilerin sayıca fazla olması ve buna karşılık tezgah sayısının çok az olması (genelde 1 adet) neticesinde öğrencilerin yeterli düzeyde pratik yapamaması.
4. CNC tezgah alınması sonrası eğitim sırasında kullanılan ölçüm ve kalibrasyon aletlerinin, kesici takım, tutucu ve uçların körelmesi, hasar görmesi vb. nedenlerden dolayı atıl duruma gelmesi neticesinde yerine eşdeğerinin alınmasının da çok pahalı olması ve böylece sürekliliğin sağlanamaması.
5. Bu tezgahların bakım onarım masraflarının da klasik tezgahlarda kullanılan hemcinslerine göre daha pahalı olması
6. Özel sektörün CNC tezgah eğitimi noktasında personellerini yetiştirmede, kendi CNC tezgahını bu amaçla kullanmasının, üretimi aksatması ve bunun sonucu olarak ta para kaybetmeye sebep olması.
7. Özel sektörün, CNC eğitimi için alım maliyeti yüksek olan mevcut tezgahını, kalifiye olmayan elemana teslim etmeme niyetinin olması veya olası kaza durumunda hem elemanın hem de tezgahın zarar görme riskinin bulunması.

Ek olarak, CNC tezgahlarındaki eğitim görevleri, yetkin beceriler edinmek için zaman ve pratik gerektirir ve bu da pahalı olabilir. Yukarıda bahsi geçen zorlukların ve problemlerin ana odağında çoğunlukla maliyet odaklı nedenlerin yer aldığı, diğer nedenlerin ise ikincil nedenler şeklinde olduğu görülmektedir. Önceleri büyük ölçekli fabrika ve atölyelerde bulunan CNC tezgahlar günümüzde en küçük atölyelerde hatta küçük dükkan mahiyetinde alanlarda da kullanılmaya başlanmıştır [29]. Tüm bu nedenlerden dolayı simülasyona dayalı

eğitim ve daha da gelişmiş hali olan sanal gerçeklik uygulamalarına dayalı eğitim, en iyi eğitim yöntemi olarak karşımıza çıkmaktadır.

CNC tezgahlarda gerçekleştirilen tipik görevler, takım yükü operasyonu, takım setinin telafi edilmesi, kodun programlanması ve kesici takımın kurulumuyla ilgilidir [30]. Bu tür görevlerin sanal bir ortamda (VE) veya simülasyon yoluyla yürütülmesi, görevin netliğini ve tamamlanma hızını sağlayan talimatları ve yönergeleri entegre ederek daha sezgisel ve zenginleştirilmiş bir eğitim deneyimine yol açar [31] ve operatörlerin açık uçlu pratik yoluyla psikomotor, uzamsal ve bilişsel becerilerini güçlendirmelerine olanak tanır [32].

Endüstriyel iş dünyası ve akademik sektörler, kullanıcı ilgisini artırmak ve ihtiyaçlarını karşılamak için teknoloji odaklı modern teknolojileri ve sanal ve simülasyon ile teorik karma öğrenme yaklaşımlarını benimsemekte ve bu stratejilere öncelik vermektedir [33, 34]. Örneğin, VR (sanal gerçeklik) simülasyonunu tezgahlarla harmanlayarak eğitim, öğrencilerin öğretim etkisini sağlamak için prosedürleri kendi hızlarında tekrarlamalarını sağlayarak anlayışlarını geliştirmekte, malzeme israfını azaltmakta ve iş kazalarını önlemektedir [35, 36]. Ayrıca, makine üreticileri ve satıcıları, değer katmak ve müşteri sadakati sağlamak için tamamlayıcı bir hizmet olarak XR, VR ve simülasyona dayalı eğitimleri uygulamaktadırlar [37, 38]. Ayrıca, öğrencileri güçlendiren ve iş gücünde başarılı olmalarına yardımcı olan bilgi, tutum ve becerileri bütünleştiren çerçeveler geliştirmek, güncelliğini yitirmiş müfredat ve laboratuvar uygulamaları için sınırlı kaynak kullanımından kaynaklanan açığı kapatmak ve üniversite mezunları ile endüstri ihtiyaçları arasındaki gereklilikleri karşılamak gerekmektedir [39, 40]. Geleceğin öğrencilerine ve endüstriyel mesleki eğitimde pratik yapan kursiyerlere eğitim vermek, teori ile pratik arasındaki açığı kapatmak için yapay zekaya entegreli simülasyon öğrenme ortamlarından yararlanmak üzere bir paradigma değişimi gerekmektedir [41].

Nitelikli operatörler giderek azalmakta (örneğin, nüfusun azalması ve çalışanların emekli olması) ve becerilerini geliştirmek için zamana ve alana ihtiyaç duymaktadır [42]. Bu bağlamda;

1. CNC otomasyonunun kalitesini artırmak ve yeni operatörler eğiterek deneyimli operatörlerin iş yükünü azaltmak için operatörlerin güvenlik ve kalite kontrol deneyimlerini kopyalamak [43].
2. Kritik endüstriyel ortamlarda bilgi transferini iyileştirmek ve operatörlerin örtük prosedürel bilgilerini çıkarmak ve karar alma süreçlerini değerlendirmek [44] amacıyla yapay zeka modelleri ve simülasyonları kullanmaya yönelik çalışmalar mevcuttur.

XR uygulamaları, iş gücünde eğitimi hızlandırmak, yeni operatörleri eğitirken üretim hattının durmasını önlemek ve talep edilen deneyim, uygulama ve becerilerin geliştirilmesi için alanlar sağlamak amacıyla sektörde önemli bir ilgi görmüştür [45, 46].

CNC simülasyonu ve sanal eğitim ortamları ile ilgili yapılan tüm çalışmalar incelendiğinde XR teknolojilerinin ve simülasyona dayalı eğitim araçları kullanımının, uzamsal ve psikomotor becerileri geliştirdiği [47, 48], gerçek zamanlı karar verme yeteneği sağladığı [49] ve CNC teknolojisinin karmaşıklığından kaynaklanan operatörün bilişsel yüküyle başa çıkmasına yardımcı olduğu [50, 51] görülmüştür.

Tüm bu yapılan çalışmalar, CNC tezgah operatörlüğü eğitiminin, başta simülasyon programları olmak üzere giderek sanal gerçeklik araçları ve buna yapay zeka unsurlarını da eklemleyerek CNC tezgah operatörlük eğitiminden başlayarak profesyonel anlamda CNC programı elde etme, bu programları çalıştırma ve hata ayıklama, daha iyi alternatifler deneme noktasında güvenli, emniyetli, kullanıcı ile interaktif etkileşimli, maliyet düşük çözümlerin geliştirileceği bir dünyaya doğru gittiğimizi göstermektedir. Bu çalışmada CNC tezgahların gerek operatörlük ve gerekse elde edilen CNC programlarının görsel ve analizleme anlamında test edilmesi, sonuçlarının görülmesi, tezgahın verdiği tepkilerin görselleştirilmesi amacıyla kullanılan başlıca CNC simülasyon yazılımları hakkında bilgi verilmeye çalışılacaktır. Kullanıcı kendi amaç, pozisyon ve ihtiyacına göre bu simülasyon programlarından faydalanma noktasında en son karar verme merciidir.

## CNC SİMÜLASYON PROGRAMLARI

CNC simülasyon programları incelendiğinde farklı amaçlara yönelik yazılımların oluşturulduğu görülmektedir. CNC simülasyon programlarının, mevcut G kodlarının gösterimi noktasında profesyonel anlamda canlandırma yapma, programın simülasyonundaki çarpma kontrolü, parametrelerin sonuçları (güç, hız, talaş hacmi, anlık çıktılar vb) hakkında detay verme, birebir tezgah kontrolü ve sonuçlarını simüle etmeye yönelik eğitim yönüne ağırlık verme, program yazımı ve takım, tezgah noktasında gerçekçi ve realistic görüntüler verme gibi amaçlara sahip olduğu görülmektedir. Son yıllarda bu programların mobil uygulamaları da oluşturulmaya başlanmıştır.

Genel anlamda CNC simülasyon programları sınıflandırılrsa Şekil 1'deki genel gruplandırma kaba olarak verilebilir.

| Program Adı | Seviye ve Amaç | Tür | Özellik |
|---|---|---|---|
| **VERICUT** | Profesyonel | G-Kod | Gerçek tezgah simülasyonu |
| **NCSimul** | Profesyonel | G-Kod | Kapsamlı doğrulama |
| **NX CAM** | Profesyonel | Entegre | CAD/CAM+Simülasyon |
| **MasterCAM Simulator** | Orta | Entegre | CAD/CAM+Simülasyon |
| **Swansoft CNC** | Eğitim | G-Kod | Öğrenci temel kullanımı |
| **CNC Simulator Pro** | Eğitim | G-Kod | Ücretsiz ve basit kullanım |
| **CAMotics** | Hobi-Eğitim | G-Kod | Açık kaynak |
| **NC Viewer** | Hobi-Eğitim | WEB | Hızlı Önizleme |
| **CİMCO** | Profesyonel | G-Kod | Kapsamlı doğrulama |

**Şekil 1.** CNC simülasyon programları kategori tablosu

Şekil 1'deki tablo genel bir ifade şeklini vermekte olup her programın diğerinin özelliklerini de kendi içine farklı oranlarda kattığı da bilinmelidir.

## 1. VERICUT Simülasyon Programı

Bu simülasyon programı, elde edilen bir CNC programının istenilen tezgah modelinde simülasyonuna yönelik çözümler sunmaktadır. Program ana görüntüsü Şekil 2'de verilmektedir.


**Şekil 2.** Vericut simülasyon yazılımı kullanıcı arayüzü [52]

Bu programın en önemli özellikleri arasında ilk olarak “doğrulama” basamağı gelmektedir. Bu aşamada, program hatalarını ortadan kaldırmaya ve işleme sırasında boşa giden parçaları ve malzemeleri önleme ön plandadır. Böylece tezgah sürelerini minimize etmeye olanak sağlamaktadır. Programın tutucu, tezgah ve fikstür araçlarını birebir simüle edebilme özelliği ve bilinen başlıca tezgah modellerini de grafik ekranda birebir görüntüleyebilme kabiliyeti programa büyük bir avantaj sağlamaktadır. Program ayrıca herhangi bir CAM programı ile elde edilmiş post çıktılarını doğrulama ve hata ayıklama özelliklerini de sunmaktadır. Program, kullanımı ile bir parçanın işlenmesi için herhangi bir test işlemesine gerek kalmayacak şekilde güvenli bir alt yapı sunmaktadır.

İkinci basamak olan “simülasyon” basamağında, mevcut post process ile üretilmiş CNC kodlarının tezgah üzerinde birebir simüle edilmesi sağlanmaktadır. Bu konuda da oldukça başarılı bir arayüze sahip program, simülasyon sırasında çarpma, fikstüre yakınlaşma, tezgah çıktısı olan güç, talaş hacmi, hızlar, dalmalar vb. sonuçları da kullanıcıya vermektedir. Takım yolu, iş parçası, takım tutucu ve tezgah çeşitleri bakımından arayüz olarak çok fazla seçeneği bulunmaktadır.

Üçüncü basamak olarak “optimizasyon” seçenekleri ile program mevcut elde edilmiş kodlar ile elde edilen sonuçların iyileştirilmesine yönelik kullanıcıya çözümler sunmaktadır. Tezgahın verdiği zaman, güç, talaş hacmi vb. verilerin optimize edilmesi takım ömrü ve zaman tasarrufu anlamında faydalar sağlamaktadır.

Yazılımın özellikle hata ayıklama noktasında öne çıkan bazı özellikleri bulunmaktadır. Devir olmaması, soğutma suyu gereksinimi, klavuz takım hataları (hatve ve delik ölçüleri hataları vb) gibi hataların ayıklandığı, tezgah limitlerinin tanımlandıktan sonra programda bu limit aşımlarının oluşmasında uyarı verilmesi gibi çok fazla kontrol mekanizması geliştirilmiştir (Şekil 3).

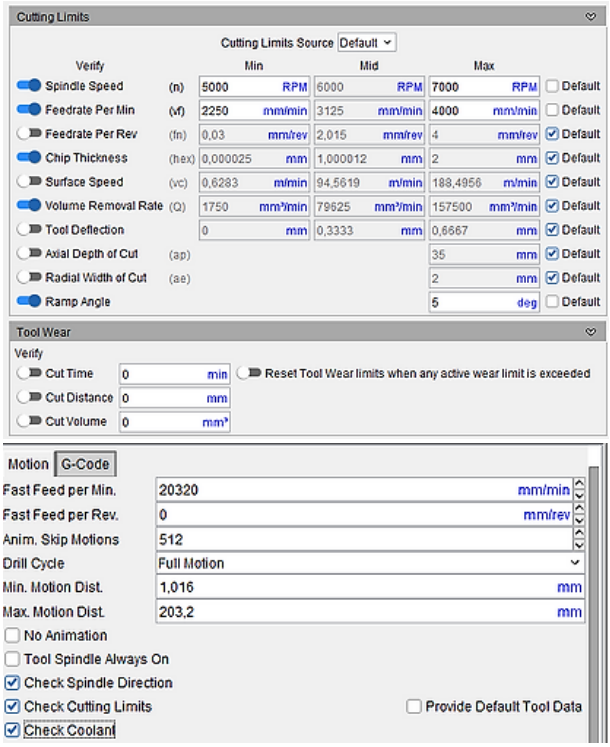


**Şekil 3.** Limit ve kontrol unsurları penceresi [53]

Bu yazılımda belirli marka tezgah modellerinin birebir eş değerinin kullanılıyor olması tezgah güvenliği, çarpışma kontrolü ve test denemesi gereksinimi noktasında avantajlar sağlamaktadır. Simülasyon yazılımı profesyonel CNC tezgah kullanıcılarına ve bu alanda çalışma yürüten kişilere hitap etmesi noktasında olduğundan dolayı acemi ve başlangıç düzeyi CNC kullanıcılarına yönelik çok fazla avantaj sağlamamaktadır.

GGTech firması ürünü olan Vericut simülasyonu Freze, torna, 3 eksen, 5 eksen ve çok eksenli işleme merkezleri ile tam uyumludur. Büyük firmalar tarafından CNC program denetimi ve test üretimi kaynaklı sorunlara çözüm odaklı bir yazılım olma özelliği taşımaktadır.

## 2. NCSimul Simülasyon Programı

Hexagon/SPRING Technologies firması tarafından geliştirilen NCSimul simülasyon yazılımı programlarını simüle etmek, doğrulamak ve optimize etmek üzerine yoğunlaşmıştır. Simülasyonun öne çıkan özellikleri olarak;

Gerçek makine özellikleri kullanılmakta, tüm tezgah, takım ve malzemeler için uygun ortamlar sağlayarak dinamik bir doğrulama yapmaktadır. Bu durum

hata riskini önemli ölçüde azaltmaktadır. Bu programa ait kullanıcı arayüz Şekil 4'te verilmektedir.

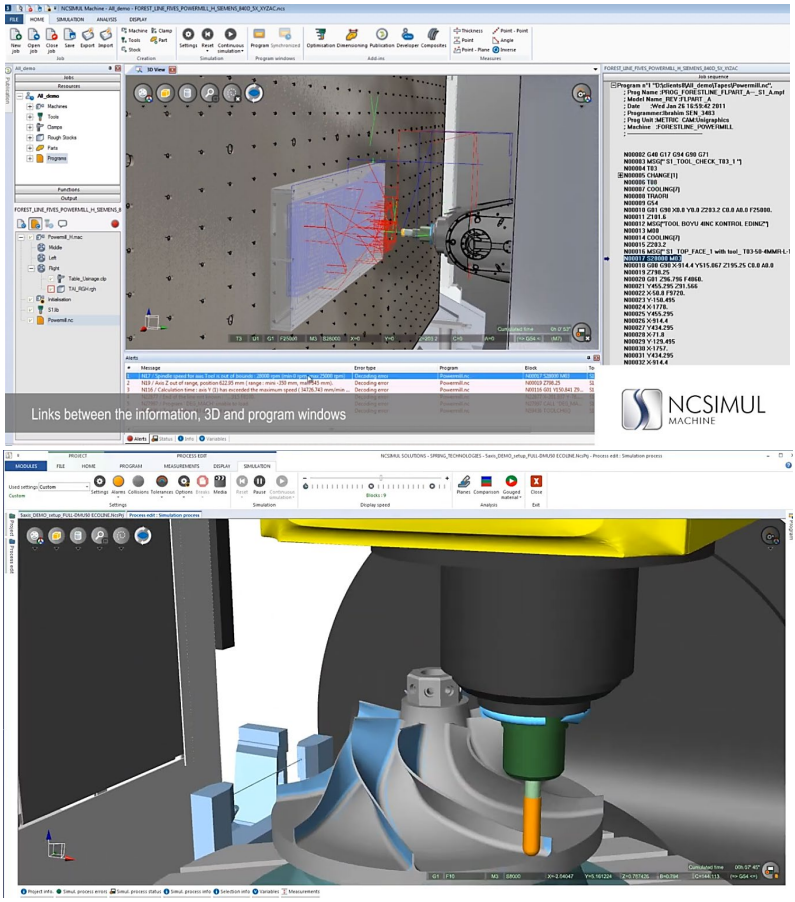


**Şekil 4.** NCSimul yazılımına ait kullanıcı arayüzü [54]

SolidWorks, Catia, HyperMill, Fusion 360, Creo, NX, SolidCAM gibi birçok yazılım ile sorunsuz çalışan NCSimul simülasyonu Okuma, Mazak, Haas, Fanuc, DMG Mori gibi başlıca marka model tezgahlara da entegre çalışmaktadır. Güçlü bir CNC kod ayıklayıcısı ve simülasyonu ile gerçekçi ölçü hassasiyeti gibi konularda da güçlü alt yapısı bulunmaktadır.

Bu programa ait başlıca özellikler şu şekilde sıralanabilir;

Doğrulama, mevcut CNC kodlarını gerçek tezgah ölçü ve modellerini kullanarak programın dinamik analizinin yapılması ve program hareketlerine göre kontrol edilebilmesi,

Kesici takım optimizasyonu, gerçek 3D grafikleri ile çarpışma algılamaların kontrol edilebilmesi, ilerleme vb. hızlar için optimizasyon yapılabilmesi.

Bu yazılım ayrıca oluşturulan macro programları da okuma yeteneğine sahiptir. NCSimul simülasyon programının en önemli avantajlarından biri simülasyon esnasında MDI modu gibi kontrollerle program içine müdahale edebilme ve düzenleme yapabilme özelliğidir. Simülasyon esnasında program içindeki çarpma vb. durumların analiz edilmesinde de oldukça etkili bir arayüzü bulunmaktadır. Program ayrıca çift ayna bulunan ve çift veya çok ganglı özellikteki tezgah tiplerini de desteklemektedir.

Farklı robot kol ve uç epilatörlere sahip tezgahların da simülasyounun yapılabildiği NCSimul programının bu yönleri ile üst düzey profesyonel anlamdaki firmalara hitap eden yönü bulunmaktadır.

Programın ağır basan diğer bir özelliği ise kompozit malzemeler üzerine kaplama, fiber sarma makineleri gibi farklı iş tezgahlarının da simülasyonuna imkan vermesidir. Ayrıca yazılımın içinde farklı modüller de mevcuttur. Bunlar:

*NCSimul machine:* NCSIMUL Machine, G-kod doğrulama, makine simülasyonu ve takım yolu optimizasyonu için üst düzey bir CNC simülasyon yazılımıdır.

*NCSimul Optitool:* NCSIMUL Optitool "boşta dolaşmayı" azaltır, ilerleme oranlarını optimize eder ve kullanıcıların daha iyi kesme stratejileri oluşturmasına olanak tanır.

*NCSimul 4CAM:* NCSIMUL 4CAM, CAM'in yeniden programlanmasına gerek kalmadan hedef makinede değişiklik yapılmasına olanak tanıyarak atölyede esneklik sağlar.

*NCSİmul Composites:* NCSIMUL Makine Kompozitleri, 3B malzeme yerleştirme simülasyonunuzu daha akıllı, daha gerçekçi ve daha verimli hale getirir. Farklı yöntemlere göre (filamentler veya şeritler) veya filament sarımı gerçekçi ve verimli bir şekilde malzeme yerleştirme simülasyonuna olanak tanır ve işleme simülasyon verilerinin otomatik olarak toplanmasını sağlar.

## 3. NX CAM, MasterCAM Simulator ve SolidCAM Simülasyon Modülleri

NX CAM Simülasyonu (Siemens NX CAM Simulation), MasterCAM Simülasyon modülü ve SoldidCAM modülü gibi CAD ve CAM programlarına entegre olan çok sayıda simülasyon yazılımı mevcuttur. Bu modüller hem CAM (takım yolu oluşturma) hem de NC kod tabanlı simülasyon özelliklerini aynı ortamda birleştirirler. CAD ve CAM programlarının devamı niteliğinde olan bu programlar, modelleme, CNC CAM ile işleme ve oluşturulan post processing ile de parça işlemesini simüle edebilme kabiliyetlerine sahiptirler. Şekil 5'te her 3 programa ait arayüzler görülmektedir.

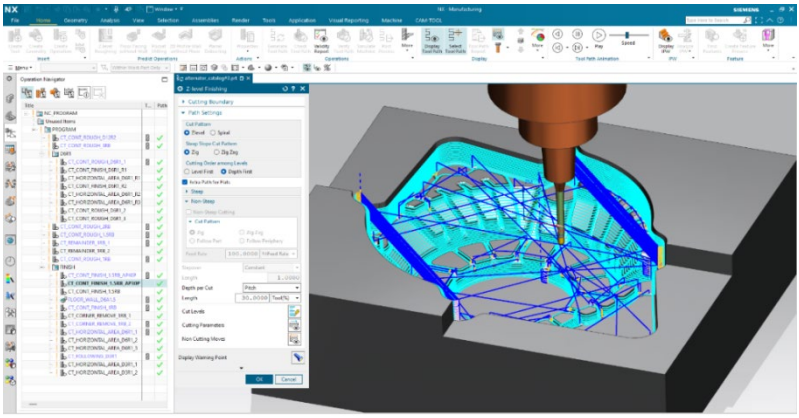

a) NX CAM arayüzü [55]

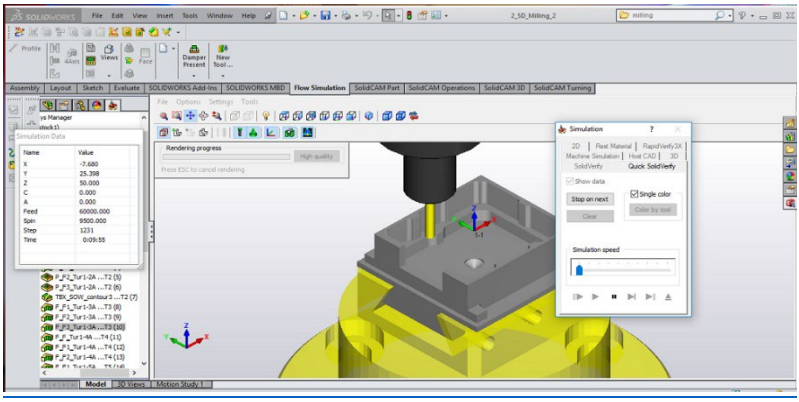

b) SolidCAM Simülasyon arayüzü [56]

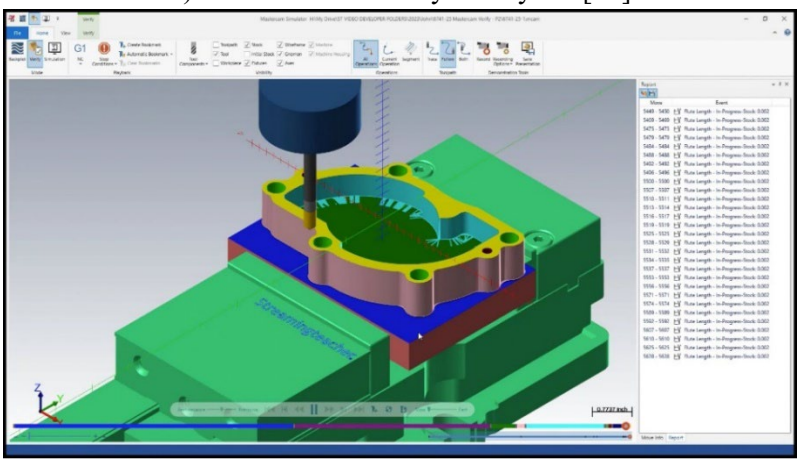

c) MasterCAM simülasyon arayüzü [57]

**Şekil 5.** NX CAM, SolidCAM ve MasterCAM simülasyon modüllerine ait arayüzler

Bu tür entegre programlarda genellikle modelleme modülüne eklemlenmiş şekilde simülasyon modülleri bulunur. Bu entegre edilmiş bütüncül yazılımın çalışma prensibi şu basamakları içerir;

a) Parçanın modellenmesi,
b) Parça için fikstür, tezgah, kesme parametreleri vb kontrollerle CAM programının yapılması ve post processor işlemleri,
c) Yapılan post processora göre simülasyonun yapılması.

Bu üç basamağa sahip simülasyon modüllerinde ana fonksiyonlar şu şekildedir:

*Takım yolu simülasyonu:* Takımın CAD modeli üzerindeki hareket şekilleri (hızlı ve talaş alarak) izlenir. Böylece takım yollarının kontrolü ve hataların görülmesi sağlanır.

*Malzeme kaldırma simülasyonu:* Takımın kaldırdığı malzeme miktarı ve fire miktarı gibi parametreler gösterilir. Böylece işleme sırası, yüzey durumu ve stok analizi yapılır. Sonraki işlemler için kütük oluşturulur.

*Makine hareket simülasyonu:* Tanımlanan tezgah modeline göre tezgah modeli oluşturulur, limitler tanımlanır ve bunlara göre işlem sıralanır. Bununla gerçeğe yakın bir hareket doğrulaması elde edilir.

Bu tür entegre simülasyon modülleri ile zaman tahmini, çarpışma kontrolü, kesme uzunluğu, talaş hacmi hesaplamaları, stok durumu ve sonraki operasyona ön işleme yapılmış parça oluşturma gibi kontroller yapılabilir ancak bu modüller profesyonel anlamdaki simülasyon yazılımları gibi kesinlik oluşturan ifadeler yerine öngörü oluşturmaya yönelik sonuçlar üretirler.

## 4. CNC Simulator PRO Simülasyon Programı

Bu simülatör programı CNC programcılık eğitimi alan tüm ilk kullanıcı profilindeki kişilerin eğitilmesine yönelik ve yaptıkları programların kontrolünü görsel olarak yapmak için tasarlanmış basit arayüzü olan ve kullanımı kolay bir simülasyon programıdır. Programa ait arayüz Şekil 6'da görülmektedir.

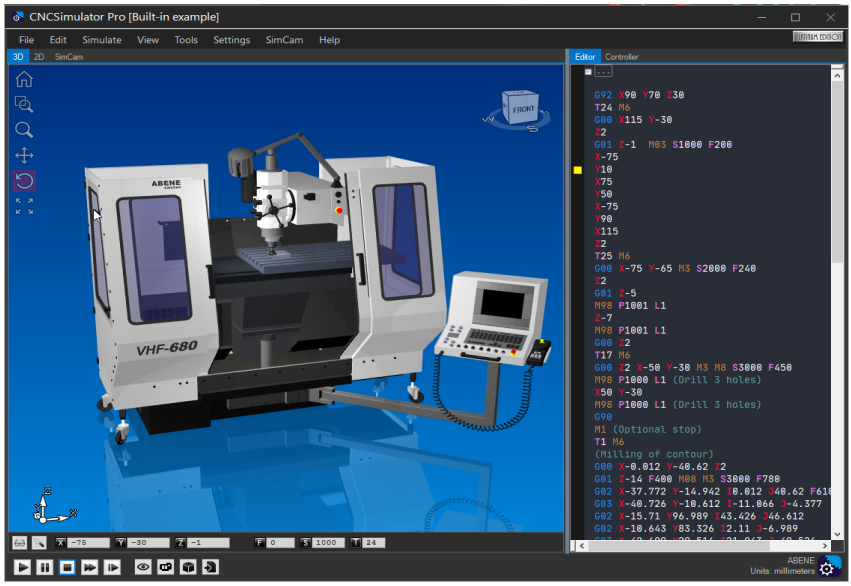


**Şekil 6.** CNC Simulator PRO programına ait arayüz [58]

Bu simülatör programı eğitim amaçlı bir simülasyon yazılımı olup çok sayıda makine modelini desteklemektedir. Ancak makine modelleri genel ölçüler ile gösterilmekte olup gerçekteki tezgahlarla ölçüsel olarak birebir eşdeğer değildir. Ancak öğrencinin kod yazma, yazdığı kodun makinedeki takım yollarını görme gibi konulardaki öngörüsünü arttırmaktadır. Ayrıca programın içinde torna freze tezgahlarının yanısıra lazer, 3d baskı, plazma ve su jeti gibi farklı tezgah tipleri de gösterilmektedir.

Programın çarpışma kontrolü ve limit aşımlarını da belirtme özelliği bulunmaktadır. Makro programlara ait simülasyon çalıştırma özelliğinin yanısıra ücretsiz oluşu da pozitif yönde bir tercih yaratmaktadır.

Ekran ve görüntü kalitesi yönünden kaliteli çıktılar üreten program, CAM ile oluşturulan kodları da simüle edebilme özelliğine sahiptir. Video oynatıcı içindeki adım adım işleme, yavaş işleme gibi özellikler sayesinde daha kontrollü simülasyon izleme olanağı sunmaktadır. Programın FANUC vb. kontrol panellerine benzer kontrol ünitesi görüntüsü de düşük çapta bir kontrol ünitesi öğrenme desteğini bereberinde getirmektedir.

Farklı takım tanımlamaları, iş parçası ve fikstür ayarlamaları, iş parçası malzeme ve ebat seçimi, program yazımında yardımcı menü desteği de programın artıları arasında sayılabilir. Programda ayrıca CNC kod yazım editörü bulunmaktadır. Kod yazımı sırasında yazılan kodun anlam ve işlevini anlatan yardım menüsünün kullanıcıyı yönlendirmesi hata payını azaltmakta, kullanıcıyı daha da motive ederek doğru yazım için altyapı sunmaktadır.

## 5. CAMotics Simülasyon Programı

Genellikle freze uygulamaları için geliştirilmiş ve CNC kod simülasyonu yapan bir açık kaynak, ücretsiz simülasyon yazımı olan CAMotics Simülation, CNC'ler için 3 eksenli GCode programlarını simüle edebilir özellikte olup, sonuçları 3B olarak görselleştirme yeteneğine sahiptir. CAMotics, Linux, OS-X veya Windows'ta çalışma özelliğine sahiptir. Program arayüzü Şekil 7'de görülmektedir.

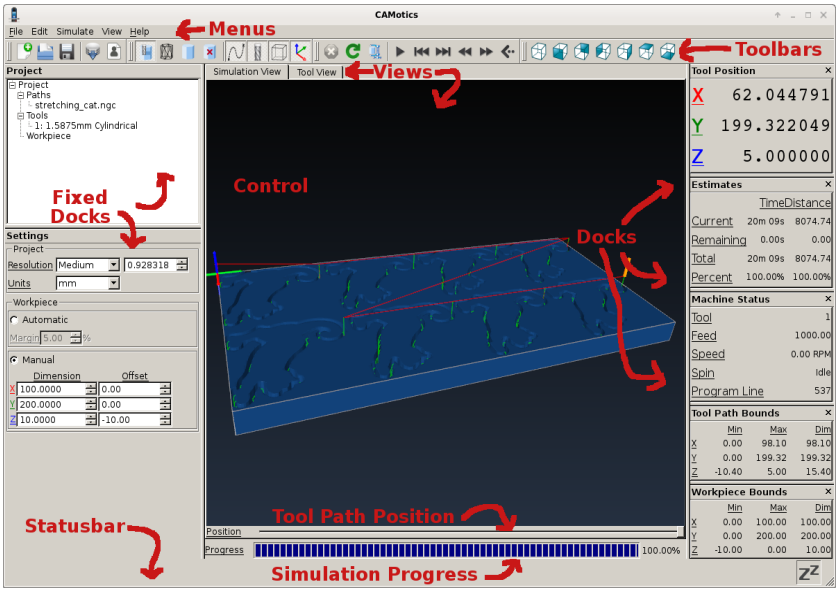


**Şekil 7.** CAMotics simülasyon programının arayüzü [59]

Bu programın devantajları arasında takım kütüphanesinin az olması, torna modülünün olmaması, sadece 3 eksen G kodlarını simüle edebilmesi, çarpışma kontrolü noktasında güvenilirliğinin zayıf olması gibi hususlar ön plana çıkmaktadır.

Genellikle CNC router mantığına yönelik işlemlere yoğunlaşan simülasyon programı, grafik ekranının tatmin edici düzeyde kaliteli olmadığı, makine modelini göstermemesi ilk başlangıç seviyesindeki kullanıcılara hitap etme özelliğini ön plana çıkarmamaktadır. Programda ayrıca simülasyon izleme, durdurma, ileri-geri simülasyon gibi özellikleri bulunan bir oynatıcı da mevcuttur.

CAMotics simülasyon programı CAM programları gibi kod üretme yeteneğine sahip değildir. Var olan bir programın simüle edilmesi veya basit elle program üretip simülasyonunu görmeye yarayan bir işlevi ön plana çıkarmaktadır. Grafik aarayüz olarak realistic yönü zayıf olan ve gerçekçi kaliteyi yakalamamış olması da dezavantajlı yanlarından sayılabilir.

Tüm özellikler gözönüne alındığında CAMotics simülasyon yazılımı, hobi ve başlangıç amaçlı kullanıcılar, açık kaynak kodlama programı tercih edenler, CNC kodlamada başlangıç bilgisine sahip olup kendini geliştirmek isteyenler ve küçük atölyelerin basit 3 eksen CNC tezgah kullanıcılarına daha çok hitap etmektedir.

## 6. CIMCO Edit Simülasyonu ve Alt modülleri

CIMCO Edit ve alt modülleri ile birlikte NC kod editörleri, DNC yolu ile makine iletişimi amacıyla çalışanları, CNC kod optimizasyonuna yönelik profesyonel anlamda çalışan kesimlere hitap eden bir CNC simülasyon programıdır. Program arayüzü Şekil 8'de görülmektedir.

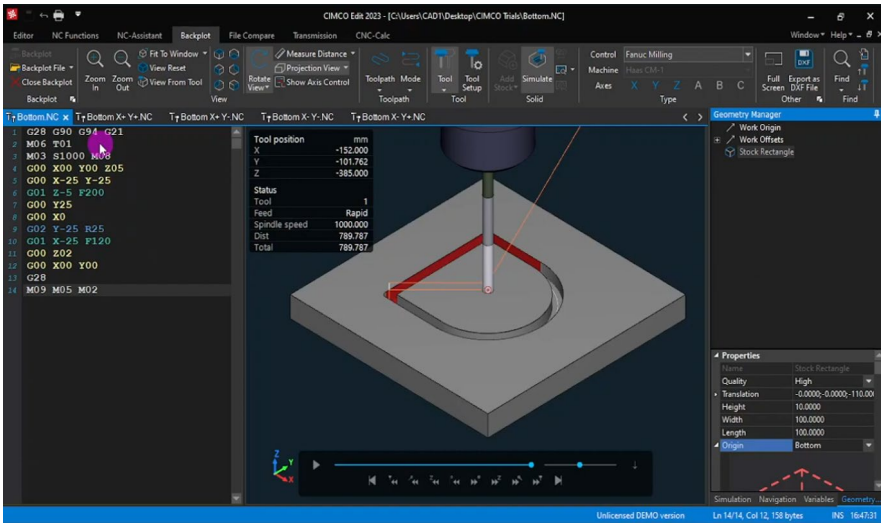


**Şekil 8.** CIMCO Edit simülasyon programı arayüzü [60]

CIMCO Edit modülü CNC kodlar arasında karşılaştırma, analiz ve temel simülasyon özelliklerini içermektedir. Ayırca CIMCO Machine Simulation modülü ile birlikte gerçek makine davranışları, knematik analiz ve çarpışma kontrolü gibi işlevleri de yerine getirir ve simüle edebilir.

Gelişmiş stok kontrol, takım hareket yolları canlandırması, program içinde düzenleme yapabilme ve eş zamanlı olarak bu değişikliği görebilme imkanı, farklı takım, stok ve takım yolu seçenekleri, program edit sayfasındaki kodun gerçek uzaydaki pozisyon ve durumunu göstermesi programın artıları arasındadır.

Program ayrıca çarpışma, dalma vb fiziksel hataları da göstermekte, farklı kontrol ünitelerine göre program simülasyonu ve var olan CNC kodları üzerinde düzenleme yapma imkanı vermesi de olumlu yönler arasında sunulabilir. Ayrıca freze ve torna simülasyonu yapması, kod yazarken kullanıcıya yazım formatı ve

anlamı noktasında açıklayıcı bilgi gösterme özelliği (NC Assistant) de vardır. Ayrıca kullanıcıya çok geniş bir takım kütüphanesi de sunmaktadır.

Programın artıları arasında 3 eksen yanında 5 eksen simülasyonu ve farklı kodlama dillerindeki (FANUC, Heidenhein, Simens vb) programları da simüle edebilmesi ve kütük, fikstür vb unsurları da program içinde eş zamanlı olarak gösterebilmesidir. Simülasyon ekranı da oldukça tatmin edici bir görüntü kalitesine sahiptir (Şekil 9).

Programın ayrıca Machine Simulation, NC-Base (NC program yönetimi), CNC-Calc (2D CAM), Mazatrol Viewer gibi eklentileri de tam sürüm ve eklenti halini oldukça güçlü hale getirmektedir.

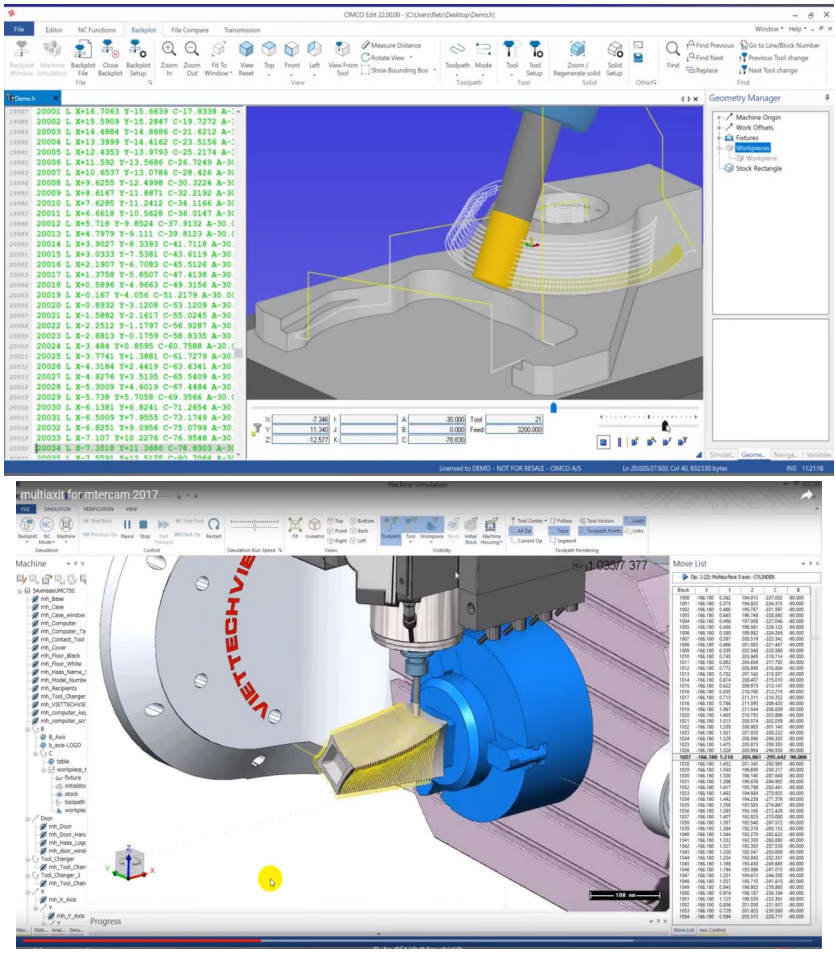


**Şekil 9.** Pogram çok eksenli hareket ve simülasyon grafik ekranı [61, 62]

Program eklentileri ile takım, spindle, akslar, tezgâh gövdesi gibi bileşenlerin hareketi ile birlikte NC kodunun makine üzerindeki etkisini simüle edebilme yönünde oldukça iddialı hale gelmektedir. Ayrıca stok ve fire miktarı konusunda da, işlem sonrası kalan bölgelerin gösterimi ve işlem sonrası kalan parçanın farklı formatta dışa aktarımı gibi özellikler de vardır.

Tüm olumlu yanların yanı sıra bazı eksi olarak tanımlanabilecek yönler de mevcuttur. NCSimul ve Vericut gibi muadillerine göre güvenilirlik anlamında daha aşağılarda bir performans sergilemesi, makine modeli içermesi noktasında profesyonel anlamdaki muadillerinden daha az sayıda makine modeli içermesi, simülasyonun iyi olmasına karşın yine profesyonel anlamdaki muadillerine göre daha az performans sergilemesi, karmaşık 5 eksenli veya knematik modellerde simülasyon performansının daha düşük seviyede olması başlıca negatif yönler olarak sayılabilir ancak yine de oldukça tatminkar bir performansa sahip olma özelliğini hala da yitirmemektedir. Fiyat performans anlamında da beklentileri oldukça iyi karşılayan bir simülasyon olma özelliğini de hala taşımaktadır.

## 7. Swansoft Simülasyon Porgramı

Swansoft programı CNC operatörlüğü, CNC programcılığı ve CAM programlarından post processing olarak türetilen hazır programların simülasyonu ve tezgah kontrollerinin kontrol edilebildiği eğitim amaçlı bir CNC simülasyon yazılımıdır. Bu programa ait arayüz Şekil 10'da görülmektedir.

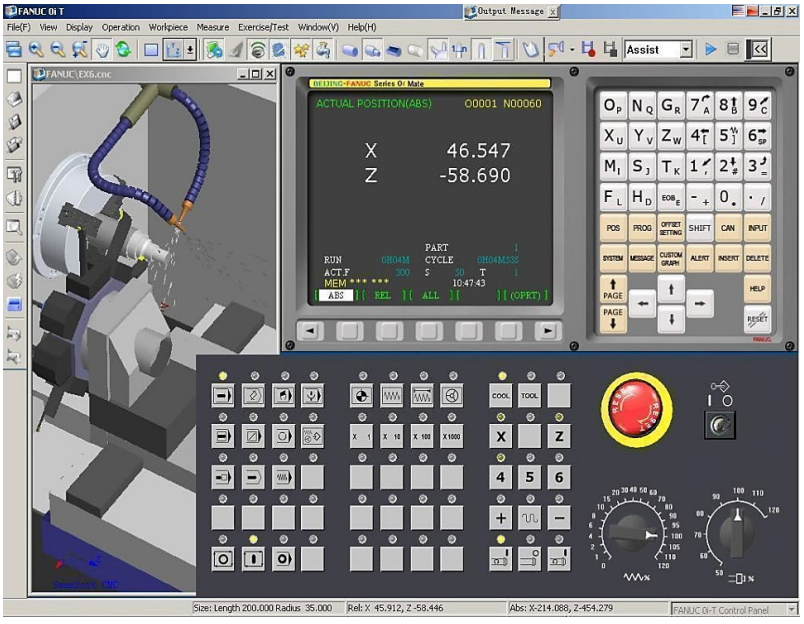


**Şekil 10.** Swansoft CNC simülasyon programı arayüzü [63]

Swansoft CNC simülatörü, mesleki eğitimde CNC kullanımına yönelik tüm eğitimlerde ve CNC tezgah gereksinimini ortadan kaldırarak veya CNC tezgâhı olan mesleki eğitim kurumlarının tamamında eğitim amaçlı ve CNC kullanımına yönelik bir simülasyon yazılımıdır. Yazılımın temel özelliği endüstride kullanılan CNC tezgah operatörlerinin tezgah üzerinde yaptıkları tüm kontrollerin programda birebir uygulanabilmesi ve eşzamanlı olarak tezgah ikizinde görülebilmesidir. Simülasyon programı içinde CNC Freze ve Torna tezgâhlarında kullanılan FANUC, SIEMENS, MITSUBISHI, MAZAK, FAGOR, HAAS, DASEN, HEIDENHAIN gibi 65 farklı kontrol ünitesi ile 150 farklı operatör paneli ve üç boyutlu makina simulasyonu mevcuttur. (Şekil 11).

Swansoft Simülatör yazılımı, kullanıcısı tezgah başındaymış gibi CNC manuel programlama yapabilme, parça işleme, tezgah kontrollerini gerçeğiyle birebir yapabilme, işleme ve tezgah mekanik hareketlerinin birebir simulasyonunu gerçek zamanlı izleyebilme ve üretilmiş olan parça üzerinde ölçme ve kontrol işlemleri yapabilme imkanlarını vermektedir. Dokunmatik ekranlı bir ekran kullanılması durumunda kullanıcıya CNC kontrol panelini kullanıyormuş izlenimi vermektedir.


**Şekil 11.** Swansoft simülasyon programında kullanılabilen kontrol paneli örnekleri [64]

Yazılımın temel özellkleri şu şekilde sıralanabilir:

- CNC torna ve frezede gerçek simülasyon,
- 50 den fazla farklı kontrol Sistemi,150'nin üzerinde ünite,
- Alt programlama ve delik çevrimleri dahil manuel programlama,
- Değişken parametrelerle macro program yapabilme,
- CAD/CAM Sisteminden alınan NC kodunu simüle etme,
- NC Kodu kontrolü ve hata ayıklama,

- Gerçek makine aksamı,talaş ve soğutma sıvısı görünümü,
- Görüntü kaydı ve tekrar oynatma ile eğitim verebilme,
- Kolay arayüz ve yaygın birçok dilde dil desteği sunma,
- İnternet üzerinden online ücretsiz güncelleme imkanı.

Bu simülasyon yazılımın gerek kullanıcı, gerek iş yerinde CNC eğitimi verme gerekse herhangi bir eğitim ortamında CNC tezgah kullanımı eğitimi veren tüm kurumlar açısından şu imkanları vermektedir;

- İşletmelerin kendi bünyelerinde bulunan tezgah ve kontrol panelini birebir simülasyonda kullanabilme yeteneği sayesinde iş akışı ve iş yapan tezgah zamanından kayıp yaşamadan kendi personelini tezgah kullanımı ile ilgili yetiştirebilme imkanı sunmaktadır.
- İşletmelerin mevcut CNC operatörlerinin eksiklerini yazılım üzerinden görme, düzeltme ve geliştirebilme kabiliyetini arttırmaktadır.
- CNC operatörü ile ilgili işe alımlarda tezgah başına geçmeden başvuru sahibini test edebilme imkanı vermektedir.
- Herhengi bir CAM yazılımdan alınan NC kodları simülasyon yazılımda hatalarını teip etmeye olanak sağlamaktadır.
- İşletmelerin veya CNC eğitim verenlerin manuel olarak yazdıkları NC programları test ederek tezgahta, kesici takımda veya iş parçasında oluşabilecek maddi hasarları önleyebilme kabiliyeti vermektedir.

Swansoft yazılım firması istenildiğinde özel olarak tasarlanmış kontrol paneli verme opsiyonu da tanımaktadır. Program içinde tezgah kontrolleri ile ilgili fikstür tanımı, stok malzeme ve boyut tanımlaması, gerçek tezgahtaki gibi referans noktası tanımlamaları için ışıklı sesli prob, mekanik prob, komparatör vb. araçları, farklı tipte kesici takım ve takım tutucu tanımlama imkanlarını vermekte ve bu araçların kullanımını CNC tezgah başındaymış gibi aynı prosedürlerle kontrol edebilme imkanı vermektedir. Tüm bunların yapılması noktasında CNC programlama, kullanım ve denetleme alanında eğitim amacıyla en avantajlı CNC simülasyon yazılımı özelliğine kavuşmaktadır.

Yazılım görsel ve grafik ekran bakımından çeşitli imkanlar sunmaktadır. Stok malzeme, takım tutucular, fikstür görünümleri, soğutucu hortum ve ayna, magazin gibi komponentlerin görünürlüğü gibi tezgah görünümleri başarılı bir şekilde verilmektedir. Ayrıca çok sayıda kontrol paneli olanağının yanısıra farklı tipte CNC tezgahları da grafik ekrana taşıyabilmekte ve görsel olarak sunabilmektedir (Şekil 12).

Swansoft simülasyonunun güvenilirlik anlamında profesyonel simülasyon programlarına göre daha alt seviyelerde olması, kinematik ve dinamik hareket

ve analizleri yapamaması, düşük grafik kalitesi, tezgah model ölçülerinin muadilleri ile kıyaslandığında ölçü tamlığı noktasında daha düşük seviyede kalması en önemli dezavantajları olarak sayılabilir. Yazılımın amaçları arasında bu özelliklerin ön planda olmaması, daha çok tezgah eğitimi ve kontrolü ile ilgili insan yetiştirme amacına yönelik bir hedef belirlenmesinin doğal sonuçları arasında bu dezavantajlarının olması normal bir durum olarak karşımıza çıkmaktadır.

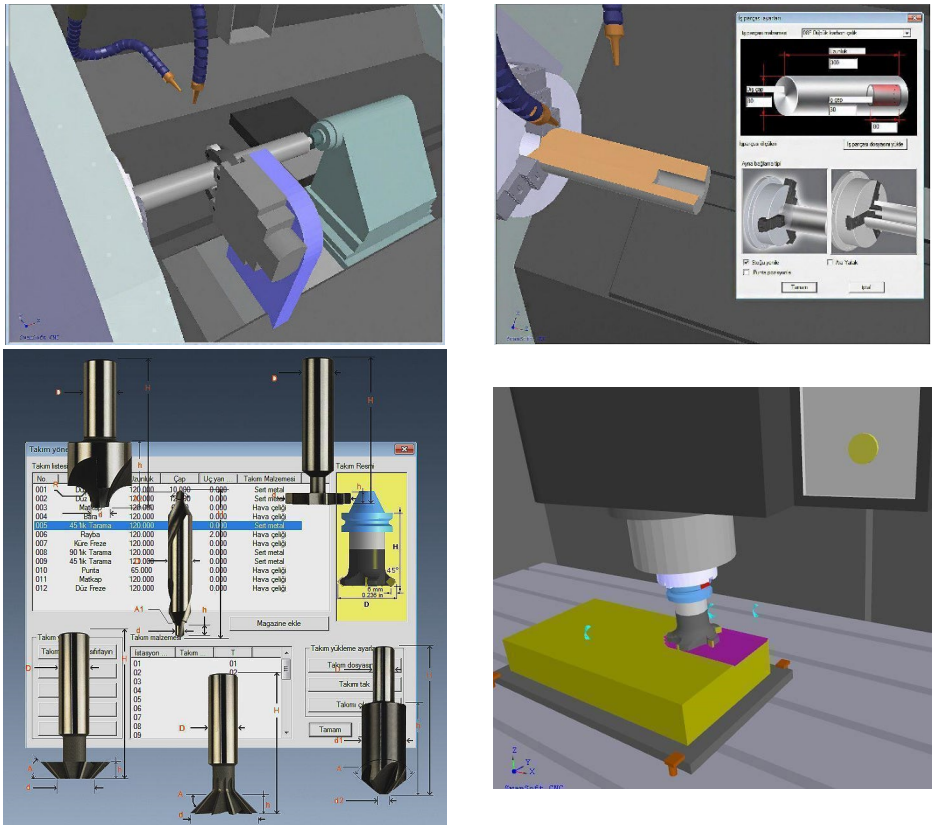

**Şekil 12.** Swansoft CNC simülasyon programında farklı tezgah kontrolleri ve görüntüleri [65]

## KAYNAKLAR


1. Baudrillard, J. (2011). Simülakrlar ve Simülasyon, Ankara: Doğu Batı Yayınları
2. Cevizci, A. (2011). Felsefe Tarihi, İstanbul: Say Yayınları
3. Okuyan, H. (2018). Jean Baudrillard'ın simülasyon kuramının temellendirildiği argümanların değerlendirilmesi, Yayımlanmamış Yüksek Lisans Tezi, Yıldız Teknik Üniversitesi Fen Bilimleri Enstitüsü, İstanbul).
4. Azevedo, A.; Almeida, A.H. Grasp the challenge of digital transition in smes—A training course geared towards decision-makers. Educ. Sci. 2021, 11, 151.
5. Dunn SV, Hansford B. Under graduate nursing students' perceptions of their clinical learning environment. Journal of Advanced Nursing. 1997; 25(6): 1299-306.
6. Sullivan R, Magarick R, Bergthold G, Blouse A, McIntosh N. Tıp Eğitimcileri İçin Eğitim Becerileri Rehberi. Ankara: Hacettepe Halk Sağlığı Vakfı; 1999. s.33-52.
7. Rhodes M, Curran C. Use of the human patient simulator to teach clinical judgment skills in a baccalaureate nursing program. Computers, Informatics, Nursing. 2005; 23(5): 256-62.
8. Rauen CA. Simulation as a teaching strategy for nursing education and orientation in cardiac surgery. Critical Care Nurse. 2004; 24(3): 46-51.
9. Tankut, Ü.S. (2008). İlköğretim 7. Sınıf Sosyal Bilgiler Dersinde Destekli Öğretimin Akademik Başarıya Ve Kalıcılığa Etkisi. (Yayımlanmamış yüksek lisans tezi). Çukurova Üniversitesi Sosyal Bilimler Enstitüsü, Adana.
10. Tekdal, M. (2002). Etkileşimli fizik simülasyonlarının geliştirilmesi ve etkin kullanılması. V. Ulusal Fen Bilimleri ve Matematik Eğitimi Kongresi, ODTÜ, Ankara
11. Bidaybekov, L. B., Bidaybekov, E. I., Sharmukhanbet, S., Kamalova, G. B., & Oshanova, N. T. (2012). The use of virtual measuring devices in teaching modeling of physical processes. Procedia-Social and Behavioral Sciences, 51, 803-806, https://doi.org/10.1016/j.sbspro.2012.08.243.]
12. di Lanzo, J. A., Valentine, A., Sohel, F., Yapp, A. Y., Muparadzi, K. C., & Abdelmalek, M. (2020). A review of the uses of virtual reality in engineering education. Computer Applications in Engineering Education, 28(3), 748-763, https://doi.org/10.1002/cae.22243.
13. Uğuz, S., Oral, O., & Aksoy, B. (2018). STEM Eğitimi için sanal laboratuvar oluşturulması. Eğitim ve Öğretim Araştırmaları Dergisi, 7(1),

69-77, İçten, T., & Güngör, B. A. L. (2017). Artırılmış gerçeklik üzerine son gelişmelerin ve uygulamaların incelenmesi. Gazi Üniversitesi Fen Bilimleri Dergisi Part C: Tasarım ve Teknoloji, 5(2), 111-136

14. Akbulut, A., Catal, C., & Yıldız, B. (2018). On the effectiveness of virtual reality in the education of software engineering. Computer Applications in Engineering Education, 26(4), 918-927, https://doi.org/10.1002/cae.21935
15. Ouyang, S. G., Wang, G., Yao, J. Y., Zhu, G. H. W., Liu, Z. Y., & Feng, C. (2018). A Unity3D-based interactive three-dimensional virtual practice platform for chemical engineering. Computer Applications in Engineering Education, 26(1), 91-100, https://doi.org/10.1002/cae.21863
16. Hee Lee, J., & Shvetsova, O. A. (2019). The Impact of VR Application on Student's Competency Development: A Comparative Study of Regular and VR Engineering Classes with Similar Competency Scopes. Sustainability, 11(8), 2221, https://doi.org/10.3390/su11082221
17. Lu, X., Yang, Z., Xu, Z., & Xiong, C. (2020). Scenario simulation of indoor post-earthquake fire rescue based on building information model and virtual reality. Advances in Engineering Software, 143, 102792, https://doi.org/10.1016/j.advengsoft.2020.102792
18. Qin, S., Wang, Q., & Chen, X., Qin, S., Wang, Q., & Chen, X. (2020). Application of virtual reality technology in nuclear device design and research. Fusion Engineering and Design, 161, 111906, https://doi.org/10.1016/j.fusengdes.2020.111906
19. Labovitz, J., & Hubbard, C. (2020). The Use of Virtual Reality in Podiatric Medical Education. Clinics in Podiatric Medicine and Surgery, 37(2), 409-420, https://doi.org/10.1016/j.cpm.2019.12.008
20. Hagita, K., Kodama, Y., & Takada, M. (2020). Simplified virtual reality training system for radiation shielding and measurement in nuclear engineering. Progress in Nuclear Energy, 118, 103127, https://doi.org/10.1016/j.pnucene.2019.103127
21. Bashabsheh, A. K., Alzoubi, H. H., & Ali, M. Z. (2019). The application of virtual reality technology in architectural pedagogy for building constructions. Alexandria Engineering Journal, 58(2), 713-723, https://doi.org/10.1016/j.aej.2019.06.002
22. O'Connor, M., Deeks, H. M., Dawn, E., Metatla, O., Roudaut, A., Sutton, M., ... & Wonnacott, M. (2018). Sampling molecular conformations and dynamics in a multiuser virtual reality framework. Science advances, 4(6), eaat2731, https://doi.org/10.1126/sciadv.aat2731

23. Uğuz, S., & Zehir, B. (2020). İmalat Mühendisliği Eğitimi için Sanal Gerçeklik Sistemi Tasarımı ve Geliştirilmesi. Gazi Üniversitesi Fen Bilimleri Dergisi Part C: Tasarım ve Teknoloji, 8(4), 845-857.
24. Samala, A.D.; Amanda, M. Immersive learning experience design (ILXD): Augmented reality mobile application for placing and interacting with 3d learning objects in engineering education. Int. J. Interact. Mob. Technol. 2023, 17, 22–35
25. Lai, Z.H.; Tao, W.; Leu, M.C.; Yin, Z. Smart augmented reality instructional system for mechanical assembly towards workercentered intelligent manufacturing. J. Manuf. Syst. 2020, 55, 69–81.
26. Cardoso, M.S.; Lepikson, H.A. Monitoring and Integration of CNC Machines in Advanced Manufacturing Environment for Predictive Operations. In Proceedings of the IX Symposium Internacional de Innovation and Technology, São Paulo, Brasil, 25–27 October 2023.
27. Lai, Y.-S.; Lin, W.-Z.; Lin, Y.-C.; Hung, J.-P. Development of surface roughness prediction and monitoring system in milling process. Eng. Technol. Appl. Sci. Res. 2024, 14, 12797–12805.
28. But, A.; Scaticailov, S. Using CAM Software to Improve Productivity. In Proceedings of the IOP Conference Series: Materials Science and Engineering, Pitesti, Romania, 22–24 May 2019.
29. Li, M., Li, Y., & Guo, H. (2020). Research and application of situated teaching design for NC machining course based on virtual simulation technology. Computer Applications in Engineering Education, 28(3), 658-674, https://doi.org/10.1002/cae.22234.
30. Wibisono, G.;Wijanarka, B.S.; Theophile, H. The link and match between the competency of vocational high schools graduates and the industry on CAD/CAM and CNC. J. Pendidik. Teknol. Kejuru. 2020, 26, 26–34.
31. Ghobrial, M.; Seitier, P.; Lagarrigue, P.; Galaup, M.; Gilles, P. Effectiveness of machining equipment user guides: A comparative study of augmented reality and traditional media. Mater. Res. Proc. 2024, 41, 2320–2328.
32. Studer, K.; Lie, H.; Zhao, Z.; Thomson, B.; Turakhia, D.G.; Liu, J. An Open-ended System in Virtual Reality for Training Machining Skills. In Proceedings of the CHI Conference on Human Factors in Computing Systems, Honolulu, HI, USA, 11–16 May 2024.
33. Mansoori, S.; Salari Koohfini, Z.; Ghasemali, M. A Comparison between the effectiveness of e-learning and blended learning in industrial training. Interdiscip. J. Virtual Learn. Med. Sci. 2020, 11, 46–53, 32.

34. Radovan, M.; Radovan, D.M. Harmonizing pedagogy and technology: Insights into teaching approaches that foster sustainable motivation and efficiency in blended learning. Sustainability 2024, 16, 2704.
35. Liu, L.; Li,W.; Chen, X. Exploration and realization about teaching experimental of CNC machine tool based on virtual simulation technology. Manuf. Technol. 2023, 23, 485–494, 34.
36. Antonelli, D.; Christopoulos, A.; Laakso, M.-J.; Dagiene˙ , V.; Juškevic˘iene˙ , A.; Masiulionyte˙ -Dagiene˙ , V.; Ma˛dziel, M.; Stadnicka, D.; Stylios, C. A virtual reality laboratory for blended learning education: Design, implementation and evaluation. Educ. Sci. 2023, 13, 528.
37. Mourtzis, D.; Zogopoulos, V.; Katagis, I.; Lagios, P. Augmented reality based visualization of CAM instructions towards Industry 4.0 paradigm: A CNC bending machine case study. Procedia CIRP 2018, 70, 368–373.,36.
38. Sibanda, V.; Kanganga, M.; Sibanda, N. Bridging the Gap between Industry and Academia-The Essence of Virtual Reality in Skills Development and Learning Factories. In Proceedings of the 13th Conference on Learning Factories, Reutlingen, Germany, 9–11 May 2023.
39. Abizar, H.; Ramdani, S.D.; Supriyatna, D. Operator competency model for mechanical engineering expertise. AIP Conf. Proc. 2023, 2671, 060005.
40. Setiawan, A.; Pratama, H.; Setyadi, K.; Asih, E.K.; Yosephine, V.S. Automated Material Handling System and Inspection System Model for Flexible Manufacturing Systems Learning. In Proceedings of the Second Asia Pacific International Conference on Industrial Engineering and Operations Management, Surakarta, Indonesia, 14–16 September 2021.
41. de Giorgio, A.; Monetti, F.M.; Maffei, A.; Romero, M.;Wang, L. Adopting extended reality? A systematic review of manufacturing training and teaching applications. J. Manuf. Syst. 2023, 71, 645–663.
42. Sorathiya, P.C.; Singh, S.A.; Desai, K.A. Mobile-based augmented reality (AR) module for guided operations of CNC surface roughness machine. Manuf. Lett. 2023, 35, 1255–1263.
43. Nguyen, H.T.; Olsson, R.; Haugen, Ø. Automatic synthesis of recurrent neurons for imitation learning from CNC machine operators. IEEE Open J. Ind. Electron. Soc. 2024, 5, 91–108.
44. Longo, F.; Padovano, A.; De Felice, F.; Petrillo, A.; Elbasheer, M. From “prepare for the unknown” to “train for what’s coming”: A digital twin-

driven and cognitive training approach for the workforce of the future in smart factories. J. Ind. Inf. Integr. 2023, 32, 100437.
45. Sorathiya, P.C.; Singh, S.A.; Desai, K.A. Mobile-based augmented reality (AR) module for guided operations of CNC surface roughness machine. Manuf. Lett. 2023, 35, 1255–1263.
46. Scoble-Williams, N.; Mallon, D.; Cantrell, S.; Zanza, M.; Griffiths, M.; Poynton, S. How play and experimentation in digital playgrounds can drive human performance. In 2024 Global Human Capital Trends; DeloiItte Insights: Mexico City, Mexico, 2024. Available online: https://www2.deloitte.com/content/dam/insights/articles/glob176836_global-human-capital-trends-2024/DI_Global-Human-Capital-Trends-2024.pdf (accessed on 28 June 2024).
47. Studer, K.; Lie, H.; Zhao, Z.; Thomson, B.; Turakhia, D.G.; Liu, J. An Open-ended System in Virtual Reality for Training Machining Skills. In Proceedings of the CHI Conference on Human Factors in Computing Systems, Honolulu, HI, USA, 11–16 May 2024.
48. Aruanno, B.; Carruba, M.C.; Mondellini, M.; Santos-Paz, J.A.; Ferrise, F.; Karaki, J.; Covarrubias, M. Enhancing inclusive education for young students with special needs through mixed reality: Exploring the potential of CNC milling machine application. Comput.-Aided Des. Appl. 2024, 21, 522–535.
49. James, S.; Eckert, G. A feasibility study on mixed reality-based visualization and interaction tool for performance improvement of metal cutting processes. Metals 2023, 13, 286.
50. Longo, F.; Padovano, A.; De Felice, F.; Petrillo, A.; Elbasheer, M. From “prepare for the unknown” to “train for what’s coming”: A digital twin-driven and cognitive training approach for the workforce of the future in smart factories. J. Ind. Inf. Integr. 2023, 32, 100437.
51. Lotti, G.; Villani, V.; Battilani, N.; Fantuzzi, C. New trends in the design of human-machine interaction for CNC machines. IFAC-PapersOnLine 2019, 52, 31–36.
52. https://www.vericut.com.tr/
53. https://www.vericut.com.tr/
54. https://cn.ncsimul.com/ncsimul-machine
55. https://www.cgsys.co.jp/en/cam-tool/img/function/nx/ctnx_main_eng.png
56. https://share.google/images/YREzayjQPKhkd5Efg
57. https://share.google/images/tTyElZZmV65YiM9Sn
58. https://share.google/images/rRMPNCyuHgQbmAZV5
59. https://share.google/images/ptT34Hgn7Lnv9pRou

60. https://youtu.be/4FEbWGXxLZU?si=XdrYGJcODEtJNk_L
61. https://youtu.be/g4a_eyLsmS0?si=ee31q-SLdyVsowBc
62. https://youtu.be/u5hH9HJa56I?si=E7KzStePZq54Z7rY
63. https://www.formaksan.com.tr/swansoft-cnc-simulator.html
64. https://www.formaksan.com.tr/gal/img/custom_unite.jpg
65. https://www.formaksan.com.tr/swansoft-cnc-simulator.html

# Chapter 6

# MECHANICAL INVESTIGATION OF HONEYCOMB ANKLE FOOT ORTHOSES

**Cem GÜZELBULUT[1], Serdar KAVELOĞLU[2]**

## 1. INTRODUCTION

Walking is one of the most fundamental and complex motor functions of the human body and requires the simultaneous and harmonious operation of the musculoskeletal system, nervous system, and sensory organs [1]. Disturbance in any of these systems lead to gait disorders that directly affect a person's independence in daily life [2]. Gait disorders are a significant public health problem because they not only reduce mobility but also increase the risk of falls, reduce quality of life, and lead to long-term physical and psychological health problems [3, 4].

In recent years, studies aimed at understanding the causes of gait disorders have revealed that a wide variety of factors, such as neurological diseases (Parkinson's disease, stroke, multiple sclerosis), orthopedic problems (musculoskeletal deformities, joint diseases), and physical decline due to aging, significantly alter gait dynamics. This has led to the critical role of gait analysis in clinical diagnosis, rehabilitation, and treatment planning [5, 6].

With the development of wearable sensor technologies, three-dimensional motion analysis systems, and artificial intelligence-based assessment methods, it has become possible to evaluate gait disorders objectively and with high accuracy [7, 8]. These new methods, which can provide more detailed and quantitative data compared to traditional clinical observations, are increasingly used both in research and clinical practice [9].

In this context, accurate classification of gait disorders is of great importance for determining effective treatment strategies and developing personalized rehabilitation approaches [10-12]. A complete understanding of the

[1]Assistant Prof. Dr., Department of Mechanical Engineering/Faculty of Engineering, Architecture and Design, Kahramanmaras Istiklal University, Türkiye,
cem.guzelbulut@istiklal.edu.tr, (ORCID: 0000-0001-9618-4032)
[2]Assistant Prof. Dr., Department of Mechanical Engineering/Faculty of Engineering, Architecture and Design, Kahramanmaras Istiklal University, Türkiye,
serdar.kaveloglu@istiklal.edu.tr, (ORCID: 0000-0003-0157-7314)

biomechanical and neurophysiological mechanisms underlying gait disorders is still a current area of research [13].

Ankle-foot orthoses (AFO) are one of the most frequently used assistive devices in clinical practice to correct these disorders [14]. AFO provides mechanical support by stabilizing the ankle joint, limiting pathological movements and maintaining the foot position required during walking [15, 16].

It is possible to add controllable stiffness to ankle-foot orthoses through different designs [17-19]. It has been shown that orthosis stiffness can be optimized for each patient by measuring biomechanical responses during walking in real time through sensors integrated into the ankle-foot orthosis [20]. A stiffness-modulating ankle-foot orthosis (SMAFO) was developed using shape memory alloy (SMA), allowing patients with foot drop to dynamically adjust the levels of support needed during walking. The prototype significantly improved locomotor control during foot lift and swing phases thanks to low-power electrical activation of the SMA elements [21]. A passive ankle-foot orthosis was designed and 3D printed using fiber-reinforced PETG-CF15 material. The design, which considered material characterization and manufacturing parameters, optimized the orthosis's mechanical strength and required rigidity during walking [22]. The mechanical behavior of a 3D-printed ankle-foot orthosis fabricated using carbon fiber-reinforced polymer (CFRP) was analyzed using the finite element method (FEM). The analysis results showed that the orthosis's stiffness and strength performance under different loads could be predicted, allowing the design to be optimized according to patient needs [23].

In this study, a new approach was developed to design ankle foot orthoses that integrate honeycomb patterns. First, CAD model of the orthosis was created, and finite element analyses were conducted to understand how much deformation occurs and what maximum stress is. Then, mechanical properties of the orthosis were investigated and future directions were discussed.

## 2. METHODS

The mechanical behavior of the orthosis was investigated using finite element method (FEM). Using FEM analysis, maximum displacement, maximum stress, maximum stress and where critical zones are obtained. In the present study, an orthosis having honeycomb pattern was considered as shown in Figure 1. Instead of trimline approach used in the previous study [24], honeycomb pattern is used and the stiffness of the structure can be tuned by orthotist depending on application.

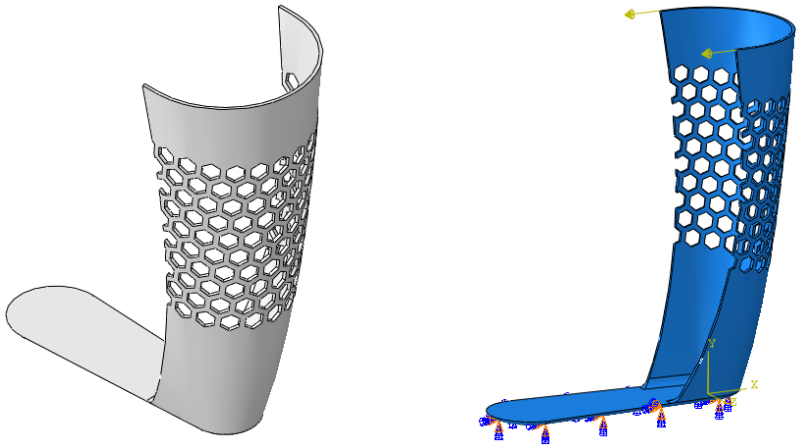

Figure 1. 3D CAD model of the orthosis and boundary conditions applied

The boundary conditions applied to analyze he orthosis is as shown in Figure 1. The bottom of sole was fixed in all degrees of freedom. The load was applied at connectors of orthosis. The amount of load applied was determined based on the previous study [24], 17 N at each connector point. Approximately 180000 nodes and 100000 10-node quadratic tetrahedron elements were used to discretize the computational domain. Static analysis was performed to obtain mechanical performance of the orthosis.

The material used in the simulations was PLA considering that the final orthosis design can be manufactured using 3D printers by anyone with ease. The elastc modulus and Poisson's ratio of PLA was set to 3000 MPa and 0.35, respectively.

## 3. RESULTS AND DISCUSSION

The displacement and von Mises stress distribution over the structure was shown in Fİgure 2. It was found that the maximum displacement obtained was around 9 mm and the maximum von Mises stress on the structure was 24.5 MPa, which is lower than yield strength of the material. Compared to the previous study [24], the maximum displament was almost same but stress on the structure was found significantly higher.

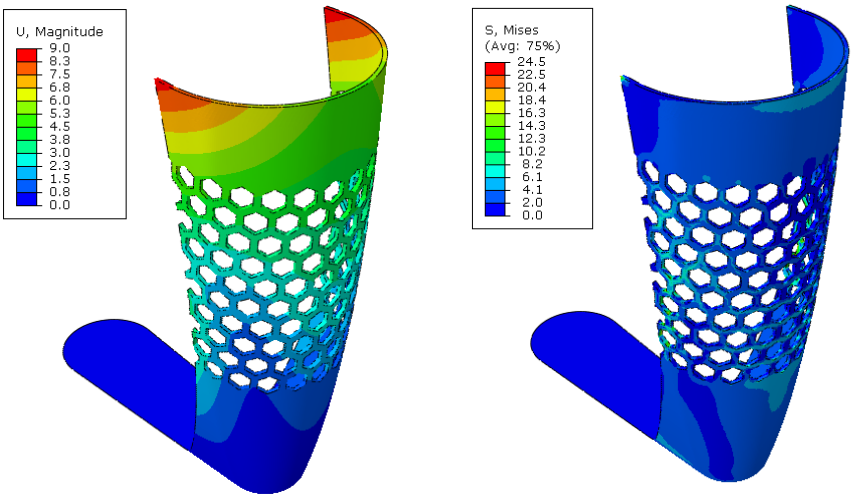


Figure 2. The displacement and von Mises stress distribution of the structure under applied loads.

Then, the region where maximum stress occurs was investigated. It was found that the maximum stress occurs at the internal sides of orthosis where honeycomb structure starts to appear, as shown in Figure 3. The reason why the relevant zone of the honeycomb pattern has higher stress is due to slenderness of the structure and stress concentration effects. Instead of bulk material usage, honeycomb pattern reduces the total material used but also causes some critical zones on the structure. In addition, it should be noted that the maximum von Mises stress is due to high compressive stress. The occurence of the sharp edges and vertices causes stress concentration effect and increases stress. In order to reduce stress concentration zones, the affected zones having sharp corners can be smoothened by defining radius features.

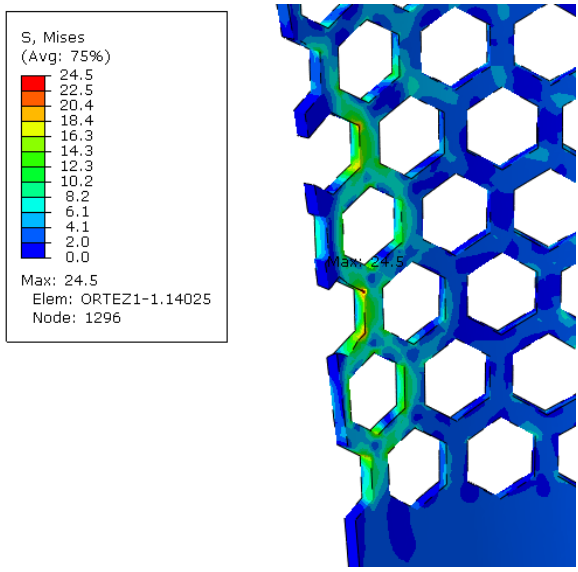


Figure 3. The maximum stress region of the orthosis

Another important aspect of orthosis is stiffness. The stiffness of such orthosis can be tuned depending on the practice and subject through cutting and reducing the honeycomb members. In addition, building the orthosis using multimaterial 3D printing allows further tuning properties to orthosis.

## 4. CONCLUSION

The present study investigates the mechanical behavior of the honeycomb ankle foot orthosis. It was found that the maximum displacement under given load was 9 mm, showing similar response traditional orthosis design. The maximum von Mises stress on the structure occured on the honeycomb pattern and was higher than conventional design due to stress concentration zone. Future studies will address stiffness regulation and design improvement of the ankle foot orthosis using multimaterials suitable for 3D printing.

## REFERENCES


1. Sarkodie-Gyan, T., & Yu, H. (2023). Challenges and Concerns to Society: The Human Locomotor System. In *The Human Locomotor System: Physiological and Technological Foundations* (pp. 99-122). Cham: Springer International Publishing.
2. Pirker, W., & Katzenschlager, R. (2017). Gait disorders in adults and the elderly: A clinical guide. *Wiener Klinische Wochenschrift*, *129*(3), 81-95.
3. Al-Momani, M., Al-Momani, F., Alghadir, A. H., Alharethy, S., & Gabr, S. A. (2016). Factors related to gait and balance deficits in older adults. *Clinical interventions in aging*, 1043-1049.
4. Montero-Odasso, M., & Masud, T. (2020). Falls and gait disorders in older adults: Causes and consequences. In *Frailty and kidney disease: A practical guide to clinical management* (pp. 13-35). Cham: Springer International Publishing.
5. Pirker, W., & Katzenschlager, R. (2017). Gait disorders in adults and the elderly: A clinical guide. *Wiener Klinische Wochenschrift*, *129*(3), 81-95.
6. Lim, M. R., Huang, R. C., Wu, A., Girardi, F. P., & Cammisa Jr, F. P. (2007). Evaluation of the elderly patient with an abnormal gait. *JAAOS-Journal of the American Academy of Orthopaedic Surgeons*, *15*(2), 107-117.
7. Jawed, A. M., Zhang, L., Zhang, Z., Liu, Q., Ahmed, W., & Wang, H. (2025). Artificial intelligence and machine learning in spine care: Advancing precision diagnosis, treatment, and rehabilitation. *World Journal of Orthopedics*, *16*(8), 107064.
8. Prakash, C., Kumar, R., & Mittal, N. (2018). Recent developments in human gait research: parameters, approaches, applications, machine learning techniques, datasets and challenges. *Artificial Intelligence Review*, *49*(1), 1-40.
9. Mohsen, F., Ali, H., El Hajj, N., & Shah, Z. (2022). Artificial intelligence-based methods for fusion of electronic health records and imaging data. *Scientific Reports*, *12*(1), 17981.
10. Loya, A., Deshpande, S., & Purwar, A. (2020). Machine learning-driven individualized gait rehabilitation: classification, prediction, and mechanism design. *Journal of Engineering and Science in Medical Diagnostics and Therapy*, *3*(2), 021105.
11. Soler, B., Ramari, C., Valet, M., Dalgas, U., & Feys, P. (2020). Clinical assessment, management, and rehabilitation of walking impairment in MS: an expert review. *Expert review of neurotherapeutics*, *20*(8), 875-886.

**12.** French, M. A., Roemmich, R. T., Daley, K., Beier, M., Penttinen, S., Raghavan, P., ... & Celnik, P. (2022). Precision rehabilitation: optimizing function, adding value to health care. *Archives of physical medicine and rehabilitation*, *103*(6), 1233-1239.

**13.** Takakusaki, K., Takahashi, M., Noguchi, T., & Chiba, R. (2023). Neurophysiological mechanisms of gait disturbance in advanced Parkinson's disease patients. *Neurology and Clinical Neuroscience*, *11*(4), 201-217.

**14.** Choo, Y. J., & Chang, M. C. (2021, August). Commonly used types and recent development of ankle-foot orthosis: a narrative review. In *Healthcare* (Vol. 9, No. 8, p. 1046). MDPI.

**15.** Zhou, C., Yang, Z., Li, K., & Ye, X. (2022). Research and development of ankle–foot orthoses: A review. *Sensors*, *22*(17), 6596.

**16.** Lora-Millan, J. S., Nabipour, M., van Asseldonk, E., & Bayón, C. (2023). Advances on mechanical designs for assistive ankle-foot orthoses. *Frontiers in bioengineering and biotechnology*, *11*, 1188685.

**17.** Yakimovich, T., Lemaire, E. D., & Kofman, J. (2009). Engineering design review of stance-control knee-ankle-foot orthoses. *Journal of Rehabilitation Research & Development*, *46*(2).

**18.** Kobayashi, T., Leung, A. K., Akazawa, Y., & Hutchins, S. W. (2011). Design of a stiffness-adjustable ankle-foot orthosis and its effect on ankle joint kinematics in patients with stroke. *Gait & posture*, *33*(4), 721-723.

**19.** Rogati, G., Caravaggi, P., & Leardini, A. (2022). Design principles, manufacturing and evaluation techniques of custom dynamic ankle-foot orthoses: a review study. *Journal of foot and ankle research*, *15*(1), 38.

**20.** Bolus, N. B., Teague, C. N., Inan, O. T., & Kogler, G. F. (2017). Instrumented ankle–foot orthosis: Toward a clinical assessment tool for patient-specific optimization of orthotic ankle stiffness. *IEEE/ASME Transactions on Mechatronics*, *22*(6), 2492-2501.

**21.** Gu, G. M., Kyeong, S., Park, D. S., & Kim, J. (2015, August). SMAFO: Stiffness modulated Ankle Foot Orthosis for a patient with foot drop. In *2015 IEEE International Conference on Rehabilitation Robotics (ICORR)* (pp. 543-548). IEEE.

**22.** Steck, P., Scherb, D., Witzgall, C., Miehling, J., & Wartzack, S. (2023). Design and additive manufacturing of a passive ankle–foot orthosis incorporating material characterization for fiber-reinforced PETG-CF15. *Materials*, *16*(9), 3503.

**23.** Ali, M. H., Smagulov, Z., & Otepbergenov, T. (2021). Finite element analysis of the CFRP-based 3D printed ankle-foot orthosis. *Procedia Computer Science*, *179*, 55-62.

**24.** Sürmen, H. K. & Arslan, Y. Z. (2021) Evaluation of various design concepts in passive ankle-foot orthoses using finite element analysis. *Engineering Science and Technology, an International Journal, 24(6),* 1301-1307.

# Chapter 7

# AI-POWERED[1] QUALITY CONTROL SYSTEMS

**Kenan ORÇANLI[2], Şükran ORUÇ[3]**

## 1. Introduction and Quality Control

Contemporary enterprises adopt strategies focused on revenue enhancement, cost reduction, and value creation to secure a competitive advantage and ensure sustainable profitability (Stancheva-Todorova, 2018, p. 126). In pursuit of these objectives, firms are transforming their production and management processes within the framework of Industry 4.0, integrating quality control practices with emerging technologies. Industry 4.0 has materialized through the incorporation of artificial intelligence (AI), the Internet of Things (IoT), cyber-physical systems, big data analytics, and cloud computing into industrial ecosystems (Sader et al., 2019, p. 131).

With the proliferation of Industry 4.0, production methods, engineering activities, and technological infrastructures have undergone a fundamental transformation. Throughout this process, quality control systems have assumed a critical role in process optimization and defect detection (Sony et al., 2020, p. 2). As enterprises leverage robotic systems and AI support for data collection, analysis, and repetitive operations, the effectiveness of quality control processes increases significantly (Souza et al., 2021, p. 1). AI has gained particular importance in rapid defect remediation and the maintenance of high-quality standards (Gür et al., 2019, p. 140; Gökten, 2018, p. 881). Furthermore, AI supports efficient resource utilization and improves environmental performance, aligning with sustainable development goals (Buchmeister et al., 2019, p. 81).

AI-based systems facilitate the development of novel models, technological tools, and quality control mechanisms within production processes (Li et al., 2017, p. 87). While these systems enhance energy and resource efficiency, they also strengthen enterprises' economic performance and competitiveness. It is anticipated that production systems will undergo radical changes in the coming

[1] AI-Powered (Artificial Intelligence-Powered) refers to a system or process that is automated and made autonomous by leveraging Artificial Intelligence (AI) and Deep Learning algorithms.

[2] Assoc. Prof. Dr., Istanbul Beykent University/Faculty of Arts and Sciences/Software Development Department/Software Development Pr. Turkey, kenanorcanli@gmail.com, (ORCID: 0000-0001-5716-4004

[3]Asst. Prof. Dr., Istanbul Beykent University/Faculty of Economics and Administrative Sciences/Department of Management Information Systems/Management Information Systems Pr., Turkey, sukranoruc@beykent.edu.tr, (ORCID: 0000-0002-8176-4058)

period, with AI becoming the primary determinant of effectiveness in quality control (Buchmeister et al., 2019, p. 1).

Currently, AI is increasingly utilized in both manufacturing and service sectors to enhance quality, minimize defects, and optimize process efficiency (Lee et al., 2019, p. 3). The integration of technology into quality control not only boosts production efficiency but also fosters positive shifts in organizational culture, leadership, and collaboration (Lee et al., 2019, p. 3). Moreover, AI systems mitigate sectoral challenges such as talent shortages, decision-making complexity, integration issues, and information overload (Buchmeister et al., 2019, p. 8).

Today, quality control is no longer limited to ensuring production efficiency; it has assumed a central role in strategic decision-making. AI-powered systems enable early defect detection, resource optimization, and continuous process improvement. Consequently, adopting AI-based quality control applications is becoming critical for enterprises aiming to enhance their competitive edge and support sustainable development. Ultimately, the structural transformation of production systems and the integration of quality management with AI will be the defining factors for future industrial performance and productivity.

### 1.1. Quality Control: Definition and Importance

If quality is accepted as the totality of characteristics of goods and services that meet the needs of internal and external customers, quality control can be defined as the sum of processes, activities, and methods that ensure the creation of these characteristics. In this context, definitions of quality control made by some quality pioneers are presented below.

According to Juran, quality control is "a managerial process for combining activities to maintain the current situation, prevent deterioration, and ensure balance. Ensuring balance refers to comparing the actual performance of the process with the targeted performance, identifying the difference, and eliminating this difference," and it is only one of the three managerial efforts applied to manage quality. These managerial efforts are quality planning, quality control, and quality improvement.

According to Ishikawa, quality control is "developing, designing, producing, and maintaining a quality product that is most economical, most useful, and always satisfies the consumer" (Qiu, 2013).

The Japanese Industrial Standards define quality control as "a system of production methods that economically produces quality goods and services that meet consumer requirements" (Qiu, 2013).

In the modern sense, according to Montgomery (2020), quality control is "the totality of techniques and activities to be applied to achieve the determined objectives and standards related to quality." These techniques and activities are, respectively, process control, calculation and recording of statistics, detection of out-of-control errors, and correction by finding the source of the error.

If the issues related to the concept of quality control in the above definitions are to be summarized, the purpose of quality control is to produce products that meet consumer demands at the most economical level possible (Orçanlı, 2017).

Quality control has many benefits for enterprises. These benefits for enterprises are listed below:

- Through quality control, customer expectations and demands are fully met; therefore, the number of customers increases, and sales and profits rise.
- Improvements occur in the quality of products and services.
- It ensures that the process is maintained within a dynamic structure to meet the changing demands of consumers.
- It increases productivity, which is one of the objectives of enterprises.
- It reduces costs in the long term.
- It ensures timely production (Orçanlı, 2017).

### 1.1.1. The Role of Quality Control in Manufacturing, Logistics, and Service Sectors

Quality control has evolved in the modern business world from being merely a technical procedure for detecting defects on the production line into a strategic management discipline that guarantees operational excellence and customer satisfaction throughout the entire value chain, from production to end-user (Bader, 2025; Ever & Demircioğlu, 2022). In the manufacturing sector, the detection and prevention of defects at their source through AI-powered systems enable the achievement of "zero-defect[4]" objectives while minimizing costs and maximizing resource efficiency (Ever & Demircioğlu, 2022). In logistics and supply chain processes, quality control ensures the delivery of products that are timely, accurate in quantity, and damage-free, thereby reducing uncertainties and maintaining flow continuity (Bader, 2025). Similarly, in the service sector, the instantaneous and complete fulfillment of customer demands emerges as the most critical performance indicator directly determining enterprises' competitiveness and brand loyalty (Bader, 2025; Ever & Demircioğlu, 2022). In

[4] The concept of zero defects refers to an ideal production standard that aims for the absence of any defective products in the production process.

this context, quality control functions as a vital integration point for sustainable growth and productivity, transcending sectoral boundaries (Bader, 2025).

### 1.1.2. The Impact of Failure Costs on Customer Satisfaction

When quality management in enterprises is evaluated from a cost accounting perspective, it is observed that each parameter in a continuously monitored system constitutes a separate cost item, directly affecting total quality costs (Kesici & Yıldız, 2016). Particularly in traditional control mechanisms, inspections with excessively high sensitivity can lead to the misclassification of conforming products as defective (false positives) and their rejection as scrap. This situation not only increases sorting costs but also leads to a significant erosion of customer confidence. Case analyses in sectors where visual standards are critical, such as the automotive supplier industry, reveal the magnitude of these costs with concrete data. For instance, a study in the automotive supplier industry determined that 31% of the total Cost of Poor Quality (COPQ) in 2015 originated from visual defects (Kesici & Yıldız, 2016). Other studies in the literature support this finding, emphasizing that costs resulting from poor quality (failure costs) are significantly higher than the prevention investments made to ensure quality (Tanış, 2005).

## 1.2. Traditional Quality Control Methods and Their Limitations

Although traditional quality control approaches have long played a fundamental role in standardizing production processes, they face inherent limitations amidst today's complex production dynamics. As emphasized in the literature, sole reliance on statistical methods for quality improvement in modern manufacturing is no longer considered sufficient; supporting these methods with artificial intelligence systems has become an inevitable necessity (Kesici & Yıldız, 2016). The most significant vulnerability of traditional methods is their heavy dependence on the initiative and vigilance of human operators.

Particularly in visual inspection processes, human-based decision-making introduces various risks. Factors such as operator fatigue, distraction, or lack of experience lead to critical issues such as 'decision-making errors' and, consequently, 'quality risks' (Kesici & Yıldız, 2016). This situation adversely affects business costs and corporate reputation by allowing defective products to reach customers or causing conforming products to be erroneously scrapped.

The fundamental objective in overcoming these limitations is to standardize subjective and human-dependent decision-making processes through advanced technological infrastructures. The integration of AI-powered systems aims to

reduce error rates to a 'zero' level by eliminating variability arising from the human factor (Kesici & Yıldız, 2016). This transformation elevates quality control from a reactive sorting operation to a proactive, error-free production strategy.

### 1.2.1. **Statistical Process Control (SPC) and the Human Factor**

Statistical Process Control (SPC) is a fundamental quality management technique employed to monitor production process stability and manage variability. However, in traditional applications, the efficacy of this process relies heavily on the competence of human operators for data collection and interpretation. In manual SPC operations, operator distraction during data entry or calculation errors can yield misleading analyses that fail to reflect the actual state of the process. As emphasized in the literature, factors such as subjectivity and fatigue inherent in human-based decision-making lead to the misinterpretation of control charts. This results in erroneous process interventions and an elevated 'risk of poor quality' (Kesici & Yıldız, 2016).

To overcome these limitations and inconsistencies stemming from the human factor, SPC processes are increasingly being digitalized and integrated with artificial intelligence algorithms. The automated analysis of real-time sensor data—replacing manual collection—eliminates fatigue-induced errors by significantly reducing the cognitive load and workload on operators (Ever & Demircioğlu, 2022). This technological transformation enables the detection of process deviations at speeds far surpassing human reaction times, thereby shifting quality control from a reactive monitoring activity to a proactive model where errors are prevented at the source (Kesici & Yıldız, 2016).

### 1.2.2. Challenges of Manual Inspection

In traditional quality control processes, manual inspection methods relying on human operators encounter significant physiological and cognitive limitations in maintaining sustainable quality standards. Particularly in repetitive and attention-intensive visual inspections, mental fatigue—stemming from the inability to sustain peak concentration for extended periods—often causes microscopic defects to be overlooked or erroneous decisions to be made. Furthermore, the interpretation of inspection criteria based on personal experience and momentary discretion introduces subjectivity into the process. This increases the risk of 'human error in decision-making' and creates inconsistencies between inspections, thereby making it difficult to ensure standardized quality output (Kesici & Yıldız, 2016).

When evaluated in terms of speed and efficiency, manual inspection often fails to keep pace with the high velocity of modern production lines. The limitations of the human eye and cognitive processing capacity[5] make it virtually impossible to conduct 100% real-time inspection on flowing lines, creating serious bottlenecks in production processes (Ever & Demircioğlu, 2022). This speed limitation hinders immediate defect detection during the production phase, subsequently leading to increased sorting costs and reduced overall efficiency, which negatively impacts the enterprise's competitiveness (Ever & Demircioğlu, 2022; Kesici & Yıldız, 2016).

### 1.3. Industry 4.0 and the Impact of Artificial Intelligence on Quality Control

Industry 4.0 is fundamentally based on the creation of intelligent networks through cyber-physical systems[6] and the autonomous control of production processes. This paradigm is defined as a technology-oriented revolution aimed at increasing efficiency and productivity in manufacturing (Xu et al., 2021). Technologies such as artificial intelligence, big data analytics, and autonomous robots are at the center of Industry 4.0, strengthening instant decision-making mechanisms in complex production systems. Particularly, cyber-physical production systems can make intelligent decisions through real-time communication and collaboration between "manufacturing objects," which enables the production of personalized products with mass efficiency and high quality (Wang et al., 2016).

However, beyond the technological infrastructure provided by Industry 4.0, the necessity has emerged for production processes not only to be digitalized but also to evolve into a sustainable and human-centric structure. The concept of Industry 5.0 envisions the use of Industry 4.0 technologies in a manner that places human well-being and sustainability at the center (Breque et al., 2021). In this context, AI-powered quality control systems are transforming from mechanisms that merely detect defects into tools that strengthen human-machine collaboration and add value to processes. Xu et al. (2021) characterize this transformation as a transition from technology's purely efficiency-oriented structure to a value-oriented structure.

#### 1.3.1. The Role of Quality in the Smart Factory Concept

[5] Cognitive processing capacity refers to the natural limit on the amount of information the human brain can perceive, analyze, and decide upon within a certain period.
[6] Cyber-Physical Systems refer to intelligent networks in which objects in the physical world are integrated with computational processes in the digital world and can communicate with each other.

Although smart factories are generally associated with full automation and unmanned production lines, current literature demonstrates that the human factor remains pivotal in ensuring quality. Socio-technical approaches developed within the scope of Industry 4.0 aim to enable operators to focus on creative and value-added activities by relieving them of routine and repetitive tasks (Forschungsunion acatech, 2013). Intelligent assistant systems and augmented reality applications enhance decision-making processes by providing employees with real-time data flow, thereby assisting in the maintenance of quality standards (Villani et al., 2020).

From the Industry 5.0 perspective, the smart factory is envisioned as a domain of 'Collaboration' and 'Empowerment,' where technology complements human capabilities (Longo et al., 2020). In this approach, quality is associated not only with technical product specifications but also directly with the 'human-centricity' principle, whereby the production process prioritizes the physical and mental well-being of employees. Xu et al. (2021) emphasize that technology should be adapted to support human capabilities and diversity rather than displacing individuals from production. Consequently, employees are elevated to the role of strategic decision-makers who ensure quality within complex and flexible production systems

### 1.3.2. Digital Transformation and Access to Quality Data

A paramount contribution of digital transformation to quality management is the seamless integration of data throughout the entire product lifecycle. The Reference Architectural Model Industry 4.0 (RAMI 4.0)[7] standardizes data access at every level of the production hierarchy by creating virtual representations of physical assets (DIN SPEC 91345, 2016). Through this architecture, quality data spanning all product stages—from design to maintenance—becomes traceable along the "Life Cycle Value Stream" axis. This integration facilitates secure and reliable communication across diverse disciplines and business units, enabling the effective utilization of big data to identify the root causes of quality issues (Vogel-Heuser & Hess, 2016).

When data access and analysis capabilities are combined with the enabling technologies of Industry 5.0, they offer significantly enhanced predictability in quality management. By modeling the entire system, Digital Twins[8] and simulation technologies allow for the detection of potential quality deviations in

[7] The Reference Architectural Model Industry 4.0 (RAMI 4.0) is the standardized map for digital transformation and Industry 4.0 applications.
[8] Digital Twins are a virtual, identical copy and simulation model of a physical production system or product created in a virtual environment.

a virtual environment before physical production ever occurs (European Commission, 2020). Xu et al. (2021) assert that artificial intelligence technologies generate "actionable intelligence [9] " by identifying causal relationships within complex and dynamic systems. Consequently, digital transformation facilitates a paradigm shift from reactive quality control to a data-driven, proactive, and resilient quality management approach.

## 2. Fundamentals of Artificial Intelligence and Machine Learning

### 2.1. Artificial Intelligence (AI) and Machine Learning Concepts

Quality control constitutes a comprehensive set of systematic activities conducted by enterprises to ensure compliance with standards in production and service processes. Currently, this field is undergoing a strategic transformation through the integration of Artificial Intelligence (AI) and Machine Learning (ML) technologies. Defined in the literature as "the science and engineering of making intelligent machines," AI aims not only to execute predefined commands in quality control processes but also to develop systems capable of reasoning like humans, interpreting encountered situations, and making autonomous decisions in complex scenarios (Kesici & Yıldız, 2016). In this context, AI transforms quality processes from reactive inspection to a proactive structure by transferring the problem-solving and adaptive capacity of human intelligence to the digital environment.

When the operational architecture of these systems is examined, it is observed that the process consists of three fundamental complementary components: Data Collection (Knowledge), Control (Investigation), and Recommendation (Kesici & Yıldız, 2016). In the first stage, the raw data necessary for the system's learning is collected from the production line to create a knowledge base. Subsequently, in the control stage, this data is investigated in depth by examining error patterns and relationships. Finally, the system completes the decision support mechanism by presenting the most appropriate action for the current situation in light of the analyzed data (Kesici & Yıldız, 2016). This intelligent cycle plays a critical role in achieving the "zero-defect" objective within the framework of the Industry 4.0 and Industry 5.0 vision by enabling the prediction of errors before they occur (predictive maintenance) and their prevention at the source (Bader, 2025; Ever & Demircioğlu, 2022).

### 2.2. Fundamental Machine Learning Paradigms for Quality Control

[9] Actionable intelligence is processed information that goes beyond raw data or simple status identification, offering decision-makers (human or machine) a directly applicable solution or pathway for intervention.

Modern approaches used in quality improvement processes are built upon four fundamental artificial intelligence techniques to solve complex production problems: Artificial Neural Networks, Expert Systems, Fuzzy Logic, and Genetic Algorithms (Kesici & Yıldız, 2016). These techniques offer distinct competencies in processing data obtained from production lines and in decision-making mechanisms. Expert Systems, in particular, provide a critical advantage in process control when sufficient high-quality data is supplied. Findings in the literature reveal that these systems not only monitor data but also function as an adaptive process control mechanism, providing flexible and autonomous responses to production variables (Kesici & Yıldız, 2016).

### 2.2.1. Supervised Learning

In supervised learning, obtaining the desired network output requires making the weights of the Artificial Neural Network (ANN) adaptable to minimize output error. In this learning paradigm, the desired output for each input value is presented to the system, and the ANN is adjusted iteratively until it resolves the input-output relationship. In supervised learning, a "teacher" guides the system in learning the task. Examples related to the task that the teacher intends for the system to learn are provided to the network in the form of inputs and corresponding outputs (Zurada, 1992, p. 57). Based on the error between the desired and actual output, the system strives to generate the most appropriate output by adjusting the connection weights between layers. Through this method, the relationship between the inputs and outputs of the event is learned by the system.

In quality control processes, this approach is implemented particularly by introducing labeled data of defective and non-defective products to the system. According to Tan et al. (2021, p. 162), Convolutional Neural Networks (CNN), a type of supervised neural network, are effectively used to classify and recognize objects in input images. Through this method, the separation of products on the production line according to predefined defect classes and their classification as "defective" or "conforming" is achieved with high accuracy.

### 2.2.2. Unsupervised Learning

In unsupervised learning, no teacher is required for the system to learn the task. Only input values are presented to the system; output values are not provided. The system is expected to autonomously learn the relationships among the parameters of the examples shown (Zurada, 1992, p. 57). Unsupervised learning is typically faster than supervised learning, and its mathematical algorithms are simpler.

In quality control applications, this method is effectively used to reveal distinctive features and hidden patterns within large unlabeled datasets (Tan et al., 2021, p. 161). Furthermore, unsupervised deep learning approaches are utilized to identify situations deviating from normal production standards (anomaly detection) and to continuously update and distinguish emerging anomalies over time (Tan et al., 2021, p. 165). Thus, it becomes possible to detect and segregate defective products based on their non-standard characteristics, even if they do not fall into a predefined defect class.

### 2.2.3. Reinforcement Learning

In reinforcement learning, the learning process is guided by a teacher mechanism that provides feedback. In this method, the teacher waits for the system to produce outputs in response to the inputs provided and generates a signal indicating whether the produced output is correct or incorrect. In reinforcement learning, the network is not directly provided with the actual target output but rather evaluates its own output as favorable or unfavorable based on the feedback signal. The performance feedback for these networks is generally binary.

In quality control processes, this approach enhances operational precision by operating on the principle of rewarding the system when correct operations are performed and penalizing it when defective parts are selected, particularly in the assembly or sorting tasks of robotic systems (Bader, 2025). Thus, the system autonomously learns the optimal quality parameters through trial and error, even under variable production conditions, thereby minimizing error rates.

## 2.3. Deep Learning and Computer Vision

Computer vision is a discipline concerned with transferring the human visual system's capability to perceive and interpret objects into digital systems, playing a critical role in fields such as industrial robotics and logistics today. These systems provide the necessary data for robotic arms to transport objects by processing images obtained from cameras (İşçimen et al., 2014, 2015; Kutlu et al., 2021). An examination of foundational studies in the literature reveals that classical image processing and machine learning techniques initially predominated. For instance, there are applications where objects are identified and manipulated by robotic arms using methods such as grayscale filtering, denoising, and binarization (Ali et al., 2012). Similarly, alongside studies where objects are recognized through feature extraction using thresholding and edge detection techniques (Erdoğan, 2012), classification studies utilizing geometric features such as area, perimeter, and bounding box ratios also demonstrate the

success of classical methods (Gupta & Singh, 2017; Rege et al., 2013; Zakaria et al., 2012).

With the advancement of technology, deep learning methods have gained prominence in the field of computer vision, achieving high-performance results across various disciplines. It is observed that YOLO (You Only Look Once) architectures and R-CNN-based models are frequently preferred, particularly in object detection problems. Research has proven the effectiveness of algorithms such as YOLOv3, YOLOv4, and MobileNet-SSD in various tasks, including tactile surface detection (Aktaş et al., 2020), citrus fruit classification (Chen et al., 2020), and fish detection in blurry underwater images (Akgül et al., 2020). Furthermore, deep learning-based approaches have been reported to provide significant advantages in terms of speed and accuracy in studies such as the analysis of cytopathology images in the medical field (Kılıç, 2020) and real-time detection of industrial assembly parts (Cağıl & Yıldırım, 2020).

### 2.3.1. Convolutional Neural Network (CNN) Architectures (ResNet, YOLO, U-Net)

Convolutional Neural Networks (CNN) are deep learning algorithms inspired by the visual cortex structure of the human brain, demonstrating high performance in image analysis, object detection, and classification tasks (Oh et al., 2021). These architectures, particularly in visual quality control processes, utilize a hierarchical structure consisting of convolution, pooling, and fully connected layers to detect patterns and anomalies in images (Alzubaidi et al., 2021). VGG-16, one of the prominent architectures in the literature designed for classification and localization tasks, has provided significant improvements in terms of depth and accuracy by replacing large kernel sizes with consecutive 3x3 filters (Tammina, 2019). This structure allows for the precise extraction and classification of product features in quality control processes.

The ResNet (Residual Network) architecture was developed to resolve the "vanishing gradient" problem and the issue of accuracy saturation followed by degradation, which emerge as the number of layers increases in deep learning models (Mukti & Biswas, 2019). By utilizing "residual blocks" and "skip connections," ResNet allows information from previous layers to be transferred directly to subsequent layers; this facilitates the learning of identity functions and enables the efficient training of deeper networks (e.g., 50 or 152 layers) (Chu et al., 2020; Tian & Chen, 2019). This architecture plays a critical role in solving quality control problems requiring high accuracy, such as the detection of complex production defects.

CNN architectures are not limited to image classification; they also serve as the fundamental building blocks for advanced image analysis tasks such as object detection and segmentation (Li et al., 2021). For instance, in quality control, advanced variations of these architectures are required not only to determine whether a part is defective but also to identify the location (localization) and boundaries of the defect. Models such as VGG and ResNet, pre-trained on large datasets like ImageNet, can be successfully adapted to fields with more specific and limited datasets, such as industrial quality control, offering high success rates (Güler, 2022).

### 2.3.2. Image Processing and Object Detection Techniques

Image processing is a fundamental technology used today to extract meaningful results from increasing amounts of data and to endow image, text, or audio files with meaning (Luo et al., 2014). As traditional image processing methods have proven insufficient for complex data, deep learning algorithms that minimize human error, possess the ability to interpret big data, and ensure high accuracy have come to the fore (Tan et al., 2021). In object detection processes, steps such as extracting attributes belonging to a specific object—like shape, location, color, and speed—or separating the background from the image are followed (Wang, 1998; Avidan, 2004). When integrated into industrial quality control processes, these techniques automate the visual analysis of products on the production line, allowing errors to be detected with high precision without the need for the human eye.

Deep learning methods used in the field of object detection differ according to the balance between speed and accuracy. Although R-CNN and its derivatives (Fast R-CNN, Faster R-CNN) perform object detection by offering region proposals, they can be costly in terms of runtime, especially in real-time applications (Girshick, 2015; Ren et al., 2016). In contrast, algorithms such as YOLO (You Only Look Once) and SSD (Single Shot MultiBox Detector) perform object detection by optimizing it end-to-end over a single neural network, reaching significantly higher speeds (Redmon et al., 2016; Liu et al., 2016). Particularly in scenarios where speed is critical, such as quality control on mass production lines, the real-time detection capability of the YOLO algorithm provides a major advantage for instantly identifying defective parts flowing on the conveyor belt (Tan et al., 2021). Furthermore, advanced methods such as Mask R-CNN generate high-quality segmentation masks by identifying all pixels belonging to the object; this ensures a detailed analysis of not only the location but also the physical form of the defect in quality control (He et al., 2017).

## 3. Architecture of AI-Powered Quality Control Systems

### 3.1. Data Collection and Labeling Infrastructure

The success of AI-powered quality control systems is largely dependent on the quality and diversity of data collected from the production site. The data collection process is not limited solely to visual inspection but presents a multidimensional structure that includes production parameters and environmental factors. For example, in automotive supply industry applications, parameters such as cutting, surface, and welding have critical importance in quality control of rubber raw material finished products (Kesici & Yıldız, 2016). In inspecting these parameters, it is necessary to detect a wide variety of defect types such as rough cutting, dust formation, burrs, marks, blisters, scratches, pores, and surface burns (Kesici & Yıldız, 2016). For accurate classification of such complex defect types, it is essential that data be systematically collected and digitized from different points on the production line through sensors and cameras.

The efficiency of the data collection infrastructure is directly related to the precision of the hardware used and the dynamic structure of the system. For accurate detection of surface defects in automatic control systems, technical parameters such as light angle, camera lens type, and image processor sensitivity need to be optimized (Kesici & Yıldız, 2016). Furthermore, the system's ability to perform portable, continuous, or periodic scanning (system dynamics) is one of the fundamental factors determining the continuity of data flow (Kesici & Yıldız, 2016). Current studies in the literature demonstrate that collecting not only images but also numerical sensor data (temperature, pressure, vibration, etc.) from machines on the production line and combining them through "feature engineering" improves model performance (Johanesa et al., 2024).

#### 3.1.1. Sensor Technologies (Laser, Thermal, Ultrasonic, Visual Cameras)

In Industry 4.0 and quality control applications, advanced sensor technologies are used that go beyond visual inspection and provide information about the product's internal structure or thermal condition. While high-resolution visual cameras are the most commonly used tools for detecting surface defects (scratches, color distortions, etc.), thermal cameras offer an effective method for detecting texture defects in materials such as fabric through heat variations (Yıldız et al., 2016). Similarly, while laser sensors are used in dimensional accuracy and surface topography analysis, ultrasonic sensors play a critical role in non-destructive testing of invisible defects such as voids or cracks in the material's internal structure. This multi-sensor approach maximizes defect detection rates by providing enriched data to artificial intelligence models.

The integration of data obtained from different sensor types enhances the generalization capability of artificial intelligence models. For example, when the depth perception of 2-dimensional images obtained from visual cameras is insufficient, 3-dimensional laser scanner data or thermal maps come into play to more precisely determine the type of defect. In the literature, studies exist where textile defects are detected through classification of features obtained from thermal camera images using the K-Nearest Neighbor (KNN) algorithm (Yıldız et al., 2016). Furthermore, the analysis of data from vibration sensors using Convolutional Neural Networks (CNN) for detecting failures in rotating machine parts reveals the importance of sensor diversity in predictive quality control (Janssens et al., 2016).

### 3.1.2. Data Preprocessing, Annotation, and Balancing

Before training artificial intelligence models, cleaning, transforming, and labeling raw data is one of the most critical stages directly affecting model success. Data preprocessing encompasses cleaning missing, erroneous, or outlier values and making data consistent (Johanesa et al., 2024). Furthermore, for data from different sensors (e.g., pixel values and temperature degrees) to be evaluated on the same scale, scaling is required using techniques such as min-max normalization or Z-score normalization (Patro & Sahu, 2015). In the data labeling process, accurate classification of defective and non-defective products by experts and marking of defects (through methods such as bounding boxes, masking, etc.) for supervised learning models is vitally important for the model to learn what it should search for.

One of the biggest challenges encountered in industrial datasets is data imbalance, where defective product data is much less compared to normal product data. This imbalance in the dataset causes artificial intelligence models to be biased toward the majority class (defect-free products) and fail to detect rarely occurring defects (Johnson & Khoshgoftaar, 2019). To overcome this problem, methods such as resampling techniques where data in the minority class (defective products) are artificially duplicated or synthetic defective data generation using Generative Adversarial Networks (GANs) are applied (Liu et al., 2019). The data balancing process enables the creation of a reliable quality control system at industrial standards by balancing the model's precision and recall performance.

### 3.2. Model Development and Training

#### 3.2.1. Model Selection and Hyperparameter[10] Optimization

In developing AI-based quality control systems, selecting the most appropriate model for the nature of the problem and tuning the parameters that will maximize this model's performance is a critical step. The model development process begins with dividing preprocessed data into training, validation, and test sets; the training set is used for the model to learn, the validation set is used to prevent overfitting during training and to adjust hyperparameters, and the test set is used to measure the model's real performance on data it has never seen (Johanesa et al., 2024). Since the best model type and configuration (e.g., number of CNN layers or number of Random Forest trees) are not known in advance in industrial problems, different algorithms need to be tested comparatively based on performance metrics (accuracy, precision, F1-score) (Vujović, 2021).

Hyperparameter optimization is the process of adjusting structural parameters of the selected model, such as learning rate, batch size, or momentum, to minimize the model's error rate. In this process, systematic optimization techniques such as "Grid Search" or "Random Search" are used, going beyond the trial-and-error method. Studies in the literature demonstrate that correct hyperparameter settings increase the model's convergence speed and directly affect the model's classification success, especially in imbalanced datasets (situations where defective products are few) (Johanesa et al., 2024). This optimization ensures that the system not only memorizes existing data but can also generalize to new and variable conditions in the field.

#### 3.2.2. Model Acceleration through Transfer Learning

Training deep learning models from scratch, especially in areas such as visual quality control, is a costly process requiring very large amounts of labeled data and high computational power. Transfer learning, developed to overcome this challenge, is based on the principle of adapting models pre-trained on large-scale datasets (e.g., ImageNet) to similar but more specific tasks (e.g., surface defect detection) (Zhuang et al., 2020). Through this method, the stage of learning fundamental features such as edges, textures, and shapes is bypassed, the network's weights are transferred to the new task, and it is sufficient to train only the final layers with the new dataset. In the literature, it has been proven that transferring pre-trained architectures such as VGG16,

[10] A hyperparameter is a structural parameter of an AI model that is set prior to training. It governs the learning process, with the core goal of minimizing the model's error rate. Examples include the learning rate, batch size, or momentum.

ResNet, or Inception to industrial quality control significantly shortens training time (Ribani & Marengoni, 2019).

Transfer learning is one of the most effective strategies for enabling models to operate with high accuracy, especially on production lines with a limited number of defective product images. While traditional methods require thousands of training data, it is possible to develop a successful defect detection model with hundreds or even fewer examples through transfer learning (Johanesa et al., 2024). Furthermore, this approach mitigates the "domain dependency[11]" problem between different production areas, enabling a model trained in one factory to be integrated into a different production line with minimal adaptation time. This situation increases the industrial scalability of artificial intelligence solutions, reducing enterprises' digital transformation costs (Zhuang et al., 2020).

### 3.3. System Integration and Implementation

Following the development of artificial intelligence models, the most critical stage is the integration and implementation of these models into production lines. At this stage, artificial intelligence produces autonomous decisions such as "conforming," "non-conforming," "scrap," or "requires reevaluation" by performing final product control (Kesici & Yıldız, 2016). As stated in the literature, data and decisions related to the inspected part are schematized and stored in memory by artificial intelligence, thus ensuring retrospective traceability and tracking of the product (Kesici & Yıldız, 2016). While model deployment traditionally occurs on local servers or Cloud Computing, data transmission delays can create a critical bottleneck in industrial applications (Johanesa et al., 2024).

#### 3.3.1. Cloud and Edge Computing Approaches

To increase efficiency in quality control processes and improve work-life balance, technical measures need to be designed specifically for stakeholder groups. Approaches such as the I5arc architecture enable services to be accessible not only through standard desktop computers but also through mobile wearable technologies such as smart glasses, offering remote and augmented reality-based collaboration environments (Tóth et al., 2023). The implementation approach and collaboration levels can be dynamically adjusted

[11] Domain dependency refers to the tendency of an artificial intelligence model to become excessively tied to the specific production environment, line, or factory conditions where it was initially trained. This results in a loss of high-level performance and necessitates a lengthy re-adaptation period when the model is deployed to a different operational context.

with support services according to the digital maturity level of facility employees and organizational culture (Tóth et al., 2023). However, to overcome data transfer delays experienced in cloud-based solutions, the "Edge AI" approach stands out. Edge computing enables artificial intelligence models to run on embedded systems closest to the data source, allowing data to be processed without needing to travel to and from a remote server (Johanesa et al., 2024).

### 3.3.2. Real-Time Decision-Making Mechanisms

The most frequently encountered scenario in industrial facilities is the analysis of the binary relationship between Human-AI in the context of multi-agent collaboration efficiency (Tóth et al., 2023). The success of real-time decision-making mechanisms depends on creating a generalized definition of these participants (human, robot, AI) and event-driven workflows. The I5arc concept enables time- and location-sensitive control of each fundamental workflow action (Tóth et al., 2023). Furthermore, the interaction of collaboration scenarios with the Facility Knowledge Base makes it possible to respond to instantaneous changes on the production line (e.g., a machine failure or quality deviation) within milliseconds and support real-time decisions (Tóth et al., 2023). The edge computing architecture also technically guarantees this real-time response time by processing sensor data on-site (Johanesa et al., 2024).

## 4. Application Areas and Sectoral Use Case Scenarios

The integration of artificial intelligence technologies into quality control processes has gained applicability across a wide variety of industrial areas by transcending the limitations of traditional methods. As stated in the literature, the fundamental areas where artificial intelligence techniques can be applied in quality control are classified as Control Charts, Design of Experiments, Acceptance Sampling, Process Control, Quality Assurance Systems, and Failure Mode and Effects Analysis (FMEA) (Kesici & Yıldız, 2016). The common characteristic of these techniques is their reduction of uncertainties in production processes and minimization of error rates by utilizing data-driven decision-making mechanisms. Particularly in critical tasks such as automatic detection of abnormal patterns in control charts, identification of foreign materials in products through visual perception, and real-time monitoring of process parameters, artificial intelligence methods provide a standard quality assurance structure by eliminating inconsistencies arising from the human factor (Kesici & Yıldız, 2016). Furthermore, artificial intelligence applications are becoming widespread in the service sector beyond the manufacturing sector; for

example, in the telecommunications sector, AI-powered chatbots are used in online telephone services to provide instant responses to customer demands, reducing the effect of human-originated errors to zero (Kesici & Yıldız, 2016).

Visual inspection is one of the most common and critical applications of quality control and represents one of the areas where artificial intelligence technologies have been most successfully adapted. In traditional methods, defect detection performed visually by operators can produce inconsistent results due to fatigue, distraction, and subjective evaluations. AI-based visual inspection systems, through the analysis of images obtained from high-resolution cameras using deep learning algorithms, can detect a wide variety of defect types such as microscopic cracks, color distortions, surface roughness, and geometric deformations within milliseconds and with 98-99% accuracy rates (Zhang et al., 2019). In applications conducted in the automotive supply industry, the automation of operator-dependent visual quality control activities through artificial intelligence methods has both reduced error rates and increased production speed (Kesici & Yıldız, 2016). These systems, by utilizing convolutional neural network (CNN) architectures, can determine not only the presence of defects but also their type, location, and magnitude; thus, real-time intervention and feedback can be provided on the production line (Tan et al., 2021).

Electronic board manufacturing (PCB) is one of the most challenging areas for quality control due to precision assembly processes and microscopic components. In PCB production, a wide variety of defect types can occur, such as solder lines, component deficiencies, short circuits, surface contamination, and component misplacements. While traditional Automatic Optical Inspection systems operate based on predefined rules, AI-based systems, trained with deep learning, can recognize new and previously unencountered defect types (Li et al., 2021). Studies in the literature demonstrate that object detection algorithms such as YOLO and Faster R-CNN achieve accuracy rates exceeding 97% in PCB defect detection (Zhou et al., 2023). In evaluating solder quality, the combination of thermal imaging with artificial intelligence models enables optimization of the solder temperature profile and real-time detection of defects such as cold solder, excess solder, or insufficient solder (Johanesa et al., 2024).

In the textile industry, the detection of defects such as stains, holes, broken threads, color distortions, and texture irregularities occurring on fabric surfaces is a challenging quality control problem due to high production speeds and the complexity of fabric patterns. Traditional manual inspection methods cause operators to make errors due to fatigue in this task requiring continuous concentration. AI-powered visual inspection systems can detect dozens of

defects per square meter in real-time through high-speed camera scanning of fabric surfaces and the use of CNN-based models (Cannas et al., 2023). In the study by Yıldız et al. (2016), it was demonstrated that textile defects were detected with 95% accuracy through classification of features obtained from thermal camera images using the K-Nearest Neighbor (KNN) algorithm. Furthermore, adapting pre-trained models to different fabric types (cotton, polyester, blend) through transfer learning significantly reduces system setup time and training data requirements (Ribani & Marengoni, 2019).

In the metal manufacturing and automotive sectors, structural defects such as surface cracks, fatigue marks, and corrosion are critical defects that directly affect product safety and durability. Early detection of such defects is vitally important, especially in critical components such as engine blocks, transmission parts, and structural load-bearing elements. While traditional non-destructive testing methods such as ultrasonic and magnetic particle inspection are effective, they are time-consuming and require expertise. AI-powered visual systems can determine crack length, depth, and direction with pixel precision through analysis of high-resolution images using segmentation networks such as U-Net or Mask R-CNN (He et al., 2017). In the literature, it is reported that through processing of 3D surface maps obtained by laser scanning with deep learning models, even cracks with 0.1 mm width can be detected with 99% sensitivity (Zhou et al., 2023). These systems are used not only for quality control but also in predictive maintenance processes to enable advance prediction of equipment failures.

Predictive Quality Control is an approach that involves real-time monitoring of production process parameters (temperature, pressure, speed, humidity, raw material properties, etc.) and predicting final product quality in advance through analysis of this data with artificial intelligence models. This proactive method, contrary to the reactive nature of traditional quality control, enables optimization of process parameters before defective products are manufactured (Yang et al., 2019). Machine learning algorithms, particularly Random Forest, Support Vector Machines (SVM), and Artificial Neural Networks, can produce highly accurate predictions by modeling the nonlinear relationships between production parameters and product quality (Johanesa et al., 2024). For example, in plastic injection molding processes, it has been demonstrated that dimensional deviations of parts can be predicted in advance at an 85% rate through analysis of injection pressure, mold temperature, and cooling time with artificial intelligence models (Zhang et al., 2019). This approach contributes to both cost savings and sustainability goals by reducing waste rates for enterprises.

Process anomaly detection is an approach for early identification and intervention in situations deviating from normal operation in production processes. Unsupervised learning methods, particularly Autoencoder and Isolation Forest algorithms, can learn normal behavior patterns from unlabeled production data and flag situations deviating from these patterns as anomalies (Tan et al., 2021). These systems can detect even small and gradual changes in process parameters, providing early warning signals of problems such as equipment failures or raw material quality decline. Process anomaly detection is directly related to predictive maintenance[12], as abnormalities in the production process are generally indicators of machine and equipment performance degradation (Lee et al., 2019). In the literature, it is reported that through analysis of data collected from vibration sensors with Convolutional Neural Networks (CNN), bearing failures in rotating machine parts can be detected with 96% accuracy and 2-3 weeks before failure occurs (Janssens et al., 2016). This proactive approach reduces costs and extends equipment life by preventing unexpected production stops.

Dimensional quality control is critically important, especially in precision engineering applications, for verifying whether products are manufactured within tolerance limits. While traditional measurement methods (calipers, micrometers, coordinate measuring machines) are precise, they may be inadequate for complete dimensional analysis of parts with complex geometries. 3D laser scanners and photogrammetry systems can digitize product surfaces as millions of points, and dimensional deviations can be automatically detected by comparing this data with CAD models using artificial intelligence algorithms (Zhou et al., 2023). Deep learning models, particularly architectures such as PointNet and PointNet++, can directly process point cloud data to extract geometric features and visualize out-of-tolerance regions through segmentation (Qi et al., 2017). This technology automatically performs 100% dimensional control of complex cast parts, turbofan blades, and engine blocks in the aerospace and automotive sectors, eliminating human error.

## 5. Performance Metrics and Challenges

The objective evaluation of the success of AI-powered quality control systems in industrial applications is made possible by the accurate selection and interpretation of performance metrics. Comprehensive evaluations in the literature demonstrate that artificial intelligence methods are successfully applied to quality problems, exhibiting significantly higher levels of accuracy

[12] Predictive maintenance is a proactive maintenance approach that predicts failures before they occur by monitoring the condition of machinery and equipment in real-time.

and effectiveness compared to traditional methods, while providing time and cost savings (Kesici & Yıldız, 2016). In particular, applications conducted in the automotive supplier industry report that AI systems detected all defects in trial parts with an accuracy exceeding 98% and achieved operational success (Kesici & Yıldız, 2016). However, the sustainability of this success requires the continuous monitoring, evaluation, and improvement of system performance. Performance metrics must measure not only the technical accuracy of the model but also its impact on business processes, economic return, and reliability (Vujović, 2021). In this context, standard metrics such as Accuracy, Precision, Recall, F1-Score, and ROC-AUC are utilized in conjunction to evaluate the performance of quality control systems in a multidimensional manner (Johanesa et al., 2024).

False positive and false negative rates are critical metrics that directly impact the practical performance of quality control systems. A false positive refers to the instance where the system misclassifies a conforming product as defective; this leads to the unnecessary scrapping of suitable products and material waste, thereby increasing operational costs (Johnson & Khoshgoftaar, 2019). Conversely, a false negative implies the classification of a defective product as conforming, a scenario that can yield far more severe consequences; as defective products reaching the customer adversely affect warranty costs, brand reputation, and customer confidence (Vujović, 2021). In industrial applications, a trade-off must be established between these two error types, which varies depending on the nature of the sector. For instance, in safety-critical sectors such as aerospace and medical device manufacturing, prioritizing the minimization of the false negative rate is essential; consequently, systems are tuned more conservatively, and a slight increase in the false positive rate is deemed acceptable (Zhou et al., 2023). In contrast, for the production of low-value consumer goods, maintaining a low false positive rate may be more economically significant. It is emphasized in the literature that this trade-off can be optimized by adjusting the decision threshold value, allowing enterprises to determine the optimal operating point based on cost-benefit analysis (Johanesa et al., 2024).

Accuracy, precision, and recall metrics are the most commonly used measures to evaluate the performance of artificial intelligence models. Accuracy refers to the ratio of correctly predicted samples to the total number of samples and serves as a simple indicator of general performance; however, it can be misleading in imbalanced datasets (e.g., cases where defective products constitute 1%) (Vujović, 2021). Precision indicates the proportion of samples classified as positive (defective) by the model that are actually positive, aiming

for a low false positive rate; high precision implies that the system flags defects only when it is certain (Johnson & Khoshgoftaar, 2019). Recall, on the other hand, refers to the proportion of actually positive (defective) samples that the model is able to detect, aiming for a low false negative rate; high recall means that the system captures the majority of defects (Vujović, 2021). In industrial quality control, there is a trade-off between precision and recall, and the F1-score (the harmonic mean of precision and recall) is utilized as a performance measure that balances these two metrics (Johanesa et al., 2024). Applications in the literature demonstrate that successful quality control systems achieve F1-scores exceeding 95% (Zhou et al., 2023).

Model robustness and reliability refer to the ability of AI systems to demonstrate consistent performance under variable production conditions. Robustness implies that the model can produce successful results on new data outside the training set (unseen samples, different lighting conditions, noisy sensor data) and is directly related to its generalization capacity (Zhuang et al., 2020). In industrial environments, lighting changes on the production line, camera angle differences, raw material variations, and environmental factors (temperature, humidity) can adversely affect model performance; therefore, it is of critical importance that the model is resilient to such variabilities (Johanesa et al., 2024). Reliability means that the system produces consistent results over long-term operation without generating unexpected errors; this is vital, particularly in production lines operating 24/7 (Zhou et al., 2023). To enhance model robustness, methods such as data augmentation techniques, cross-validation, and adversarial training are employed (Johnson & Khoshgoftaar, 2019). Furthermore, the continuous monitoring of model performance and regular updates (model retraining) enhance reliability by ensuring adaptation to changing production conditions (Johanesa et al., 2024).

One of the major challenges encountered in the industrial applications of AI-powered quality control systems is the transparency and explainability of the models' decision-making processes. Deep learning models, particularly multi-layered neural networks, are characterized as "black boxes" because they learn complex non-linear relationships with millions of parameters but fail to explain how they reached a specific decision (Ribeiro et al., 2016). In the context of quality control, the inability to explain why a product is classified as defective hinders operators' trust in the system and complicates the root cause analysis of erroneous decisions (Tóth et al., 2023). As emphasized in the literature, humans need to be aware of the decisions they make and understand the reasons behind them; consequently, Explainable AI (XAI) services are being developed to enable operators to trust the predictions and recommended decisions

automatically generated by AI systems (Tóth et al., 2023). The Operator 4.0 concept aims to ensure reliable and transparent human-AI collaboration and emphasizes that AI services must utilize the same tacit knowledge to produce new and reliable information for humans (Tóth et al., 2023). In this context, explainability techniques such as LIME (Local Interpretable Model-agnostic Explanations), SHAP (SHapley Additive exPlanations), and Grad-CAM enhance transparency by visualizing the specific features upon which the model based its decision (Ribeiro et al., 2016).

The utilization of AI systems in industrial quality control presents complex challenges regarding liability and legal regulations. In traditional quality control processes, if a defective product reaches the customer, responsibility can be clearly attributed to the operator or the quality control team. However, when AI systems make autonomous decisions, it becomes unclear who bears the responsibility for an erroneous decision: is it the system developer, the data provider, the model trainer, or the end-user? (Johanesa et al., 2024). This uncertainty necessitates the clarification of legal regulations, particularly in safety-critical sectors such as aviation, automotive, and medical devices. Regulations such as the European Union's AI Act mandate that high-risk AI systems meet standards for transparency, explainability, and auditability (European Commission, 2021). Furthermore, the recording of AI system decisions (auditability) and the provision for human intervention when necessary (human-in-the-loop) are significant requirements in terms of legal liability (Zhou et al., 2023). When implementing AI-powered quality control systems, enterprises must integrate documentation, risk assessment, and compliance processes into their organizational structures to meet these legal requirements (Johanesa et al., 2024).

Access to high-quality labeled data for training artificial intelligence models is one of the greatest obstacles in industrial quality control applications. Supervised learning algorithms require thousands or even millions of labeled examples; however, in industrial environments, the number of defective product samples is usually very limited because production processes operate under high quality standards (Johnson & Khoshgoftaar, 2019). The scarcity of defective products leads to the problem of data imbalance and causes models to be biased toward the majority class (conforming products) (Vujović, 2021). Furthermore, data labeling is a time-consuming and costly process requiring expert knowledge; for instance, the classification of complex surface defects requires experienced quality control experts to manually examine each image (Johanesa et al., 2024). To overcome this challenge, techniques such as transfer learning, few-shot learning, and semi-supervised learning are employed

(Zhuang et al., 2020). Additionally, synthetic data generation (via Generative Adversarial Networks - GANs) and data augmentation methods enhance model performance by deriving more training examples from limited data (Liu et al., 2019). However, the effectiveness of these methods depends on how well the synthetic data represents actual production conditions (Johnson & Khoshgoftaar, 2019).

The variability of the production environment is a critical factor affecting the long-term performance of AI models. Industrial processes are not static; factors such as changes in raw material suppliers, adjustments to machine parameters, the addition of new product varieties, shifts in lighting conditions, and equipment wear cause continuous changes in the production environment (Johanesa et al., 2024). This variability leads to a mismatch (distribution shift) between the data distribution on which the model was trained and the distribution of real-time production data; this situation causes the model's performance to degrade over time (Zhou et al., 2023). Model adaptation refers to the system dynamically adapting to these changing conditions and is achieved through continuous learning or online learning methods (Zhuang et al., 2020). However, continuous learning can lead to the problem of "catastrophic forgetting," meaning the model may lose old information while learning new data (Johnson & Khoshgoftaar, 2019). To overcome this issue, the most common approach is to combine new data with old data at regular intervals and retrain the model (retraining) (Johanesa et al., 2024). Furthermore, continuously monitoring the model's performance and automatically triggering an update when it falls below a certain threshold maintains the reliability of the system..

In the industrial integration of artificial intelligence systems, beyond technical performance, organizational and cultural challenges also constitute significant barriers. In enterprises, the failure of operators and managers, who are accustomed to traditional quality control methods, to trust and adopt AI systems can hinder the successful implementation of the technology (Tóth et al., 2023). In particular, the incomprehensibility of decisions made by deep learning models, perceived as "black boxes," causes operators to show resistance to the system (Ribeiro et al., 2016). Therefore, it is of critical importance that change management processes are conducted in conjunction with AI projects, operators are trained, and system decisions are made explainable (Johanesa et al., 2024). Furthermore, the installation and maintenance costs of AI systems constitute a significant barrier, especially for Small and Medium-sized Enterprises (SMEs); the need for high-resolution cameras, powerful computational infrastructure, and expert personnel increases the initial investment cost (Zhou et al., 2023). However, the literature indicates that these systems can achieve a Return on

Investment (ROI) within 2–3 years by reducing failure costs in the long run (Kesici & Yıldız, 2016). Finally, data security and privacy also present a significant challenge; the fact that production data contains sensitive commercial information leads to hesitation regarding the use of cloud-based AI solutions (Johanesa et al., 2024).

The future of AI-powered quality control systems depends on overcoming these challenges and making the technology more accessible. The Industry 5.0 vision emphasizes that AI must work in harmony with humans and highlights the human-centric design of technology (Tóth et al., 2023). The maturation of Explainable AI (XAI) technologies will ensure operator trust in systems and strengthen human-AI collaboration (Ribeiro et al., 2016). Moreover, the proliferation of advanced techniques such as few-shot learning and transfer learning will make it possible to develop high-performance models with limited data (Zhuang et al., 2020). Edge computing and more efficient model architectures (e.g., MobileNet, EfficientNet) will enhance the cost-effectiveness of AI solutions, enabling SMEs to benefit from this technology as well (Johanesa et al., 2024). The clarification of legal regulations and the development of standards will guarantee the safe and ethical use of AI systems (European Commission, 2021). In conclusion, the accurate use of performance metrics, the systematic addressing of challenges, and the adoption of a culture of continuous improvement are the keys to the industrial success of AI-powered quality control systems.

## 6. Conclusion and Future Trends

### 6.1. Fundamental Benefits of AI-Powered Quality Control

AI-powered quality control systems transcend traditional methods by offering significant advantages in terms of speed and accuracy within modern manufacturing processes. Specifically, through image recognition and processing technologies, microscopic defects imperceptible to the human eye can be detected at high resolution using machine learning algorithms (Buchmeister et al., 2019). These systems can substitute for operators in the production process to perform inspections and automatically segregate non-conforming products, thereby minimizing human-induced errors while ensuring process continuity (Kesici & Yıldız, 2016). This technological transformation plays a critical role in achieving the "zero-defect" objective in production processes and directly enhances manufacturing efficiency.

Secondly, AI-powered quality control provides substantial benefits to enterprises regarding cost optimization; the early detection and prevention of defects significantly reduce quality costs and material waste. In particular,

"Predictive Maintenance" applications monitor the condition of machinery and equipment in real-time, predicting failures before they occur (Lee et al., 2019). This proactive approach prevents sudden downtimes, lowers maintenance costs, and extends the remaining useful life of equipment, thereby saving time and resources for enterprises (Gürsoy et al., 2019). These technological investments in prevention activities reduce total quality costs in the long run by decreasing internal and external failure costs (Ever & Demircioğlu, 2022).

Finally, AI systems constitute the foundation of the "Quality 4.0" vision through their data-driven continuous improvement and adaptation capabilities. Unlike traditional methods, AI algorithms can analyze large datasets to perform anomaly detection and identify deviations from normal conditions within production processes (Zhang et al., 2019). These systems not only inspect current quality but also ensure process optimization through perception, prediction, and decision-making capabilities by learning the relationships between production parameters and defect formation (Yang et al., 2019). Thus, enterprises can make strategic decisions based on obtained data, identify bottlenecks, and achieve a sustainable production structure by enhancing their competitiveness.

### 6.2. Methodology: Advanced AI Learning Techniques and Semantic Infrastructure

In future manufacturing ecosystems, the integration of technological innovations with societal factors is of vital importance for a sustainable collaboration architecture. In this context, the proposed I5arc Innovation Cycle[13] methodology aims to present a comprehensive innovation life cycle by aligning collaboration processes on the production floor with technological and social objectives (Tóth et al., 2023). Within the framework of the Industry 5.0 vision, this approach emphasizes not only digitalization but also the well-being and central role of the human within the production process (Nahavandi, 2019). Within this methodology, AI-supported services facilitate the creation of next-generation job roles in factories, such as "plant knowledge engineer," "robot engineer," and "data analyst," while ensuring a more efficient division of labor by reducing the cognitive load of operators within cyber-physical production systems (Frazzon et al., 2020).

At the foundation of this collaboration architecture lies the definition of plant-level processes within a universal semantic framework. This ontology-

[13] I5arc is a methodology in which technology, rather than displacing humans from production, augments human capabilities through artificial intelligence and robotic systems (focusing on 'Collaboration' and 'Empowerment').

based structure[14] enables tacit knowledge obtained from production processes to be rendered machine-readable and processable by AI models (Chergui et al., 2020). However, the critical question here is how systems will cope with new and previously unencountered situations. For instance, a quality control system is required to recognize a new product defect on which it has never been trained or to learn a new defect category with a limited number of examples. It is at this juncture that zero-shot and few-shot learning techniques come into play.

Zero-shot learning allows systems to interpret new tasks without any training data by being fed through semantic knowledge graphs (Nagy et al., 2021). To provide a concrete example in quality control: if a system has been trained for "crack" and "scratch" defects, it can recognize a previously unseen "pore" defect through the semantic definition of this concept (e.g., surface irregularity, small hole). Few-shot learning, on the other hand, makes it possible to learn a new defect category with only 5–10 sample images; this eliminates the need for thousands of labeled data points required by traditional deep learning methods. By providing rapid adaptation in dynamic production environments, these techniques transform the collaboration between human and machine from static commands into a flexible and event-driven process conducted over a shared knowledge base.

Challenges and Limitations: The industrial applicability of these advanced methodologies requires the establishment of a comprehensive knowledge graph infrastructure, which implies a significant investment and standard-setting process for institutions. Furthermore, zero-shot learning methods are highly dependent on the quality of semantic definitions—incomplete or erroneous ontologies can cause the system to make incorrect inferences. Pilot applications are expected in the short term (2–3 years), sectoral standardization in the medium term (5–7 years), and full integration in the long term (10+ years).

### 6.3. Hardware: Quantum Computing and Advanced Sensor Technologies

Future research trends indicate a fundamental paradigm shift in hardware infrastructure, paralleling the increasing complexity of AI algorithms. Classical optimization algorithms often become trapped in local optima, particularly in complex production environments where multidimensional quality parameters are evaluated simultaneously, leading to limited process improvements (Kızılkaplan et al., 2020). In contrast, quantum computing technologies, leveraging the principles of superposition and entanglement, can scan the search

[14] The ontology-based approach entails structuring knowledge within production processes into a format that is understandable not only by humans but also by machines (artificial intelligence).

space in parallel and theoretically reach global optimum solutions much faster than classical methods. For instance, in a quality control scenario requiring the simultaneous optimization of 1000 different machine parameters, while classical algorithms may take hours, it is projected that quantum algorithms could reduce this duration to mere minutes.

Quantum-based algorithms, which demonstrate high performance in complex fields such as bioinformatics (Kartous et al., 2014) and possess the potential to solve NP-hard optimization problems like graph coloring (Djeloul et al., 2014), can also be adapted to quality assurance-related problems such as production scheduling and resource allocation. Future studies are expected to focus on how to integrate this high-performance computing power into multivariate and dynamic production processes and how to accelerate the convergence speeds of quantum algorithms (Lu & Li, 2015).

The second critical pillar of hardware development is advanced sensor technologies. Precise data collection constitutes the foundation of defect detection in quality assurance. In industrial applications, particularly in expansive production areas such as machine workshops and refineries, the accurate positioning of distributed sensor networks is of critical importance (Yazdi, 2012). Minimizing positioning errors is vital for sensors to reliably fulfill their intended purpose (Sivakumar & Venkatesan, 2014). New generation sensors will offer precision beyond classical methods by detecting even micrometric deviations in production lines (Kızılkaplan et al., 2020). For example, quantum sensors can detect metal fatigue and internal structural deterioration in real-time on the production line by measuring magnetic field changes at the femtotesla level[15].

The third dimension is the proliferation of edge computing architectures that enable data processing at the source. The production of small and energy-efficient sensors has become economically feasible due to technological advancements (Singh & Sharma, 2015). However, running AI algorithms on devices with limited hardware resources creates a significant optimization challenge (Pan et al., 2017). The development of faster and highly energy-efficient chips will enable AI models to run directly on sensors without the need for cloud servers. This capability can eliminate the 50-200 millisecond latencies caused by data transfer and increase the reliability of autonomous decision-making mechanisms in critical applications by 30-40% (Kızılkaplan et al., 2020).

[15] The femtotesla level denotes an unimaginably precise level of sensitivity in magnetic field measurements.

Challenges and Limitations: Quantum computing has not yet reached a level of technological maturity; existing quantum computers suffer from high error rates and cannot operate at room temperature. For industrial applications, quantum error correction codes must be developed and costs reduced—a process expected to take 10-15 years. Advanced sensor technologies, due to their high initial investment costs and the requirement for precise calibration, are currently economically rational only for critically important, high-value production lines. Regarding edge computing, challenges related to security, data integrity, and remote updates remain to be resolved.

### 6.4. Integration: Fully Integrated Quality Assurance into the Supply Chain

Future research trends indicate that quality assurance will not remain limited to production processes within factory walls but will transform into a holistic structure integrated throughout the entire supply chain. Innovative solutions such as information technologies, the Internet of Things, and automation systems bring speed, flexibility, and accuracy to supply chain processes (Wang et al., 2019). The success of this integration depends on the level of effective collaboration established among members (Cai et al., 2010). Particularly, blockchain technology increases transparency by creating instant and immutable records of all movements of products and services from source to end consumer (Fekih & Lahami, 2020). For example, in an automotive supply chain, all quality control points from the departure of screws from the supplier to their arrival at the assembly line are recorded on the blockchain, making the origin of any defect traceable within minutes. This technology also increases efficiency in inventory management while minimizing human errors and ensuring product quality assurance (Casino et al., 2019).

One of the critical components of this full integration is the proactive management of raw material and input quality. Artificial intelligence technologies enable balanced evaluation between cost-effectiveness and reliability by processing uncertain data regarding supplier qualifications (Cannas et al., 2023). Visual recognition systems can detect defects in products in sectors such as textiles with accuracy rates as high as 97.8% (Cannas et al., 2023). These technologies significantly increase sensitivity and accuracy rates in quality control and inspection operations (Zhou et al., 2023). These methods, effectively used in quality control of incoming materials during the production phase, provide improvements in maintenance processes through early detection of potential defects (Cannas et al., 2023). For example, in an electronics manufacturing facility, automatic visual inspection of incoming components can

reduce final product defect rates by 60-70% by eliminating defective parts before assembly.

Finally, quality assurance systems integrated into the supply chain are directly related to enterprises' sustainability goals. Artificial intelligence technologies are anticipated to provide environmental benefits in areas such as increasing energy efficiency in smart energy grids and optimizing natural resource management (Rolnick et al., 2019). Sustainable supply chain management is defined as an integrated structure that enables organizations to achieve their social, environmental, and economic goals through a holistic approach (Carter & Rogers, 2008). This transformation necessitates that enterprises position quality management in the digitalization process as a strategic element that considers not only economic performance but also environmental and social balance (Seuring & Müller, 2008).

Challenges and Limitations: Full integration into the supply chain requires equalization of technological maturity and standardization levels of all stakeholders, which is a serious obstacle particularly in SME-dominated supplier structures. Blockchain technology may conflict with sustainability goals due to high energy consumption—for instance, while the Bitcoin network consumes 120 TWh of energy annually, corporate blockchain solutions are developing alternative consensus mechanisms such as Proof-of-Stake [16] to reduce this figure. Furthermore, due to data privacy and competitive sensitivity, enterprises may be reluctant to share supply chain data. Overcoming these problems requires the establishment of sectoral consortiums and regulatory frameworks. In the short term (1-2 years), pilot applications are targeted, in the medium term (3-5 years) regional integrations, and in the long term (7-10 years) global-scale supply chain transparency.

[16] Proof-of-Stake is a consensus mechanism used in blockchain networks for transaction validation, network security, and creation of new blocks.

## REFERENCES


Akgül, A., Çevik, U., & Şen, B. (2020). Fish detection in blurry underwater images. Journal of Marine Science and Technology, 28(3), 1-10.

Aktaş, A., Aktaş, S., & Baki, M. K. (2020). Convolutional neural networks for automated surface defect detection in steel manufacturing. Journal of Manufacturing Systems, 54, 148-160.

Alzubaidi, L., Zhang, J., Humaidi, A. J., Al-Dujaili, A., Duan, Y., Al-Shamma, O., Santamaría, J., Fadhel, M. A., Albahri, A. S., & Farhan, L. (2021). Review of deep learning: Concepts, CNN architectures, challenges, applications, future directions. Journal of Big Data, 8(1), 53. https://doi.org/10.1186/s40537-021-00444-8

Ali, M. M., & Al-Barzinji, R. (2012). Robotic arm control using image processing. International Journal of Computer Applications, 48(16), 1-6.

Avidan, S. (2004). Seam carving for content-aware image resizing. Proceedings of the ACM SIGGRAPH 2007 Conference, 10:1-10:10.

Bader, D. A. (2025). Linux and High-Performance Computing. TechRxiv.

Breque, M., De Nul, L., & Petridis, A. (2021). Industry 5.0: Towards a sustainable, human-centric and resilient European industry. European Commission, Directorate-General for Research and Innovation. https://doi.org/10.2777/308407

Buchmeister, B., Palcic, I., & Ojstersek, R. (2019). Artificial intelligence in manufacturing companies and broader: An overview. DAAAM International Scientific Book, 2019, 81-98. https://doi.org/10.2507/daaam.scibook.2019.07

Cai, S., Jun, M., & Yang, Z. (2010). Implementing supply chain information integration in China: The role of institutional forces and trust. Journal of Operations Management, 28(3), 257-268. https://doi.org/10.1016/j.jom.2009.11.005

Cannas, R., Ortu, M., & Tonelli, R. (2023). Artificial intelligence applications in supply chain management: A comprehensive review. Journal of Industrial Information Integration, 29, 100345. https://doi.org/10.1016/j.jii.2022.100345

Carter, C. R., & Rogers, D. S. (2008). A framework of sustainable supply chain management: Moving toward new theory. International Journal of Physical Distribution & Logistics Management, 38(5), 360-387. https://doi.org/10.1108/09600030810882816

Casino, F., Dasaklis, T. K., & Patsakis, C. (2019). A systematic literature review of blockchain-based applications: Current status, classification and open

issues. Telematics and Informatics, 36, 55-81. https://doi.org/10.1016/j.tele.2018.11.006

Chen, J., Liu, H., & Zhang, Y. (2020). Citrus fruit classification using deep learning. Computers and Electronics in Agriculture, 178, 105762. https://doi.org/10.1016/j.compag.2020.105762

Chergui, W., Zidat, S., & Marir, F. (2020). An approach to the acquisition of tacit knowledge based on an ontological model. Journal of King Saud University-Computer and Information Sciences, 32(7), 818-828. https://doi.org/10.1016/j.jksuci.2018.09.012

Chu, Y., Yue, X., Yu, L., Sergei, M., & Wang, Z. (2020). Automatic image captioning based on ResNet50 and LSTM with soft attention. Wireless Communications and Mobile Computing, 2020, 8909458. https://doi.org/10.1155/2020/8909458

Çağıl, G., & Yıldırım, İ. (2020). Surface defect detection with machine vision: Cement industry application. European Journal of Science and Technology, (Special Issue), 116-128.

DIN SPEC 91345. (2016). Reference architecture model Industrie 4.0 (RAMI4.0). Beuth Verlag.

Djeloul, H., Layeb, A., & Chikhi, S. (2014). Quantum inspired cuckoo search algorithm for graph coloring. International Journal of Bio-Inspired Computation, 7(3), 183-194. https://doi.org/10.1504/IJBIC.2015.069558

Erdoğan, T. (2012). Görüntü işleme teknikleri ile nesne tanıma [Yüksek lisans tezi, Fırat Üniversitesi]. YÖK Ulusal Tez Merkezi.

European Commission. (2020). Enabling technologies for Industry 5.0: Results of a workshop with Europe's technology leaders. Publications Office of the European Union. https://doi.org/10.2777/082634

Ever, D., & Demircioğlu, E. N. (2022). Yapay zeka teknolojilerinin kalite maliyetleri üzerine etkisi [The effect of artificial intelligence technologies on quality costs]. Çukurova Üniversitesi Sosyal Bilimler Enstitüsü Dergisi, 31(1), 59-72. https://doi.org/10.35379/cusosbil.998326

Fekih, M., & Lahami, M. (2020). Blockchain technologies: Opportunities for solving real-world problems in developing countries. Telematics and Informatics, 53, 101431. https://doi.org/10.1016/j.tele.2020.101431

Forschungsunion & acatech. (2013). Recommendations for implementing the strategic initiative INDUSTRIE 4.0: Final report of the Industrie 4.0 Working Group. acatech – National Academy of Science and Engineering.

Frazzon, E. M., Agostino, Í. R., Broda, E., & Freitag, M. J. (2020). Manufacturing networks in the era of digital production and operations:

A socio-cyber-physical perspective. Annual Reviews in Control, 49, 288-294. https://doi.org/10.1016/j.arcontrol.2020.04.008

Girshick, R. (2015). Fast r-cnn. In Proceedings of the IEEE international conference on computer vision (pp. 1440-1448).

Gökten PO (2018). Karanlıkta üretim: Yeni çağda maliyetin kapsamı. Muhasebe Bilim Dünyası Dergisi, 20(4), 880-897.

Gupta, A., & Singh, P. K. (2017). Deep learning based defect detection in manufacturing: A review. International Journal of Computer Applications, 173(8), 1-5.

Gür, YE, Ayden, C., & Yücel, A. (2019). Yapay zekâ alanındaki gelişmelerin insan kaynakları yönetimine etkisi. Fırat Üniversitesi Uluslararası İktisadi ve İdari Bilimler Dergisi, 3(2), 137-158.

Güler, T. (2022). Gerçek zamanlı duygu durumu analizi: Derin öğrenme tabanlı akıllı sistem tasarımı [Yüksek lisans tezi, Bartın Üniversitesi]. YÖK Ulusal Tez Merkezi.

Gürsoy, M. Ü., Çolak, U. C., Gökçe, M. H., Akkulak, C., & Ötleş, S. (2019). Endüstri için kestirimci bakım [Predictive maintenance for industry]. International Journal of 3D Printing Technologies and Digital Industry, 3(1), 56-66.

He, K., Gkioxari, G., Dollár, P., & Girshick, R. (2017). Mask R-CNN. Proceedings of the IEEE International Conference on Computer Vision, 2961-2969.

İşçimen, A., Yurdakul, G., & Kaynar, O. (2014). Detection and classification of textile fabric defects by artificial neural networks. Tekstil ve Konfeksiyon, 24(4), 324-331.

Janssens, O., Slavkovikj, V., Vervisch, B., Stockman, K., Loccufier, M., Verstockt, S., Van de Walle, R., & Van Hoecke, S. (2016). Convolutional neural network based fault detection for rotating machinery. Journal of Sound and Vibration, 377, 331-345. https://doi.org/10.1016/j.jsv.2016.05.027

Johanesa, T. V. A., Equeter, L., & Mahmoudi, S. A. (2024). Survey on AI applications for product quality control and predictive maintenance in Industry 4.0. Electronics, 13(5), 976. https://doi.org/10.3390/electronics13050976

Johnson, J. M., & Khoshgoftaar, T. M. (2019). Survey on deep learning with class imbalance. Journal of Big Data, 6(1), 27. https://doi.org/10.1186/s40537-019-0192-5

Kartous, W., Layeb, A., & Chikhi, S. (2014). New quantum cuckoo search algorithm for multiple sequence alignment. Journal of Intelligent Systems, 23(3), 261-275. https://doi.org/10.1515/jisys-2013-0093

Kesici, B., & Yıldız, M. S. (2016). Kalite kontrol faaliyetlerinde yapay zekâ kullanımı ve bir otomotiv yan sanayisinde uygulanması [The use of artificial intelligence in quality control activities and its application in an automotive sub-industry]. Yalova Sosyal Bilimler Dergisi, 6(12), 307-323.

Kılıç, S. (2020). AI applications in automotive quality control and zero defect manufacturing. International Journal of Automotive Engineering and Technologies, 9(3), 108-117.

Kızılkaplan, E., Eren, T., & Yalçınkaya, F. (2020). Kablosuz sensör ağlarında konum belirlemede sezgisel algoritmaların kuantum davranışları ile karşılaştırılması [Comparison of heuristic algorithms with quantum behaviors in localization in wireless sensor networks]. Uluslararası Mühendislik Araştırma ve Geliştirme Dergisi, 12(2), 587-602. https://doi.org/10.29137/umagd.702832

Kutlu, H., Baki, M. K., & Arslanoğlu, Y. (2021). Industrial quality control with deep learning based object detection models. Journal of the Faculty of Engineering and Architecture of Gazi University, 6(2), 118-129.

Lee, S. M., Lee, D., & Kim, Y. S. (2019). The quality management ecosystem for predictive maintenance in the Industry 4.0 era. International Journal of Quality Innovation, 5(1), 1-11. https://doi.org/10.1186/s40887-019-0029-5

Li, Z., Liu, F., Yang, W., Peng, S., & Zhou, J. (2021). A survey of convolutional neural networks: Analysis, applications, and prospects. IEEE Transactions on Neural Networks and Learning Systems, 33(12), 6999-7019. https://doi.org/10.1109/TNNLS.2021.3084827

Li, BH, Hou, BC, Yu, WT, Lu, XB, & Yang, CW (2017). Applications of artificial intelligence in intelligent manufacturing: a review. Frontiers of Information Technology & Electronic Engineering, 18(1), 86-96.

Liu, W., Anguelov, D., Erhan, D., Szegedy, C., Reed, S., Fu, C. Y., & Berg, A. C. (2016). SSD: Single shot multibox detector. European Conference on Computer Vision (pp. 21-37). Springer.

Liu, K., Li, A., Wen, X., Chen, H., & Yang, P. (2019, September). Steel surface defect detection using GAN and one-class classifier. In 2019 25th International Conference on Automation and Computing (ICAC) (pp. 1-6). IEEE. https://doi.org/10.23919/IConAC.2019.8895110

Longo, F., Padovano, A., & Umbrello, S. (2020). Value-oriented and ethical technology engineering in Industry 5.0: A human-centric perspective for the design of the factory of the future. Applied Sciences, 10(12), 4182. https://doi.org/10.3390/app10124182

Lu, K., & Li, H. (2015). Quantum-behaved flower pollination algorithm. In 14th International Symposium on Distributed Computing and Applications for Business Engineering and Science (DCABES) (pp. 66-69). IEEE. https://doi.org/10.1109/DCABES.2015.20

Luo, Z., Huang, S., Morvan, M., & Yang, M. H. (2014). Image based quality control of steel products. IEEE International Conference on Image Processing (ICIP), 3233-3237.Montgomery, D. C. (2020). Introduction to statistical quality control. John wiley & sons.

Mukti, I. Z., & Biswas, D. (2019, December). Transfer learning based plant diseases detection using ResNet50. In 2019 4th International Conference on Electrical Information and Communication Technology (EICT) (pp. 1-6). IEEE. https://doi.org/10.1109/EICT48899.2019.9068805

Nagy, L., Ruppert, T., & Abonyi, J. (2021). Ontology-based analysis of manufacturing processes: Lessons learned from the case study of wire harness production. Complexity, 2021, 8603515. https://doi.org/10.1155/2021/8603515

Nahavandi, S. (2019). Industry 5.0—A human-centric solution. Sustainability, 11(16), 4371. https://doi.org/10.3390/su11164371

Oh, G., Ryu, J., Jeong, E., Yang, J. H., Hwang, S., Lee, S., & Lim, S. (2021). Drer: Deep learning-based driver's real emotion recognizer. Sensors, 21(6), 2166. https://doi.org/10.3390/s21062166

Orçanlı, K. (2017). Çok değişkenli kalite kontrol grafikleri ve yapay sinir ağları yöntemiyle döküm sanayisinde bir istatistik süreç kontrol uygulaması. Yayımlanmamış Doktora Tezi). Atatürk Üniversitesi Sosyal Bilimler Enstitüsü.

Pan, J. S., Dao, T. K., Chu, S. C., & Nguyen, T. T. (2017). An improvement of flower pollination algorithm for node localization optimization in WSN. Journal of Information Hiding and Multimedia Signal Processing, 8(2), 486-499.

Patro, S., & Sahu, K. K. (2015). Normalization: A preprocessing stage. arXiv. https://doi.org/10.48550/arXiv.1503.06462

Qi, C. R., Su, H., Mo, K., & Guibas, L. J. (2017). PointNet: Deep learning on point sets for 3D classification and segmentation. Proceedings of the IEEE Conference on Computer Vision and Pattern Recognition, 652-660.

Redmon, J., Divvala, S., Girshick, R., & Farhadi, A. (2016). You only look once: Unified, real-time object detection. Proceedings of the IEEE Conference on Computer Vision and Pattern Recognition, 779-788.

Rege, A. A., & Memane, R. (2013). 2D geometric shape recognition using edge detection. International Journal of Engineering Research and Applications, 3(6), 906-910.

Ren, S., He, K., Girshick, R., & Sun, J. (2016). Faster R-CNN: Towards real-time object detection with region proposal networks. IEEE Transactions on Pattern Analysis and Machine Intelligence, 39(6), 1137-1149.

Ribeiro, M. T., Singh, S., & Guestrin, C. (2016). "Why should I trust you?" Explaining the predictions of any classifier. Proceedings of the 22nd ACM SIGKDD International Conference on Knowledge Discovery and Data Mining, 1135-1144.

Ribani, R., & Marengoni, M. (2019, October). A survey of transfer learning for convolutional neural networks. In 2019 32nd SIBGRAPI Conference on Graphics, Patterns and Images Tutorials (SIBGRAPI-T) (pp. 47-57). IEEE. https://doi.org/10.1109/SIBGRAPI-T.2019.00010

Rolnick, D., Donti, P. L., Kaack, L. H., Kochanski, K., Lacoste, A., Sankaran, K., Ross, A. S., Milojevic-Dupont, N., Jaques, N., Waldman-Brown, A., Luccioni, A., Maharaj, T., Sherwin, E. D., Mukkavilli, S. K., Körding, K. P., Gomes, C., Ng, A. Y., Hassabis, D., Platt, J. C., ... Bengio, Y. (2019). Tackling climate change with machine learning. arXiv. https://doi.org/10.48550/arXiv.1906.05433

Qiu, P. (2013). Introduction to statistical process control. CRC press.

Sader, S., Husti, I., & Daróczi, M. (2019). Industry 4.0 as a key enabler toward successful implementation of total quality management practices. Periodica Polytechnica Social and Management Sciences, 27(2), 131-140.

Seuring, S., & Müller, M. (2008). From a literature review to a conceptual framework for sustainable supply chain management. Journal of Cleaner Production, 16(15), 1699-1710. https://doi.org/10.1016/j.jclepro.2008.04.020

Singh, S. P., & Sharma, S. C. (2015). Range free localization techniques in wireless sensor networks: A review. Procedia Computer Science, 57, 7-16. https://doi.org/10.1016/j.procs.2015.07.357

Sivakumar, S., & Venkatesan, R. (2014). Error minimization in localization of wireless sensor networks using modified cuckoo search with mobile anchor positioning (MCS-Map) algorithm. International Journal of Computer Applications, 95(6), 1-8. https://doi.org/10.5120/16594-6285

Sony, M., Antony, J., & Douglas, J. A. (2020). Essential ingredients for the implementation of Quality 4.0: a narrative review of literature and future directions for research. The TQM Journal, 32(4), 779-793.

Souza, FF, Corsi, A., Pagani, RN, Balbinotti, G., & Kovaleski, JL (2021). Total quality management 4.0: adapting quality management to Industry 4.0. The TQM Journal, 1-21.

Stancheva-Todorova, E. P. (2018). How artificial intelligence is challenging accounting profession. Journal of International Scientific Publications, 12(1), 126-141.

Tammina, S. (2019). Transfer learning using VGG-16 with deep convolutional neural network for classifying images. International Journal of Scientific and Research Publications, 9(10), 143-150. https://doi.org/10.29322/IJSRP.9.10.2019.p9420

Tanış, V. N. (2005). Teknolojik değişim ve maliyet muhasebesi [Technological change and cost accounting]. Nobel Kitabevi.

Tian, X., & Chen, C. (2019, September). Modulation pattern recognition based on Resnet50 neural network. In 2019 2nd IEEE International Conference on Information Communication and Signal Processing (ICICSP) (pp. 34-38). IEEE. https://doi.org/10.1109/ICICSP48821.2019.8958555

Tóth, Á., Nagy, L., Kennedy, R., Bohuš, B., Abonyi, J., & Ruppert, T. (2023). The human-centric Industry 5.0 collaboration architecture. MethodsX, 11, 102260. https://doi.org/10.1016/j.mex.2023.102260

Villani, V., Sabattini, L., Barańska, P., Callegati, E., Czerniak, J. N., Debbache, A., Ejarque, G., Falck, A. C., Giuliani, M., Hohwieler, E., Ijspeert, A. J., Ilievski, M., Kalogeras, A., Krüger, J., Kyrarini, M., León, A., Liem, A., Mazhar, O., Mazza, N., ... Fantuzzi, C. (2020). The INCLUSIVE system: A general framework for adaptive industrial automation. IEEE Transactions on Automation Science and Engineering, 18(4), 1969-1984. https://doi.org/10.1109/TASE.2020.3017010

Vogel-Heuser, B., & Hess, D. (2016). Guest editorial: Industry 4.0—Prerequisites and visions. IEEE Transactions on Automation Science and Engineering, 13(2), 411-413. https://doi.org/10.1109/TASE.2016.2523639

Vujović, Ž. (2021). Classification model evaluation metrics. International Journal of Advanced Computer Science and Applications, 12(6), 599-606. https://doi.org/10.14569/IJACSA.2021.0120670

Wang, Y., Ma, C., Liu, C., & Zhang, Y. (2019). Artificial intelligence for quality control in smart supply chain. Procedia Computer Science, 162, 46-55.

Wang, Z. (1998). Fuzzy neural network for machine vision inspection. Fuzzy Sets and Systems, 96(3), 373-381.

Wang, S., Wan, J., Zhang, D., Li, D., & Zhang, C. (2016). Towards smart factory for Industry 4.0: A self-organized multi-agent system with big data based feedback and coordination. Computer Networks, 101, 158-168. https://doi.org/10.1016/j.comnet.2015.12.017

Xu, X., Lu, Y., Vogel-Heuser, B., & Wang, L. (2021). Industry 4.0 and Industry 5.0—Inception, conception and perception. Journal of Manufacturing Systems, 61, 530-535. https://doi.org/10.1016/j.jmsy.2021.10.006

Yang, J. P., Wang, W. L., & Zhou, S. K. (2019). A design of integrated quality management system based on artificial intelligence (AI) technology. DEStech Transactions on Computer Science and Engineering, 15-20. https://doi.org/10.12783/dtcse/icaen2019/28735

Yazdi, P. G. (2012). Localization of wireless sensor networks for industrial applications [Master's thesis, Eastern Mediterranean University]. EMU Institutional Repository.

Yıldız, K., Buldu, A., & Demetgul, M. (2016). A thermal-based defect classification method in textile fabrics with K-nearest neighbor algorithm. Journal of Industrial Textiles, 45(5), 780-795. https://doi.org/10.1177/1528083714542827

Zakaria, Z., & Shakaff, A. Y. M. (2012). Shape recognition using geometric features. International Journal of Computer Science & Information Technology, 4(2), 105.

Zhang, Y., Peng, P., Liu, C., & Zhang, H. (2019, October). Anomaly detection for industry product quality inspection based on Gaussian restricted Boltzmann machine. In 2019 IEEE International Conference on Systems, Man and Cybernetics (SMC) (pp. 3413-3418). IEEE. https://doi.org/10.1109/SMC.2019.8914055

Zhou, Y., Wang, H., & Li, Z. (2023). Computer vision applications in Industry 4.0: A comprehensive review. Journal of Manufacturing Systems, 66, 1-15. https://doi.org/10.1016/j.jmsy.2022.11.018

Zhuang, F., Qi, Z., Duan, K., Xi, D., Zhu, Y., Zhu, H., Xiong, H., & He, Q. (2020). A comprehensive survey on transfer learning. Proceedings of the IEEE, 109(1), 43-76. https://doi.org/10.1109/JPROC.2020.3004555.

Zurada, J. (1992). Introduction to artificial neural systems. West Publishing Co.

# Chapter 8

# FERRANTI EFFECT IN MODERN POWER GRIDS

**Ramazan SOLMAZ**[1]

## INTRODUCTION

Sebastian Pietro Innocenzo Adhemar Ziani de Ferranti established a 10 kV transmission line in 1890 to supply electric power from the world's first central power station in Deptford to the city lighting system of London, located approximately 9.6 km away. When the grid was commissioned, power transmission began successfully; however, several problems soon emerged. Electrical engineers observed that the voltage measured at the receiving end (London) was significantly higher than the voltage at the sending end (Deptford). Shortly afterward, transformers located at the receiving station burned out, causing the system to collapse. This phenomenon was later named the Ferranti Effect [1]. After the Ferranti Effect was identified, it was reported that this phenomenon particularly occurs in long transmission lines operating under light-load or no-load conditions [2].

The structure of electrical power grids has evolved in parallel with technological advancements. Semiconductor switching components used in grids, capacitive loads connected to the system, and the types of cables employed significantly alter the grid's dynamics. In particular, with urbanization, underground cabling has been widely adopted to eliminate the risks associated with high voltage, which in turn gives the grid a capacitive characteristic.

The operation of a medium-voltage grid structured with Cross-Linked Polyethylene (XLPE) cables has therefore become increasingly important. These underground cables behave like capacitors, and in the absence of significant load demand, voltage rise at the receiving end can reach critical levels, potentially leading to various faults. Such faults often cause partial or complete discharge in high-voltage connection elements [3]. In cases of total discharge or short circuit, high-voltage components such as disconnectors and circuit breakers may be severely damaged. This poses a serious threat to energy

[1]Assistant Professor, Kahramanmaraş Istiklal University, Faculty of Engineering, Architecture and Design, Software Engineering Department ramazan.solmaz@istiklal.edu.tr ORCID: 000-0001-8933-2922

supply security. Moreover, excessive voltage rise can also damage devices connected to the grid.

The Ferranti phenomenon can manifest differently depending on several characteristics of power grids, including line length (short, medium, or long), grid topology (radial, ring, or meshed structures), voltage level (high or medium voltage), installation type (overhead, underground, or submarine systems), and operating conditions (no-load, light-load, or capacitive load scenarios). Despite its potential to cause major technical and operational issues in power systems, this phenomenon has been addressed in a limited number of studies. It has remained insufficiently investigated in the literature.

Foqa *et al.* (2023) experimentally validated a method developed to mitigate the Ferranti effect. They reported that the phenomenon predominantly occurs in long transmission lines and under low-load conditions, where capacitive charging leads to voltage imbalance within the power system [4]. Chavan *et al.* (2016) emphasized that this effect originates from the inherent nature of transmission lines and demonstrated through simulations that the Static Synchronous Series Compensator (SSSC) can mitigate the Ferranti effect due to its dynamic voltage control capability [5]. Yarlagadda *et al.* (2022) proposed a fuzzy logic-based Static Var Compensator (SVC) method to eliminate the Ferranti effect and maintain voltage control, showing through simulation results that this approach effectively ensures a stable voltage profile [6].

Park *et al.* (2015) observed that the Ferranti effect can occur during the partial energization process of a de-loaded grid following large-scale blackouts. They noted that the reactive power capacity of black-start generators plays a crucial role in this process. The study further indicated that the tendency of these generators to operate in the capacitive region can amplify voltage rise, making it critical to consider the Ferranti effect during restoration operations [7].

Kashef *et al.* (2023) highlighted that, in long and lightly loaded lines, the Ferranti effect may pose serious risks, including insulation failures, voltage instability, and equipment damage at the receiving end. They proposed the strategic placement of shunt reactors as a mitigation solution. Simulation studies confirmed that shunt reactors improve the voltage profile and enhance transmission efficiency [8]. Similarly, Song-Manguelle *et al.* (2013) identified capacitive currents, dielectric losses, and thermal limits as the main factors constraining the power transfer capability of high-voltage alternating current (HVAC) submarine cables. Their findings revealed that the Ferranti effect becomes more pronounced over long submarine distances, limiting system capacity. As a solution, they recommended compensation methods such as shunt reactors. They suggested that while HVAC systems are suitable for

medium distances, high-voltage direct current (HVDC) technology is more advantageous for long-distance applications [9].

Salcedo *et al.* (2013) investigated sustained overvoltages in dense meshed underground grids caused by feedback currents. They demonstrated that the combined influence of neutral shift, the Ferranti effect, and current interruption could generate voltages exceeding 3 p.u. Simulation results further indicated that these overvoltages persist longer under peak load conditions and reach their highest magnitudes in no-load scenarios [10].

Overall, existing studies on the Ferranti effect tend to share similar approaches and do not sufficiently address the phenomenon in the context of modern grid architectures. The increasing urban population and the widespread use of underground cabling for high-voltage transmission, as well as the intensive application of XLPE cables across sea, river, lake, and strait crossings, significantly alter grid parameters. These changes directly affect grid stability and voltage behavior, emphasizing the necessity of assessing possible scenarios in secondary and intermediate grids utilizing XLPE cables. Considering the limited availability of energy resources [11, 12, 13], a comprehensive analysis of such effects is essential for establishing a stable and reliable power grid.

Efficient use of existing energy resources is a key strategy for managing growing energy demand and limited supply. An optimized design of power grids for energy transmission can minimize potential losses. In this context, every aspect of grid design must be carefully considered. This study examines, as a case study, a radial distribution grid constructed with XLPE cables operating at a voltage level of 31.5 kV [14]. The Ferranti phenomenon observed in this grid is analyzed in detail, and its impact on grid performance and voltage stability is thoroughly evaluated.

## USE OF XLPE CABLES IN MEDIUM-VOLTAGE GRIDS AND THE FERRANTI PHENOMENON

Cables used in power grids have a significant impact on the grid capacitance. The geometry and arrangement of XLPE cables (Figure 1), combined with the proximity of conductors and the use of insulation with a high dielectric constant, result in higher system capacitance where they are employed. Consequently, underground grids exhibit greater capacitive behavior compared to overhead lines, and the Ferranti effect can be observed even in relatively short medium-voltage (MV) lines.

$$C = \frac{2\pi\varepsilon}{ln\left(\frac{D}{r}\right)} \tag{1}$$

Here, $C$ represents the capacitance $(F/m)$, $\varepsilon = \varepsilon_0 \varepsilon_r$ is the permittivity of the insulation, $D$ denotes the distance between conductors, and $r$ is the radius of the conductor.

The dielectric constant of the insulation $(\varepsilon_r)$ is directly proportional to the capacitance. For overhead lines, $\varepsilon_r \approx 1$, whereas for XLPE cables, $\varepsilon_r \approx$ 2.3–2.5. Cables used in underground grids are insulated and arranged closely together. This configuration results in a higher and more uniform electric field intensity between the conductors while simultaneously reducing the distance between them $(D)$. Consequently, underground grids constructed with XLPE cables exhibit increased capacitance compared to overhead lines.

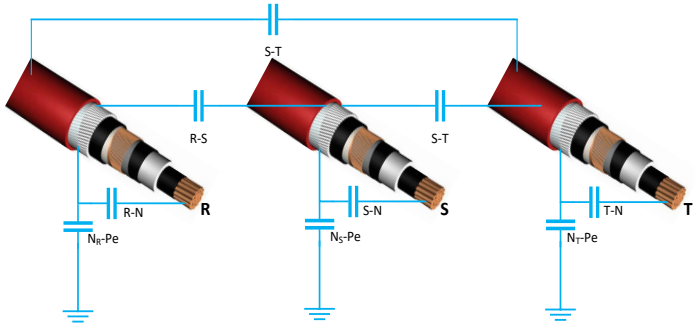


**Figure 1.** Three-phase XLPE underground cable layout and capacitance representation [3]

**Figure 2.** π-equivalent circuit model of a medium-voltage transmission line [3]

In Figure 2, $R$, $L$, and $C$ represent the total line parameters, $I_s$ and $V_s$ denote the sending-end current and voltage, and $I_r$ and $V_r$ indicate the receiving-end current and voltage, respectively. In this case, the grid is under no-load conditions, so $I_r = 0$, $R \approx 0$, and $I_L = I_{C2}$.

$$I_L = \frac{V_S}{X_L + X_C}, \qquad X_L = j\omega L, \qquad X_C = -\frac{j}{\omega C/2} = -\frac{j2}{\omega C} \tag{2}$$

$$V_R = I_L \times X_C = \frac{V_S}{X_L + X_C}.X_C = \frac{V_S}{j\omega L - \frac{j2}{\omega C}} \cdot \left(-\frac{j2}{\omega C}\right) = V_S \cdot \frac{-j2}{\omega C} \cdot \frac{1}{j\omega L - \frac{j2}{\omega C}} = V_S \cdot \frac{-j2}{\omega C} \cdot \frac{\omega C}{j(\omega^2 LC - 2)} = V_S \cdot \frac{-2}{(\omega^2 LC - 2)} \quad (3)$$

$$\frac{V_R}{V_S} = \frac{-2}{(\omega^2 LC - 2)} \rightarrow \frac{V_S}{V_R} = \frac{\omega^2 LC - 2}{-2} \quad (4)$$

Equation 4 illustrates the variation of the $V_S/V_R$ ratio with respect to $\omega^2 LC$. Depending on the value of $\omega^2 LC$, the system exhibits different operating regimes: $\omega^2 LC < 2$, $\omega^2 LC = 2$, $\omega^2 LC > 2$, and $\omega^2 LC > 4$.

1) Case $0 < \omega^2 LC < 2$;
$\omega^2 LC = 0 \Rightarrow V_S/V_R = 1 \rightarrow V_S = V_R$
$\omega^2 LC = 1 \Rightarrow V_S/V_R = 0.5 \rightarrow V_R = 2V_S$
$\omega^2 LC = 1.5 \Rightarrow V_S/V_R = 0.25 \rightarrow V_R = 4V_S$

In the range $0 < \omega^2 LC < 2$, the receiving-end voltage ($V_R$) becomes higher than the sending-end voltage ($V_S$). The Ferranti effect is observed within this range.

2) Case $\omega^2 LC = 2$ (Resonance condition):
$\frac{V_S}{V_R} = \frac{0}{-2} = 0, \Rightarrow V_R \rightarrow \infty$ ($V_S$ when constant)

In the resonance condition, the receiving-end voltage ($V_R$) theoretically tends toward infinity. This represents a limiting case for the model and defines the boundary condition given by the ideal formula. In a real power grid, the voltage is constrained by resistance, losses, and protective devices. Although the probability is low, this scenario could potentially pose a hazardous condition.

3) Case $\omega^2 LC > 2$ and $\omega^2 LC > 4$;
$\omega^2 LC = 3 \Rightarrow V_S/V_R = (3-2)/-2 = -0.5 \Rightarrow V_R = -2V_S$
$\omega^2 LC = 4 \Rightarrow V_S/V_R = (4-2)/-2 = -1 \Rightarrow V_R = -V_S$
$\omega^2 LC = 10 \Rightarrow V_S/V_R = (10-2)/-2 = -4 \Rightarrow V_R = -0.25V_S$
$\omega^2 LC = 20 \Rightarrow V_S/V_R = (20-2)/-2 = -9 \Rightarrow V_R = -0.11V_S$

For $\omega^2 LC > 2$, phase reversal occurs, corresponding to a 180° phase difference. Since $| V_S/V_R | < 1$, the sending-end voltage is still larger in absolute

value ($|V_R| > |V_S|$), meaning that despite the phase reversal, a voltage rise at the receiving end is observed.

For $\omega^2 LC > 4$, $V_S/V_R < 0$ and $|V_S/V_R| > 1$, indicating phase reversal and a reduction in the receiving-end voltage in absolute terms ($|V_R| < |V_S|$). In this case, both the phase (polarity) changes and the voltage magnitude decrease at the receiving end.

Exceeding the $\omega^2 LC > 2$ threshold in practical systems depends on the distributed L and C parameters of the line and the operating frequency, and is rarely observed under typical transmission line conditions. In grids constructed with XLPE cables, the phenomenon may occur under no-load conditions, making open-ended grids a potential risk.

**NUMERICAL ANALYSIS**

The sending- and receiving-end voltage expressions for the grid, whose equivalent circuit is shown in Figure 2, were approximately obtained in Equation (3). The line has a single-phase length of 5.4 km (for three phases: $5.4 \times 3 = 16.2$km) [3], with a frequency of 50 Hz, a sending-end voltage $V_S = 31.5$kV, and an inductance $L = 1$mH/km. Solutions were calculated for a capacitance range of $C = 0.001 - 1000\mu F/km$. Using these values, the $V_R/V_S$ ratios were analyzed as a function of grid capacitance. Simulation solutions were implemented in Python, and visualizations were developed using a PyQt5 GUI. The developed program enables interactive analysis of the $V_R/V_S$ ratios as a function of capacitance. Screenshots for some key values are presented in Figures 3–5.

For $C' = 1$ nF, $\omega^2 LC = 2.590 \times 10^{-5}$, and $V_R \cong V_S$. The calculated values are in good agreement with the simulation results (Figure 3).

Total line capacitance: $C_{total} = C_{per\_km} * line\_length = 0.001\mu F/km * 16.2km = 16.2\mu F$

Total line inductance: $L_{total} = L_{per\_km} * line\_length = 1mH/km * 16.2km = 16.2mH$

Voltage rise ratio formula: $VR/VS = -\frac{2}{(2\pi f)^2 * L_{total} * C_{total} - 2} = -\frac{2}{(2*50*3.14)^2 * 16.2e-3 * 16.2e-9 - 2} \cong 1$

Absolute voltage rise: $VR = VR/VS * VS = 1 * 31.5kV = 31.5kV$

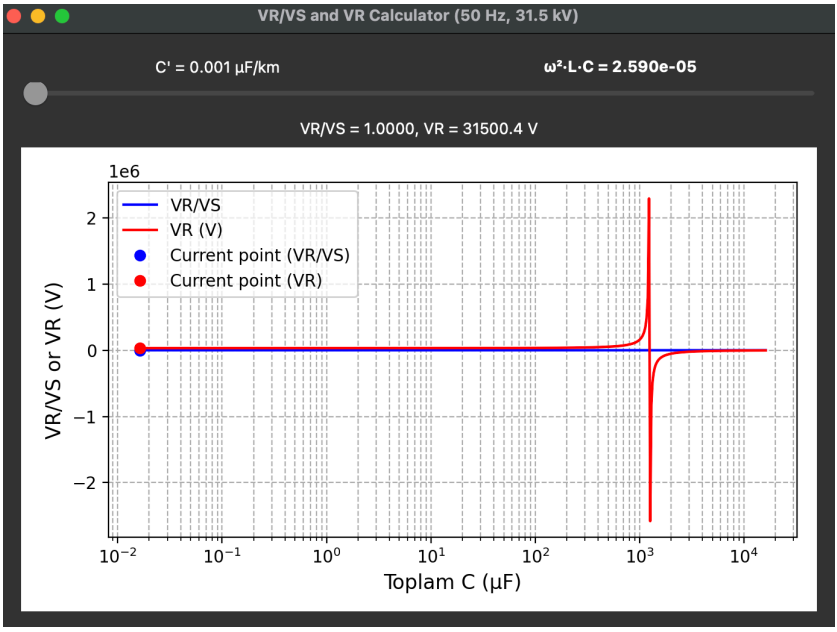


**Figure 3.** $V_R/V_S$ curve for the case $\omega^2 LC \approx 0$

In Figure 4, the $V_R/V_S$ ratio and the $V_R$ curve are presented for the condition $0 < \omega^2 LC < 2$. As the line capacitance per kilometer increases, the receiving-end voltage ($V_R$) becomes higher than the sending-end voltage. Within this range ($0 < \omega^2 LC < 2$), the $V_R$ voltage increases, indicating the presence of the Ferranti Effect in the grid. In Figure 4, for $C' = 6.330\,\mu F$ and $\omega^2 LC = 0.16$, the receiving-end voltage was calculated as $V_R = 34{,}312.9\,V$. The voltage difference $V_R - V_S = 34{,}312.9 - 31{,}500 = 2{,}812.9\,V$, showing that the receiving-end voltage exceeds the sending-end voltage.

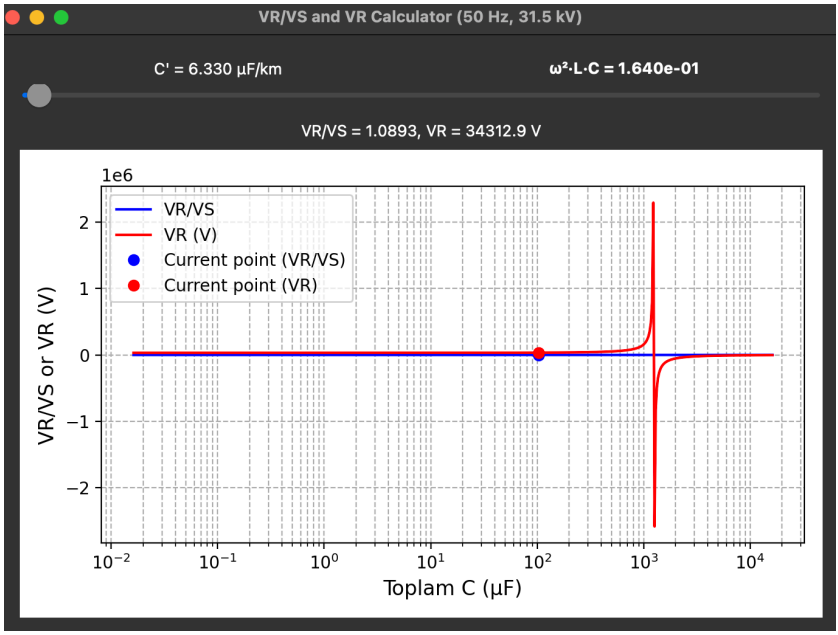


**Figure 4.** The Ferranti effect observed in the grid as a function of capacitance

In Figure 5a, for $V_R/V_S \approx 2$, the receiving-end voltage was found to be $V_R = 64{,}590.4\,V$ when $C' = 39.558\,\mu F$. It is observed that the receiving-end voltage increases exponentially with the rise in grid capacitance. When the line capacitance per kilometer is increased by 30% ($C' = 52.216\,\mu F/km$), the $V_R/V_S$ ratio reaches approximately 3. This result clearly demonstrates the significant influence of capacitance on the voltage behavior of the grid.

In Figure 5b, for the condition $\omega^2 LC \approx 2$, with $C' = 52.216\,\mu F/km$, the ratio $V_R/V_S = 61$ was calculated. These results indicate that the grid theoretically reaches a resonance condition. However, considering the influence of other parameters affecting the actual system, the occurrence of resonance is deemed highly unlikely. The resistive components of XLPE cables, protection systems, and connected loads serve as damping factors, preventing resonance. Nevertheless, the possibility of resonance is considered a critical phenomenon for power systems. Therefore, in grids composed of XLPE cables, taking preventive measures against such conditions is crucial to ensure the continuity of the energy supply.

Figure 5c corresponds to the condition $\omega^2 L_{total} C_{total} > 2$, where a phase inversion phenomenon is observed in the grid. The calculated $V_R$ values are negative, and as the value of $\omega^2 L_{total} C_{total}$ increases, the $V_R$ voltage decreases exponentially.

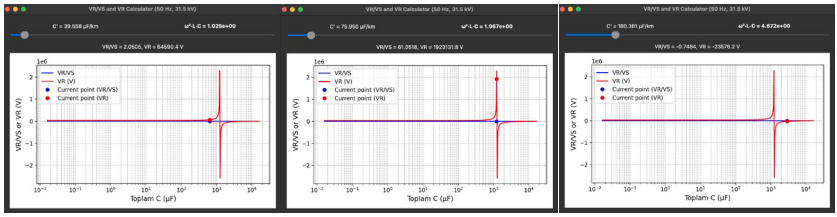


(a) (b) (c)

**Figure 5.** $V_R/V_S$ and $V_R$ curves: **a)** $\omega^2 L_{\text{total}} C_{\text{total}} \approx 1$, **b)** $\omega^2 L_{\text{total}} C_{\text{total}} > 1$, c) $\omega^2 L_{\text{total}} C_{\text{total}} > 2$.

## CONCLUSIONS AND RECOMMENDATIONS

In this study, an example of a medium-voltage (MV) grid constructed with XLPE underground cables was analyzed to investigate the Ferranti Effect and to numerically evaluate the influence of capacitance on grid performance. The analysis results indicate that under light-load or no-load conditions, the receiving-end voltage increases logarithmically as the grid capacitance rises. It was also found that the grid theoretically reaches a resonance condition when $\omega^2 L_{\text{total}} C_{\text{total}} \approx 2$. The findings demonstrate that due to the highly capacitive characteristics of XLPE cables, the Ferranti Effect may occur even in short medium-voltage distribution lines.

Therefore, during the design stage of XLPE-based grids, accurate modeling of cable capacitance and line length is essential. Appropriate compensation components (such as reactive power controllers or voltage regulators) should be incorporated to ensure proper voltage regulation. Furthermore, implementing real-time voltage monitoring and load management strategies can minimize the risk of overvoltage at the receiving end, thereby improving grid stability and enhancing the reliability of energy supply.

## REFERENCES


1. Hong, S. (1995). Forging scientific electrical engineering: John Ambrose Fleming and the Ferranti effect. *Isis*, *86*(1), 30-51.
2. Venu, Y., Nireekshana, T., Phanisaikrishna, B. (2021). Mitigation of Ferranti Effect Using Thyristor Controlled Reactor. In: Komanapalli, V.L.N., Sivakumaran, N., Hampannavar, S. (eds) Advances in Automation, Signal Processing, Instrumentation, and Control. i-CASIC 2020. Lecture Notes in Electrical Engineering, vol 700. Springer, Singapore. https://doi.org/10.1007/978-981-15-8221-9_236
3. Tekin, M., & Solmaz, R. (2024). Effects of cross-linked polyethylene (XLPE) conductors in medium voltage power grids and load analysis. *Electric Power Systems Research*, *236*, 110930.
4. Foqha, T., Alsadi, S., Refaat, S. S., & Abdulmawjood, K. (2023). Experimental validation of a mitigation method of Ferranti effect in transmission line. IEEE Access, 11, 15878-15895.
5. Chavan, G., Acharya, S., Bhattacharya, S., Das, D., & Inam, H. (2016, July). Application of static synchronous series compensators in mitigating Ferranti effect. In 2016 IEEE Power and Energy Society General Meeting (PESGM) (pp. 1-5). IEEE.
6. Yarlagadda, V., Lakshminarayana, G., Ambati, G., Nireekshana, T., & Karthika, G. A. (2022, March). Mitigation of Ferranti effect and voltage control in transmission systems using fuzzy logic controlled SVC. In 2022 International Conference on Smart Technologies and Systems for Next Generation Computing (ICSTSN) (pp. 1-6). IEEE.
7. Park, J. M., Lee, H. J., Yu, W. K., Jang, B. T., & Lee, K. S. (2015). Primary restoration path selection considering Ferranti effect and reactive power capability of black-start generators. Journal of Electrical Engineering & Technology, 10(3), 1377-1382.
8. Kashef, H. H., Amer, R. Y., El-Nemr, M. K., & Omara, A. M. (2023, December). Mitigating Ferranti effect and enhancing transmission line efficiency through shunt reactor placement in remote grids. In 2023 24th International Middle East Power System Conference (MEPCON) (pp. 1-7). IEEE.
9. Song-Manguelle, J., Todorovic, M. H., Chi, S., Gunturi, S. K., & Datta, R. (2013). Power transfer capability of HVAC cables for subsea transmission and distribution systems. IEEE Transactions on Industry Applications, 50(4), 2382-2391.

10. Salcedo, R., Ran, X., De Leon, F., Czarkowski, D., & Spitsa, V. (2013). Long duration overvoltages due to current backfeeding in secondary networks. IEEE transactions on power delivery, 28(4), 2500-2508.
11. Zhao, Z., Xu, H., & Bao, G. (2025). Study on energy resource-project mode-load demand chain flexibility adaptation of park-level integrated energy systems. Energy, 320, 135246.
12. Tan, Y., & Luo, Z. (2025). Energy management of distributed energy systems: A novel heuristic operation strategy considering complementarities of various energy resources. Energy and Buildings, 329, 115261.
13. Khan, S. A., Tao, Z., Agyekum, E. B., Fahad, S., Tahir, M., & Salman, M. (2025). Sustainable rural electrification: Energy-economic feasibility analysis of autonomous hydrogen-based hybrid energy system. International Journal of Hydrogen Energy, 141, 460-473.
14. Solmaz, R., Sarı, M., Baltacı, F., Tekin, M. (2022). OG-AG Elektrik Şebekelerinde Dinamik Kontrollü Kompanzasyon Uygulaması. Kahramanmaraş Sütçü İmam Üniversitesi Mühendislik Bilimleri Dergisi, 25(3), 480-490. https://doi.org/10.17780/ksujes.1142549

**Appendix-1: Python code**

```
#!/usr/bin/env python3
# -*- coding: utf-8 -*-
"""
Created on Wed Oct  1 18:59:36 2025
@author: ramazansolmaz
"""
#!/usr/bin/env python3
# -*- coding: utf-8 -*-
"""
This PyQt5 application calculates and plots the voltage rise (VR and VR/VS) along a transmission line as a function of the line capacitance per km (C'), allowing interactive exploration with a slider.
"""

import sys
import numpy as np
from PyQt5.QtWidgets import QApplication, QWidget, QVBoxLayout,QHBoxLayout, QLabel, QSlider
from PyQt5.QtCore import Qt
from matplotlib.backends.backend_qt5agg import FigureCanvasQTAgg as FigureCanvas
from matplotlib.figure import Figure

# Line parameters
L_per_km = 1e-3       # H/km (example inductance)
line_length_km = 5.4*3  # km
f = 50                # Hz
w = 2 * np.pi * f
VS = 31.5e3           # V (31.5 kV)

class VRVSApp(QWidget):
    def __init__(self):
        super().__init__()

        self.setWindowTitle("VR/VS and VR Calculator (50 Hz, 31.5 kV)")
        self.setGeometry(200, 200, 700, 500)
```

```
    layout = QVBoxLayout()

    # Label to show selected C'
    # Layout for C' and omegaLC side by side
    hlayout_top = QHBoxLayout()
    self.labelC = QLabel("C' = 0.001 μF/km", self)
    self.labelC.setAlignment(Qt.AlignCenter)

    self.labelOmegaLC = QLabel("ω²·L·C = ?", self)
    self.labelOmegaLC.setAlignment(Qt.AlignCenter)

    hlayout_top.addWidget(self.labelC)
    hlayout_top.addWidget(self.labelOmegaLC)

    # Slider for C' (0.001 μF/km to 1000 μF/km)
    self.slider = QSlider(Qt.Horizontal)
    self.slider.setMinimum(1)        # 0.001 μF/km
    self.slider.setMaximum(1000000)  # 1000 μF/km
    self.slider.setValue(0)
    self.slider.valueChanged.connect(self.update_values)

    # Label to show VR/VS and VR
    self.labelResult = QLabel("VR/VS = ?, VR = ? V", self)
    self.labelResult.setAlignment(Qt.AlignCenter)

    # Matplotlib figure for plotting
    self.figure = Figure(figsize=(6, 4))
    self.canvas = FigureCanvas(self.figure)

    layout.addLayout(hlayout_top)
    layout.addWidget(self.slider)
    layout.addWidget(self.labelResult)
    layout.addWidget(self.canvas)

    self.setLayout(layout)
    self.update_values()

def update_values(self):
    # Slider gives integer; convert to float in μF/km
```

```
        C_uFkm = self.slider.value() / 1000.0  # 0.001 steps
        self.labelC.setText(f"C' = {C_uFkm:.3f} µF/km")



        # Convert to Farad
        C_total = C_uFkm * 1e-6 * line_length_km
        L_total = L_per_km * line_length_km
        print(C_total,L_total)

        # VR/VS formula
        VR_VS = -2 / (w**2 * L_total * C_total - 2)
        VR = VR_VS * VS
        print (VR,VR_VS)

        self.labelResult.setText(f"VR/VS = {VR_VS:.4f}, VR = {VR:.1f} V")

        # --- Plot VR/VS and VR vs C_total ---
        C_values_total_uF = np.linspace(0.001, 1000, 500) * line_length_km  #
µF (total)
        C_total_values = C_values_total_uF * 1e-6   # Farad

        VRVS_values = -2 / (w**2 * L_total * C_total_values - 2)
        VR_values = VRVS_values * VS

        # w^2 * L_total * C_total (bilimsel gösterim, kalın font)
        omegaLC = w**2 * L_total * C_total
        self.labelOmegaLC.setText(f"<b>ω²·L·C = {omegaLC:.3e}</b>")



        self.figure.clear()
        ax = self.figure.add_subplot(111)
        ax.plot(C_values_total_uF,          VRVS_values,          label="VR/VS",
color='blue')
        ax.plot(C_values_total_uF, VR_values, label="VR (V)", color='red')

        # Current point (selected C')
        ax.plot([C_total * 1e6], [VR_VS], 'bo', label="Current point (VR/VS)")
        ax.plot([C_total * 1e6], [VR], 'ro', label="Current point (VR)")
```

```
        ax.set_xlabel("Toplam C (µF)", fontsize=12)
        ax.set_ylabel("VR/VS or VR (V)", fontsize=12)
        ax.set_xscale('log')  # Log scale for wide C range
        ax.grid(True, which="both", ls="--")
        ax.legend(loc='upper left', fontsize=10)
        self.figure.tight_layout()
        self.canvas.draw()

if __name__ == "__main__":
    app = QApplication(sys.argv)
    window = VRVSApp()
    window.show()
    sys.exit(app.exec_())
```

# Chapter 9

# IMPACT OF TITANIUM ALLOYING ON THE STABILITY AND SURFACE WEAR RESPONSE OF PM 316L STAINLESS STEEL

**Mehmet Akif ERDEN[1], Harun ÇUĞ[2]**

## 1. INTRODUCTION

Powder metal (PM) processing has come into the spotlight as an efficient method for producing stainless steel parts, allowing the creation of stainless steel parts close to the desired shape, involving less machining, and having controlled porosity properties. As for the stainless steel produced by powder metal processing, 316L stainless steel, an austenitic material, has remained popular owing to advantages such as corrosion resistance, weldability, and stability against high-temperature conditions. However, the stainless steel material's strength and resistance to wear could be inadequate for some applications, promoting the creation of new alloying processes designed specifically for powder metal processing.

Additions of titanium were observed to cause considerable microstructural transformations in the stainless steel matrix prepared by the powder metallurgy method [1-15]. Titanium has the capability of easily forming carbides and nitride compounds that are thermally stable and play the most important role in improving the microstructure and strengthening the properties of the austenitic steel. These compounds are particularly effective for powder metals, as the diffusion rates and presence of pores significantly influence the phase formation processes during the powder metallurgy process [16-20].

Previous research works have already shown that controlled additions of Ti can enhance the values of hardness, yield strength, and tensile strength through the stabilization of grain boundaries and the suppression of dislocations, but excessive values above the optimum levels of Ti can cause an excessive amount of carbide and nitride particles to gather along the grain boundaries, thus contributing to the brittleness and the generation of pores, which reduces the

[1]Prof.Dr., Department of Biomedical Engineering/Faculty of Engineering and Natural Sciences, Karabuk University, Turkey, makiferden@karabuk.edu.tr (ORCID: 0000-0003-1081-4713)
[2]Assoc.Prof.Dr Department of Mechanical Engineering/Faculty of Engineering and Natural Sciences, Karabuk University, Turkey, hcug@karabuk.edu.tr (ORCID: 0000-0002-6322-4269)

values of the corresponding strengths and the frictional properties, as depicted below [21-27]. The influence of Ti, therefore, needs to be assessed both as an alloying component and as an agent influencing the grains, which varies according to the levels and heat treatments.

Wear resistance performance represents one of the most important factors that are affected by the addition of titanium. Titanium precipitates can improve the stability and strength of the contact surface during the process of sliding, thereby increasing the stability and strength of the contact surface. Along with the inherent corrosion resistance properties of 316L stainless steel, the optimal addition of titanium provides an effective means for the development of wear-resistant stainless steel that can withstand dynamic loading conditions [28-37].

These findings are supported by the most up-to-date research, which illustrates that the addition of Ti may influence the behavior of surface roughness during machining and milling operations, where higher strength and lower ductility are shown to affect the chip flow and the tool-material interaction [38-40]. In addition, the characteristics of titanium during the process of sintering, particularly during the use of nitrogen-hydrogen atmospheres, are important factors that influence the distribution and morphology of the precipitates formed during the process, as explained in the literature [41, 42, 43]. The densification rate and the amount of nitride formed during the process are significant for Ti-containing stainless steel, as it emphasizes the importance of proper processing conditions for the production of superior material properties, as discussed in the literature [44, 45, 46]. Therefore, a systematic investigation is necessary to elucidate how Ti additions interact with 316L powder, compaction pressure, and the sintering atmosphere throughout the powder-metallurgy (PM) process.

Despite several studies addressing Ti-modified stainless steels, there is limited work focusing on the combined evaluation of microstructure, density, hardness, and wear response for Ti-reinforced 316L produced under PM conditions and sintered in nitrogen–hydrogen environments [47–49]. Additionally, comparative assessments of multiple Ti concentrations (0.5%, 1%, and 2%) under identical manufacturing and wear-testing conditions are missing in the current literature.

This study aims to investigate the effects of Ti additions (0–2 wt%) on the microstructure, density, and wear behavior of 316L stainless steel produced by powder metallurgy and sintered at 1250°C for 2 h in a nitrogen–hydrogen atmosphere, supported by optical microscopy, SEM/EDX, profilometry, and tribological characterization.

## 2. EXPERIMENTAL STUDIES

The 316L stainless-steel specimens were prepared using powder metallurgy with Ti additions of 0, 0.5, 1, and 2 wt%. Titanium powder was homogeneously mixed with 316L base powder for each composition. The mixed powders were then compacted in an ASTM E8M-standard steel mold using a uniaxial cold-pressing pressure of 700 MPa. This compaction pressure helps to provide the necessary green strength and assists in the densification process during the subsequent sintering step [50]. After the compaction process, the samples were removed from the dies without developing cracks around the edges and were packed into sealed containers before undergoing the sintering process.

The process of sintering was performed using the nitrogen and hydrogen atmosphere-controlled Protherm PTF 16/75/610 furnace located inside the Mechanical Metallurgy Laboratory of Karabük University. All the samples were subjected to the process of sintering at 1250°C for 2 h using nitrogen and hydrogen gases. The rates of heating and cooling were controlled carefully. The use of the nitrogen and hydrogen atmosphere assisted in the creation of Ti-containing nitrides and carbides, and, as such, it affected the stability and the consequent strength of the alloy.

After the process of sintering, the densities were measured based on Archimedes' principle. Afterwards, the sintered samples were cold-mounted and proceeded to metallographic processing. Grinding was conducted using SiC papers ranging from 240 to 7000 mesh, followed by the polish process that provided the necessary surface quality for the examination using an optical microscope and scanning electron microscopes. Micrographs were taken using the Nikon Epiphot 200 optical microscope to examine the grain structure, distribution of pores, and the content of carbide and nitride for varying levels of Ti.

Wear testing was performed using the 4D-ECN tribometer, and the testing environment was dry. Stroke length and testing length were 10mm and 100m, and the masses applied were 10 N and 20 N. The chrome steel counterpart (AISI 52100, 6mm diameter) was used. The diagram of the wear testing rig is shown in Fig. 1. After wear testing, the samples were ultrasonically cleaned, and their mass difference was measured using a precision balance, as shown in Table 1. The depth of the wear track and volumes were determined using the Mitutoyo SJ-410 Profilometer, and 2-D wear profiles are shown in Fig. 5. SEM examinations of the worn surfaces were performed using a Zeiss scanning electron microscope. SEM images at 100× magnification for all compositions are provided in Figure 3. Additionally, EDX analyses were conducted to identify the elemental distribution and detect tribochemical changes occurring during sliding, with the corresponding elemental maps shown in Figure 4. These datasets enabled correlation between Ti

content, microstructure, and wear-damage mechanisms, thereby guiding interpretation of the tribological performance of the Ti-modified 316L alloys.

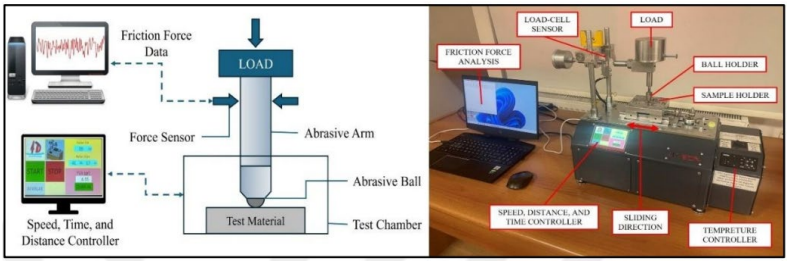


Figure 1. Wear test device

## 3. EXPERIMENTAL RESULTS AND EVALUATION

### 3.1. OPTICAL MICROSCOPE-SEM-EDX Analysis Results of Samples

Optical micrographs presented in Figure 2 show clear microstructural evolution with increasing Ti content. The unalloyed 316L specimen exhibits the largest grain size and a relatively uniform, spherical pore distribution. With 0.5 wt% Ti addition, grain refinement and a more homogeneous precipitation field are evident. The 1 wt% Ti sample displays further grain refinement and a higher number density of fine Ti-containing precipitates. At 2 wt% Ti, precipitates become coarser and partially coalesce along prior particle boundaries, and pore connectivity is visibly increased.

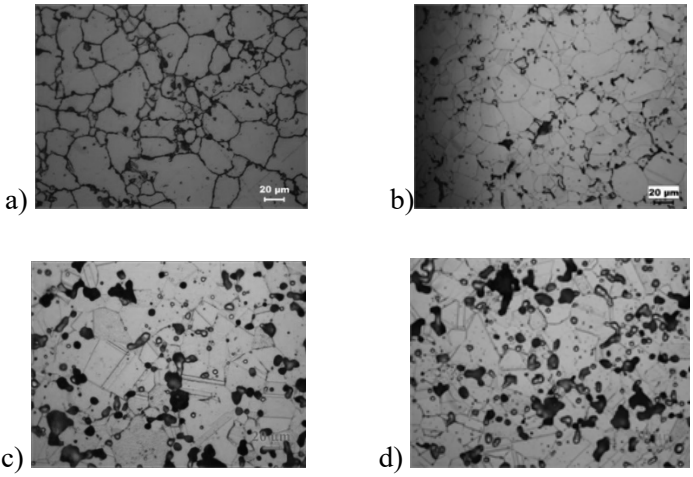


Figure 2. Optical images of the produced sample. a) 316 L, b) 316L+0,5%Ti, c) 316L+1%Ti and d) 316L+2%Ti,

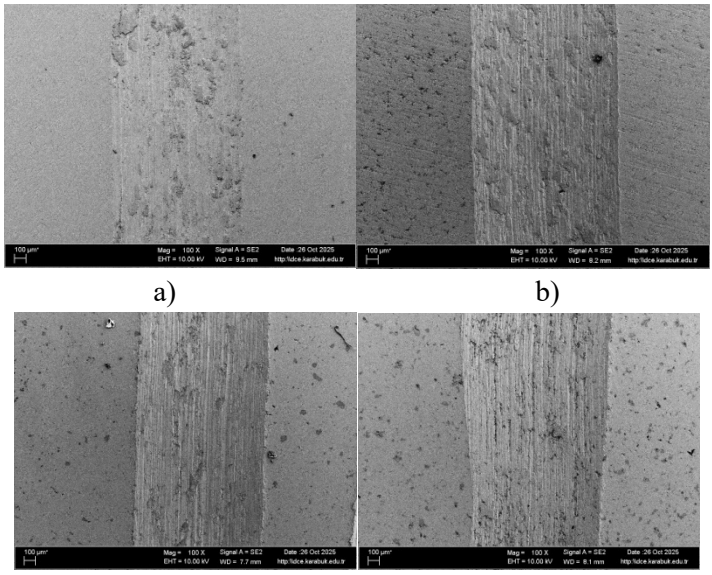

Figure 3. SEM analysis results of the samples after the wear test (10N 100X). a) 316 L, b) 316L+0,5%Ti, c) 316L+1%Ti and d) 316L+2%Ti,

SEM imaging and EDX mapping (Figures 3 and 4) confirm the formation of Ti-rich carbides/nitrides in all Ti-containing samples. The 0.5 wt% and 1 wt% Ti alloys show finely dispersed TiC/TiN-type precipitates within the matrix and along grain boundaries. In the 2 wt% Ti sample, Ti-rich phases concentrate preferentially at grain boundaries and triple junctions, producing a network of larger precipitates that coincide with increased local porosity and discontinuous matrix bonding as observed in the SEM images [51,52].

Bulk density measurements (Archimedes) indicate a monotonic trend of slight densification improvement from unalloyed 316L to 0.5 wt% and 1 wt% Ti, followed by a measurable density reduction at 2 wt% Ti. The density decrease at 2 wt% correlates with the enlarged precipitate clusters and increased pore connectivity observed in Figures 2 and 3, consistent with carbide/nitride accumulation that impedes complete sinter bonding [53].

Mechanical behavior inferred from microstructural features and corroborated by hardness testing (not tabulated here) shows that the 0.5 wt% and 1 wt% Ti alloys achieve enhanced matrix strengthening due to fine, dispersed precipitates that block dislocation motion. The 2 wt% Ti sample demonstrates a reduction in effective mechanical integrity because coarse precipitates at grain boundaries and increased porosity promote brittle fracture tendencies under load; fracture-relevant features are visible in the SEM wear-track cross-sections (Figure 3).

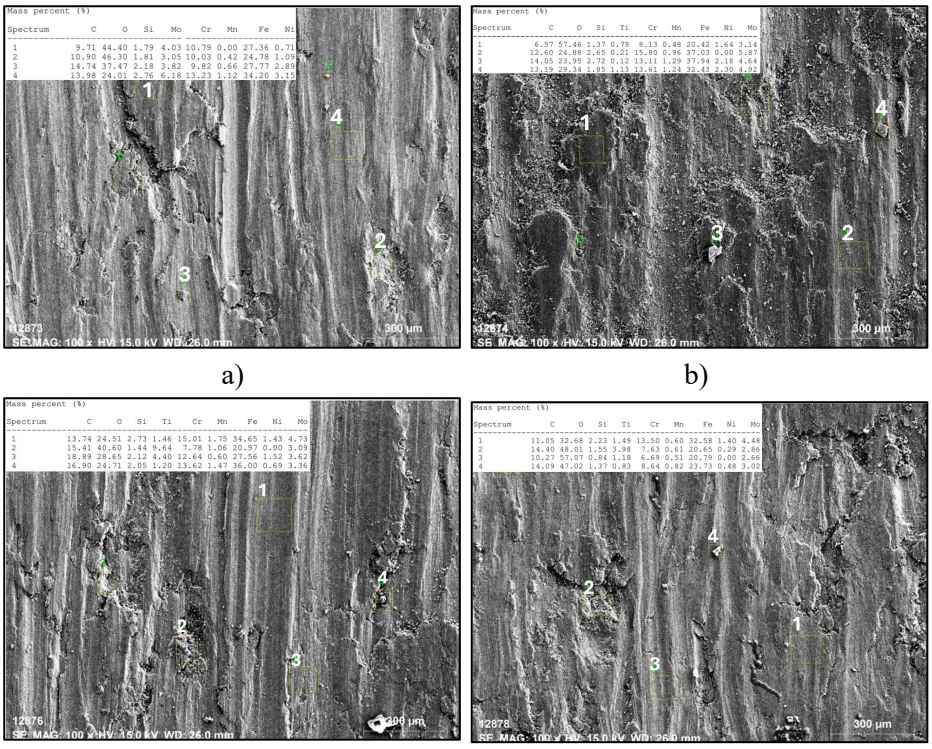


Figure 4. SEM-EDX analysis results of the samples after the wear test (20N). a) 316 L, b) 316L+0,5%Ti, c) 316L+1%Ti and d) 316L+2%Ti,

Mass-loss results from the reciprocating wear tests are summarized in Table 1. At 10 N, the mass losses decrease continuously with Ti content: 316L = 0.0060 g, 0.5 wt% Ti = 0.0051 g, 1 wt% Ti = 0.0046 g, and 2 wt% Ti = 0.0042 g, indicating improved resistance to material removal at this load as Ti content rises. At 20 N, the unalloyed 316L shows 0.0100 g loss while Ti-containing samples show higher absolute losses (0.5 wt% Ti = 0.0088 g, 1 wt% Ti = 0.0081 g, 2 wt% Ti = 0.0075 g); within the Ti-containing group, mass loss at 20 N decreases as Ti increases from 0.5 to 2 wt%. These trends demonstrate that Ti additions reduce wear under the lower load and that among Ti-containing alloys, higher Ti content reduces wear at the higher load, despite all Ti-modified specimens exhibiting greater 20 N loss than the unalloyed reference in this dataset.

SEM wear-track morphologies in Figure 3 reveal that at 10 N, the unalloyed 316L displays broader but shallower abrasion grooves and notable plastic deformation. The 0.5 wt% and 1 wt% Ti samples show reduced ploughing and less surface smear at 10 N, while the 2 wt% Ti sample exhibits the shallowest

grooves and smallest detached debris volumes, consistent with the monotonic decrease in 10 N mass loss (Table 1). At 20 N, Ti-containing samples exhibit increased oxidative debris and micro-cracking along precipitate-rich boundaries; EDX maps in Figure 4 indicate Ti enrichment within the wear tracks and elevated oxygen signals associated with tribo-oxidation, explaining the higher 20 N mass losses for Ti alloys relative to the unalloyed specimen.

Profilometric 2D area-loss data presented in Figure 5 corroborate the mass-loss trends: projected wear areas at 10 N decrease with increasing Ti content, while at 20 N the largest wear area is seen for 0.5 wt% Ti and decreases progressively for 1 wt% and 2 wt% Ti. Overall, Figure 5 indicates that area loss is minimized for the 2 wt% Ti composition under the tested conditions, despite its increased porosity; this suggests that the surface hardening effect of dense Ti-rich precipitates at higher Ti contents can locally reduce material removal area even when bulk densification is partially compromised [54-56].

Table 1. Weight loss results measured on a precision balance after the abrasion test.

| | Weight loss 10N (gr) | Weight loss 20N (gr) |
|---|---|---|
| 316 L | 0,0060 | 0,0100 |
| 316L+0,5%Ti | 0,0051 | 0,0088 |
| 316L+1%Ti | 0,0046 | 0,0081 |
| 316L+2%Ti | 0,0042 | 0,0075 |

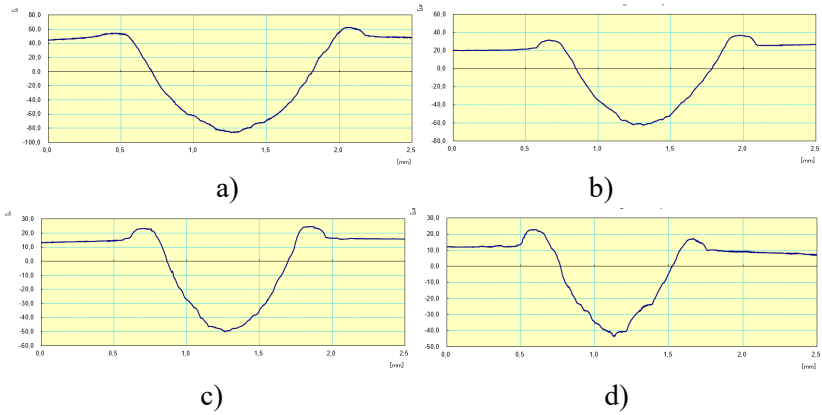

a) b) c) d)

Figure 5. 2D wear graph and area loss measured on the Mitutoyo SJ-410 device. a) 316 L, b) 316L+0,5%Ti, c) 316L+1%Ti and d) 316L+2%Ti,

In summary, the combined microstructural, SEM/EDX, profilometric, and mass-loss results indicate an optimal trade-off in the examined composition range: 0.5–1 wt% Ti provides microstructural refinement and improved wear resistance at moderate loads, while 2 wt% Ti yields the lowest mass and area losses at 10 N and the best performance among Ti-alloyed samples at 20 N, albeit accompanied by increased precipitate coarsening and porosity that may negatively affect other mechanical properties. Taken together, Table 1, Figures 2–5, and the accompanying SEM/EDX analyses present a consistent dataset that clearly connects Ti content with changes in precipitate morphology, porosity development, and the resulting tribological behavior.

## 4. GENERAL RESULTS

The combined insights obtained from the microstructural analyses, mechanical testing, and tribological assessments of the Ti-modified 316L stainless-steel composites can be summarized as follows.

- Ti additions refined the microstructure up to 1 wt% and produced dispersed Ti-based precipitates that enhanced matrix integrity and reduced wear at lower loads.
- At 2 wt% Ti, the microstructure exhibited coarse precipitate clusters along with elevated porosity; however, this composition still produced the lowest mass and area losses among all Ti-containing samples under both applied loads.
- Optical, SEM, and EDX analyses demonstrated the direct relationship between Ti-rich precipitate morphology, grain-boundary chemistry, and tribological response.
- Wear mass-loss and area-loss results showed consistent improvement with increasing Ti content during 10 N tests, while at 20 N, all Ti-modified alloys exhibited higher losses than unalloyed 316L but improved progressively from 0.5 to 2 wt% Ti.
- Profilometric analyses confirmed that wear-track depth and projected area decreased with increasing Ti concentration, indicating improved resistance to material removal.
- Overall, Ti additions in the range of 0.5–2 wt% produced notable modifications in the sintered microstructure and tribological performance of 316L stainless steel, with each composition contributing unique mechanisms for strengthening and improving wear resistance.

## REFERENCES


1. Sun, Y., et al. Wear behavior of powder-processed stainless steels. Wear, 2018.
2. Torres, H., & Amigó, V. Influence of sintering atmosphere on 316L microstructure. Mater. Des., 2017.
3. Albayrak, S., Gül, C., Emin, N., Gökmen, U., Karakoç, H., Uzun, A., & Çinici, H. (2023). Electrochemical, mechanical, and antibacterial properties of the AZ91 Mg alloy by hybrid and layered hydroxyapatite and tantalum oxide sol–gel coating. Materials Testing, 65(11), 1628-1644.
4. Li, J., et al. Effect of alloying additions on porosity evolution in PM steels. Mater. Sci. Eng. A, 2020.
5. Zhang, P., et al. Carbide formation in Ti-modified stainless steels. J. Alloys Compd., 2016.
6. Krawczyk, J., et al. TiC/TiN precipitation strengthening in sintered steels. Metals, 2019.
7. Toptan, F., et al. Microstructural refinement by reactive alloying. Mater. Charact., 2018.
8. Wang, L., & Shi, Y. Sintering kinetics of 316L stainless steel powders. Powder Metall., 2015.
9. Kumar, S., et al. Role of precipitates in grain-boundary stabilization. Acta Mater., 2020.
10. Rayment, J., et al. Titanium alloy additions in stainless steels. Mater. Sci. Technol., 2017.
11. Chen, W., et al. Influence of TiC precipitates on wear. Tribology Int., 2018.
12. Albartouli, A. B. M., & Uzun, A. (2023). Mechanical and Electrical Properties of Graphene Nanosheet Reinforced Copper Matrix Composites Materials Produced by Powder Metallurgy Method. Science of Sintering, 55(3).
13. Park, J., et al. Nitrogen-hydrogen atmospheres in sintering. J. Mater. Process. Technol., 2015.
14. Zhao, Y., et al. High-pressure compaction effects in PM stainless steels. Powder Technol., 2016.
15. Souza, R., et al. Wear mechanisms in austenitic PM stainless steel. Wear, 2019.
16. Guo, Y., et al. Micro-mechanisms of Ti-carbide strengthening. Mater. Sci. Eng. A, 2017.

17. Leitao, C., et al. Tribo-oxidation phenomena in stainless steels. Tribology Letters, 2018.
18. Amirsadeghi, A., et al. Effect of Ti on porosity formation in PM alloys. Metall. Mater. Trans. A, 2016.
19. Liu, X., et al. Precipitate-controlled grain refinement. Mater. Lett., 2019.
20. Singh, J., & Prakash, C. Mechanical behavior of Ti-alloyed 316L steel. J. Mater. Eng. Perform., 2021.
21. Blais, C., et al. Densification during sintering of stainless steel powders. Powder Metall., 2009.
22. Kim, S., et al. SEM/EDX characterization of wear tracks. Surf. Coat. Technol., 2016.
23. Yurt, O. E., & Uzun, A. (2022). Investigation of mechanical properties of SiC-reinforced seamless aluminium pipes fabricated using powder metallurgy followed by hot extrusion. International Journal of Materials Research, 113(10), 920-931.
24. Özkan, N., et al. Wear testing using ball-on-disk systems. Tribology Int., 2017.
25. Mahathanabodee, S., et al. Influence of carbide clustering on wear. Wear, 2020.
26. Huang, P., et al. Effects of alloying on sintering shrinkage. Mater. Des., 2015.
27. Zhang, D., et al. Formation of Ti-rich phases in steel alloys. J. Mater. Sci., 2018.
28. Cevik, M., et al. Sintered 316L: microstructure and wear. Metals, 2016.
29. Basu, J., et al. Toughness reduction with carbide networks. Mater. Sci. Eng. A, 2018.
30. Guo, S., et al. Titanium carbide precipitation behavior. Ceram. Int., 2017.
31. Li, X., et al. Porosity and wear correlation in PM steels. Tribology Int., 2019.
32. Fatih Kilicaslan, M., Uzun, A., & Karakose, E. (2018). Production of Melt-Spun Al-20Si-5Fe Alloy and Boron Carbide (B4C) Composite Material. Archives of Metallurgy and Materials, 63(2).
33. Fang, Z., et al. Powder metallurgy stainless steels. Int. Mater. Rev., 2017.
34. Sharifi, S., et al. Densification and grain growth control. Metall. Res. Technol., 2018.
35. Krauss, G. Steels: Processing, Structure, and Performance, ASM International.
36. German, R. M. Sintering: From Empirical Observations to Scientific Principles, 2014.

37. Callister, W.D. Materials Science and Engineering.

38. ASTM E8/E8M – Standard Test Methods for Tension Testing of Metallic Materials.
39. Uzun, A., Asikuzun, E., Gokmen, U., & Cinici, H. (2018). Vickers microhardness studies on B4C reinforced/unreinforced foamable aluminium composites. Transactions of the Indian Institute of Metals, 71(2), 327-337.
40. ASTM G99 – Standard Test Method for Wear Testing.
41. Zhang, L., et al. Surface roughness in Ti-modified steels. J. Manuf. Process, 2020.
42. De Souza, M., et al. Wear-track depth analysis. Wear, 2017.
43. Zhang, Y., et al. Tribological behavior of modified stainless steels. Tribology Int., 2022.
44. Cheng, X., et al. High-temperature sintering mechanisms. J. Mater. Process. Technol., 2018.
45. Ren, S., et al. Grain-boundary segregation effects. Acta Mater., 2019.
46. Li, J., et al. Strengthening mechanisms in PM alloys. Mater. Sci. Eng. A, 2021.
47. Kim, H., et al. Ball-on-flat sliding wear studies. Wear, 2016.
48. Song, Q., et al. Oxidation and wear correlations. Surf. Coat. Technol., 2019.
49. Zhou, X., et al. Microstructural effects on tribology. Tribology Letters, 2016.
50. Reddy, A., et al. Effect of nitrogen in sintering atmospheres. Powder Metall., 2021.
51. Luo, J., et al. Ti-based precipitate coarsening. J. Alloys Compd., 2018.
52. Manjunath, K., et al. Wear analysis by profilometry. Tribol. Int., 2020.
53. Smith, T., et al. Mechanical implications of Ti additions. Mater. Today Commun., 2022.
54. Uzun, A., Karakoc, H., Gokmen, U., Cinici, H., & Turker, M. (2016). Investigation of mechanical properties of tubular aluminum foams. International Journal of Materials Research, 107(11), 996-1004.
55. Han, P., et al. Relationship between porosity and wear. Mater. Charact., 2017.
56. Xu, W., et al. High-load wear mechanisms in PM steels. Wear, 2021.

# Chapter 10

# A YOLO-BASED MULTI-OBJECT DETECTION APPROACH FOR EARLY FOREST FIRE RESPONSE

**Begüm EROL[1], Salih BÜTÜNER[2]**

## 1. INTRODUCTION

The effects of climate change in the world and in Türkiye have become more evident in recent years. The increase in global warming, the decrease and seasonal variation in precipitation, as well as the rise in both prolonged rainy and dry periods, have led to significant environmental changes (Shang et al., 2024). These changes disrupt the balance of natural ecosystems across the globe, making many regions more vulnerable and unprotected against fires.This situation makes the situation difficult for people, especially in forest ecosystems, by increasing both the frequency of fires and the size of the areas they affect. The frequency and impact of forest fires have become a major global issue, not only due to their environmental consequences but also because of their economic and social effects (Bowman et al., 2020).

In previous years, forest fires were a natural part of the life cycle. However, depending on climate change and human factors, it can reach much more destructive dimensions today. A large amount of vegetation is destroyed as a result of a forest fire. Consequently, the structure of the soil deteriorates, carbon emissions to the atmosphere increase, and the concentration of greenhouse gases rises. Thus, forest fires have become a feedback mechanism that negatively reinforces climate change. In addition, secondary effects such as erosion caused by tree destruction, water pollution, reduced oxygen levels, and habitat loss make it difficult for ecosystems to recover to their original state (Agbeshie et al., 2022; Vallet et al., 2025).

The effects of forest fires are not limited to ecological aspects alone. When they reach local economies, infrastructure, and residential areas, forest fires can

[1]Assist. Prof. Dr., Department of Industrial Engineering, Faculty Of Engıneerıng, Archıtecture And Desıgn, İstiklal University, Kahramanmaraş, Turkey, begum.erol@istiklal.edu.tr, (0000-0001-9131-3317)
[2]Res. Assist., Department of Software Engineering, Faculty Of Engıneerıng, Archıtecture, Istanbul Beykent University, Istanbul, Turkey, salihbutuner@beykent.edu.tr, (0000-0003-0737-4016)

directly threaten human life. Dense smoke and gases released during forest fires reduce air quality, increase respiratory diseases in people, and have negative effects on public health in the long term. Such health issues also have adverse economic consequences for countries. Therefore, forest fires require an integrated disaster management approach, as they affect both the environment and human health (Butt et al., 2020).

In addition to prevention, the early detection and rapid response to fires are of great importance. Traditional monitoring methods rely on tools such as watchtowers, terrestrial patrols and satellite-based observations, but these methods may be insufficient for continuous monitoring of large forest areas. Moreover, most of these systems can only trigger alarms after a fire reaches a certain size, which often results in missed opportunities for early intervention. This situation has increased the need for more automatic, faster, and more reliable detection systems to enable early response and effective fire suppression.

As a developing structure in recent years, artificial intelligence, computer vision and deep learning (DL) based approaches offer promising solutions for preventing forest fires. When combined with unmanned aerial vehicles (UAVs) and satellite imaging technologies, these systems have the potential to detect fire and smoke at an early stage and to perform this detection in real time. DL based models can distinguish complex patterns, color changes, and shape variations in forest fire images with high accuracy. However, it can detect not only fire or smoke but also objects such as people, vehicles or animals affected by fires.

Systems developed with DL models can establish decision-support mechanisms in fire management, thereby enabling early detection and prevention of fires. In particular, DL based object detection methods, such as the You Only Look Once (YOLO) series, have been widely used in recent years for early forest fire detection due to their high accuracy and real-time processing capabilities. Different versions of the YOLO architecture have shown significant improvements in both speed and accuracy and have been optimized to adapt to various operational scales and hardware conditions.

This study aims to develop an artificial intelligence–based system that enables the early detection of forest fires and the identification of objects such as humans and vehicles at the scene. In this context, the YOLOv11n model was selected due to its advantages of higher detection accuracy and low latency. Thanks to its lightweight and efficient structure, YOLOv11n can operate effectively even on limited hardware resources, providing rapid detection in the early stages of forest fires. This capability significantly supports early

intervention processes and contributes to mitigating the adverse impacts of disasters. This approach is considered an innovative AI solution for the increasing frequency of forest fires associated with climate change. Furthermore, it aims to contribute to the scientific literature while establishing a practical and sustainable technological infrastructure for disaster management.

## 2. RELATED WORKS

Forest fires have devastating effects on ecosystems, threatening biodiversity and causing economic losses. Therefore, the early detection of fires and rapid intervention are crucial for disaster management and environmental protection (Cheng et al., 2024). The limitations of traditional methods, particularly their ineffectiveness over large areas and challenging terrains, have directed researchers toward more advanced technologies (Özel et al., 2024; Cheng et al., 2024). In this context, DL techniques, especially in the field of image processing, offer promising results for the detection and monitoring of forest fires (Özel et al., 2024).

In recent years, both basic DL methods and various domain-specific DL-based approaches have been employed for the detection and monitoring of forest fires (Özel et al., 2024; Cheng et al., 2024; Hong et al., 2024). Ayrıca, bu çalışmalarda hem orijinal veri kaynakları oluşturulmuş hem de mevcut hazır veri setleri kullanılmıştır (Boroujeni ve arkadaşları, 2025). There are multiple studies in this context in the literature (Özel et al., 2024).

One such study by Dewangan et al. (2021) introduced the FIgLib dataset, which contains approximately 25,000 labeled images obtained from fixed cameras, and developed the DL model SmokeyNet. Similarly, Pereira et al. (2021) created a dataset of over 150,000 images derived from Landsat-8 satellite data and evaluated the performance of various DL architectures. Sdraka et al. (2023) presented the FLOGA dataset, consisting of images from the Greece region, and achieved high accuracy in mapping burned areas using a new DL model called BAM-CD. In another study, Xu et al. (2024) developed the Sen2Fire dataset using Sentinel-2 and Sentinel-5P data to investigate the effects of different spectral band combinations on fire detection.

Due to the limitations of traditional methods, YOLO architectures have been widely used within DL based approaches for real-time fire and smoke detection (Özel et al., 2024; Cheng et al., 2024; Alkhammash, 2025). In recent years, various versions of the YOLO architecture (YOLOv1–v13) and different model sizes and configurations (nano, small, medium, large, x-large) have been adapted for forest fire detection, leading to numerous studies in this field. In their study, Al-Smadi et al. (2023) compared YOLOv3, YOLOv5, and

YOLOv7 models, reporting that the YOLOv5x model achieved the highest accuracy. Similarly, Raita-Hakola et al. (2023) optimized the YOLOv5 model using transfer learning for smoke detection in Boreal forests. Zhou and Jiang (2025) developed the YOLOv11n model and presented it as FEDS-YOLOv11n, improving performance in small object detection.

There are several review studies covering DL based approaches for the detection and monitoring of forest fires (Özel et al., 2024; Cheng et al., 2024; Hong et al., 2024; Boroujeni et al., 2025). Such reviews are valuable resources for understanding the existing literature and identifying directions for future research. Hong et al. (2024) examined the applications of transfer learning techniques in forest fire detection. Özel et al. (2024) compiled studies published between 2013 and 2023, providing a comprehensive analysis of how image processing, computer vision, and DL methods have been used in fire detection and suppression systems. While Cheng et al. (2024) thoroughly addressed the role of DL methods in forest fire detection, Boroujeni et al. (2025) analyzed all datasets created and utilized in this field over the past twenty years.

Comprehensive review studies on the evolution and applications of YOLO architectures are also available (Terven and Cordova-Esparza, 2023; Brahmbhatt et al., 2023; Alkhatib et al., 2023; Dutta and Mondal, 2024). These reviews examine the development, improvements, and various applications of YOLO architectures in detail. Innovations in different YOLO versions, performance evaluations, and their use across various domains have been thoroughly analyzed. It comparatively analyzes the technical specifications and performance of YOLO versions. Additionally, the impact of YOLO on real-time computer vision research and its potential future developments have been discussed. For example, Terven and Cordova-Esparza (2023) provide a detailed examination of developments from YOLOv1 through YOLOv8 and YOLO-NAS.

DL based studies for the detection and monitoring of forest fires are generally classified into three main categories in the literature: fire classification, fire localization, and fire segmentation (Cheng et al., 2024). Under these categories, both image- and video-based approaches have been developed. While methods such as coping with insufficient data, combining multi-scale information, integrating attention mechanisms, designing lightweight networks and energy-friendly models are prominent in image-based fire classification studies, two-stream architectures have been frequently preferred in video-based classifications. In video-based classification, two-stream architectures are commonly used. Similarly, in fire localization and segmentation studies, multi-level feature integration, the use of attention

mechanisms, pure DL approaches, and transfer learning methods are widely applied (Cheng et al., 2024).

In this study, object detection will specifically focus on the classification of fire, smoke, humans, and vehicles in images. Accordingly, in addition to the general literature framework summarized above, a summary of studies in the literature relevant to the tasks targeted in this project is presented in Table 1.

**Table 1:** Existing literature on forest fire detection

| **Paper** | **Objective** | **Proposed Method** | **Data Source** | **Data Type, Task & Class Labels** |
|---|---|---|---|---|
| Yunu-sov et al. (2024) | To accurately detect both large- and small-scale forest fires using a YOLOv8 and transfer learning (TranSDet)-based ensemble approach. | YOLOv8 and TranSDet ensemble models | A specially compiled dataset from the internet: 7,000 images in total, augmented to 24,000 images | Image data – Detection – Two classes: Fire, No Fire |
| Zheng et al. (2024) | To propose an enhanced deep convolutional neural network (MDCNN) model, strengthened with transfer learning, capable of detecting forest fires from video images with high accuracy. | AlexNet-based MDCNN model | Real images collected from various scenarios containing both fire and non-fire scenes | Image data – Detection – Two classes: Fire, No Fire |
| Cao et al. (2024) | To improve the precision, accuracy, and speed of forest fire detection through architectural enhancements within a YOLOv5-based framework. | YOLOv5 (re-parameterized convolution, attention mechanism, etc.) | Images collected from multiple sources such as VisiFire, Forestry Images, and news visuals (2,876 images in total) | Image data – Detection – Three classes: Small, Medium, Large fire categories |
| Alkham-mash et al. (2025) | To compare YOLOv9, YOLOv10, and YOLOv11 models in terms of fire and smoke detection performance. | YOLOv9, YOLOv10, YOLOv11 | Smoke and Fire Dataset (11,667 images), D-Fire Dataset (21,527 images) | Image data – Detection – Three classes: Smoke, Fire, None |
| Li et al. (2025) | To enhance detection accuracy, speed, and reliability for multi-scale forest fires using the proposed YOLOGX model built upon the YOLOv8 architecture. | YOLOGX | D-Fire Dataset (21,527 images) | Image data – Detection – Four classes: Fire, Smoke, Fire + Smoke, None |
| Wang et al. (2025) | To propose a lightweight and real-time enhanced YOLOv8 model (DSS-YOLO) for early | DSS-YOLO (YOLOv8n + dynamic | mytest-hrswj open-source dataset: 2,384 | Image data – Detection – Two classes: Fire, No |

| | | | | |
|---|---|---|---|---|
| | and accurate detection of small, partially occluded, and rapidly spreading fires. | convolution + attention module) | labeled images (forest, indoor, building, lighter, etc. fire scenarios) | Fire |
| Kowals-ki et al. (2025) | To develop a real-time system capable of detecting fire and smoke from camera images to improve the accuracy of early warning systems. | YOLOv8 | Roboflow “fire-smoke-dataset” (6,600 images) | Image data – Detection – Two classes: Fire, Smoke |
| Alam et al. (2025) | To propose an optimized, resource-efficient, and interpretable CNN model (FireNet-CNN) for real-time forest fire detection. | FireNet-CNN | A combination of real and synthetic fire and non-fire images collected from multiple video and visual sources | Image data – Detection – Two classes: Fire, No Fire |

As shown in Table 1, most studies in the existing literature on image-based fire detection focus solely on binary classification (e.g., “fire / no fire,” “smoke / no smoke”). The diversity of target objects in these studies is therefore quite limited. Unlike previous work, this study aims to enhance situational awareness in fire scenes by employing multi-class object detection. In addition to fire and smoke, the proposed approach also includes additional classes such as humans and vehicles.

As shown in Table 1, another need frequently emphasized in the literature as a direction for future studies is increasing data diversity and ensuring generalizability across different scenarios (e.g., low light conditions, various geographic regions, nighttime scenes). The Aerial Rescue dataset, which is planned to be used in this study, consists of images from diverse environments annotated with fire, human, and vehicle labels. Additional classes can be included to further enhance diversity. In this respect, the study aims to provide a comprehensive object recognition capability that can support emergency response during fire incidents by utilizing different YOLOv11 architectures.

## 3. MATERIAL METHOD

In this section, the dataset, methods, and implementation details used in the study are presented.

### 3.1 Dataset and Preprocessing

In this study, the *Aerial Rescue Object Detection* dataset, an open-source image collection containing rescue missions labeled with fire, human, and vehicle classes, was used. This dataset is not yet widely adopted in the literature. It was obtained from the Kaggle platform and includes 30,000 aerial

images related to rescue operations, along with a corresponding JSON annotation file. A few representative images from the dataset are shown in Figure 1.

The dataset was created within the framework of the *German Rescue Robotics Center* research project. It is designed for object detection tasks focused on aerial images and rescue scenarios. However, the dataset in its original form is not directly compatible with YOLO models. Therefore, the labels were extracted from the JSON file and reconstructed to align with the YOLO architecture.

**Figure 1.** Representative samples from the *Aerial Rescue Object Detection* dataset (Kaggle, 2023).

### 3.2 Object Detection Model: The YOLO Family and Its Evolution

A large number of DL models have been developed for object detection in recent years (Redmon et al., 2016). Many models, such as Region-Based Convolutional Neural Networks (R-CNNs), detect objects through a two-stage process. In the first stage, bounding boxes or Regions of Interest (ROIs) are generated to locate potential objects. In the second stage, these regions are classified (Redmon et al., 2016).

In contrast, YOLO models simplify this process by performing detection in a single stage. The model processes the input image only once to generate predictions. Therefore, YOLO is an efficient computer vision approach used for both object detection and real-time image segmentation (Rawat et al., 2024).

The original YOLO model was the first to integrate bounding box regression and class prediction into a single, end-to-end differentiable network (Redmon et al., 2016). This architecture enables YOLO models to operate faster, more accurately, and more efficiently than two-stage or region-based alternatives (Redmon et al., 2016).

The first YOLO model was introduced by Redmon and colleagues in 2015. Since then, various versions have been released, including YOLOv3, YOLOv4, YOLOv5, YOLOv6, YOLOv7, YOLOv8, YOLO-NAS, YOLOv9, YOLOv10, and YOLOv11 (Terven & Cordova-Esparza, 2023; Rawat et al., 2024). Each new version aims to overcome the limitations of its predecessors while improving performance, accuracy, and efficiency through new architectural strategies and technical optimizations.

For example, YOLOv3 employed the Darknet-53 backbone and achieved improvements in small object detection through multi-scale predictions. YOLOv4 was built on the CSPDarknet-53 backbone, which used Cross Stage Partial (CSP) connections to reduce parameter count and enhance feature reuse. With the addition of the PANet neck, it combined features from different levels to produce stronger feature representations.

YOLOv5, developed by Ultralytics, is a PyTorch-based version supporting additional tasks such as segmentation, pose estimation, and classification. YOLOv6, which uses the ResNet-50 backbone, achieved state-of-the-art performance on the COCO dataset.

YOLOv7 preserved the CSPDarknet-53 backbone while incorporating an enhanced attention mechanism and an updated label assignment approach. In addition, it extends its capabilities to tasks such as instance segmentation and pose estimation. Both YOLOv8 and YOLO-NAS are open-source and highly adaptable frameworks, allowing continued refinement and customization (Chopde et al., 2022).

YOLOv9 introduced innovative components such as the Generalized Efficient Layer Aggregation Network (GELAN) and Programmable Gradient Information (PGI), which reduce information loss and improve gradient flow during training. These features enhanced both accuracy and efficiency.

YOLOv10 provides an end-to-end solution for real-time object detection. It eliminates the Non-Maximum Suppression (NMS) step through a consistent dual assignment strategy, reducing inference latency. In addition, the model employs an efficient classification head with reduced complexity, a downsampling method that separates spatial and channel information, and a rank-based block structure — all of which contribute to improved accuracy and computational performance.

YOLOv11 brought major architectural innovations compared to earlier versions. The model features a transformer-based backbone and a dynamic head design, achieving superior results in small object detection and overall accuracy (Terven & Cordova-Esparza, 2023). Additionally, several attention mechanisms and data processing strategies have been integrated to further improve efficiency (Terven & Cordova-Esparza, 2023; Brahmbhatt et al., 2023; Alkhatib et al., 2023; Dutta & Mondal, 2024).

The evolution of the YOLO family has continued with YOLOv12 and YOLOv13. YOLOv12 centers around attention mechanisms and is designed for real-time object detection. It preserves the high-speed advantage of earlier CNN-based versions while leveraging the powerful representation capabilities of attention-based architectures. YOLOv12 demonstrates superior performance compared to YOLOv10 and YOLOv11 in both accuracy and speed, achieving higher mAP scores with lower latency (Tian, Ye & Doermann, 2025).

YOLOv13 is a lightweight yet high-accuracy detector developed for real-time object detection. With its Hypergraph-based Adaptive Correlation Enhancement (HyperACE) mechanism, it captures global high-order correlations and overcomes the local information limitations of previous YOLO versions. Moreover, its Full-Pipeline Aggregation-and-Distribution (FullPAD) structure improves information flow and representational capacity. As a result, YOLOv13 achieves higher accuracy with fewer parameters and lower computational cost compared to YOLOv11 and YOLOv12 (Lei et al., 2025).

### 3.3 YOLOv11n Model

In this study, the YOLOv11n model was chosen to achieve high-accuracy and low-latency detection of smoke and flames in the early stages of forest fires. YOLOv11n is the lightest and most efficient version of the YOLOv11 family, specifically optimized for real-time object detection on resource-constrained hardware (Terven & Cordova-Esparza, 2023). The model's transformer-based backbone, dynamic head design, and Partial Self-Attention (PSA) mechanism capture long-range dependencies, providing a notable improvement in the detection of small objects (Brahmbhatt et al., 2023; Dutta & Mondal, 2024).

The YOLOv11 architecture incorporates several innovative components—such as NMS-free training, a dual-label assignment strategy, and large-kernel convolutional layers—which enhance detection accuracy while reducing inference time (Alkhatib et al., 2023). These features offer significant advantages for real-time applications that require rapid decision-making, such as forest fire detection.

The YOLOv11 family is available in five variants designed to meet different hardware capacities and performance requirements: n (nano, 2.6M parameters), s (small, 9.4M), m (medium, 20.1M), l (large, 25.3M), and x (extra-large, 56.9M) (Rawat et al., 2024). All versions share the same core architecture but differ in parameter count, computational cost, and accuracy levels.

Due to its low parameter count and optimized architecture, the YOLOv11n model can operate efficiently even on platforms with limited computational resources—such as embedded systems, fixed surveillance cameras, or unmanned aerial vehicles (Terven & Cordova-Esparza, 2023). This lightweight structure also reduces power consumption, providing sustainable processing performance during long-term field monitoring.

In conclusion, the YOLOv11n model presents a balanced architecture that combines high speed, low latency, and satisfactory detection accuracy. Its use enhances the effectiveness of early warning systems for forest fires and enables rapid response in disaster management processes. The general architecture of the YOLOv11n model is illustrated in Figure 2.

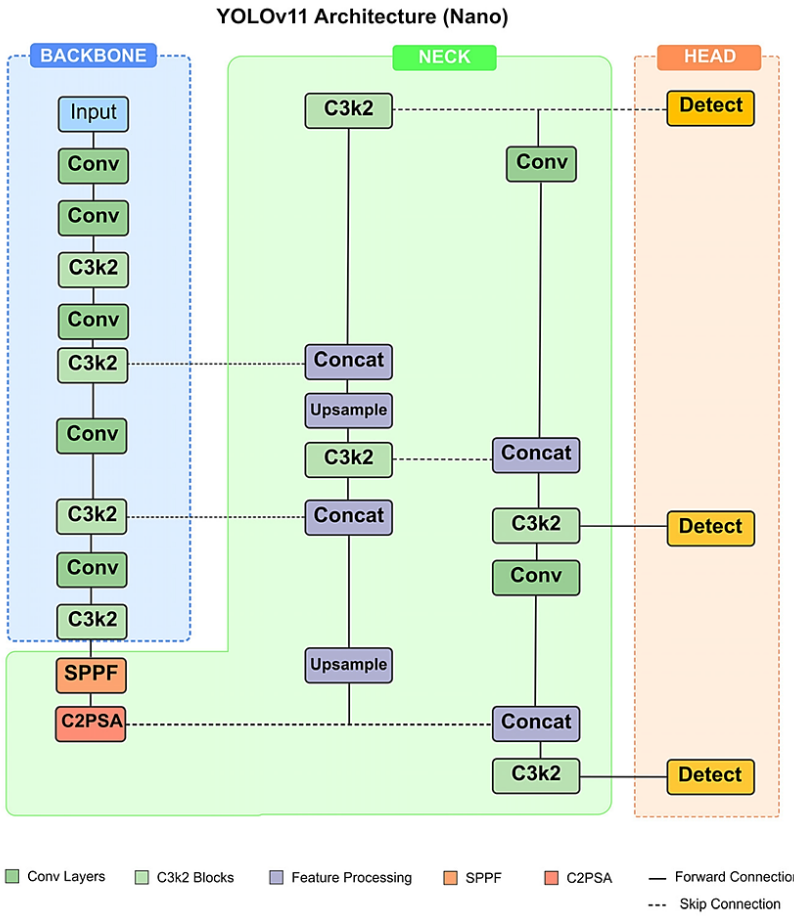


**Figure 2.** The architecture of the YOLOv11n model (Yaniz et al., 2025)

### 3.4 Implementation of YOLO-Based Model

The study was implemented in Python using the Ultralytics and PyTorch libraries, with the *Aerial Rescue Object Detection* dataset and the YOLOv11n model. In the application, the nano version of the pre-trained YOLOv11 model was employed. The YOLOv11n model consists of a total of 100 layers and contains 2,582,737 parameters.

All images in the dataset were randomly divided into 70% training, 10% validation, and 20% testing subsets. In the YOLOv11n configuration, only the following parameters were adjusted: number of epochs= 50, image size = 320, and batch size = 4.

The YOLOv11n model was trained with the *Aerial Rescue Object Detection* dataset to perform multi-object detection. To evaluate the model's performance, the precision, recall, and mean average precision (mAP50 and mAP@0.5:0.95)

metrics were used. Precision and recall are computed as shown in Equations (1) and (2). Precision represents the percentage of correctly predicted positive instances among all predicted positives, while recall indicates the percentage of correctly predicted positives among all actual positives.

$$Precision = \frac{TP}{TP + FP} \quad (1)$$

$$Recall = \frac{TP}{TP + FN} \quad (2)$$

Here, TP (true positive) counts correctly identified forest fires, FP (falsepositive) counts non-fire events wrongly labeled as fires, and FN (false negative) counts actual fires that were missed.

Mean Average Precision (mAP) is a widely used metric in computer vision to assess the accuracy of object detection models. It is based on the precision (P) and recall (r) values for each class. The average precision (AP) is calculated using Equation (3), and the mean of AP values across all classes yields the mAP value, as shown in Equation (4).

A key concept in this evaluation is the Intersection over Union (IoU), which measures the overlap between the predicted bounding box and the ground truth box. mAP@0.5 (mAP50) refers to the average precision calculated at a single IoU threshold of 0.50. This metric provides an overall indication of the model's detection capability but offers a more tolerant evaluation.

In contrast, mAP@0.5:0.95 is the mean of AP values computed at ten different IoU thresholds ranging from 0.50 to 0.95, with increments of 0.05 (i.e., 0.50, 0.55, ..., 0.95). This metric provides a more comprehensive and realistic assessment, as it captures not only detection accuracy but also the precision of bounding box localization.

$$AP = \int_0^1 P(r)dr \quad (3)$$

$$\text{mAP} = \frac{1}{\text{m}} \sum_{\text{i=1}}^{\text{m}} \text{AP(i)} \quad (4)$$

## 4 RESULTS and DISCUSSION

The YOLOv11n-based multi-object detection model developed in this study was trained on the *Aerial Rescue Object Detection* dataset. The performance metrics of the model are presented in Table 2.

According to Table 2, the model achieved an overall Precision (P) of 86.3%, Recall (R) of 79.1%, mAP@0.5 of 88.1%, and mAP@0.5:0.95 of 61.1%. These results indicate that the YOLOv11n model can perform object detection with high accuracy despite its compact and lightweight architecture.

When analyzed by class, the *"human"* category achieved the highest accuracy, with P = 0.876 and R = 0.811, showing that the model can effectively distinguish human objects. The *"vehicle"* class also demonstrated strong performance (P = 0.865, R = 0.808). However, the *"fire"* class exhibited a relatively lower recall value (R = 0.754).

This difference is likely due to the high intra-class variation in the *fire* category, as fire objects can appear in diverse shapes, colors, and intensities.

**Table 2** Performance metrics of the YOLOv11n model

| Class | Number of Images | Number of Instances | Precision (P) | Recall (R) | mAP@0.5 | mAP@0.5:0.95 |
|---|---|---|---|---|---|---|
| Fire | 2544 | 7671 | 0.849 | 0.754 | 0.864 | 0.589 |
| Human | 1135 | 3743 | 0.876 | 0.811 | 0.896 | 0.654 |
| Vehicle | 1094 | 10,989 | 0.865 | 0.808 | 0.882 | 0.591 |
| All | 2974 | 22,403 | 0.863 | 0.791 | 0.881 | 0.611 |

Additionally, the class-based confusion matrix and the normalized confusion matrix of the model are presented in Figure 3(a) and Figure 3(b). Figure 3 illustrates the distribution between the model's predictions and the ground truth labels, as well as the normalized accuracy ratios for each class.

The confusion matrix in Figure 3(a) shows that the model occasionally confuses the *"fire"* class with the *"background"* class, whereas the *"vehicle"* and *"human"* classes are more distinctly separated. When the normalized confusion matrix (Figure 3(b)) is examined, the correct classification rates for each class are observed as follows: *fire*: 0.84, *human*: 0.86, *vehicle*: 0.86, and *background*: 0.46. These values confirm that distinguishing between *fire* and *background* remains the most challenging aspect for the model.

The variations in the loss functions during training and validation are shown in Figure 4. Both the training (train) and validation (val) stages demonstrate that *box loss*, *cls loss*, and *dfl loss* values consistently decrease, while *precision*, *recall*, *mAP@0.5*, and *mAP@0.5:0.95* metrics steadily increase throughout the

iterations. This trend indicates that the model achieves stable convergence without showing signs of overfitting.

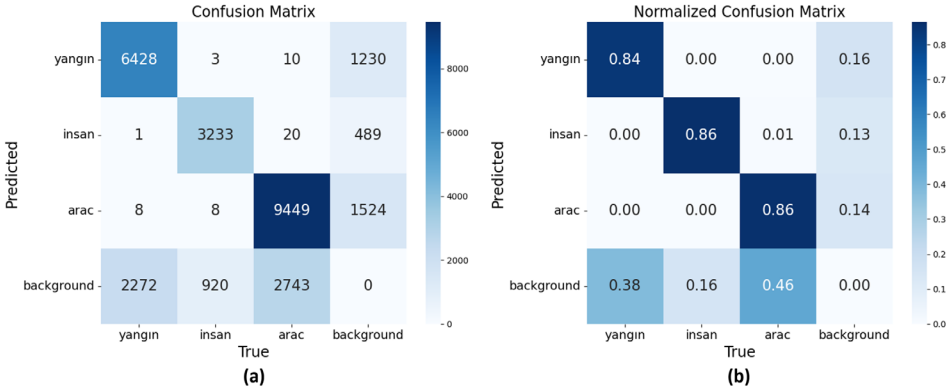


**Figure 3**. Confusion matrices of the YOLOv11n model on the Aerial Rescue Object Detection dataset: (a) Raw Confusion Matrix, (b) Normalized Confusion Matrix.

Finally, Figure 5 presents sample detection results. As shown in the images, the model successfully detects *fire*, *human*, and *vehicle* objects in most cases. However, in certain scenes, small or partially occluded fire regions are occasionally missed. This limitation is one of the main factors contributing to the relatively lower mAP@0.5:0.95 value.

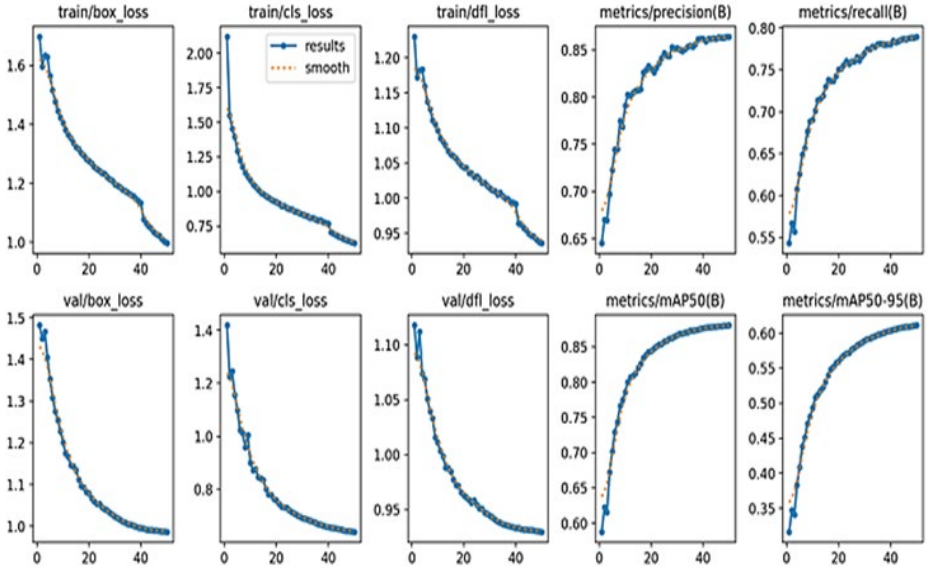


**Figure 4.** YOLOv11n training and validation loss functions

Overall, the YOLOv11n model produced satisfactory accuracy results despite its low parameter count and high processing speed. It is anticipated that the mAP scores could be significantly improved by using a larger and more

diverse dataset, higher-resolution input images, longer training durations, and ensemble learning approaches.

## 5 CONCLUSION

In this study, an artificial intelligence–based multi-object detection system was developed to enable early detection of forest fires and to identify objects such as humans and vehicles at the scene. The system was implemented using the YOLOv11n model, which is lightweight and efficient enough to operate effectively even on devices with limited hardware resources.

Training and testing were conducted on the *Aerial Rescue Object Detection* dataset. The model demonstrated high accuracy and fast detection performance. The obtained results showed that the model can reliably distinguish critical objects, particularly the *"human"* and *"vehicle"* classes, achieving high precision and recall values. The relatively lower performance observed in the *"fire"* class is attributed to the high intra-class variation, as fires can appear in diverse shapes, colors, and intensities. Both the confusion matrices and the sample detection images confirm that the model possesses reliable and fast object detection capability overall.

The main contributions of this study include presenting an artificial intelligence solution that can support early intervention processes and offering a lightweight model applicable in disaster management even under hardware constraints. Additionally, the high accuracy achieved by the system demonstrates its potential for real-time deployment.

However, the study also has certain limitations. The dataset used contains a limited number of medium-resolution images, and the high variability within the *fire* class restricted the model's full performance. Furthermore, constraints in training duration and parameter settings prevented the model from reaching its maximum potential.


**Figure 5.** YOLOv11n object detection results

For future research, expanding the dataset is crucial to improve model accuracy and sensitivity. The model should be trained with high-resolution images captured under varying conditions, such as smoke, fog, different lighting, day and night scenarios, and diverse weather environments. This would enhance the model's ability to perform reliable detections across different contexts.

In addition, the performance could be further improved through technical advancements in YOLO architectures and by incorporating ensemble learning techniques. In this regard, enhancing the proposed approach in terms of both data diversity and algorithmic optimization is considered a critical step toward increasing its reliability for early warning systems and disaster management applications.

## REFERENCE


Alam, G. M. I., Tasnia, N., Biswas, T., Hossen, M. J., Tanim, S. A., & Miah, M. S. U. (2025). Real-Time Detection of Forest Fires Using FireNet-CNN and Explainable AI Techniques. IEEE Access. https://doi.org/10.1109/ACCESS.2025.3552352

Agbeshie, A. A., Abugre, S., Atta-Darkwa, T., & Awuah, R. (2022). A review of the effects of forest fire on soil properties. Journal of Forestry Research, 33(5), 1419–1441.

Aerial Rescue Object Detection Dataset from Kaggle. (2023). Kaggle. https://www.kaggle.com/datasets/julienmeine/rescue-object-detection

Alkhatib, W., Albattah, W., & Khan, M. A. (2023). The YOLO Framework: A Comprehensive Review of Evolution, Improvements, and Applications. Computers, 13(12), 336. https://doi.org/10.3390/computers13120336

Alkhammash, E. H. (2025). A comparative analysis of YOLOv9, YOLOv10, YOLOv11 for smoke and fire detection. Fire, 8(1), 26. https://doi.org/10.3390/fire8010026

Al-Smadi, Y., Alauthman, M., Al-Qerem, A., Aldweesh, A., Quaddoura, R., Aburub, F., ... & Alhmiedat, T. (2023). Early wildfire smoke detection using different YOLO models. Machines, 11(2), 246.

Boroujeni, S. P. H., Mehrabi, N., Afghah, F., McGrath, C. P., Bhatkar, D., Biradar, M. A., & Razi, A. (2025). Fire and smoke datasets in 20 years: An in-depth review. arXiv preprint arXiv:2503.14552.

Bowman, D. M., Kolden, C. A., Abatzoglou, J. T., Johnston, F. H., van der Werf, G. R., & Flannigan, M. (2020). Vegetation fires in the Anthropocene. Nature Reviews Earth & Environment, 1(10), 500–515.

Brahmbhatt, M., Shah, S., & Sanghvi, J. (2023). A comprehensive review of YOLO architectures in computer vision: From YOLOv1 to YOLOv8 and YOLO-NAS. arXiv preprint arXiv:2304.00501.

Butt, E. W., Conibear, L., Reddington, C. L., Darbyshire, E., Morgan, W. T., Coe, H., ... & Spracklen, D. V. (2020). Large air quality and human health impacts due to Amazon forest and vegetation fires. Environmental Research Communications, 2(9), 095001.

Cao, L., Shen, Z., & Xu, S. (2024). Efficient forest fire detection based on an improved YOLO model. Visual Intelligence, 2(20), 1–13. https://doi.org/10.1007/s44267-024-00053-y

Cheng, G., Chen, X., Wang, C., Li, X., Xian, B., & Yu, H. (2024). Visual fire detection using deep learning: A survey. Neurocomputing, 127975.

Chopde, A., Magon, A., & Bhatkar, S. (2022, April). Forest Fire Detection and Prediction from image processing using RCNN. In Proceedings of the 7th World Congress on Civil, Structural, and Environmental Engineering (pp. 10–12). Virtual.

De Almeida Pereira, G. H., Fusioka, A. M., Nassu, B. T., & Minetto, R. (2021). Active fire detection in Landsat-8 imagery: A large-scale dataset and a deep-learning study. *ISPRS Journal of Photogrammetry and Remote Sensing*, *178*, 171-186.

Dewangan, A., Pande, Y., Braun, H. W., Vernon, F., Perez, I., Altintas, I., ... & Nguyen, M. H. (2022). FIgLib & SmokeyNet: Dataset and deep learning model for real-time wildland fire smoke detection. Remote Sensing, 14(4), 1007.

Dutta, A., & Mondal, A. (2024). YOLOv1 to YOLOv10: The Fastest and Most Accurate Real-Time Object Detection Systems. arXiv preprint arXiv:2408.09332.

Hong, Z., Hamdan, E., Zhao, Y., Ye, T., Pan, H., & Cetin, A. E. (2024). Wildfire detection via transfer learning: a survey. Signal, Image and Video Processing, 18(1), 207–214.

Kowalski, S., Malinowski, J., Drzymała, A. J., & Korzeniewska, E. (2025). Application of the YOLO algorithm in fire and smoke detection systems for early detection of forest fires in real time. Przegląd Elektrotechniczny, 101(2), 44–47. https://doi.org/10.15199/48.2025.02.11

Lei, M., Li, S., Wu, Y., Hu, H., Zhou, Y., Zheng, X., ... & Gao, Y. (2025). YOLOv13: Real-Time Object Detection with Hypergraph-Enhanced Adaptive Visual Perception. arXiv preprint arXiv:2506.17733.

Li, C., Du, Y., Zhang, X., & Wu, P. (2025). YOLOGX: An improved forest fire detection algorithm based on YOLOv8. Frontiers in Environmental Science, 12, 1486212. https://doi.org/10.3389/fenvs.2024.1486212

Özel, B., Alam, M. S., & Khan, M. U. (2024). Review of Modern Forest Fire Detection Techniques: Innovations in Image Processing and Deep Learning. Information, 15(9), 538.

Raita-Hakola, A. M., Rahkonen, S., Suomalainen, J., Markelin, L., Oliveira, R., Hakala, T., ... & Pölönen, I. (2023). Combining YOLOv5 and transfer learning for smoke-based wildfire detection in boreal forests. The International Archives of the Photogrammetry, Remote Sensing and Spatial Information Sciences, 48, 1771–1778.

Rawat, S., Rawat, A. S., Mewad, V. S., & Vaidya, H. (2024, April). Comparative Image Processing and Object Detection in Aerial Search and Rescue. In 2024 International Conference on Cognitive Robotics and Intelligent Systems (ICC-ROBINS) (pp. 676–681). IEEE.

Redmon, J., Divvala, S., Girshick, R., & Farhadi, A. (2016). You only look once: Unified, real-time object detection. In Proceedings of the IEEE conference on computer vision and pattern recognition (pp. 779–788).

Sdraka, M., Dimakos, A., Malounis, A., Ntasiou, Z., Karantzalos, K., Michail, D., & Papoutsis, I. (2024). FLOGA: A machine learning ready dataset, a benchmark and a novel deep learning model for burnt area mapping with Sentinel-2. IEEE Journal of Selected Topics in Applied Earth Observations and Remote Sensing.

Shang, D., Zhang, F., Yuan, D., Hong, L., Zheng, H., & Yang, F. (2024). Deep learning-based forest fire risk research on monitoring and early warning algorithms. Fire, 7(4), 151.

Terven, J., Córdova-Esparza, D. M., & Romero-González, J. A. (2023). A comprehensive review of YOLO architectures in computer vision: From YOLOv1 to YOLOv8 and YOLO-NAS. Machine Learning and Knowledge Extraction, 5(4), 1680–1716.

Tian, Y., Ye, Q., & Doermann, D. (2025). Yolov12: Attention-centric real-time object detectors. arXiv preprint arXiv:2502.12524.

Vallet, L., Abdallah, C., Lauvaux, T., Joly, L., Ramonet, M., Ciais, P., ... & Mouillot, F. (2025). Soil smoldering in temperate forests: a neglected contributor to fire carbon emissions revealed by atmospheric mixing ratios. Biogeosciences, 22(1), 213–242.

Wang, H., Fu, X., Yu, Z., & Zeng, Z. (2025). DSS-YOLO: An improved lightweight real-time fire detection model based on YOLOv8. Scientific Reports, 15, 8963. https://doi.org/10.1038/s41598-025-93278-w

Xu, Y., Berg, A., & Haglund, L. (2024, July). SEN2FIRE: A Challenging Benchmark Dataset for Wildfire Detection Using Sentinel Data. In IGARSS 2024 - IEEE International Geoscience and Remote Sensing Symposium (pp. 239–243). IEEE.

Yániz, J., Casalongue, M., Martinez-de-Pison, F. J., Silvestre, M. A., Consortium, B., Santolaria, P., & Divasón, J. (2025). An AI-Based Open-Source Software for Varroa Mite Fall Analysis in Honeybee Colonies. Agriculture, 15(9), 969.

Yunusov, N., Islam, B. M. S., Abdusalomov, A., & Kim, W. (2024). Robust forest fire detection method for surveillance systems based on YOLOv8 and transfer learning approaches. Processes, 12(5), 1039. https://doi.org/10.3390/pr12051039

Zheng, S., Zou, X., Gao, P., Zhang, Q., Hu, F., Zhou, Y., ... & Chen, S. (2024). A Forest Fire Recognition Method Based on Modified Deep CNN Model. Forests, 15(1), 111. https://doi.org/10.3390/f15010111

Zhou, K., & Jiang, S. (2025). Forest Fire Detection Algorithm Based on Improved YOLOv11n. Sensors, 25(10), 2989.

# Chapter 11

# IMAGE-BASED CLASSIFICATION OF POTATO DISEASES USING RESNET VARIANTS AND STACKING ENSEMBLE MODEL DESIGN

**İbrahim ARUK**[1]

## INTRODUCTION

One significant economic sector that supports national development is agriculture. It gives people who live close to the land food. Increased agricultural output is necessary to meet the growing demand for food due to population growth [1, 2].

The agriculture sector is severely harmed by agricultural pests and bad weather. Plant leaves, stems, roots, and fruits can also be harmed by a number of diseases. Plant diseases lower crop yields and quality. Global food shortages and insecurity are a result of these detrimental effects getting worse [3, 4]. Effectively monitoring and treating plant diseases in agriculture is challenging. The safety of the production cycle depends on these processes [5]. One of the world's main staple foods is the potato plant. In many parts of the world, potatoes are grown in large numbers [6, 7].

Potato plants are very susceptible to diseases, which causes a number of problems with production [8]. The main diseases that affect this plant are early blight and late blight. These two diseases are caused by the pathogens Alternaria solani and Phytophthora infestans [9]. Dark spots on the leaves, fruit, and stems of the plant are common signs of early blight. Late blight affects the leaves, stems, and tubers. It causes water-soaked lesions that cause the leaves of the plant to fall off quickly [10, 11].

Detecting plant diseases in large agricultural areas using traditional methods is a very time-consuming and costly task. Recently, machine learning and deep learning architectures have been utilized to detect these diseases early and accurately. This enables the provision of fast, accurate, and less costly solutions compared to traditional methods. These methods in the field of artificial intelligence work with data sets containing a large number of images. Trained

[1] Department of Software Engineering, Faculty of Engineering, Architecture and Design, Kahramanmaras Istiklal University, 46050, Kahramanmaras, Turkey,
ibrahim.aruk@istiklal.edu.tr, (ORCID: 0009-0003-7483-4542)

models make predictions with high success rates, diagnosing and classifying diseases.

Convolutional Neural Networks (CNN), one of the deep learning architectures, consist of convolutional, pooling, and fully connected layers that can learn hierarchical representations of image features [12]. Developed by He et al. [13], the ResNet architecture, which has a popular place among CNN architectures, has many variants depending on the number of layers. CNN architectures have computational cost and training constraints that become more difficult depending on the number of layers. The ResNet architecture was developed to overcome these difficulties. The fundamental innovation in the architecture is the skip connections unit. These connections ensure that information is transferred to deeper layers of the network without distortion by skipping some layers. This prevents the model's performance from declining even as the network's depth increases and facilitates training [14].

Significant advancements in machine learning (ML) technologies incorporate algorithms that will help achieve fast and accurate results for classifying plant diseases. Among the basic classification algorithms, Support Vector Machines (SVM) [15], K-Nearest Neighbor (KNN) [16], Random Forest (RF) [17], and Decision Tree (DT) [18] algorithms were used in our study.

Stacking, a method of ensemble learning, makes it easier to combine decisions from different classification models. This method ensures success that is superior to the effectiveness of individual models [19, 20]. In our study, we built a new model using a stacking learning method framework.

## 1. EXPERIMENTAL STUDIES

### 1.1. Dataset

Hughes and Salathe [21] released the PlantVillage dataset in 2015. It is free to use. This dataset is a valuable resource for studying plant diseases in agriculture. It is often used in academic research. The collection has pictures of leaves from pepper, potato, and tomato plants that are 256×256 pixels in size and have labels.

In our study, we focused on potato plant diseases within the PlantVillage dataset. There are a total of 2,152 images divided into 3 classes: early blight, late blight, and healthy potato plant leaves. Table 1 provides the detailed numbers for these classes. Additionally, Figure 1 shows sample leaf images for all classes.

Table 1. Distribution of potato disease dataset by class

| Potato disease class | Number of images |
|---|---|
| Early blight | 1.000 |
| Late blight | 1.000 |
| Healthy | 152 |
| Total | 2.152 |

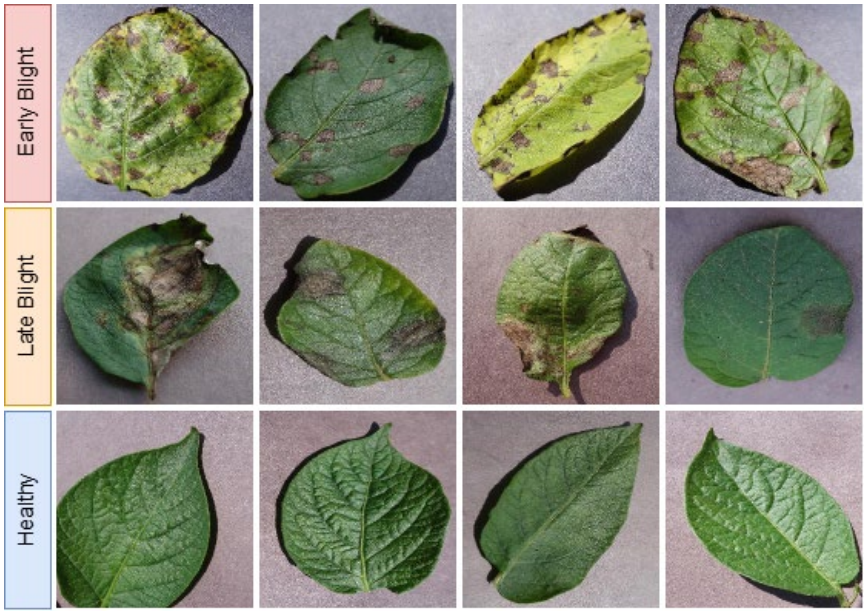


Figure 1. Sample images of the potato disease dataset by class

### 1.2. Proposed method

In this study, a stacking ensemble model was developed for the automatic classification of diseases on potato plant leaves in the obtained dataset. This hybrid structure, created using deep learning and traditional machine learning methods, aims to achieve performance above that of individual models. In this context, the model is based on deep feature extractors based on transfer learning and a multi-layer classifier architecture.

The created architecture is shown in Figure 2. In the first step of this architecture, the dataset was divided into three different subsets: 70% training data, 15% validation data, and 15% test data. The training and validation data were used to train both the basic classifiers and the meta-learner. During the feature extraction phase from the images, five pre-trained variants of the ResNet architecture at different depths were used. These are the ResNet18, ResNet34, ResNet50, ResNet121, and ResNet154 models. Feature vectors were obtained

from each of these architectures for the training images, providing a suitable input for the machine learning algorithms in the subsequent stage.

The classification performance was analyzed using four traditional machine learning classifiers on the extracted features. These algorithms are SVM, KN, RF, and DT. Evaluations performed on the test data identified the two models with the highest classification performance. These models were ResNet18 and ResNet101. Subsequently, a stacking ensemble architecture was created using these two models. This hybrid architecture also used logistic regression as a meta-learner. The logistic regression model combines the prediction probabilities of the base classifiers on the validation data to make the final classification decision. This allows the integration of information from networks of different depths and SVM-based decision mechanisms. During the testing phase of the hybrid architecture, the same pipeline used in training was followed to evaluate the overall success of the stacking architecture.

The design of the proposed model benefits from both the powerful feature extraction capabilities of deep learning and the decision boundary formation advantages of classical machine learning algorithms. Thus, it aims to quickly, accurately, and reliably distinguish potato diseases through images. The details of the model's architecture are presented along with the flowchart and algorithmic steps.

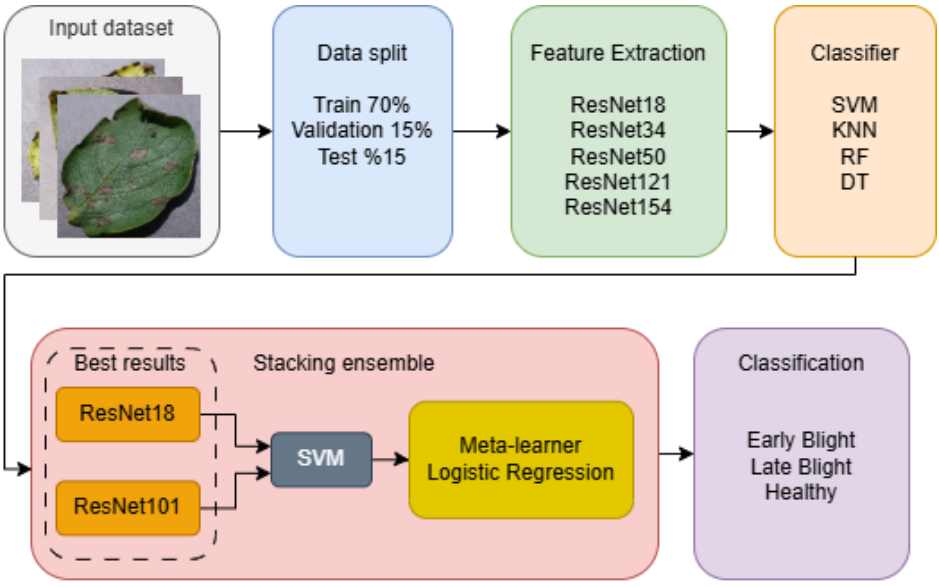


Figure 2. Proposed model architecture

## 2. EXPERIMENTAL RESULTS AND EVALUATION

In the evaluations conducted, the classification performance of deep features extracted from five different ResNet architectures was analyzed using four different machine learning algorithms. The evaluations were performed using accuracy, precision, sensitivity, and F1-score metrics. When the results given in Table 2 are evaluated, it is seen that the SVM classifier achieved higher success compared to other algorithms.

Table 2. Comparative performance results of ResNet architectures with different machine learning classifiers

| **Models** | **Classifiers** | **Accuracy** | **Precision** | **Recall** | **F1-score** |
|---|---|---|---|---|---|
| ResNet18 | SVM | **0.9938** | **0.9956** | 0.9839 | **0.9896** |
| | KNN | 0.9537 | 0.9113 | 0.9550 | 0.9300 |
| | RF | 0.9660 | 0.9759 | 0.9406 | 0.9568 |
| | DT | 0.8796 | 0.8619 | 0.8900 | 0.8749 |
| ResNet34 | SVM | 0.9815 | 0.9657 | **0.9867** | 0.9755 |
| | KNN | 0.9228 | 0.8857 | 0.9328 | 0.9027 |
| | RF | 0.9630 | 0.9600 | 0.9267 | 0.9419 |
| | DT | 0.8488 | 0.8519 | 0.8211 | 0.8345 |
| ResNet50 | SVM | 0.9877 | 0.9795 | 0.9794 | 0.9794 |
| | KNN | 0.9568 | 0.9070 | 0.9572 | 0.9279 |
| | RF | 0.9691 | 0.9636 | 0.9194 | 0.9390 |
| | DT | 0.9012 | 0.8212 | 0.8822 | 0.8440 |
| ResNet101 | SVM | **0.9938** | 0.9839 | 0.9839 | 0.9839 |
| | KNN | 0.9568 | 0.9368 | 0.9456 | 0.9402 |
| | RF | 0.9784 | 0.9716 | 0.9494 | 0.9599 |
| | DT | 0.9136 | 0.8977 | 0.9144 | 0.9040 |
| ResNet152 | SVM | 0.9877 | 0.9593 | 0.9794 | 0.9689 |
| | KNN | 0.9568 | 0.9110 | 0.9456 | 0.9261 |
| | RF | 0.9815 | 0.9744 | 0.9633 | 0.9687 |
| | DT | 0.9198 | 0.8739 | 0.9072 | 0.8887 |

The models with the highest classification performance using the SVM algorithm were the ResNet18 and ResNet101 architectures, with accuracy rates of 0.9938. The ResNet18 architecture, using the SVM algorithm, demonstrated successful performance in positive identifications with a high precision value of 0.9956. This

model achieved a balance between metrics with an F1-score of 0.9896. Similarly, the ResNet101 architecture achieved balanced and high results across all metrics with the SVM algorithm.

After the SVM algorithm, the RF classification algorithm was found to be the second most successful. RF showed high accuracy rates ranging from 0.9630 to 0.9815 with all ResNet variants. In particular, the ResNet152 architecture with the RF algorithm yielded the closest result to the model performance achieved with the SVM algorithm, with an accuracy of 0.9815 and an F1-score of 0.9687.

The KNN algorithm generally lagged slightly behind the RF algorithm, showing acceptable accuracy rates ranging from 0.9228 to 0.9568 with the ResNet34 architecture. However, the KNN algorithm's precision metric of 0.9113 achieved with the ResNet18 architecture is lower than the RF model's value of 0.9759 achieved with the same architecture, indicating that this model has a higher tendency to produce false positives.

The evaluations revealed that the DT algorithm delivered the weakest and most variable performance. The DT algorithm provided the lowest accuracy and F1-score values across all ResNet architectures. The observation of the lowest performance with an accuracy rate of 0.8488 in the ResNet34 model indicates that this classifier is insufficient for the current problem.

When the ResNet architectures tested at different depths are evaluated overall, it is seen that architectural depth does not have a linear effect on performance. The shallowest model in the evaluation, the ResNet18 architecture, achieved an accuracy of 0.9938 with the SVM algorithm, while deeper architectures such as ResNet34 (0.9815 accuracy) and ResNet50 (0.9877 accuracy) achieved lower performance. The deepest architecture in the studies, ResNet152, showed lower performance than both ResNet18 and ResNet101 architectures with an accuracy of 0.9877, indicating that feature quality may reach saturation as model depth increases. These results show that shallower models can produce more discriminative features for this task.

Based on all evaluations, using ResNet-based deep features in a hybrid structure with the SVM algorithm has been shown to be the approach with the highest performance for our study. The classification of features obtained from the ResNet18 and ResNet101 architectures using the SVM method exhibits outstanding classification performance, attaining accuracy rates of 0.9900.

After the tests, the ResNet18 and ResNet101 models were chosen for the suggested model made in this study because they did better with the SVM method. When using the SVM classifier, analyses always show that the suggested architecture improves performance on all parameters compared to the baseline models.

Table 3 shows how well the submodels and the suggested model did. The proposed model achieved an accuracy rate of 0.9969, surpassing the accuracy

rates of the ResNet18 and ResNet101 models, which were 0.9938. The improvement in performance went beyond just the overall accuracy score. The proposed model achieved a precision value of 0.9978, signifying the highest reliability in positive class predictions.

Table 3. Comparative evaluation of the proposed model and its constituent submodels

| **Model** | **Classifier** | **Accuracy** | **Precision** | **Recall** | **F1-score** |
|---|---|---|---|---|---|
| ResNet18 | SVM | 0.9938 | 0.9956 | 0.9839 | 0.9896 |
| ResNet101 | SVM | 0.9938 | 0.9839 | 0.9839 | 0.9839 |
| **Proposed Model** | SVM | **0.9969** | **0.9978** | **0.9861** | **0.9918** |

The proposed model has surpassed the recall values of 0.9839 achieved by both the ResNet18 and ResNet101 architectures, reaching a recall metric of 0.9861. As a result, it has become better at finding positive cases.

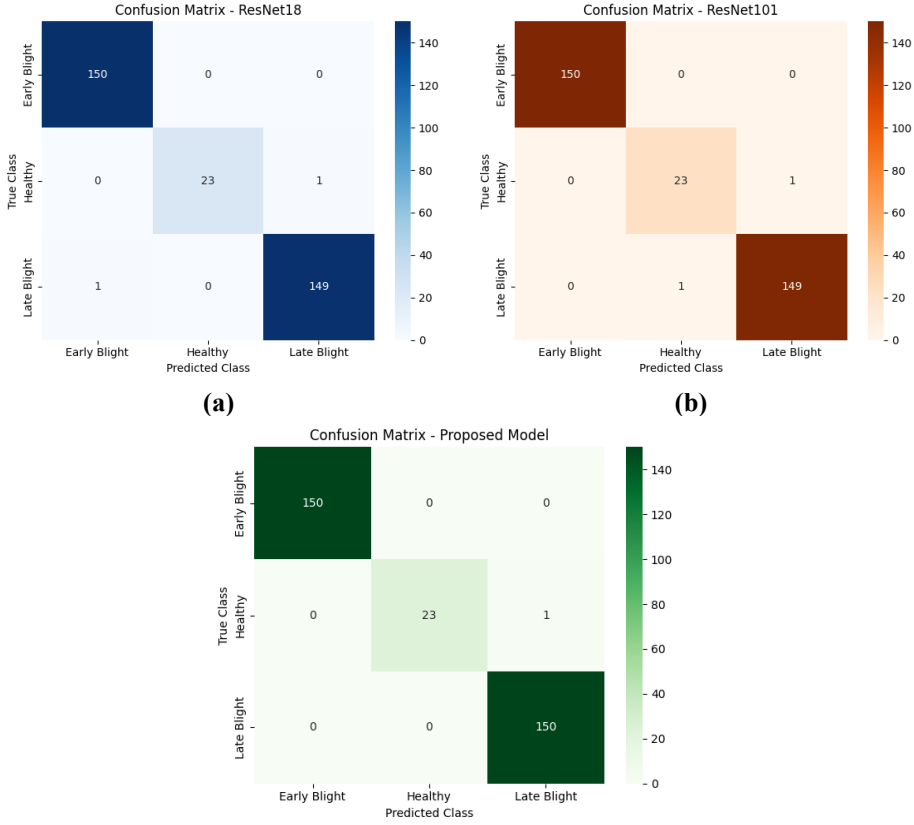


Figure 3. Confusion matrices: (a) ResNet18, (b) ResNet101, (c) Proposed model.

The proposed model did better on the F1-score, which shows that it worked well. The F1-score of 0.9918 was higher than the success rates of 0.9896 for the ResNet18 architecture and 0.9839 for the ResNet101 design. This outcome indicates that the suggested model attains equilibrium between Precision and Sensitivity metrics.

Figure 3 shows the confusion matrices for ResNet18, ResNet101, and the proposed model. Both ResNet18 and ResNet101 architectures correctly predicted all instances of the early blight class. Again, both models misclassified only one instance each from the healthy and late blight classes. The proposed model achieved higher accuracy than the other models, making an incorrect prediction for only one example belonging to the healthy class in three different class predictions. The results show that the proposed model is better at diagnosing diseases on potato leaves than the ResNet architectures that make up the model.

## 3. CONCLUSION

This thorough study has resulted in the creation of a stacking ensemble model for classifying diseases in potato foliage within the agricultural domain. Evaluations utilizing the PlantVillage dataset have clarified the classification of features extracted from ResNet architectures at five unique depths, utilizing four distinct machine learning algorithms. Based on the results, it was observed that the integration of ResNet18 and ResNet101 architectures with the SVM algorithm produced enhanced performance metrics in comparison to standalone models. The proposed model demonstrated superior performance compared to individual models, achieving an accuracy of 0.9969 and an F1-score of 0.9918, the highest recorded.

The model developed in this study can improve the prompt and accurate identification of plant diseases in agriculture. It can save time and money by giving manufacturers and researchers a good way to make decisions. The proposed technique's future utility and applicability across various plant species and diseases can be evaluated.

## REFERENCES


1. Pooniya, V., et al., *Conservation agriculture based integrated crop management sustains productivity and economic profitability along with soil properties of the maize-wheat rotation.* Scientific Reports, 2022. **12**(1): p. 1962.
2. Thai, H.-T., K.-H. Le, and N.L.-T. Nguyen, *FormerLeaf: An efficient vision transformer for Cassava Leaf Disease detection.* Computers and Electronics in Agriculture, 2023. **204**: p. 107518.
3. Iqbal, Z., et al., *An automated detection and classification of citrus plant diseases using image processing techniques: A review.* Computers and electronics in agriculture, 2018. **153**: p. 12-32.
4. Pacal, I., et al., *A systematic review of deep learning techniques for plant diseases.* Artificial Intelligence Review, 2024. **57**(11): p. 304.
5. Hu, Y., et al., *Detection of late blight disease on potato leaves using hyperspectral imaging technique.* Guang pu xue yu guang pu fen xi= Guang pu, 2016. **36**(2): p. 515-519.
6. Afzaal, H., et al., *Detection of a potato disease (early blight) using artificial intelligence.* Remote Sensing, 2021. **13**(3): p. 411.
7. Mukiibi, A., et al., *A Systematic Review of Vegetation Indices for Potato Growth Monitoring and Tuber Yield Prediction from Remote Sensing.* Potato Research, 2025. **68**(1): p. 409-448.
8. Tang, D., et al., *Genome evolution and diversity of wild and cultivated potatoes.* Nature, 2022. **606**(7914): p. 535-541.
9. Ponnuru, M.D.S. and L. Amasala. *Revolutionizing Potato Farming: A CNN-Powered Approach for Early Blight and Late Blight Detection to Ensure Global Food Security*. in *2024 IEEE International Students' Conference on Electrical, Electronics and Computer Science (SCEECS)*. 2024.
10. Norouzi, M., et al., *CRISPR/Cas StNRL1 gene knockout increases resistance to late blight and susceptibility to early blight in potato.* Frontiers in Plant Science, 2024. **14**: p. 1278127.
11. Medina, D.P., et al., *Web components for late blight (Phytophthora infestans (Mont.) De Bary) and early blight (Alternaria solani Sor.) outbreaks forecast on Solanum tuberosum L. in Cuba under future climate scenarios.* Smart Agricultural Technology, 2025: p. 101003.
12. Aruk, I., *CILT KANSERI SINIFLANDIRMASIIÇIN HIBRIT DERIN ÖGRENME MODELLERININ GELISTIRILMESI.* Erciyes Üniversitesi, Fen Bilimleri Enstitüsü, 2024.

13. He, K., et al. *Deep residual learning for image recognition*. in *Proceedings of the IEEE conference on computer vision and pattern recognition*. 2016.
14. Sarwinda, D., et al., *Deep Learning in Image Classification using Residual Network (ResNet) Variants for Detection of Colorectal Cancer.* Procedia Computer Science, 2021. **179**: p. 423-431.
15. Cortes, C. and V. Vapnik, *Support-vector networks.* Machine Learning, 1995. **20**(3): p. 273-297.
16. Steinbach, M. and P.-N. Tan, *kNN: k-nearest neighbors*, in *The top ten algorithms in data mining*. 2009, Chapman and Hall/CRC. p. 165-176.
17. Parmar, A., R. Katariya, and V. Patel. *A review on random forest: An ensemble classifier*. in *International conference on intelligent data communication technologies and internet of things*. 2018. Springer.
18. Safavian, S.R. and D. Landgrebe, *A survey of decision tree classifier methodology.* IEEE transactions on systems, man, and cybernetics, 1991. **21**(3): p. 660-674.
19. Wolpert, D.H., *Stacked generalization.* Neural networks, 1992. **5**(2): p. 241-259.
20. Yang, Y., et al., *Classification of Parkinson's disease based on multi-modal features and stacking ensemble learning.* Journal of Neuroscience Methods, 2021. **350**: p. 109019.
21. Hughes, D. and M. Salathé, *An open access repository of images on plant health to enable the development of mobile disease diagnostics.* arXiv preprint arXiv:1511.08060, 2015.

# Chapter 12

# SOLUTION OF LAKE POLLUTION MODEL WITH A NUMERICAL METHOD

**Musa ÇAKMAK[1], Sertan ALKAN[2]**

## INTRODUCTION

Water resource pollution constitutes one of the most critical global environmental problems today, creating adverse effects across a wide spectrum, from biodiversity to human health. Lakes, in particular, are water basins of great importance, serving as both sources of drinking water and key components of ecological balance. Understanding the concentration and dynamics of pollutants entering lake systems as a result of industrialization, urbanization, and agricultural activities is vital for combating pollution and developing sustainable management strategies. These dynamics are typically modeled mathematically through systems of Ordinary Differential Equations (ODEs).Lake pollution models often involve high-order differential equations with variable coefficients due to time-varying pollutant inputs and fluctuating flow rates. Analytical (closed-form) solutions for such complex systems are rarely possible. Therefore, the need for numerical methods to accurately predict the long-term behavior of the system is inevitable. In this study, the Chebyshev Collocation Method, a leading member of the Spectral Methods family, is adopted for solving the system of lake pollution models. The method relies on transforming the system into an easily solvable system of linear algebraic equations by satisfying the differential equations at selected collocation points. The primary objective of this study is to demonstrate the efficiency and reliability of the Chebyshev Collocation Method for solving the high-order differential equations of a coupled lake pollution model system. Within the scope of this work, the differential system will be converted into a matrix equation involving unknown Chebyshev coefficients, and combined with the initial conditions to obtain the final solution. The remainder of the paper is organized as follows: Section 2 presents the problem modeling, Section 3

[1] Asst. Prof. Dr., Department of Basic Sciences, Faculty of Engineering, Architecture and Design, Kahramanmaraş İstiklal University, Turkey,
musa.cakmak@istiklal.edu.tr, (ORCID: 0000-0001-6791-0971)
[2] Prof. Dr., Department of Management Information Systems, Söke Faculty of Business Administration, Aydin Adnan Menderes University, Aydin, Turkey,
sertan.alkan@adu.edu.tr, (ORCID: 0000-0002-4272-7414)

details the mathematical formulation of the Chebyshev Collocation Method, Section 4 discusses the numerical application and evaluation of results. Estimated error functions is given in Section 5, given and finally, Section 6 provides the conclusion.

This paper introduces the Chebyshev collocation method to solve a class of systems of linear differential equations that proves highly effective in modeling natural systems:

$$\sum_{k=0}^{1}\sum_{r=1}^{3} P_{jkr}(x)u_r^{(k)}(x) = g_j(x), \quad j = 1,2,3 \qquad (1)$$

with the initial conditions

$$u_1(0) = \delta_{11}, u_2(0) = \delta_{22}, \quad u_3(0) = \delta_{33} \qquad (2)$$

Here, $u_r^{(0)}(x) = u_r(x)$, $u_r^{(1)}(x) = u_r'(x)$ and $u_r(x)$ are unknown functions. In the modeling, $P_{jkr}$ and $g_j(x)$ are continuous functions defined on [-1,1]. $\delta_{11}$, $\delta_{22}$ and $\delta_{33}$ are arbitrary constants.

The objective of this work is to determine the approximate solutions of the model using by the truncated Chebyshev series defined as

$$u_r(x) = \sum_{n=1}^{N+1} c_{rn}T_n(x) \qquad r = 1,2,3. \qquad (3)$$

where $T_n(x)$ expresses the Chebyshev polynomials; $c_{rn}$ are the unknown Chebyshev polynomial coefficients ($1 \le c_{rn} \le 3(N+1)$ and N is the chosen any positive integer.

**FUNDAMENTAL PROPERTIES and RELATIONS OF CHEBYSHEV POLYNOMIALS**

The Chebyshev polynomials were firstly studied by Chebyshev, P. L., Lanczos and Clenshaw, C. W. [1,3]. The definition form of those polynomials is given as

$$T_n(x) = 2xT_{n-1}(x) - T_{n-2}(x) \quad , \quad n \ge 3 \qquad (4)$$

In the formula, $T_1(x) = 1$ and $(x) = x$. The first few Chebyshev polynomials are

$$\begin{gathered} T_1(x) = 1 \\ T_2(x) = x \\ T_3(x) = 2x^2 - 1 \\ T_4(x) = 4x^3 - 3x \\ T_5(x) = 8x^4 - 8x^2 + 1 \\ T_6(x) = 16x^5 - 20x^3 + 5x \\ T_7(x) = 32x^6 - 48x^4 + 18x^2 - 1 \\ T_8(x) = 64x^7 - 112x^5 + 56x^3 - 7x \\ T_9(x) = 128x^8 - 256x^6 + 160x^4 - 32x^2 + 1 \\ T_{10}(x) = 256x^9 - 576x^7 + 432x^5 - 120x^3 + 9x \\ \vdots \end{gathered} \tag{5}$$

Let us assume that the approximate solution of the model (1) is the series form in (3). Our aim is to determine the matrix form of eq. (1) using the series in eq. (3). First, we can express Chebyshev polynomials given in (5) in matrix form as

$$T(x) = L(x)M \tag{6}$$

In eq.(6), $T(x) = [T_1(x) \quad T_1(x) \quad \cdots \quad T_{N+1}(x)]$,

$L(x) = [1 \quad x \quad x^2 \quad x^3 \quad \cdots \quad x^N]$ and

$$M = \begin{bmatrix} 1 & 0 & -1 & 0 & 1 & 0 & -1 & 0 & 1 & 0 & \cdots \\ 0 & 1 & 0 & -3 & 0 & 5 & 0 & -7 & 0 & 9 & \cdots \\ 0 & 0 & 2 & 0 & -8 & 0 & 18 & 0 & -32 & 0 & \cdots \\ 0 & 0 & 0 & 4 & 0 & -20 & 0 & 56 & 0 & -120 & \cdots \\ 0 & 0 & 0 & 0 & 8 & 0 & -48 & 0 & 160 & 0 & \cdots \\ 0 & 0 & 0 & 0 & 0 & 16 & 0 & -112 & 0 & 432 & \cdots \\ 0 & 0 & 0 & 0 & 0 & 0 & 32 & 0 & -252 & 0 & \cdots \\ 0 & 0 & 0 & 0 & 0 & 0 & 0 & 64 & 0 & -576 & \cdots \\ 0 & 0 & 0 & 0 & 0 & 0 & 0 & 0 & 128 & 0 & \cdots \\ 0 & 0 & 0 & 0 & 0 & 0 & 0 & 0 & 0 & 256 & \cdots \\ \vdots & \vdots & \vdots & \vdots & \vdots & \vdots & \vdots & \vdots & \vdots & \vdots & \ddots \end{bmatrix}$$

The approximate solution in eq.(3) can be expressed in the matrix form of

$$u_r(x) = T(x)C_r \tag{7}$$

In eq.(7), $C_r$ matrix is defined by

$$C_r = [c_{r1} \quad c_{r2} \quad \cdots \quad c_{r(N+1)}], \quad r = 1,2,3$$

With the help of eq.(6), the matrix form in eq.(7) is expressed as

$$\begin{aligned} u_r(x) \cong u_{rN}(x) &= T(x)C_r = L(x)MC_r \\ u_r'(x) \cong u_{rN}'(x) &= T(x)C_r = L(x)BMC_r \\ u_r''(x) \cong u_{rN}''(x) &= T(x)C_r = L(x)B^2MC_r \end{aligned} \tag{8}$$

Moreover,

$$L(x) = L(x)\,, L'(x) = L(x)B,\ L''(x) = L(x)B^2 \tag{9}$$

The collocation points of Chebyshev polynomials are defined as

$$x_i = a + \frac{(b-a)i}{N}, \quad i = 0,1,2,\ldots N. \tag{10}$$

By replacing the collocation points into eq. (8), we achieve

$$u_r^{(k)}(x_i) = L(x_i)B^{(k)}MC_r, \quad k = 0,1 \tag{11}$$

where,

$$B = \begin{bmatrix} 0 & 1 & 0 & 0 & 0 & 0 & \cdots & 0 \\ 0 & 0 & 2 & 0 & 0 & 0 & \cdots & 0 \\ 0 & 0 & 0 & 3 & 0 & 0 & \cdots & 0 \\ 0 & 0 & 0 & 0 & 4 & 0 & \cdots & 0 \\ 0 & 0 & 0 & 0 & 0 & 5 & \cdots & 0 \\ 0 & 0 & 0 & 0 & 0 & 0 & \ddots & 0 \\ \vdots & \vdots & \vdots & \vdots & \vdots & \vdots & \vdots & N \\ 0 & 0 & 0 & 0 & 0 & 0 & 0 & 0 \end{bmatrix}, \quad L\begin{bmatrix} L(x_0) \\ L(x_1) \\ \vdots \\ L(x_N) \end{bmatrix} = \begin{bmatrix} 1 & x_0 & \cdots & x_0^N \\ 1 & x_1 & \cdots & x_1^N \\ 1 & \vdots & \ddots & \vdots \\ 1 & x_N & \cdots & x_N^N \end{bmatrix},$$

$$P_{jkr} = \text{diagonal}\left[P_{jkr}(x_0) \quad P_{jkr}(x_1) \quad \cdots \quad P_{jkr}(x_N)\right]$$

And

$$G_j = \left[g_j(x_0) \quad g_j(x_1) \quad \cdots \quad g_j(x_N)\right]^T \quad j = 1,2,3. \tag{12}$$

Thus, we can get the following expression

$$\left[\sum_{k=0}^{1}\sum_{r=1}^{3} P_{jkr}B^{(k)}M\right]C_r = G_j, \quad k = 0,1, j = 1,2,3. \tag{13}$$

Briefly, Eq. (13) can also be written in the form,

$$WC = G \quad \text{or} \quad [W, G] \tag{14}$$

Where

$$W = \begin{bmatrix} w_{11} & w_{12} & w_{13} \\ w_{21} & w_{22} & w_{23} \\ w_{31} & w_{32} & w_{33} \end{bmatrix}, C = \begin{bmatrix} C_1 \\ C_2 \\ C_3 \end{bmatrix}, G = \begin{bmatrix} G_1 \\ G_2 \\ G_3 \end{bmatrix} \tag{15}$$

$w_{11} = \sum_{k=0}^{1}\sum_{r=1}^{1} P_{jkr}B^{(k)}M$

$w_{12} = \sum_{k=0}^{1}\sum_{r=2}^{2} P_{jkr}B^{(k)}M \text{ for } j = 1,$

$w_{13} = \sum_{k=0}^{1}\sum_{r=3}^{3} P_{jkr}B^{(k)}M$

$w_{21} = \sum_{k=0}^{1}\sum_{r=1}^{1} P_{jkr}B^{(k)}M$

$w_{22} = \sum_{k=0}^{1}\sum_{r=2}^{2} P_{jkr}B^{(k)}M \text{ for } j = 2,$

$w_{23} = \sum_{k=0}^{1}\sum_{r=3}^{3} P_{jkr}B^{(k)}M$

$w_{31} = \sum_{k=0}^{1}\sum_{r=1}^{1} P_{jkr}B^{(k)}M$

$w_{32} = \sum_{k=0}^{1}\sum_{r=2}^{2} P_{jkr}B^{(k)}M \text{ for } j = 3.$

$w_{33} = \sum_{k=0}^{1}\sum_{r=3}^{3} P_{jkr}B^{(k)}M$

On the other hand, if the initial or boundary values are written in place and the necessary changes are made, a new augmented matrix is obtained. The new augmented matrix

$$\widetilde{W}C = \widetilde{G} \qquad \text{or} \qquad [\widetilde{W}, \widetilde{G}] \tag{16}$$

where

$$\widetilde{W} = \begin{bmatrix} \widetilde{w}_{11} & \widetilde{w}_{12} & \widetilde{w}_{13} \\ \widetilde{w}_{21} & \widetilde{w}_{22} & \widetilde{w}_{23} \\ \widetilde{w}_{31} & \widetilde{w}_{32} & \widetilde{w}_{33} \end{bmatrix}, \widetilde{G} = \begin{bmatrix} \widetilde{G}_1 \\ \widetilde{G}_2 \\ \widetilde{G}_3 \end{bmatrix} \tag{17}$$

The procedure requires replacing rows in the W matrix that are either all zeros or possess the same common factor, should the matrix be singular. Once this is done, solving the linear system (16) yields the unknown Chebyshev coefficients C, which are then plugged into (3) to find the Chebyshev polynomial solution.

**ERROR ESTIMATION**

To verify the reliability of the proposed method, this section presents the estimated error functions $E_{1,N}(x), E_{2,N}(x)$ and $E_{3,N}(x)$. The function $E_{i,N}(x)$, $i = 1,2,3$ may also serve as a useful indicator in cases where the exact analytical solutions are unavailable. For discrete points $x_k \in [a, b]$, the error functions $E_{1,N}(x_k), E_{2,N}(x_k)$ and $E_{3,N}(x_k)$ are defined accordingly

$$E_{1,N}(x) = \left| \sum_{k=0}^{1} \sum_{r=1}^{1} P_{1kr}(x) u_{r,N}^{(k)}(x) - g_1(x) \right| \cong 0$$

$$E_{2,N}(x) = \left| \sum_{k=0}^{1} \sum_{r=2}^{2} P_{2kr}(x) u_{r,N}^{(k)}(x) - g_2(x) \right| \cong 0$$

and

$$E_{3,N}(x) = \left| \sum_{k=0}^{1} \sum_{r=3}^{3} P_{3kr}(x) u_{r,N}^{(k)}(x) - g_3(x) \right| \cong 0$$

where $u_{1,N}(x), u_{2,N}(x)$and $u_{3,N}(x)$ are the approximate solutions of eq.(1).

**NUMERICAL EXAMPLES**

Let us consider that the lake model whose general form of the equation is given as follows.[11]

$$\frac{d\phi}{dx} = \frac{14}{850}\phi_2(x) + \frac{32}{1180}\phi_3(x) - \frac{24}{2900}\phi_1(x) - \frac{22}{2900}\phi_1(x) + f(x)$$

$$\frac{d\phi_2}{dx} = \frac{24}{2900}\phi_1(x) + \frac{8}{1180}\phi_3(x) - \frac{14}{850}\phi_2(x) - \frac{18}{2900}\phi_2(x)$$

$$\frac{d\phi_3}{dx} = \frac{22}{2900}\phi_1(x) + \frac{18}{850}\phi_2(x) - \frac{32}{1180}\phi_3(x) - \frac{8}{1180}\phi_3(x) \quad (18)$$

where $\phi_i(0) = 0$ for $i = 1,2,3$.

**Example1**

If $f(x) = 100$ is taken in the equation system given in (18), the approximate error values of the numerical solution of this system of equations are shown below in the form of tables.

**Table 1. Table 1 reports the computed numeric amounts of $E_{1,N}(x)$ at several discretization levels of N.**

| x | $E_{1,3}(x)$ | $E_{1,5}(x)$ | $E_{1,7}(x)$ |
|---|---|---|---|
| 0.0 | $3.99839.10^{-5}$ | $2.66311.10^{-10}$ | $2.84217.10^{-14}$ |
| 0.2 | $3.07076.10^{-5}$ | $1.24602.10^{-14}$ | $2.62633.10^{-14}$ |
| 0.4 | $2.46301.10^{-5}$ | $6.21422.10^{-10}$ | $3.21324.10^{-14}$ |
| 0.6 | $1.43302.10^{-4}$ | $6.86713.10^{-15}$ | $3.7424.10^{-14}$ |
| 0.8 | $3.42582.10^{-4}$ | $5.59275.10^{-9}$ | $2.79322.10^{-16}$ |
| 1.0 | $6.39742.10^{-4}$ | $2.2726.10^{-8}$ | $1.92648.10^{-13}$ |

**Table 2. Table 2 reports the computed numeric amounts of $E_{2,N}(x)$ at several discretization levels of N.**

| x | $E_{2,3}(x)$ | $E_{2,5}(x)$ | $E_{2,7}(x)$ |
|---|---|---|---|
| 0.0 | $3.43765.10^{-5}$ | $4.67142.10^{-10}$ | $2.98195.10^{-15}$ |
| 0.2 | $2.64011.10^{-5}$ | $4.27345.10^{-17}$ | $2.4266.10^{-15}$ |
| 0.4 | $2.11759.10^{-5}$ | $1.09.10^{-9}$ | $2.37072.10^{-15}$ |
| 0.6 | $1.23205.10^{-4}$ | $1.98064.10^{-16}$ | $2.27145.10^{-14}$ |
| 0.8 | $2.94537.10^{-4}$ | $9.80998.10^{-9}$ | $1.03508.10^{-13}$ |
| 1.0 | $5.50023.10^{-4}$ | $3.98628.10^{-8}$ | $1.22727.10^{-12}$ |

**Table 3. Table 3 reports the computed numeric amounts of $E_{3,N}(x)$ at several discretization levels of N.**

| x | $E_{3,3}(x)$ | $E_{3,5}(x)$ | $E_{3,7}(x)$ |
|---|---|---|---|
| 0.0 | $5.60743.10^{-6}$ | $2.00823.10^{-10}$ | $2.79752.10^{-15}$ |
| 0.2 | $4.30651.10^{-6}$ | $2.48859.10^{-17}$ | $2.35187.10^{-15}$ |
| 0.4 | $3.45418.10^{-6}$ | $4.68588.10^{-10}$ | $2.43897.10^{-15}$ |
| 0.6 | $2.0097.10^{-5}$ | $5.45179.10^{-18}$ | $2.09855.10^{-14}$ |
| 0.8 | $4.80445.10^{-5}$ | $4.21729.10^{-9}$ | $9.79106.10^{-14}$ |
| 1.0 | $8.97189.10^{-5}$ | $1.71369.10^{-8}$ | $1.15587.10^{-12}$ |

**Example2**

If $f(x) = 1 + \sin(x)$ is taken in the equation system given in (18), the approximate error values of the numerical solution of this system of equations are shown below in the form of tables.

**Table 4. The numerical evaluation of $E_{1,N}(x)$, carried out for different values of N, is presented in Table 4.**

| x | $E_{1,3}(x)$ | $E_{1,5}(x)$ | $E_{1,7}(x)$ |
|---|---|---|---|
| 0.0 | $1.75974.10^{-2}$ | $1.16361.10^{-4}$ | $3.71146.10^{-7}$ |
| 0.2 | $1.36255.10^{-2}$ | $3.05311.10^{-16}$ | $3.08915.10^{-7}$ |
| 0.4 | $1.09728.10^{-2}$ | $2.73076.10^{-4}$ | $3.15482.10^{-7}$ |
| 0.6 | $6.3838.10^{-2}$ | $1.11022.10^{-16}$ | $2.80206.10^{-6}$ |
| 0.8 | $1.51992.10^{-1}$ | $2.45292.10^{-3}$ | $1.28478.10^{-5}$ |
| 1.0 | $2.81558.10^{-1}$ | $9.92951.10^{-3}$ | $1.52021.10^{-4}$ |

**Table 5. The numerical evaluation of $E_{2,N}(x)$, carried out for different values of N, is presented in Table 5.**

| x | $E_{2,3}(x)$ | $E_{2,5}(x)$ | $E_{2,7}(x)$ |
|---|---|---|---|
| 0.0 | $4.22008.10^{-5}$ | $1.47554.10^{-7}$ | $2.94352.10^{-10}$ |
| 0.2 | $3.24102.10^{-5}$ | $1.27752.10^{-16}$ | $2.44451.10^{-10}$ |
| 0.4 | $2.59957.10^{-5}$ | $3.44292.10^{-7}$ | $2.4937.10^{-10}$ |
| 0.6 | $1.51248.10^{-4}$ | $2.7053.10^{-16}$ | $2.21488.10^{-9}$ |
| 0.8 | $3.61577.10^{-4}$ | $3.09862.10^{-6}$ | $1.01669.10^{-8}$ |
| 1.0 | $6.75213.10^{-4}$ | $1.25912.10^{-5}$ | $1.20567.10^{-7}$ |

**Table 6. The numerical evaluation of $E_{3,N}(x)$, carried out for different values of N, is presented in Table 6.**

| x | $E_{3,3}(x)$ | $E_{3,5}(x)$ | $E_{3,7}(x)$ |
|---|---|---|---|
| 0.0 | $4.10451.10^{-5}$ | $1.53161.10^{-7}$ | $3.2743.10^{-10}$ |
| 0.2 | $3.15226.10^{-5}$ | $1.61941.10^{-16}$ | $2.71922.10^{-10}$ |
| 0.4 | $2.52838.10^{-5}$ | $3.57376.10^{-7}$ | $2.77393.10^{-10}$ |
| 0.6 | $1.47106.10^{-4}$ | $2.62656.10^{-16}$ | $2.46377.10^{-9}$ |
| 0.8 | $3.51674.10^{-4}$ | $3.21639.10^{-6}$ | $1.13094.10^{-8}$ |
| 1.0 | $6.56721.10^{-4}$ | $1.30698.10^{-5}$ | $1.34115.10^{-7}$ |

**Figure 1. $E_{i,7}(x)(i = 1, 2, 3)$ for Examp.1 for $N = 7$ are depicted in the interval $[-1, 1]$.**

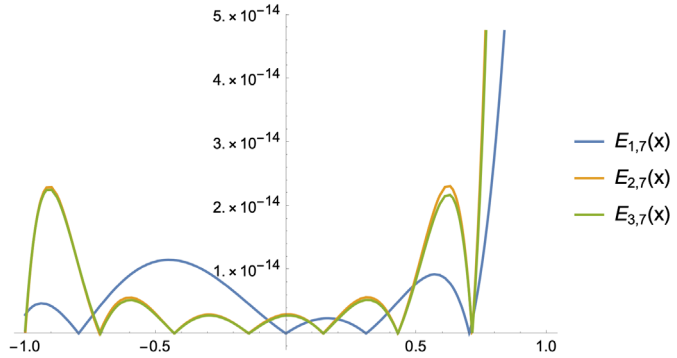


**Figure 2. $E_{i,7}(x)(i = 1, 2, 3)$ for Examp.2 for $N = 7$ are depicted in the interval $[-1, 1]$.**

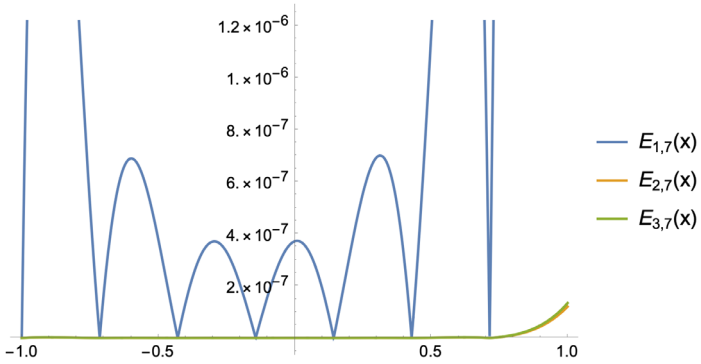


## CONCLUSION

In this work, we focused on the approximate solution of the lake pollution model differential equation and the approximate error values were presented in tables. While performing these operations, Chebyshev collocation method was used. In addition, a graphical representation of the approximate error values found is also presented.

## REFERENCES


1. Chebyshev, P. L., ( 1854), Théorie des Mécanismes Connus Sous le Nom de Parallélogrammes, Mémories Presentes Academie Imperiale des Science de St-Pétersbourg VII, (539-568).
2. Lanczos, Cornelius, (1938), Trigonometric Interpolation of Empirical and Analytical Functions, Journal of Mathematics and Physics Volume 17 Issue 1 (123-199).
3. Clenshaw, C. W., (1957), The Numerical Solution of Linear Differantial Equations in Chebyshev Series, Proceedings of the Cambridge Philosophical Society, Vol.53 ,(134-149).
4. Mason, J. C. ve Handscomb, D. C., ( 2003), Chebyshev Polynomials, Chapman&Hall/Crc Press LLC.
5. Fox, L. ve Parker, I. B. , (1968), Chebyshev Polynomials in Numerical Analysis, Oxford University Press.
6. Rivlin, Theodore J.J., (1974), The Chebyshev Polynomials, John Wiley & Sons Inc. Inc..
7. Ayşegül Akyüz, Mehmet Sezer, (2003), Chebyshev polynomial solutions of systemsof high-order linear differential equations with variable coefficients, Applied Mathematics and Computation 144 237–247.
8. M. Sezer, M. Kaynak, (1996), Chebyshev polynomial solutions of linear differential equations, Int. J. Math. Educ. Sci. Technol. 27 (4) (1996) 607–618.
9. Montri Thongmoona, Sasitorn Pusjuso, (2010), The numerical solutions of differential transform method and the Laplace transform method for a system of differential equations, Nonlinear Analysis: Hybrid Systems 4 , 425–431.
10. A. Akyüz, ( 2000), Doğrusal integrodiferansiyel denklem sistemlerinin Chebyshev sralama yöntemi ile yaklaşıık çözümleri. Ph.D. Thesis, Dokuz Eyl€ul University Graduate School of Natural and Applied Sciences.
11. Yeloglu, T., (2023), On the Solution of lake Pollution Model by Sinc Collocation Method, THERMAL SCIENCE, Vol. 27, No. 4B, pp. 3385-3392.